Title
Millimeter and Near-Infrared Observations of Neptune's Atmospheric Dynamics

Author
Cook, Statia Honora Luszcz

Publication Date
2012

Peer reviewed|Thesis/dissertation

Millimeter and Near-Infrared Observations of Neptune's Atmospheric Dynamics

By

Statia Honora Luszcz Cook

A dissertation submitted in partial satisfaction of the

requirements for the degree of

Doctor of Philosophy

in

Astrophysics

in the

Graduate Division

of the

University of California, Berkeley

Committee in charge:

Professor Imke de Pater, Chair
Professor Eugene Chiang
Professor Carl Heiles
Professor Kristie Boering

Fall 2012

Millimeter and Near-Infrared Observations of Neptune's Atmospheric Dynamics

Abstract

Millimeter and Near-Infrared Observations of Neptune's Atmospheric Dynamics

by

Statia Honora Luszcz Cook

Doctor of Philosophy in Astrophysics

University of California, Berkeley

Professor Imke de Pater, Chair

The atmospheric chemistry and dynamics of the ice giants are critical to comprehending planetary diversity within our Solar System and beyond. The bulk composition of these planets, which can be investigated through the composition of their atmospheres, is intimately tied to their formation in the circumstellar disk. In this dissertation, I take a multi-wavelength approach to studying chemistry and large-scale circulation in the atmosphere of Neptune, one of the two local examples of ice giant planets.

In equilibrium, the molecule carbon monoxide (CO) should be confined to the warm interiors of the giant planets. Its presence in the upper atmosphere, therefore, indicates disequilibrium processes at work: either rapid transport from deeper levels where the molecules are thermodynamically stable, or production high in the atmosphere as a result of infall of material from the planet's environment. Using millimeter-wave interferometry with the Combined Array for Research in Millimeter-wave Astronomy (CARMA), I observe Neptune in two rotational transitions of CO. Radiative transfer modeling yields a CO profile with $0.1^{+0.2}_{-0.1}$ parts per million (ppm) of CO in the troposphere, and $1.1^{+0.2}_{-0.3}$ ppm in the stratosphere. The stratospheric abundance implies an infall rate of oxygen-bearing material of 0.5–20 $\times$ 10^8 cm^{-2} s^{-1} to Neptune's upper atmosphere, which is consistent with supply by (sub)kilometer-sized comets. I also revisit the calculation of Neptune's internal oxygen abundance using revised calculations for the $CO \rightarrow CH_4$ conversion timescale in the deep atmosphere (Visscher & Moses 2011), in the context of my derived CO profile. The best-fit solution of 0.1 ppm of CO in the troposphere implies a global O/H enrichment of at least 400, and likely more than 650 times the protosolar value. This is one order of magnitude greater than Neptune's observed carbon enrichment relative to solar. However, the CO profile is also consistent with 0.0 ppm of CO in the troposphere, in which case no over-enrichment of oxygen in the interior is required.

Maps of Neptune in and near the CO (2–1) line from CARMA show spatial variations in the intensity at the 2–3% level. Variations at frequencies in the CO line are consistent

with variations in zonal-mean temperature near the tropopause. At continuum wavelengths, I observe a gradient in the brightness temperature, increasing by 2–3 K from 40°N to the south pole. This corresponds to an opacity decrease of about 0.3 (30%) near the south pole at altitudes below 1 bar, or a factor of 100 decrease in the opacity at altitudes below 4 bar. A global circulation pattern in which moist air rises at mid- southern and northern latitudes and dry air subsides near the equator and south pole is consistent with the south polar brightening observed in the millimeter.

At near-infrared wavelengths, observations are sensitive to sunlight reflected from clouds and hazes in the upper atmosphere. These clouds act as tracers of atmospheric dynamics, which aid in the determination of Neptune's large-scale circulation. Near-infrared images of Neptune from the W.M. Keck II telescope from July 2007 show that the unresolved cloud feature typically observed within a few degrees of Neptune's south pole had split into a pair of bright spots. A careful determination of disk center places the cloud centers within 2 degrees of, but not directly at, Neptune's south pole. When modeled as optically thick, perfectly reflecting layers, the two features are found to be in the troposphere, at pressures greater than 0.4 bar. Images with comparable resolution taken two days later reveal only a single feature near the south pole. The changing morphology of these circumpolar clouds suggests they may form in a region of strong convection surrounding a Neptunian south polar vortex.

Additional near-infrared observations were performed with the OSIRIS integral-field spectrograph on the Keck telescope. I present three-dimensional data cubes covering more than 90% of the visible hemisphere of Neptune, with a spatial resolution of 0.035" per pixel and spectral resolution of R $\sim$ 3800, in the H (1.47–1.80 μm) and K (1.97–2.38 μm) broad bands. In my preliminary radiative transfer analysis of these data, I find that the observed spectra are generally well fit by models with three cloud layers: a stratospheric haze layer, a tropospheric haze layer and a low albedo, optically thick bottom cloud at 2 bar. Models are consistent with a north-south hemispheric asymmetry in the properties of the clouds, with both bright and dark features in the north at higher altitudes than equivalent regions in the south. The range of derived altitudes between the highest and deepest features is nearly 5 atmospheric scale heights. The highest concentration of features can be found within a bright band extending from 30 to 45°S. I find that these features can all be fit by hazes at the same altitude, by varying only the haze particle densities. In contrast, I find that two features near 60°S appear to be at very different altitudes, even though they are at the same latitude.

To my family. I love you.

Contents

List of Figures

List of Tables

Acknowledgments

I would like to start off by extending my sincere thanks to Professors Kristie Boering, Eugene Chiang, Carl Heiles and Imke de Pater for serving as my dissertation committee. I owe additional thanks to Eugene for acting as my academic advisor, and for teaching me how to think like a scientist. Carl, thank you for taking interest in my research and for teaching me the importance of readable fonts and clear labels in figures and presentations. Both of you have gone beyond the call of duty, and I am grateful for your words of wisdom and encouragement.

Imke, as chair of this department, you have been insanely busy, but you have always made me a priority. For that, I cannot thank you enough. Thank you also for making sure I had the tools I needed to do my research and to grow as a scientist, by helping me acquire data, sending me to summer schools and conferences, and making sure I had funding. Not every graduate student is so lucky.

On the topic of funding, I have to acknowledge that the ability to pursue a Ph.D. in astrophysics is truly a gift. I am grateful to live in a society that recognizes the value in learning about the universe we live in, even when more practical, tangible gains are not obvious. I would like to acknowledge the two fellowships that have supported me over the majority of my graduate career: the UC Berkeley Chancellor's Fellowship and the NASA Earth and Space Science Fellowship. I have also received substantial support from the National Science Foundation and from CARMA grants. I would never have made it to Berkeley in the first place without the financial support of my parents.

I have had the pleasure to be a part of two different communities at Berkeley. From the planetary side of things, I have been enriched by the seminars and discussions held by the Center for Integrative Planetary Science. I would like to acknowledge Máté Ádámkovics, Katherine de Kleer and Mike Wong for helping build the foundations of a flexible and useful giant planet near-infrared radiative transfer code. This code would not exist without Mate's framework, and Katherine has been an invaluable sounding board for ideas over the past couple of years. I hope we continue to collaborate in the future.

I never envisioned myself becoming a radio astronomer, but I am so glad that I did. The people in the Radio Astronomy Lab community have been incredibly generous with their time and have made Berkeley a place where I want to be. I have to extend particular acknowledgement to Mel Wright, Dick Plambeck, Peter Williams, Chat Hull and Amber Bauermeister for helping me navigate the complex world of interferometry. Chat and Amber:

I look back fondly on our days observing together at CARMA- there is nothing like clearing snow at 4am to bring people together. I would also like to thank Laura Perez for teaching me the fundamentals of being a CARMA observer, and the CARMA staff, especially Nikolaus Volgenau, for being welcoming, patient and supportive as I grew from an inept, bumbling sleep-deprived newbie to a slightly less inept yet equally sleep-deprived experienced observer. I am certain I would not have survived my many weeks of CARMA observing without Cecil's excellent cooking.

I could not have asked for a better group of graduate students than those at Berkeley. Yookyung and Sarah: I have enjoyed having you as officemates at one time or another, as has Charlie. Sorry about the dog hair. I have to acknowledge my MONSTER class – to quote Peter Williams: "it must be some bizarre statistical fluke for my classmates to all be so awesome." Above all, Amber Bauermeister has filled a lot of shoes – classmate, officemate, trail guide, sounding board, co-observer, collaborator, co-organizer, and friend to name just a few. Puzzling out various problems with Amber has been perhaps the greatest pleasure of my graduate student career, and I doubt I would have gotten to this point if not for her help, humor and exceptional formatting advice.

There are several other individuals to whom I owe special thanks. Hope Weiss is another person who has filled many roles in my life; most importantly she is the best friend anyone could ever have. Joe Harrington, my research advisor at Cornell University, taught me how to code and helped me appreciate my potential to be a good scientist. I would also like to acknowledge the incredible volunteers I have met at Oakland Animal Services and Chabot Space and Science Center. Thank you for welcoming me into your ranks and sharing with me your kindness, enthusiasm, and faith that we can make the world a better place. My sincere thanks go to Dexter Stewart for her constant smile and unrelenting help with several administrative challenges during my time as a graduate student. I probably would have had several panic attacks without you!

I often feel that graduate school is, more than anything else, a test of endurance. Thank you to my family for believing in me even when I was ready to quit. To the members of Edge Cruise 2012, my life is so much richer with you in it. I look forward to many more adventures with all of you. Dan and Maggie: it's great having you as family, even better to have you as such dear friends as well. To Ilene, Phil and Dina – all I can say is I lucked out tremendously. Mom, you have always been my biggest supporter, and you give me the strength to face even the greatest challenges one day at a time. We have, after all, conquered mountains together. Dad, thank you for reminding me how exciting the universe is. Thank you both for loving me deeply and for supporting me in every way and in every path I take.

Finally, I have to thank Charlie Bones Cook, for the joy and laughter he brings to my life; and my husband, Jonathan, who has held my hand through exams, proposals and papers; traveled the world with me on my astronomical adventures; and most recently, without complaint, proofread this entire thesis. Jon, there are no words to adequately express how much I love you and how much I love our life together. Now, on to the next adventure!

Chapter 1

Introduction

Solar System science has the unique advantage over most subfields of astronomy that the objects of study are close enough to explore directly. Recent and ongoing space programs exist for all of the terrestrial planets and for the gas giants Jupiter and Saturn. However, the ice giants Uranus and Neptune have been visited only once by spacecraft, with the flyby of *Voyager 2*. This neglect is due to the unique technological and financial challenges of sending spacecraft to orbit such distant objects. In spite of this, we have developed a rich understanding of Neptune's properties by complementing the *Voyager* data with Earth-based observations. However, conventional ground-based approaches are limited by the Earth's atmosphere to a maximum spatial resolution of about 0.5", which is roughly half of one Neptune radius. In this chapter I present an overview of how our understanding of Neptune has developed over time. I discuss some of the most interesting questions that remain about Neptune's composition and dynamics, and the technology we can use to overcome the main challenge of ground-based observation: Earth's atmosphere.

1.1 Neptune and its atmosphere: a historical perspective

The discovery of Neptune in 1846 marked the first time in history that a planet was predicted to exist before it was observed. Not long before, in 1781, the planet Uranus had been discovered fortuitously by William Herschel. Within 10 years of this discovery, it became clear that Uranus was not following the path expected from orbital calculations. Astronomers began to surmise that something – perhaps an unknown trans-uranian planet – was causing Uranus' orbital deviations. Two astronomers, John Adams and Urbain le Verrier, independently used the perturbations of Uranus' orbit to predict the location of this unseen planet. Using the results of le Verrier's calculations, astronomer J. G. Galle successfully identified Neptune with a 9-inch refractor telescope by searching the sky for a 'star' that appeared to move between nights.

Since its discovery, Neptune has completed just over one orbit around the Sun. The great distance that separates Neptune and the Sun – 30 times larger than the separation between the Sun and Earth – makes Neptune both very dim (its average magnitude is 7.8, which is too faint to see with the naked eye) and very small (only 2.5” across - Fig. 1.1) when observed from Earth. Due to blurring by the atmosphere, the resolution of traditional Earth-based optical telescopes is limited to 0.5”; as a result, Neptune looked like nothing more than a fuzzy blue disk for many years after its discovery, and progress towards understanding its physical properties was very slow until the flyby of the spacecraft *Voyager 2* in 1989.

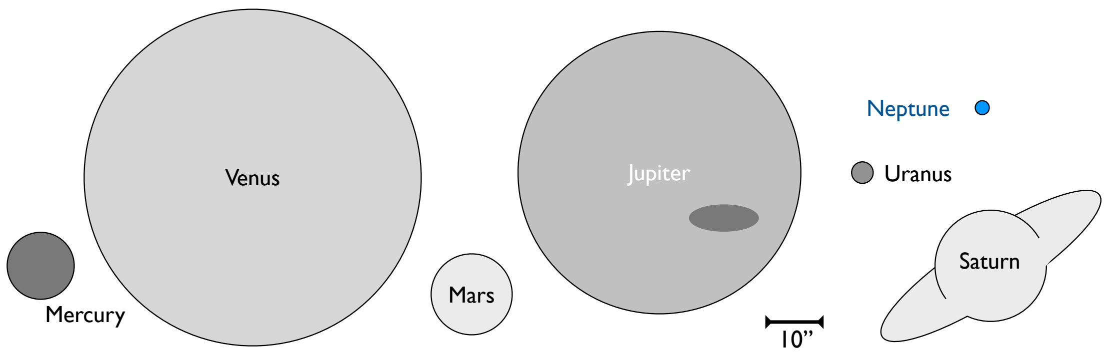

Figure 1.1: Angular sizes of the planets at closest approach to Earth in 2012. Angular size of Jupiter's Great Red Spot is also shown – Neptune is smaller on the sky than even this single (albeit large) storm on Jupiter. Scale is indicated.

1.1.1 Three types of planets

Among the first properties that were measured for Neptune were its distance, mass and radius. Approximate orbital parameters (which uniquely describe a planet's path around the Sun) were calculated for Neptune within a few years of its discovery by charting its motion across the sky (Newcomb 1866). Once its distance from Earth was known, Neptune's radius could be estimated from its angular size, which is related to physical size by

$$\delta \approx d/D$$

for small angular diameter (δ), where d is the physical diameter of the planet and D is the distance to the planet. Early measurements of Neptune's angular size, which were made using a micrometer, had large uncertainties, but it was clear from these observations that Neptune was similar in diameter to the planet Uranus. Neptune's mass was estimated with much greater accuracy than its radius using the orbit of Neptune's largest moon, Triton, which was discovered the same year as Neptune itself. The mass of Neptune was determined to be about 17 Earth masses, or 1/20 of a Jupiter mass. From mass and radius, average density can be easily calculated:

$$\rho = \frac{3M}{4\pi R^3}$$

Average density is the first clue to a planet's composition, but in itself does not uniquely determine the composition. Furthermore, matter acts differently at the high pressures and moderate temperatures of planetary interiors than it does under normal Earth conditions. Models of interior structure and composition require knowledge of the equation of state of the potential constituents of the planets. Much of this theory was not developed until the first half of the 20th century, and even today the experimental data on equations of state remain limited to a small area of the pressure – temperature phase space.

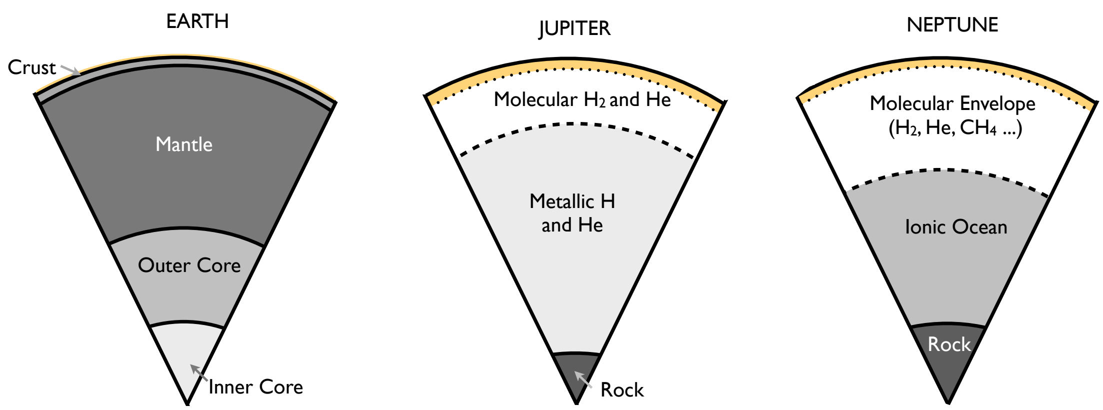

Figure 1.2: Structure of the three main types of planets in our Solar System. While the bulk compositions of Jupiter and Saturn are very different than Uranus and Neptune, the observable atmospheres of all four giant planets (yellow) are very similar.

First-order estimates of the composition of the planets are made by determining the relative amounts of the three categories of matter that comprise our Solar System: 'gas', which in this context refers to hydrogen and helium, the elements that constitute more than 98% of the Sun; 'ices', or condensable volatiles, which are gaseous at room temperature but condense at the cooler temperatures of the outer Solar System, like water, ammonia and methane; and 'rock', the solid material that makes up most of the Earth. Based on their densities, we can divide the planets in our Solar System into three distinct compositional classes. The terrestrial bodies, like Earth, are 'rocky'. At the other extreme, Jupiter and Saturn are 80-90% hydrogen and helium, and therefore are referred to as the 'gas giants'. Uranus and Neptune are intermediate in density between the rocky terrestrial planets and the gas giants. Since they lie between the extremes of rock and gas, their densities are hardest to translate into composition, because a mix of gas and rock can closely mimic the density behavior of ice. However, most models require Uranus and Neptune to be dominated by ices. Fig. 1.2 shows the general structure of three planets: Earth, Jupiter and Neptune, representing the three compositional classes.

1.1.2 Spectroscopy

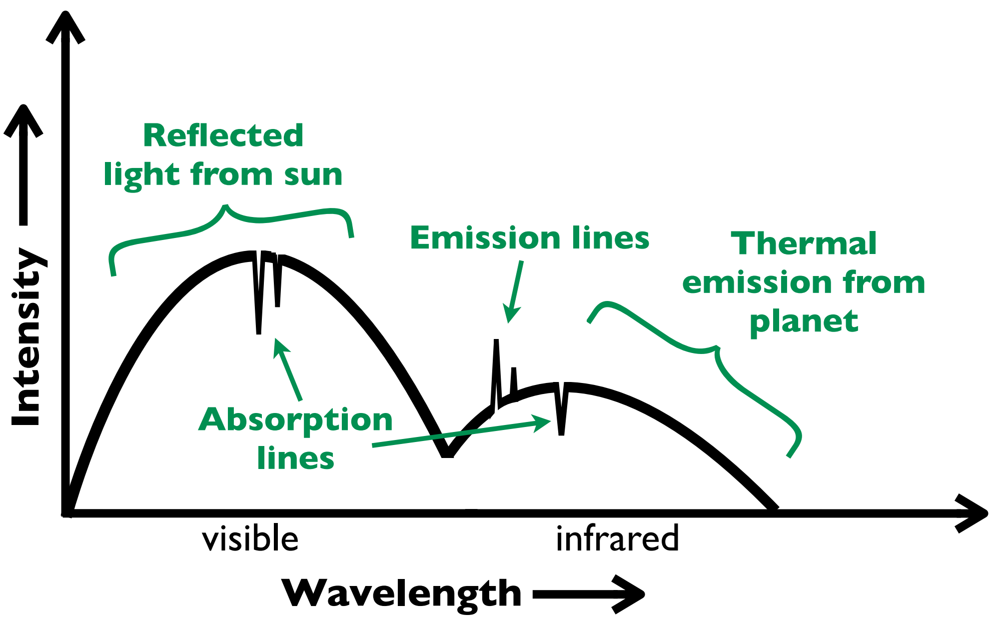

Figure 1.3: Simple model of a planet spectrum. Reflected sunlight peaks in the visible, and thermal emission from the planet peaks in the infrared. Absorption and emission lines occur due to molecular and atomic transitions in the atmosphere.

The field of spectroscopy, which is the study of light and how it interacts with matter, was developed around the same time that Neptune was discovered. A planet's spectrum, which is the intensity of light as a function of wavelength, is a critical tool for understanding many of the properties of its atmosphere. For giant planets, which do not have surfaces, spectroscopy is also one of our main tools for measuring bulk properties. The toy model in Fig. 1.3 illustrates several of the main properties of planetary spectra. At visible wavelengths, we observe planets in reflected sunlight. Sunlight is scattered off of clouds and other particles in the atmosphere, as well as absorbed and emitted by the gases that compose the atmosphere.

Absorption lines

Absorption lines in the giant planet atmospheres were first discovered in 1909. It took another 20 years before these lines were identified as methane (and ammonia in the case of Jupiter) with laboratory measurements. In spite of the difficulty associated with detecting hydrogen and helium (they lack electric dipole moments and mostly absorb during collisions) it was eventually shown that the atmospheres of all four giant planets are composed primarily of these light gases. Thus, we find that, in contrast to the huge diversity seen in terrestrial planet atmospheres, and in spite of the bulk compositional differences between the gas giants and ice giants, all of the giant planets in our Solar System (to first order) have the same atmospheric composition.

Thermal emission

At longer wavelengths, thermal emission from the planet itself begins to dominate over light reflected from the Sun. This thermal emission depends on the temperature of the atmosphere where the atmosphere becomes opaque – that is, where the optical depth of the atmosphere exceeds one. This component of the planet's spectrum allows us to determine the planetary energy balance, defined as the ratio of the average total infrared energy flux from the planet to the value for thermalized sunlight alone. Neptune's energy balance implies that it is emitting about twice as much energy as it receives. Jupiter and Saturn also radiate more energy than they absorb from the Sun, which indicates that these planets have significant internal heat sources, whereas Uranus and the terrestrial planets do not. One major consequence of Neptune's intrinsic heat flux is that its interior is convective, which means that heat is transported by large-scale motions of the material. This process causes material to mix efficiently, and forces the temperature profile to follow an adiabat, where the change in temperature with altitude ($dT/dz \equiv$ the 'lapse rate') is given by:

$$\frac{dT}{dz} = -\frac{g}{c_p} \tag{1.1}$$

where g is the acceleration due to gravity and c_p is the specific heat of the gas at constant pressure. This lapse rate (the 'dry' adiabatic lapse rate) is modified by condensation into clouds, which releases latent heat and decreases the rate at which temperature decreases with altitude:

$$\frac{dT}{dz} = -\frac{g}{c_p + L_s dw_s/dT}$$

where L_s is the latent heat of condensation, and w_s is the mass fraction of the condensates. I will discuss clouds more in the following sections.

1.1.3 The *Voyager* era

Voyager 2 was the first and only spacecraft to travel to Neptune. In contrast to the crawling pace of discovery during the preceding century, the *Voyager* era represented an

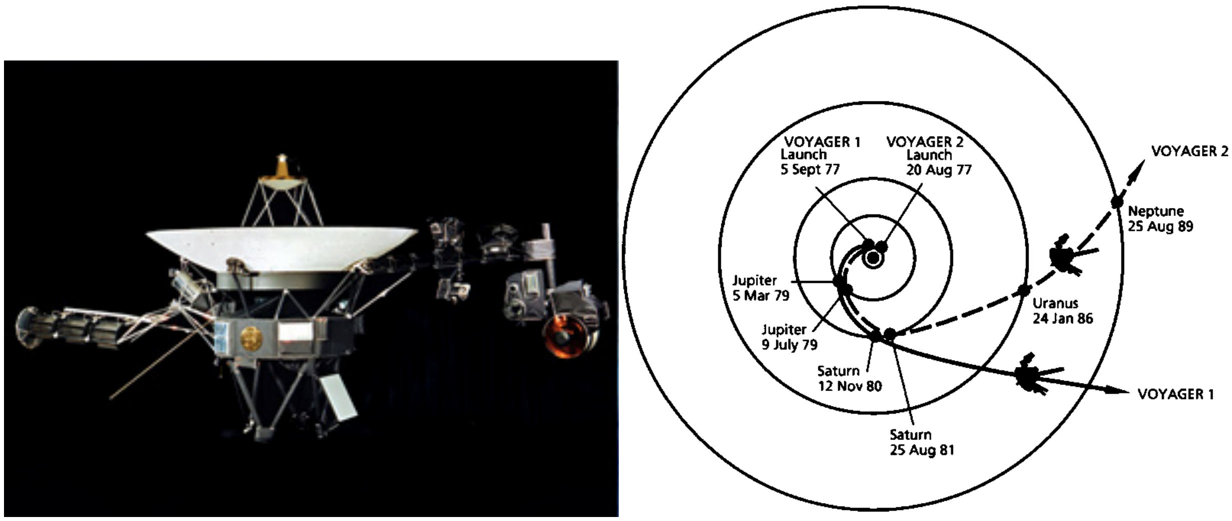

Figure 1.4: Left: the *Voyager* spacecraft. Right: flight paths of *Voyager 1* and *Voyager 2*. *Image credit: NASA*.

enormous step forward in our understanding of the distant planet. *Voyager* grew out of the 'Grand Tour' – a mission conceived in the 1970's to explore the outer planets in a series of four launches – two to Jupiter, Saturn and Pluto, and two to Jupiter, Uranus and Neptune. The timing of the Grand Tour was critical because in the late 1970's all four giant planets were to be aligned, which would allow the spacecraft to use gravity boosts from Jupiter to speed them on their way to the outer Solar System. However, during the Vietnam War, NASA's budget was slashed. Among the cuts was the Grand Tour. *Voyager* was the reincarnation of the Grand Tour, a leaner mission of only two launches. These spacecraft would primarily target Jupiter and Saturn, with an option, if all went well, to continue on to Uranus and Neptune.

Figure 1.4 shows the flight paths of the two *Voyager* spacecraft. Both spacecraft successfully launched in 1977, reaching Jupiter in 1979 and Saturn in 1980. At Saturn there was a serious expectation that damage by impacts of dust grains from the rings would terminate *Voyager*'s useful data gathering. Indeed, after *Voyager 2* passed through Saturn's rings on its way to Uranus, the main platform, carrying the cameras and most of the other science instruments, got stuck. Fortunately, within a week the platform became unstuck, and *Voyager 2* continued on to reach Uranus in 1986 and Neptune in August of 1989, 12 years after its launch.

In the six months surrounding closest approach, *Voyager* took more than 9000 images of Neptune, passing within a few thousand miles of the planet. For reference, the Earth is on average three billion miles from Neptune – about a million times further away. Although there had been hints of atmospheric activity on Neptune from earlier ground-based observations, *Voyager* strikingly revealed Neptune's dynamic nature. In contrast with Uranus, which appeared nearly featureless in *Voyager* images, Neptune proved to have many discrete bright cloud features and light and dark bands. The smallest cloud features were observed to change morphology or shear apart completely on timescales as short as minutes. Such rapid evolution of the atmosphere was not observed on any of the other giant planets. On larger scales, a storm the size of Earth, nicknamed the Great Dark Spot, was discovered. The existence of the Great Dark Spot showed astronomers that Jupiter's famous Great Red Spot was not as unique as it was once thought. Prior to *Voyager*, Neptune had gained somewhat of a reputation as Uranus' sister planet, based on the similarity of their masses, radii and temperatures. In some ways, Neptune upheld this reputation throughout the *Voyager* encounter. Neptune's wind profile – the way the wind speed changes with latitude – is very similar to Uranus, and different from Jupiter and Saturn, where the winds are organized into much narrower bands. However, the winds on Neptune are shockingly fast – reaching 400 m s^{-1}, or 900 mph. This means Neptune, the most distant planet and therefore the planet with the least solar energy available to power its winds, has the fastest winds in

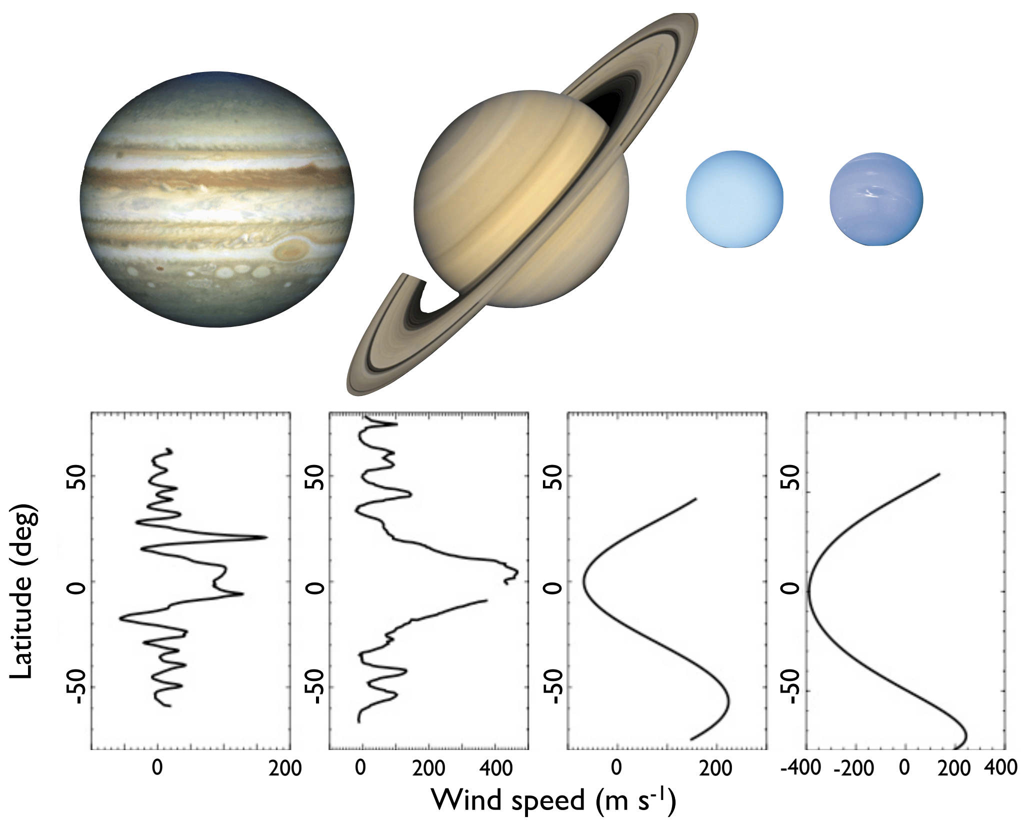

Figure 1.5: *Voyager* images of the four giant planets. From left to right: Jupiter, Saturn, Uranus and Neptune. Below each planet is its wind profile, as determined by tracking clouds in the atmosphere. *Image credit: adapted from NASA images.*

the Solar System (Fig. 1.5).

1.1.4 Vertical structure

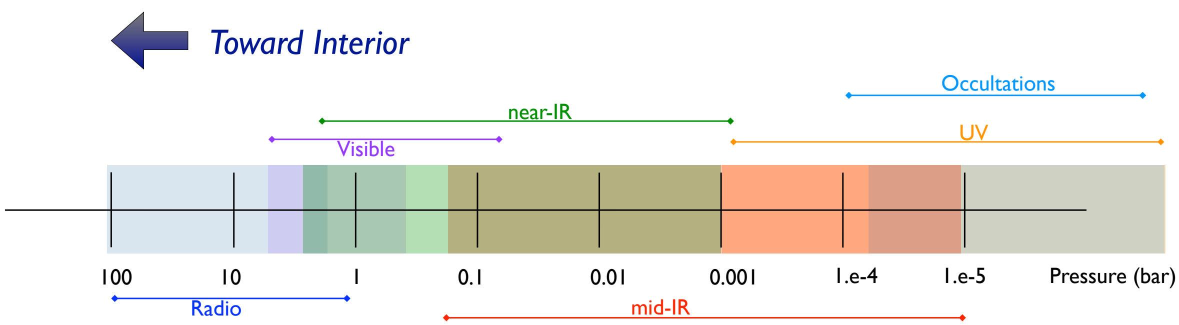

Figure 1.6: Approximate atmospheric pressure levels probed at different wavelengths. At the longest (radio) wavelengths, pressures of greater than 10 bar can be sensed. UV observations and stellar occultation measurements can probe the highest altitudes in the atmosphere.

With the addition of a wealth of new data from *Voyager*, astronomers were able to synthesize a detailed picture of the structure of Neptune's middle and upper atmosphere. Models of the vertical structure utilize the fact that the opacity is a strong function of wavelength, so that as you observe at different wavelengths, you probe different levels in the atmosphere. Figure 1.6 shows the approximate depths probed at different parts of the electromagnetic spectrum. Depths are measured in units of pressure: 1 bar is approximately the pressure of air at the Earth's surface. Since Neptune is surface-less, the atmosphere extends to much higher pressures. In hydrostatic equilibrium, altitude (z) and pressure (P) are related by the ideal gas law:

$$P(z) = P(0)\ e^{-\int dz/H}$$

H is the pressure scale height, defined as

$$H = \frac{kT(z)}{g\mu_a m_p}$$

where k is the Boltzmann constant, μ_a is the atmospheric mean molecular weight, and m_p is the mass of a proton. One scale height is the distance over which the pressure decreases by a factor of e (≈ 2.7). On Earth, one pressure scale height is about 8.5 km; on Neptune $H \sim 23$ km at 1 bar. We can see from Fig. 1.6 that we probe the atmosphere over many scale heights by observing at many different wavelengths.

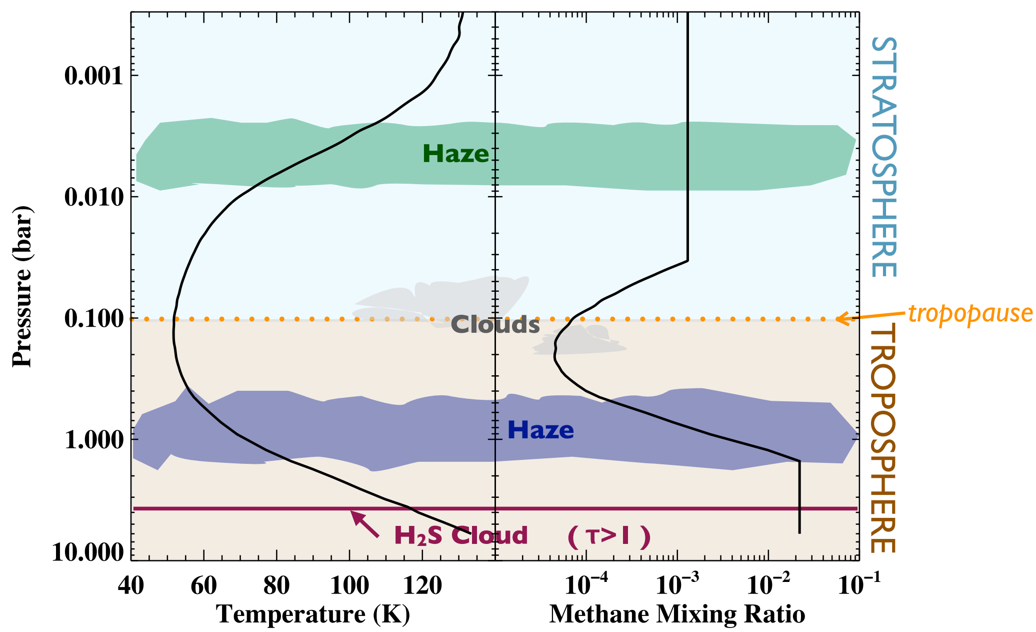

Figure 1.7: Vertical structure of Neptune's upper atmosphere, as determined after *Voyager*. Left plot: thermal profile, from *Voyager* occultation measurements (Lindal 1992). Right: methane mole fraction (fraction of methane molecules per unit volume): values above and below condensation are observed; in between, the curve follows the saturation vapor pressure curve, assuming 100% humidity.

Troposphere

Figure 1.7 illustrates several characteristics of Neptune's atmosphere. The curve on the left is a temperature-pressure, or thermal, profile, which illustrates how the temperature behaves as a function of altitude (pressure). In the upper atmosphere this can be derived from observations (e.g. Lindal 1992), while at deeper levels that cannot be probed directly, an adiabat is assumed (Eq. 1.1). Like on Earth, the temperature in Neptune's lower atmosphere decreases with altitude – this region of the atmosphere is called the 'troposphere'. The troposphere is where clouds form from trace species as they reach cooler levels where the temperature falls below the condensation temperature. The trace species that form clouds on giant planets are water, ammonia, hydrogen sulfide and methane (either pure or in solution). Most of these clouds condense at higher pressures than those shown in Fig. 1.7, and form global, optically thick layers. The top global cloud layer is likely H_2S; above this level, methane condenses into localized clouds like those seen in Fig. 1.8. As a result of cloud formation, the upper atmosphere is depleted in condensable species relative to the deep atmosphere.

Stratosphere

Almost all Solar System planets, including Neptune, have temperature inversions high in their atmospheres: moving out from the deep atmosphere (the troposphere), the temperature decreases to some minimum, and then begins to increase. The stratosphere is defined as the region where temperature increases with altitude. The temperature minimum that separates the stratosphere and troposphere, or 'tropopause', acts as a cold trap for condensable species, limiting the amount of these species in the upper atmosphere. The presence of a species in excess of its cold trap value implies that there is a mechanism either for carrying it up from deeper levels or for producing it in the stratosphere. For example, this is the case for methane on Neptune, as illustrated in Fig. 1.7. In this figure, the observed value for the methane mole fraction (fraction of methane molecules per unit volume) below the tropopause must decrease as methane reaches the condensation level. However, the observed stratospheric methane ratio is about an order of magnitude higher than the minimum value at the tropopause.

Methane plays an important role in Neptune's stratosphere, where it is photodissociated by UV photons, which sets off the wide array of chemical reactions that creates a variety of hydrocarbons. These hydrocarbons then sink until cooler temperatures cause them to condense and form hazes. These hazes absorb solar radiation, heating the upper atmosphere and giving rise to the temperature inversion. Similar processes happen on most other planets. On Earth, the warming agent is ozone.

Clouds and hazes are readily observed in *Voyager* images of Neptune; however their properties are difficult to measure. Understanding the altitude and composition of cloud features, and how these characteristics vary in location and time, is critical to understanding Neptune's atmospheric circulation and dynamics.

1.1.5 Post-*Voyager*

Decades after *Voyager 2* left Neptune for the outer reaches of the Solar System, much of what was learned by its flyby remains the state of the art. The physics behind several of the surprising phenomena observed by *Voyager* remains largely unresolved, such as what drives Neptune's fast winds, how clouds are formed and what they are made of, and Neptune's bulk composition and structure. Since it will likely be several decades before the next spacecraft visits Neptune, we are faced with the challenge of pursuing these mysteries from the ground. To do this, we must look for ways to deal with the detrimental effects of Earth's atmosphere on astronomical light.

High angular resolution techniques

Just as in the planets we study, Earth's own atmosphere affects the light passing through it, in ways that can substantially degrade observations. At some wavelengths, molecules in Earth's atmosphere, especially water and oxygen lines, absorb nearly all of the radiation.

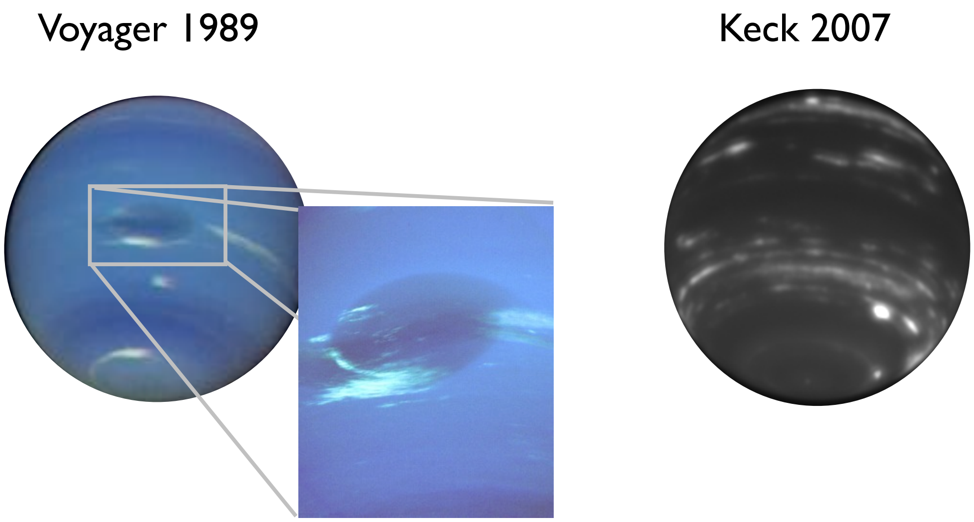

Figure 1.8: Left: *Voyager* image of Neptune in the methane band at 890 nm *Image credit: NASA/JPL*. Right: Keck AO image of Neptune in H band (1.6 μm) (Image adapted from Chapter 4).

Astronomers who wish to observe from Earth must therefore utilize atmospheric 'windows': wavelengths that are relatively clear of telluric (Earth) absorption lines and bands.

As mentioned in Section 1.1, turbulence in the atmosphere severely limits our ability to perform detailed observations from the ground. Without the atmosphere, astronomical resolution at a given wavelength depends only on the size of the telescope:

$$\sin\theta \approx \frac{\lambda}{D} \tag{1.2}$$

where θ is the angular resolution, λ is the wavelength of light being observed, and D is the diameter of the primary mirror of the telescope. However, turbulence perturbs the light from celestial objects as it travels to the ground, effectively reducing the resolution (at optical wavelengths) of a large telescope like the 10-meter Keck telescope to that of a 20-inch telescope. Perhaps the most straightforward way to circumvent this limitation is with a space-based observatory, such as the Hubble Space telescope, which avoids the atmosphere altogether. This technique has the added benefit of allowing observations at wavelengths that Earth's atmosphere blocks completely, such as the far-infrared. However space-based observatories have limited payloads, are expensive to build and are difficult to service.

Alternatively, one can employ strategies to reduce the effects of atmospheric distortion.

Two such techniques are adaptive optics and interferometry. Adaptive optics (AO) is a technique that uses a deformable mirror to compensate for atmospheric distortions in real time. Before reaching the detector, incoming light from the science target and a 'guide star' (point source) encounter a deformable mirror (Fig. 1.9). A beamsplitter directs the light from this guide star onto a wavefront sensor, which reconstructs the shape of the wavefront. The shape of the deformable mirror is then modified so that the light from the science target is corrected before it reaches the detector. The entire process must occur very rapidly, since atmospheric distortions vary on millisecond timescales. Because atmospheric coherence is much shorter at visible wavelengths, this technique works best longward of 1 μm, in the near-infrared. Adaptive optics has been a critical breakthrough for ground-based astronomy: AO systems implemented on large telescopes, such as the 10-m Keck telescope, produce images that rival Hubble. A near-infrared image of Neptune, with and without adaptive-optics correction, is shown in Fig. 1.9.

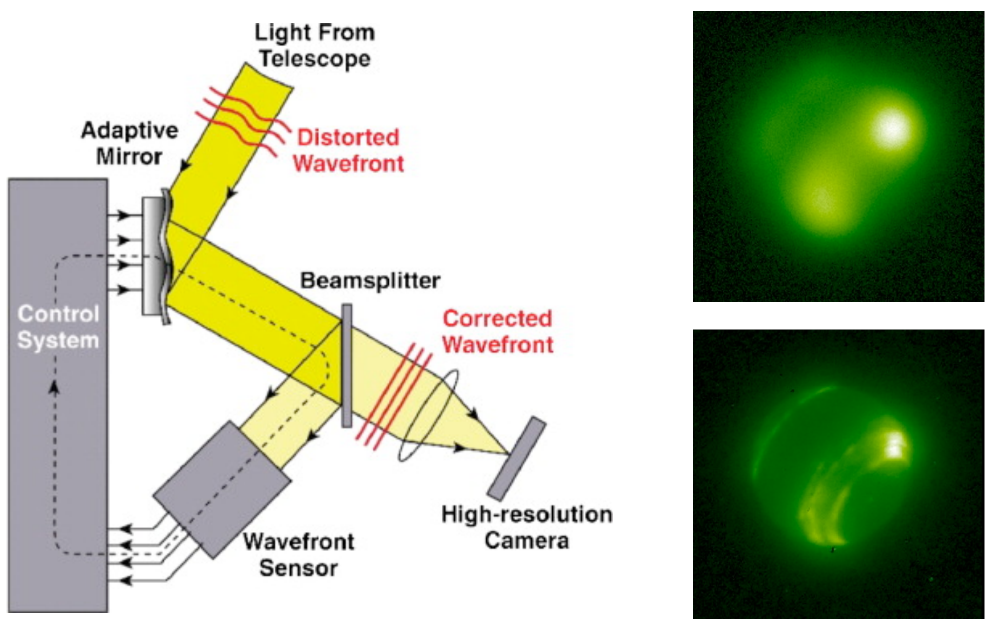

Figure 1.9: Left: diagram of an adaptive optics system. Right: Keck near-infrared image of Neptune with (bottom) and without (top) the benefit of the adaptive optics correction. *Image credit: Claire E. Max, UCSC (left) and Wizinowich et al. (2000) (right).*

At radio (millimeter and centimeter) wavelengths, interferometry is routinely used to make high angular resolution observations. Since the maximum theoretical resolution is given by the ratio of the wavelength and the telescope size (Eq. 1.2), longer wavelength observations require much larger telescope diameters to achieve the same resolution. This problem can be circumvented by using several smaller telescopes working together as one: an interferometer. For an interferometer, D is the length of the longest baseline, or distance between two radio telescopes, or 'antennas', rather than the size of each individual antenna. At millimeter wavelengths, variations in the water vapor density, rather than temperature variations, are the principle cause of atmospheric distortions. However, in interferometry, the fluctuations caused by the atmosphere can be calibrated out of the data in software, after the observations are taken. As a result, interferometry can obtain the highest angular resolution of any observational technique.

Long-term variability and global circulation

Observations with the Hubble and Keck telescopes in the 1990's provided our first detailed look at Neptune after *Voyager*. These data revealed that Neptune had changed dramatically since the *Voyager* flyby, indicative of significant variability of both individual features and the planet as a whole. Dominant features that were present throughout the *Voyager* era, such as the large storm named the Great Dark Spot, have since disappeared. The overall appearance of Neptune has changed as well: the average number of bright clouds has increased since *Voyager*, and the locations of the highest activity seem to have moved to different latitudes (Fig. 1.8). Such dramatic changes are surprising for a planet with 40-year seasons. On a global scale, observations have shown that the total brightness of Neptune has increased steadily since monitoring began in the 1950's. It remains unclear what drives the long term variability.

Maps of Neptune in the mid-infrared and radio, combined with *Voyager* results, provide a growing body of evidence for large-scale vertical and meridional circulation, in addition to the fast zonal jets. Conrath et al. (1991) determined that the tropopause temperature varies with latitude, with a minimum at mid-latitudes. They interpreted this temperature structure as evidence of a global circulation pattern in which moist air rises at mid latitudes and dry air sinks at the equator and poles. Since that time, observations at radio and mid-infrared wavelengths have corroborated this scenario, showing a south polar brightness temperature enhancement consistent with subsidence of dry air near the south pole.

Several questions remain about the global circulation of Neptune, such as: How deep does it go? Is it important for transporting material? Understanding these issues is key to addressing the further questions of: How and where is material brought up from the interior? How are the upper and lower atmospheres connected? And what are the roles of solar and internal heating in driving the circulation?

1.2 Outline of this dissertation

In this dissertation I use ground based observations in the millimeter and near-infrared to investigate Neptune's atmospheric composition and large-scale circulation. In Chapters 2 and 3, I present disk-integrated spectra and spatially-resolved maps of Neptune in the CO (1–

0) and (2–1) rotational transitions from the Combined Array for Research in Millimeter-wave Astronomy(CARMA). In Chapter 2 I present new determinations of Neptune's vertical CO profile, and derive constraints on the global oxygen abundance. I calculate the infall rate of CO to Neptune's upper atmosphere, and compare this to estimates of the cometary impact rate. The radiative transfer code developed for this project is also described. In Chapter 3 I present the first maps of Neptune's millimeter intensity, both in the continuum and within the CO line, and translate brightness variations into potential latitudinal gradients in the composition and temperature. Appendix A discusses one of the main challenges faced in determining Neptune's millimeter continuum spectrum: flux calibration of the data.

Chapters 4 and 5 focus on observations of Neptune in the near-infrared. Chapter 4 presents observations of clouds near the south pole, which support the idea of a Neptunian south polar vortex. Chapter 5 describes a more general, but preliminary, study of the properties of Neptune's clouds across the disk. I use the integral-field spectrograph OSIRIS on the Keck telescope to obtain spectra of individual features across more than 90% of the visible hemisphere. The radiative transfer code used to derive cloud properties of near-infrared cloud features is presented in Appendix B. Finally, I summarize in Chapter 6 and discuss some future directions for the study of ice giants at both millimeter and near-infrared wavelengths.

Chapter 2

Constraining the Origins of Neptune's Carbon Monoxide Abundance with CARMA Millimeter-wave Observations

We present observations of Neptune's 1- and 3-mm spectrum from the Combined Array for Research in Millimeter-wave Astronomy (CARMA). Radiative transfer analysis of the CO (2–1) and (1–0) rotation lines was performed to constrain the CO vertical abundance profile. We find that the data are well matched by a CO mole fraction of $0.1^{+0.2}_{-0.1}$ parts per million (ppm) in the troposphere, and $1.1^{+0.2}_{-0.3}$ ppm in the stratosphere. A flux of 0.5–20 $\times 10^8$ CO molecules cm^{-2} s^{-1} to the upper stratosphere is implied. Using the Zahnle et al. (2003) estimate for cometary impact rates at Neptune, we calculate the CO flux that could be formed from (sub)kilometer-sized comets; we find that if the diffusion rate near the tropopause is small (200 cm^2 s^{-1}), these impacts could produce a flux as high as $0.5^{+0.8}_{-0.4} \times 10^8$ CO molecules cm^{-2} s^{-1}. We also revisit the calculation of Neptune's internal CO contribution using revised calculations for the CO$\rightarrow$CH$_4$ conversion timescale in the deep atmosphere (Visscher & Moses 2011). We find that an upwelled CO mole fraction of 0.1 ppm implies a global O/H enrichment of at least 400, and likely more than 650, times the protosolar value. [1]

[1]This chapter has been accepted for publication in Icarus (Luszcz-Cook and de Pater, 2012) and has been reproduced with permission from the coauthor.

2.1 Introduction

In equilibrium, carbon monoxide (CO) should be confined to the warm interiors of the Solar System giant planets. Therefore, its detection in the upper atmospheres of all four of these planets (Beer 1975; Noll et al. 1986; Encrenaz et al. 2004; Marten et al. 1991) indicates disequilibrium processes at work. Two pathways exist for enriching the atmosphere in CO: vertical mixing from the deep atmosphere and external supply from the environment.

CO production occurs via the net thermochemical reaction

$$CH_4 + H_2O = CO + 3H_2. \tag{2.1}$$

At the temperatures and pressures of Neptune's atmosphere, the left-hand side of this equation dominates, with nearly all of the carbon present in the form of CH_4. Indeed, CH_4 has been observed in Neptune's troposphere at an abundance of 2.2% (Baines et al. 1995). CO is more stable and therefore more abundant at the warmer temperatures of the deep atmosphere. Consequently, CO abundances in the upper atmosphere can exceed their equilibrium value if convective transport from the warm interior is more rapid than the CO destruction rate (Prinn & Barshay 1977; Fegley & Prinn 1986). The CO abundance originating from the interior therefore depends on the internal water abundance (Eq. (1)) as well as the speed of vertical mixing, and thereby acts as a chemical probe of the deep atmosphere (Fegley & Lodders 1994; Lodders & Fegley 1994, 2002; Visscher et al. 2010).

An alternative source of CO in giant planet atmospheres is the planetary environment. Observations of stratospheric water and CO_2 (Feuchtgruber et al. 1997; de Graauw et al. 1997; Lellouch et al. 1997) indicate an external supply of oxygen to the giant planets, which could originate from rings and icy satellites or interplanetary dust (meteoroids) (Feuchtgruber et al. 1997; Encrenaz et al. 1999). Oxygen then forms CO by combining in the stratosphere with the byproducts of methane photolysis (Rosenqvist et al. 1992; Moses et al. 2000). However, the CO/H_2O ratios observed for Jupiter and Neptune seem to be inconsistent with oxygen supply by these mechanisms (Lellouch et al. 2002; Bézard et al. 2002; Lellouch et al. 2005). Shock chemistry due to infall of comets also can produce significant amounts of CO in the upper atmosphere, as demonstrated by the 1994 impact of comet Shoemaker-Levy 9 with Jupiter (Lellouch et al. 1995). Infall of (sub)kilometer-sized comets has been shown to be sufficient for supplying Jupiter's observed stratospheric CO abundance if the eddy mixing coefficient near the tropopause is smaller than 300 cm^2 s^{-1} (Bézard et al. 2002). Once it is produced, CO is stable and is removed from the stratosphere by downward transport.

Atmospheric CO enrichment by these two very different pathways can be distinguished by measuring the vertical CO profile: a uniform distribution of CO throughout the upper atmosphere indicates that CO is being mixed up to observable levels from the deep atmosphere. If instead CO is being produced in the stratosphere of the planet, then downward transport will act as a sink, and there will be a higher CO abundance in the stratosphere than the troposphere. Early measurements of Neptune's stratospheric (Marten et al. 1993; Rosenqvist et al. 1992; Marten et al. 2005) and tropospheric (Guilloteau et al. 1993; Naylor et al. 1994; Courtin et al. 1996; Encrenaz et al. 1996) CO mole fractions were all roughly consistent with a CO abundance of 1 part per million (ppm), which led several authors to tentatively conclude that Neptune's CO was internal in origin (e.g. Courtin et al. 1996; Marten et al. 2005). However, the estimates of Neptune's CO abundance from these observations were highly divergent. More recent observations (Lellouch et al. 2005; Hesman et al. 2007) suggest that both internal and external sources play a role in supplying CO to Neptune: these experiments simultaneously determine the stratospheric and tropospheric abundances from the shapes of CO rotational lines. Figure 1 illustrates the contributions of the various atmospheric levels to the line intensity at a range of frequency offsets from line center, for the three lowest CO rotational transitions. Peaks in the contribution functions range from above 0.1 mbar at line center, down to several bars in the far wings indicating that characterization of the full CO vertical profile requires both high frequency resolution to measure the shape of the narrow (∼10 MHz wide) central line peak, and broad frequency coverage (of order 6-10 GHz) to probe the CO mole fraction below the tropopause. From their analyses of the CO (2–1) and CO (3–2) lines, respectively, Lellouch et al. (2005) and Hesman et al. (2007) conclude that Neptune's CO mixing ratio is measurably higher in the stratosphere, indicating that CO has both an internal and external origin. Such a dual origin is also indicated for Jupiter and Saturn (Bézard et al. 2002; Cavalié et al. 2009). Quantitatively, however, the Lellouch et al. (2005) and Hesman et al. (2007) Neptunian CO profiles are inconsistent to within their quoted uncertainties, particularly in the upper stratosphere. Uncertainties in calibration and in Neptune's thermal profile may be responsible for discrepancies between these published CO values. Recent observations at infrared wavelengths have not resolved the discrepancy: Fletcher et al. (2010) found a CO mixing ratio of 2.5×10^{-6} (mole fraction of 2.1 ppm) at altitudes above 10 mbar, which is consistent with the Hesman et al. (2007) result, whereas Lellouch et al. (2010) favor a 1 ppm stratospheric mole fraction in agreement with Lellouch et al. (2005).

In this paper we present new observations and modeling of the CO (2–1) and (1–0) rotational lines in Neptune's millimeter spectrum in order to better constrain the vertical CO profile. We investigate how the uncertainty in Neptune's atmospheric thermal profile affects these constraints. This is followed by a discussion of the implications of our derived CO profile on Neptune's global oxygen abundance: updated laboratory measurements of reaction rates have shown that the chemical scheme proposed by Prinn & Barshay (1977) and adopted by Lodders & Fegley (1994) is actually too slow to be relevant for CO quenching kinetics (Griffith & Yelle 1999). Visscher & Moses (2011) have further revised the kinetic scheme for $CO \rightarrow CH_4$ conversion using new values for the reaction rate coefficients. Using this new rate-limiting step, we calculate the CO mole fraction that is transported upwards from Neptune's deep atmosphere, assuming an effective mixing length scale as determined by Smith (1998). We also use the Zahnle et al. (2003) impact rates to determine the effectiveness of cometary impacts in supplying oxygen to Neptune's atmosphere for stratospheric CO production.

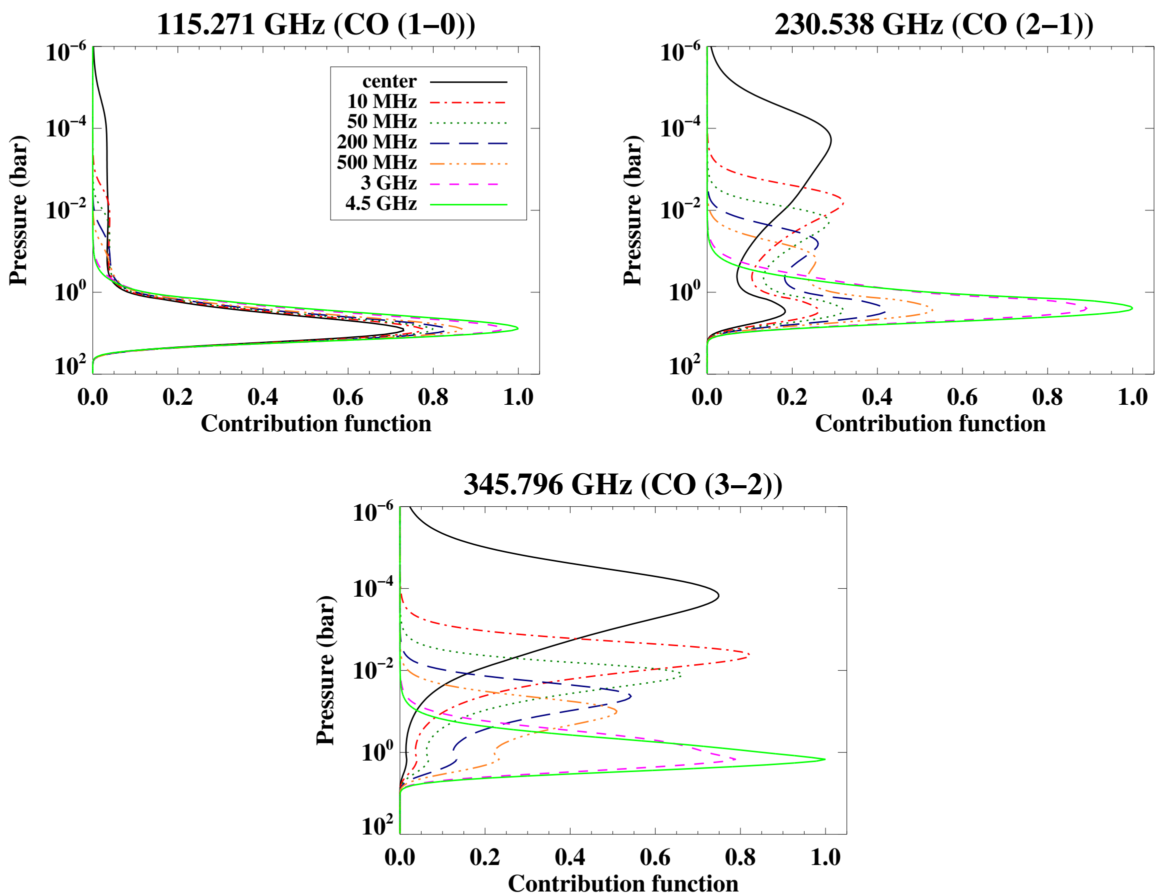

Figure 2.1: Contribution functions for the CO (1–0), (2–1), and (3–2) lines, illustrating the altitudes contributing to the line at offsets from 0 to 4.5 GHz from line center. The contribution functions include H_2-H_2, H_2-He and H_2-CH_4 collision-induced absorption, and absorption due to a constant 1 ppm abundance of CO. Close to line center, the emission originates in the stratosphere; at larger offsets from line center, deeper levels contribute to the line. The CO (1–0) and (2–1) lines are the subject of this work; the CO (3–2) line was observed most recently by Hesman et al. (2007).

2.2 Data

2.2.1 Observations

Disk-integrated observations of Neptune in the J = 1–0 and J = 2–1 transitions of CO were performed with the Combined Array for Research in Millimeter-wave Astronomy (CARMA) in March and April 2009. CARMA is a 23 element interferometer that combines six 10-meter antennas, nine 6-meter antennas, and eight 3.5-meter antennas. Our observations were performed with the 6- and 10-meter antennas only, for a total of 105 baselines and 2900 m^2 of total collecting area. CARMA rotates between 5 different standard antenna configurations; our CO (2–1) data were taken in CARMA's D array, which consists of baselines of 11–148 meters for a synthesized beam of 3.0×1.9 arcseconds at 230 GHz. Our CO (1–0) data were observed in CARMA's C array, with baselines of 26–370 meters for a synthesized beam of 2.1×1.8 arcseconds at 115 GHz. In both sets of observations, the beam size is comparable to the size of the planet; therefore we do not obtain information about spatial variations in the CO distribution.

Table 2.1: Correlator setups used in the observations. At 1 mm, each track uses one of setups 'a-d', while all 3-mm tracks use correlator setup 'e'. Bands ("windows") 1–3 are located in the same sideband as the CO line center frequency: Band 2 is always a 62 MHz band centered at the CO line rest frequency, and Bands 1–3 are wide (500 MHz) bands offset from line center. Bands 4–6 correspond to Bands 1–3 in the opposite sideband; these data are also recorded, and the wide-band data from both sidebands are used in our analysis.

Configuration/setup		a	b	c	d	e
Band 1	sideband	LSB	USB	LSB	USB	USB
	bandwidth (MHz)	500	500	500	500	500
	center frequency (GHz)	231.288	230.318	230.758	229.538	114.521
Band 2[a]	sideband	LSB	USB	LSB	USB	USB
	bandwidth (MHz)	62	62	62	62	62
	center frequency (GHz)	230.538	230.538	230.538	230.538	115.271
Band 3	sideband	LSB	USB	LSB	USB	USB
	bandwidth (MHz)	500	500	500	500	500
	center frequency (GHz)	230.288	229.218	232.538	230.688	115.521
Band 4	sideband	USB	LSB	USB	LSB	LSB
	bandwidth (MHz)	500	500	500	500	500
	center frequency (GHz)	235.788	221.818	239.258	225.538	110.021
Band 5[b]	sideband	USB	LSB	USB	LSB	LSB
	bandwidth (MHz)	62	62	62	62	62
	center frequency (GHz)	236.538	221.598	239.478	224.538	109.271
Band 6	sideband	USB	LSB	USB	LSB	LSB
	bandwidth (MHz)	500	500	500	500	500
	center frequency (GHz)	236.788	222.918	237.478	224.388	109.021

[a]centered on the CO line
[b]not used

At the time of our observations the CARMA correlator had three dual bands (or “windows") with configurable bandwidth of either 500, 62, 31, 8 or 2 MHz. Each band could be placed independently anywhere within the 4 GHz IF bandwidth, and appears symmetrically in the upper and lower sidebands of the first local oscillator. The sideband, total bandwidth, and central frequency of the 6 windows (3 in each sideband) for each of our correlator setups are given in Table 2.1. In each setup, we tuned the receivers to the CO (1–0) or (2–1) rest frequency in either the lower (setup a,c) or upper (setup b,d,e) sideband. Band 2 was always configured with a bandwidth of 62 MHz across 63 channels, to observe the CO line center at a resolution of 0.98 MHz per channel. Bands 1 and 3 were each configured for maximum bandwidth (500 MHz across 15 channels) and positioned at a frequency offset from the CO line center. Bands 4–6 correspond to Bands 1–3 in the opposite sideband. For the CO (1–0) line observations, we configured Band 1 at an offset of -0.75 GHz and Band 3 at an offset of $+0.30$ GHz (correlator setup ‘e’ in Table 2.1). For the CO (2–1) line, we alternated between 4 different correlator setups of the 500 MHz bands (Table 2.1, setups ‘a-d’) to extend our frequency coverage of the broad CO line wings. Frequency offsets of the 500 MHz bands from line center vary from $0.15 - 9.3$ GHz.

Each individual observation consisted of a $3.6 - 6.8$ hour track, with a 15 minute observation of a passband calibrator, followed by a series of observing cycles of 15 minutes on source and 3 minutes on a phase calibrator. Optical pointing was performed every hour. No planets were available for primary flux calibration, so we observed MWC349 when it was available. The quality of the data from tracks shorter than 3 hours and tracks with very poor weather were too low, and hence the data were rejected (2 of 8 tracks at both 1 mm and 3 mm). Weather conditions during the remaining observations were generally fair to good, with typical root mean square (rms) path errors of 150-400 μm on a 100-m baseline, and zenith optical depths of $0.1 - -0.2$. The total time on source was about 14.9 hours at 1 mm and 18.6 hours at 3 mm. These observations are summarized in Table 2.2.

2.2.2 Calibration

The data are reduced and calibrated using the MIRIAD software package (Sault et al. 2011). Prior to any calibration, flagging is performed: we flag 10 edge channels for the narrow bands and 3 edge channels for the wide bands; the narrow window that is not centered on the emission core of the CO line (Band 5: see Table 2.1); and any bad data. After performing passband calibration using our bright quasar observations, time-dependent gain solutions are derived using the wide-band data, and then applied to the full data set. We do an initial self calibration using the phase calibrator. This first calibration is performed in two steps: a record-by-record phase solution is found for the phase calibrator, to remove short-term variations. Then, a phase and amplitude self calibration is performed using an 18 minute interval and applied to the Neptune data. Finally, a record-by-record phase-only self calibration is performed on Neptune itself to remove short-term phase variations in the Neptune data.

Table 2.2: Summary of observations (all in 2009)

Line	Frequency (GHz)	Date	Correlator setup[a]	T_{int} (hours)[b]	Calibrators	rms path (μm)	τ_{zen}
CO (2–1)	230.538	07 Mar	a	2.33	3C454.3[c],2229-085[d]	208	0.22
		08 Mar	b	2.08	3C454.3[c], 2229-085[d]	165	0.24
		10 Mar	c	2.83	3C454.3[c], 2229-085[d]	157	0.19
		11 Mar	d	2.33	3C454.3[c], 2229-085[d]	133	0.23
		27 Mar	a	2.57	3C454.3[c], 2229-085[d]	162	0.17
		28 Mar	a	2.71	3C454.3[c], 2229-085[d], MWC349[e]	147	0.23
CO (1–0)	115.271	16 Apr	e	4.25	1751+096[c], 3C446[d], MWC349[e]	413	0.12
		17 Apr	e	3.40	3C446[c,d], MWC349[e]	306	0.12
		23 Apr	e	3.03	3C454.3[c], 3C446[d], MWC349[e]	335	0.16
		24 Apr	e	2.25	3C454.3[c], 3C446[d], MWC349[e]	424	0.18
		28 Apr	e	3.15	3C454.3[c], 3C446[d], MWC349[e]	200	0.11
		29 Apr	e	2.50	3C454.3[c], 3C446[d]	180	0.10

[a] as specified in Table 1
[b] time on source
[c] Passband calibrator
[d] Phase calibrator
[e] Flux calibrator

CO (J=2–1)

For this set of observations, only one track (28 March 2009) contains observations of the primary flux calibrator, MWC349. We flux calibrate this track using an assumed value of 1.86 Jy for MWC349 at 230 GHz, based on flux density measurements obtained with CARMA between 2007 and 2011[2]. We estimate the flux calibration to be accurate to better than 20%. For a first pass at the flux calibration of the other tracks, we use our phase calibrator as a secondary flux calibrator. We then bin the Neptune visibility data into 8 (u, v) bins between 0 and 80 $k\lambda$, and adjust the flux of the phase calibrator to align the binned (u, v) data as much as possible: these adjustments are about 2–5%. From the deviation of these fits, we estimate the remaining error in day-to-day gains to be less than 3%.

CO (J=1–0)

All but one of our 3-mm tracks contains primary flux calibrator data (Table 2.2). However, we find that in general, the flux determination from the primary flux calibrator is very sensitive to bad/noisy data. We are able to get more stable fluxes by using our best primary flux calibrator data from 28 April 2009, and applying the same procedure as for the 1-mm data. We use a flux density of 1.29 Jy for MWC349 at 3 mm[1].

2.2.3 Imaging

Our 3-mm data sets are all observed with the same correlator setup; therefore, we combine all the 3-mm data prior to imaging. In contrast, the 1-mm tracks are observed at different frequencies and we image each track separately. After imaging each channel, we deconvolve the dirty maps using the CLEAN algorithm. Figure 2.2 shows several of our final maps. Each map represents a single channel of data: the top row are 1-mm channel maps from a day with typical weather conditions (11 March), and the bottom row are examples of 3-mm channel maps. Below each map is a scan in Right Ascension through the center of Neptune.

2.2.4 Flux determination and error estimate

The flux density in each channel is determined as the integrated intensity over a hand-selected region, chosen to include all of the signal from Neptune, as indicated by the solid line in each map in Fig. 2.2. To quantify the errors in the determined flux density, we then shift this region to 8 different positions outside of the source (indicated by dashed lines in Fig. 2.2). The error in each channel is estimated as the standard deviation of the integrated fluxes of these regions. We also calculate the flux errors using the rms of the pixel values in the residual maps. We find that the two methods of error estimation are in good agreement.

[2] http://cedarflat.mmarray.org/fluxcal/primary_sp_index.htm

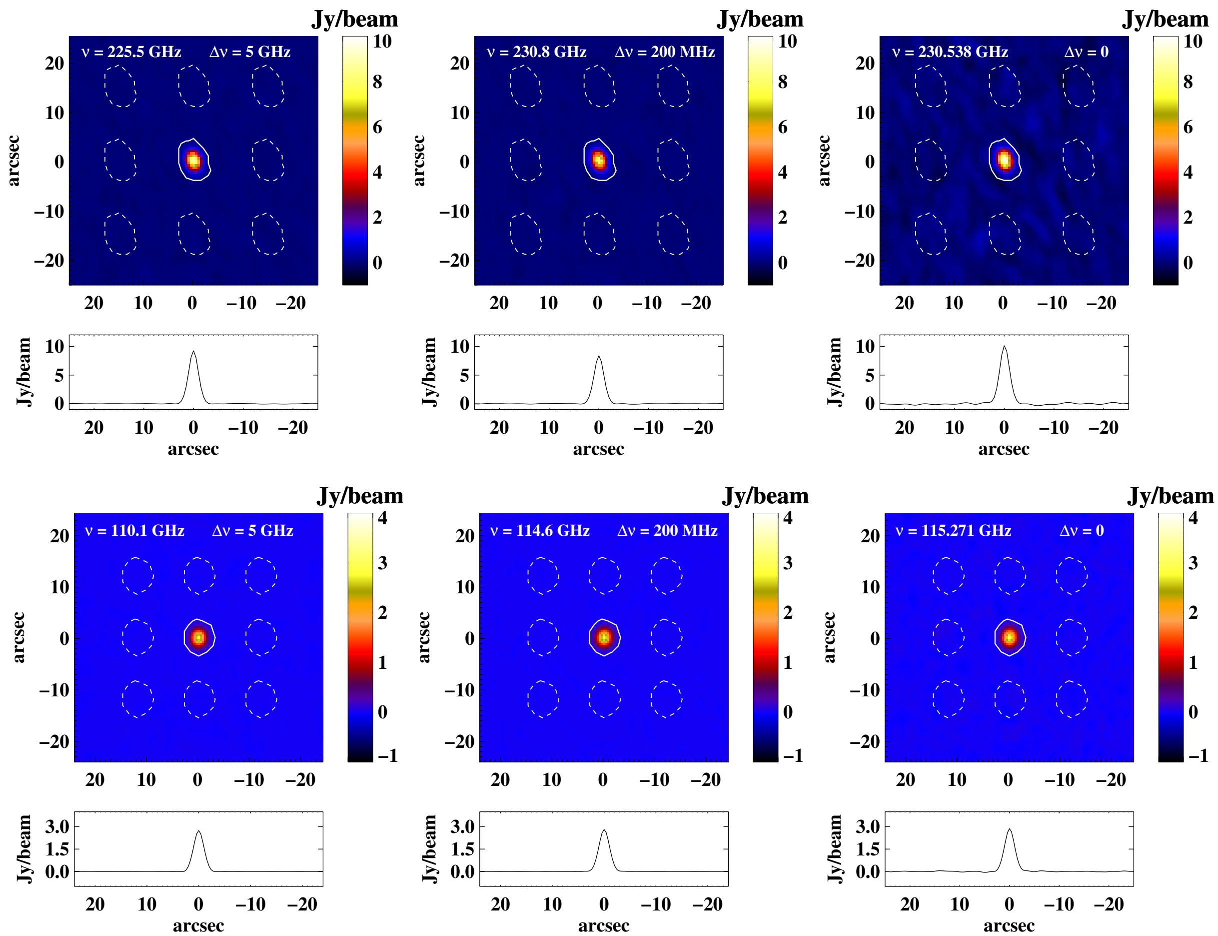

Figure 2.2: Representative channel maps; color scale indicates intensity in Jy/beam. The top row are maps from a typical 1-mm day (11 March); the bottom row are the channel maps created from all days of 3-mm data. The left-most figures are wideband channels, roughly 5 GHz from line center. In the middle column are maps from wide channels in the absorption, about 500 MHz from line center. Maps on the right are from narrow channels at line center. Below each map is a scan through the map Right Ascension (a value of 0 on the y- axis). Neptune is unresolved in the maps; the total flux in each channel is determined by summing over the region indicated by the solid white line. The error is estimated by the regions indicated by dashed lines- see Section 2.2.3 for discussion.

These error estimates do not include systematic effects, such as errors in the bandpass calibration or in the assumed flux of the calibrator; however, they are useful weights for fitting the data to models (see Sections 2.4 and 2.5). Raw spectra, with uncertainties, are shown in Fig. 2.3; for reference, the individual 1-mm tracks are differentiated by color. A frequency-binned version of the data is plotted in black, using a bin interval of three times the channel width.

2.3 Model

To model Neptune's millimeter spectrum, we developed a line-by-line radiative transfer code that integrates the equation of radiative transfer, assuming local thermodynamic equilibrium (LTE)

$$B_\nu(T_D, \mu) = \int_0^\infty B_\nu(T) e^{-\tau/\mu} d\tau/\mu \tag{2.2}$$

over a model atmosphere consisting of 2000 plane-parallel layers extending from 200 bar to 5 μbar. In this equation, T_D is the disk brightness temperature, $\mu = \cos\theta$ with θ defined as the angle between the line of sight and local vertical, $B_\nu(T)$ is the Planck function for temperature T, and τ is the optical depth. The code is optimized for least-squares fitting of the CO altitude profile (Section 2.4), and has been thoroughly tested against the microwave radiative transfer code described in de Pater et al. (1991a), after the latter was updated as described by de Pater et al. (2005). The de Pater et al. (1991a) code has been further revised to include the Orton et al. (2007b) H_2 absorption coefficients (Section 2.3.2), and absorption due to CO using subroutines from de Pater et al. (1991b) that were updated with the parameters described in Section 2.3.2. We find that the two radiative transfer codes produce consistent model spectra for the same input parameters, except at the CO line center, because the new code includes the effect of Doppler broadening on the shape of the emission peak (Section 2.3.4) and the revised de Pater et al. (1991a) code does not. The details of the new model are described below.

2.3.1 Composition

Neptune's upper atmosphere is dominated by H_2 and He. Conrath et al. (1991) estimated the relative abundances of these two species using constraints on the atmospheric mean molecular weight from Voyager infrared and radio occultation measurements; they found a best-fit helium mole fraction of 0.19±0.032. The detection of HCN on Neptune (Marten et al. 1991) led Marten et al. (1993) to suggest a scenario (originally proposed by Romani et al. 1989) in which Neptune's nitrogen is predominantly present as N_2, rather than NH_3. Such a high N_2 abundance is greater than expected from thermochemical equilibrium arguments (e.g. Fegley et al. 1991, for Uranus), but could be the source of atomic nitrogen for the production of stratospheric HCN (Marten et al. 1993), and would help explain the observed atmospheric NH_3 deficit (Romani et al. 1989, discussed below). Reanalysis of the Conrath et al. (1991) data (Conrath et al. 1993) showed that a mole fraction of 0.003 of N_2 and 0.15 of He is consistent with the Voyager measurements. Using spectra from the Infrared

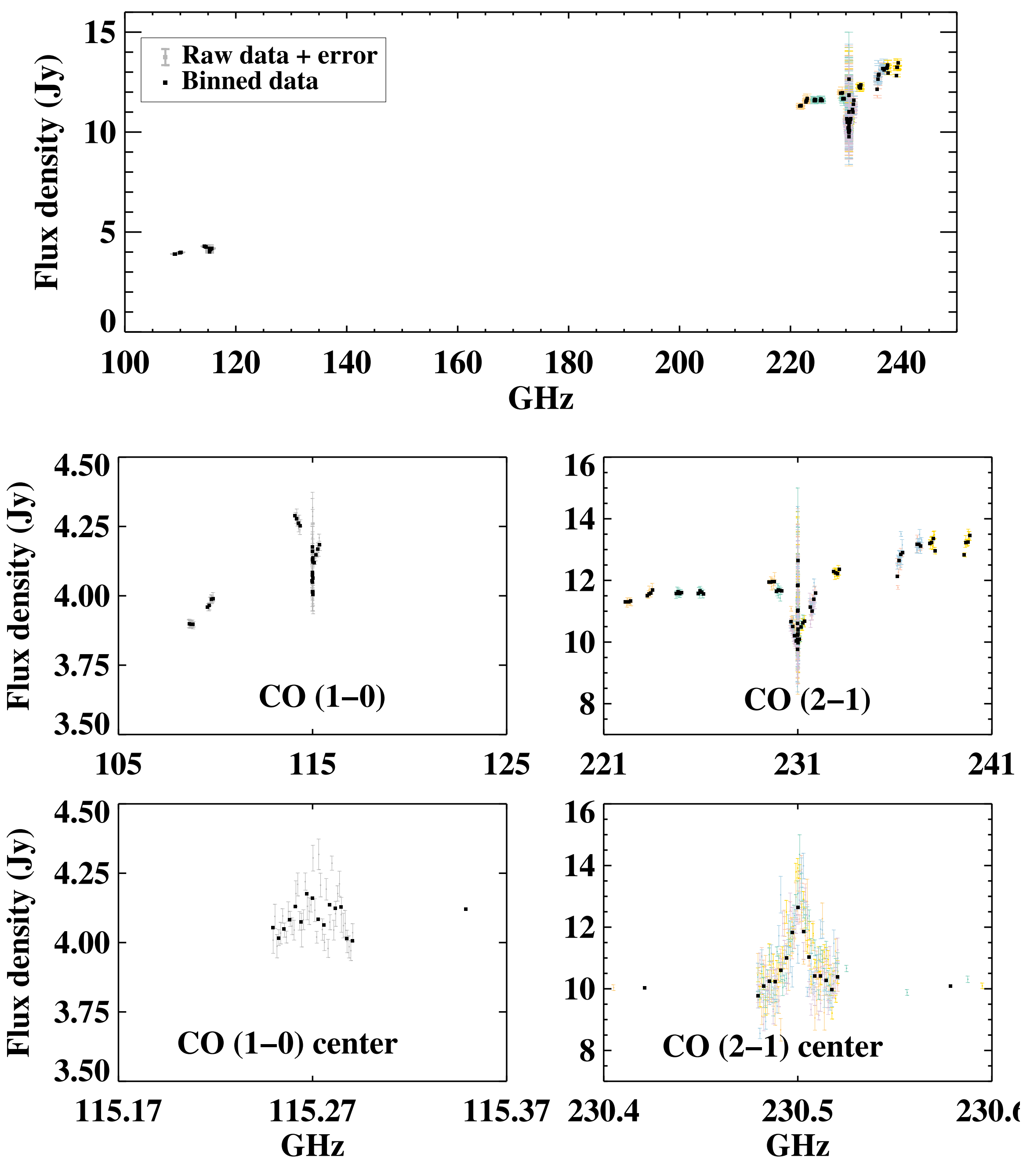

Figure 2.3: Raw CO (1–0) and (2–1) spectra. Each grey point corresponds to the flux density calculated from a single 3-mm channel map; colors are used to delineate between individual tracks at 1 mm. Error bars are calculated using the method described in Section 2.2.3. Black points are binned to 3 times the width of the individual channels.

Space Observatory Long-Wavelength Spectrometer (ISO-LWS), Burgdorf et al. (2003) found a He/(H_2+He) mass ratio of $26.4^{+2.6}_{-3.5}$%, and an N_2 mixing ratio of less than 0.7%. They determined that the correlation of their value of the He mole fraction with the Conrath et al. (1993) results gives an N_2 mole fraction of 0.3 ± 0.2%. Accordingly, for our atmospheric models we maintain a He/H_2 ratio of 0.15/0.847 and an N_2/H_2 ratio of 0.003/0.847 by number throughout our model atmosphere; these numbers are consistent with the solutions of both Conrath et al. (1993) and Burgdorf et al. (2003) within the 1σ uncertainties. Since the presence of N_2 in Neptune's atmosphere is not certain, we also tested models with the same He/H_2 ratio and no N_2; the difference was negligible.

Previous observations have shown that CH_4 is supersaturated in Neptune's stratosphere (Orton et al. 1987; Orton et al. 1990; Yelle et al. 1993). We adopt the stratospheric CH_4 profile recently derived by Fletcher et al. (2010) from AKARI infrared data, which has a mole fraction of 9×10^{-3} at 50 mbar. Below the methane condensation level, we adopt a mole fraction of 0.022 as measured by Baines et al. (1995), which implies an enrichment factor of ~ 50 over the protosolar C/H ratio (Asplund et al. 2009).

While the composition of Neptune's deep troposphere has yet to be uniquely determined, data from centimeter wavelengths suggest that NH_3 is depleted in Neptune's atmosphere (Romani et al. 1989; de Pater et al. 1991a). Good fits to the cm wavelength range are obtained by enhancing H_2S 30-50 times over the solar S/H value (de Pater et al. 1991a; Deboer & Steffes 1996) and using a solar abundance of nitrogen in NH_3. Hoffman et al. (2001) suggest that PH_3 may be an important source of microwave absorption as well; however, Moreno et al. (2009) determined an upper limit of phosphorous in Neptune's upper atmosphere of 0.1 times the solar abundance, from observations of the PH_3 (1–0) transition. Due to the uncertainty in our absolute flux calibration (as much as 20%, see Section 2.2), we do not attempt to constrain the abundances of species other than CO from our data. However, we do investigate the potential effect of these absorbers on the 1- and 3-mm spectra: using the code described by de Pater et al. (1991a, 2005), we model the deep atmosphere with a 10-50 times solar enrichment of H_2O and H_2S, a solar abundance of NH_3, and 0.1 times solar PH_3. Trace species are removed from the model atmosphere at higher altitudes by condensation, when the partial pressures of the trace gases exceed the saturation vapor pressure (see de Pater et al. (2005) for a detailed description). Figure 2.4 shows the effects on the microwave spectrum of absorption due to each of these gases individually, as well as that from all gases combined.

2.3.2 Opacity

To determine the optical depth $\tau_\nu(z)$ we consider the following sources of opacity:

Collision-induced H_2 absorption

For Neptune, the dominant millimeter-wave opacity source is collision-induced absorption by H_2 with H_2, He, and CH_4. We use the absorption coefficients calculated from revised ab-initio models of Orton et al. (2007b), assuming an equilibrium distribution of hydrogen. These authors incorporate a correction to the Borysow models (Borysow et al. 1985, 1988; Borysow 1991, 1992, 1993), and show that the new coefficients are an improvement at low temperatures. In practice, we find that spectra produced using the Orton et al. (2007b) coefficients are 1.6-2 K higher than those made using the Borysow et al. (1985) models.

CO

The absorption due to the CO (1–0) and (2–1) rotation lines is calculated assuming a Voigt line shape profile. The H_2 broadened line half-width is determined from a fit to the data of Mengel et al. (2000) and is ∼2.8 MHz/Torr at 300 K for the CO (1–0) and (2–1) lines. The remaining line parameters are taken from the HITRAN 2008 database (Rothman et al. 2009). A Van Vleck-Weisskopf line shape was tested using the updated de Pater et al. (1991a) code and found to be a nearly identical match to the Voigt line shape in the atmospheric region probed.

Additional microwave absorbers

We model several other potential sources of radio-wavelength opacity (H_2O, NH_3, H_2S, PH_3) using the updated de Pater et al. (1991a) code and the abundances from Section 2.3.1. We find that H_2O and NH_3 do not affect the spectrum at 1-3 mm wavelengths (Fig. 2.4). The far wings of the PH_3 (1–0) line at 266.9 GHz could influence the high frequency wing of the CO (2–1) line; however, for a 0.1 times solar abundance of PH_3 the line is too weak to significantly affect the CO profile. We note that a 0.1 times solar abundance of PH_3 is an upper limit (Moreno et al. 2009); larger values would also be inconsistent with the available data according to our own models, as shown. We find that absorption due to H_2S is important at wavelengths longer than 1 mm; at 3 mm the addition of > 10 times solar abundance of H_2S decreases the continuum level by ∼20 K.

We therefore incorporate H_2S absorption into our new radiative transfer code following the formalism described by Deboer & Steffes (1994); line parameters are taken from the JPL catalog (Pickett et al. 1998), while parameters for the Ben Reuven line shape come from Deboer & Steffes (1994). We choose as our nominal atmospheric model no H_2S absorption, and additionally investigate models with absorption due to 10 and 50 times solar H_2S abundances. We note that high H_2S abundances give a best fit to the cm wavelength region (Section 2.3.1; Fig. 2.4).

2.3.3 Thermal profile

The observed shapes of the CO absorption lines depend strongly on both the CO abundance and the temperature-pressure (TP) profile in the atmosphere. Therefore, we look at a range of TP profiles to understand the effect of uncertainties in the TP profile on our derived CO altitude profile. Our nominal TP profile is that of Fletcher et al. (2010);

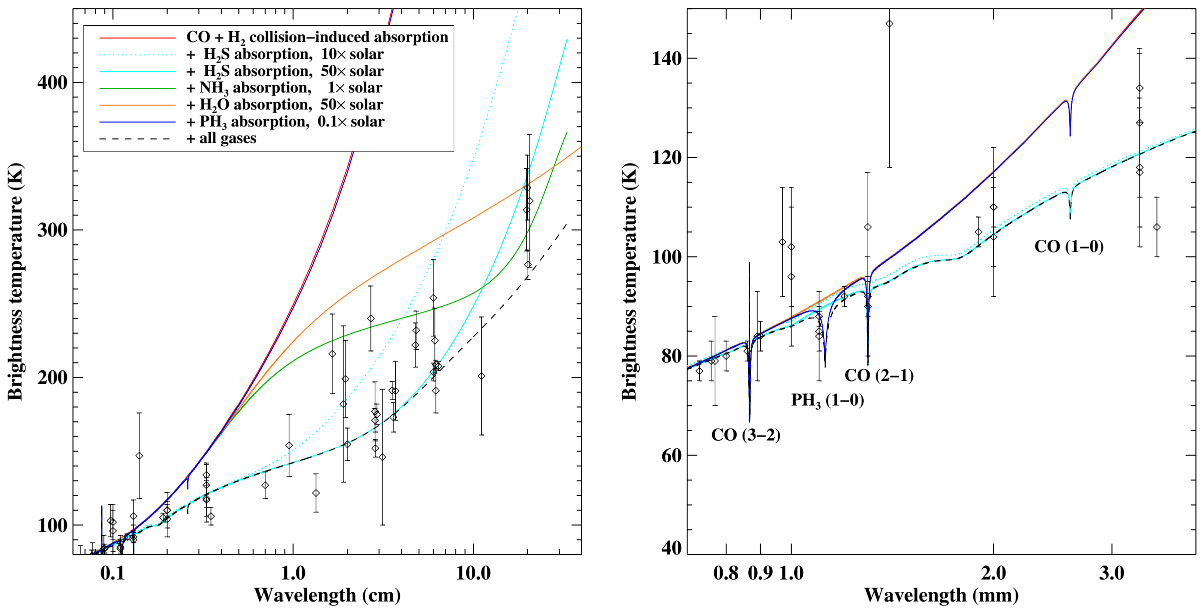

Figure 2.4: Model atmosphere calculations. All models include CO and H_2 collision-induced absorption (see Section 2.3.2); the red line represents these two opacity sources only. Opacity due to a 10 and 50 times protosolar abundance of H_2S (cyan, dashed and solid lines, respectively); a 50 times protosolar abundance of H_2O (orange); a protosolar abundance of NH_3 (green) and a 0.1 times protosolar abundance of PH_3 (blue) are included. The black dashed model contains all of these absorptions (note that a 50 times protosolar abundance was used for H_2S, rather than the 10 times solar value). A compilation of microwave data taken before 1991 is plotted for comparison (diamonds); these data are described in de Pater et al. (1991a) and references therein. The right plot zooms in on millimeter wavelengths, and shows the importance of H_2S opacity at these wavelengths.

they adopt the TP profile of Moses et al. (2005) below the tropopause and retrieve the stratospheric temperature profile from mid-infrared AKARI spectra. Fits to HD lines in Neptune's 51-220 μm spectrum from Herchel/PACS (Lellouch et al. 2010) are sensitive to the 10-500 mbar levels; these authors favor a thermal profile much like that of Fletcher et al. (2010) in the stratosphere as well.

Figure 2.5 shows a selection of published TP profiles, including our nominal profile and the profiles used in the recent CO studies of Lellouch et al. (2005), Marten et al. (2005) and Hesman et al. (2007). Published profiles generally match the Voyager RSS occultation profile (Lindal 1992) at ∼1 bar (T = 71.5 K), and assume an adiabatic extrapolation down to deeper levels. Our nominal profile is slightly warmer than the Lindal (1992) profile at the tropopause, which could be due to seasonal changes in the atmospheric temperature since the Voyager era (Orton et al. 2007a; Hammel & Lockwood 2007a). At altitudes above

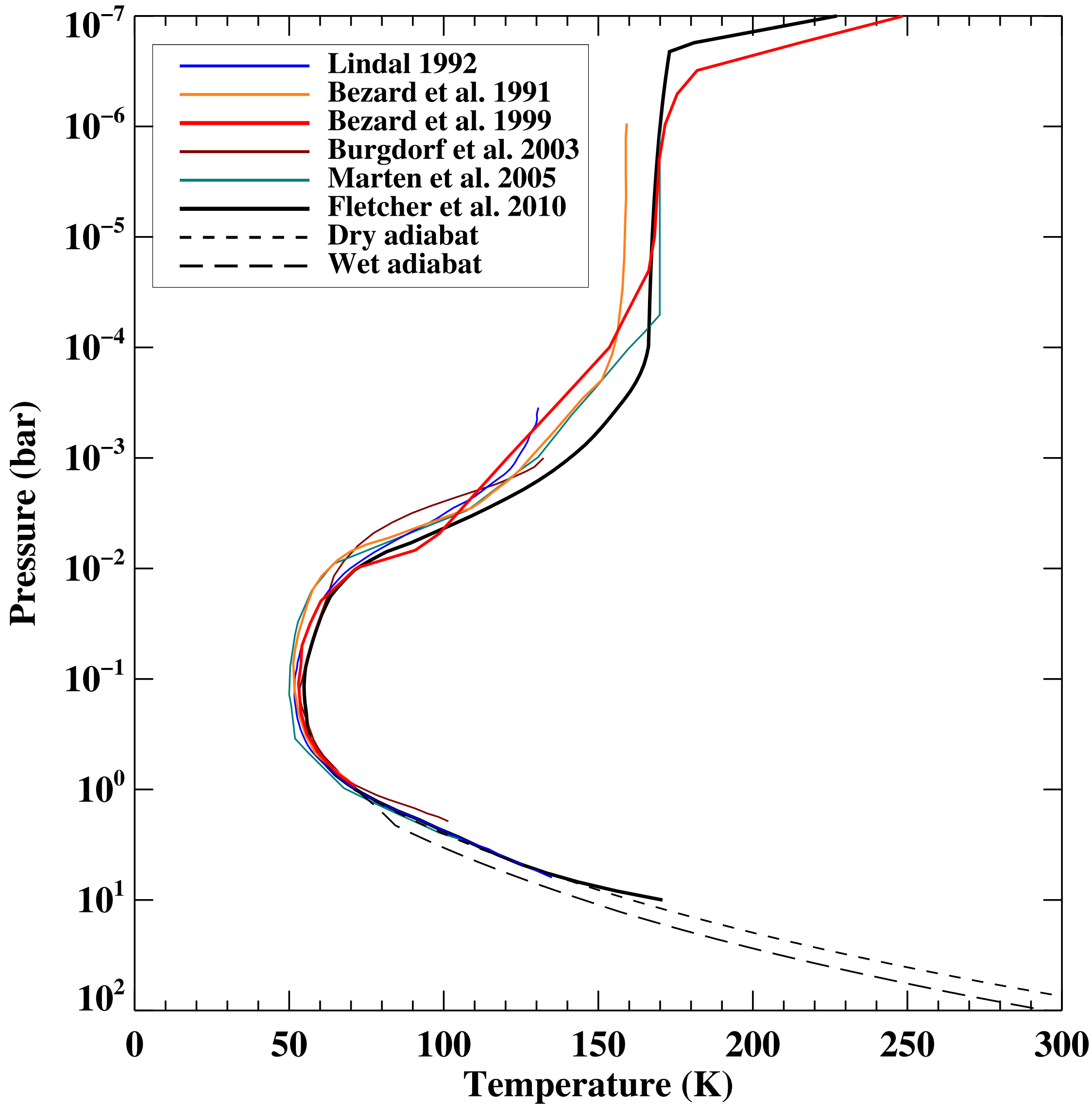

Figure 2.5: Selected temperature-pressure (TP) profiles for Neptune from the literature. The Marten et al. (2005) thermal profile (teal) was derived from their submillimeter data concurrently with CO abundance. Lellouch et al. (2005) adopted the Bezard et al. (1991) TP profile (orange) in their study; the thermal profile used by Hesman et al. (2007) was based on the Burgdorf et al. (2003) profile (brown). Our nominal choice for this work is the Fletcher et al. (2010) profile (thick black line), and we also consider the Bézard et al. (1999) profile (thick red line). At pressures greater than 1 bar, we follow a dry adiabat (black, short-dashed line).

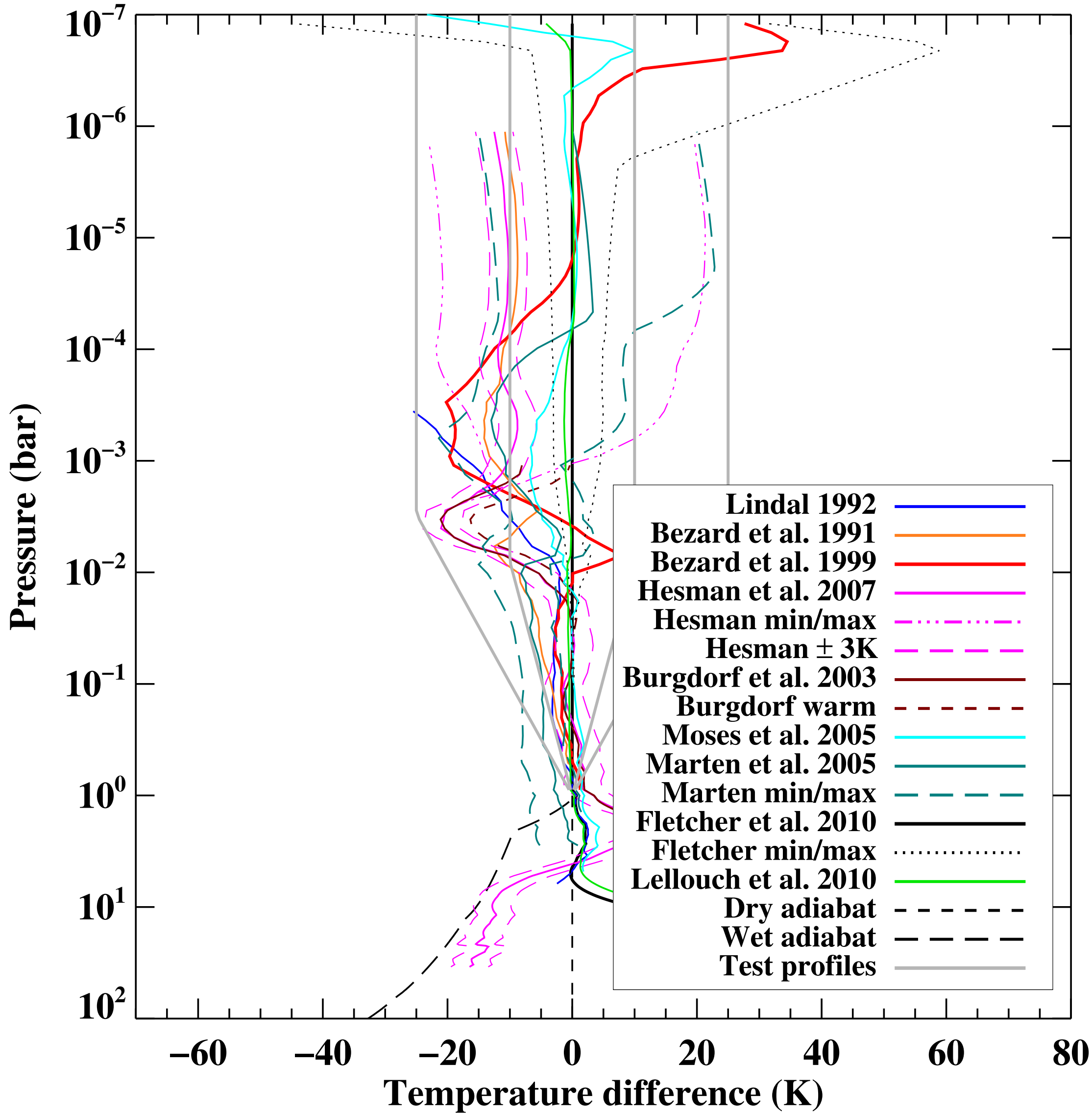

Figure 2.6: Difference between selected TP profiles and our nominal TP profile. Line colors are the same as in Fig. 2.5; several additional thermal profiles are also shown. Published alternate profiles/uncertainties are included as broken lines. The light grey lines indicate our nominal test profiles, chosen to span the range of published profiles above 1 bar (see Section 2.3 for details). From left to right, these are the 'extreme cool', 'moderate cool', 'moderate warm' and 'extreme warm' TP profiles.

1 bar, the published profiles diverge greatly. We consider four additional TP profiles that span the range of published profiles; each of these test profiles matches the nominal profile at altitudes below 1 bar. The 'extreme low' and 'extreme high' profiles decrease/increase steadily to ± 25 K from the nominal profile, respectively, between 1 and 0.003 bar and then remain at ± 25 K from nominal as the pressure continues to decrease. The 'moderate low' and 'moderate high' profiles decrease/increase steadily to ± 10K from the nominal profile, respectively, between 1 and 0.008 bar and then remain at ± 10 K from nominal as the pressure continues to decrease. These offsets are illustrated in Fig. 2.6. While these test profiles envelope the published profiles and their error bars, they do not represent all of the possible TP profile shapes. For example, the profile of Bézard et al. (1999) is $\sim$20 K cooler than our nominal profile around 10^{-3} bar, and warmer than our nominal profile at higher and lower pressures. The provisional temperature profile from the analysis of 2005 Spitzer Infrared Spectrometer data, reported in Line et al. (2008), is similar to the Bézard et al. (1999) profile. We do not test all of the published TP profiles, but we do consider the Bézard et al. (1999) profile in addition to our nominal profile and four test profiles. The profiles used in the analyses of Lellouch et al. (2005) and Hesman et al. (2007) are most similar to our 'moderate cool' profile.

At pressures greater than 1 bar, where the temperature profile is unknown, we assume the atmosphere is convective and extrapolate adiabatically. We consider two possibilities: a dry adiabat (nominal) and a wet adiabat (see de Pater et al. (1991a, 2005) for a detailed description). In the adiabatic extrapolation, we assume that the specific heat of hydrogen is near that of normal hydrogen (though the opacity for equilibrium hydrogen is used- this is the "intermediate" hydrogen case (Massie & Hunten 1982; de Pater & Mitchell 1993)).

2.3.4 Disk averaging

To account for variations in viewing geometry on Neptune's disk-averaged spectrum, we calculate $T_B(\nu, \mu)$ for 25 different viewing angles μ, which represent the average spectra within 25 concentric rings. Doppler broadening due to the planet's rotation, which has a velocity of $V_{eq} = 2.7$ km s^{-1} at Neptune's equator, affects the shape of the emission peak in the center 2 MHz of the line. Following Moreno et al. (2001), the velocity at a given distance x from the central meridian is:

$$V = \frac{x}{R} V_{eq} \tag{2.3}$$

where

$$x = R\cos(lat)\sin(\Delta long)\cos(SEPL)$$

We define R as the planetary radius, lat as planetary latitude, $\Delta long$ as longitude from the central meridian and $SEPL$ as the latitude of the sub-earth point. We divide the disk into 100 values of x. At each x, we calculate the average spectrum given the relative contribution of each representative viewing angle μ. We then shift the spectrum in frequency given the value of $V(x)$. Finally we coadd the Doppler-shifted spectra to get our final disk-averaged spectrum. Once the disk-averaged spectrum is computed, models are convolved to the instrumental resolution (∼1 MHz near the peak, ∼33 MHz in the wings).

2.4 Analysis

To determine Neptune's vertical CO profile, we perform robust non-linear least-squares fitting to the data weighted by the data errors using the MPFIT IDL package (Markwardt 2009). We first consider models in which the CO mole fraction $n_{\rm CO}/n_{\rm TOT}$ is held constant throughout the atmosphere. This corresponds to the case where Neptune's observed CO primarily comes from vertical mixing from deep levels in the atmosphere. In addition to the value of $n_{\rm CO}/n_{\rm TOT}$, these fits have two additional free parameters. These are amplitude correction factors for the 1- and 3-mm data, which account for the uncertainty in the absolute flux calibration of the data. In practice, we find the values of these flux density correction parameters to be in the range of 5–10% at both wavelengths.

The least-squares fitting procedure is performed for models that use our nominal TP profile as well as each of the test thermal profiles described in Section 2.3.3. We also perform the fit on the 1-mm and 3-mm datasets separately. We report the fitted values for the CO mole fraction, 1- and 3-mm amplitude correction factors, and the statistical errors from the covariance matrices of the fits in Table 2.3. We also report the reduced chi-squared $(\widehat{\chi^2})$ of the best fit:

$$\widehat{\chi^2} = \frac{1}{M-N}\sum_{m=0}^{M-1}\frac{\delta y_m^2}{\sigma^2_{meas,m}} \tag{2.4}$$

where M is the $\widehat{\chi^2}$number of data points, and N is the number of fit parameters (in this case, three), so that $M-N$ is the number of degrees of freedom (DOF) for the fit. The parameter δy_m is the difference between the data and model value for point m, and $\sigma_{meas,m}$ is the measurement error for point m. Our values of $\widehat{\chi^2}$ are greater than one: this is discussed in detail in Section 2.5.

Following previous authors (Lellouch et al. 2005; Hesman et al. 2007) we repeat the fitting process using a two-level CO profile. In this case the CO abundance is assumed to be constant within each of two levels, above and below some transition pressure. Fits of this form are representative of the scenario in which CO is produced in the stratosphere and diffuses downward, along with being mixed upward from the interior. In addition to the CO mole fractions and the 1- and 3- mm amplitude correction factors, the pressure that defines the transition between the two atmospheric levels must also be determined. We find that our fitting procedure does not perform well when we allow this transition pressure to be a free parameter; the fitting program will rarely vary the pressure level from its start value. Therefore, for each model thermal profile, we perform a series of fits: in each run we fix the pressure level, testing transition pressures in steps of 0.1 in $\log P$(bar) from -3.0 (1

Table 2.3: Best-fit one-level CO profiles. The CO mole fraction is held constant as a function of altitude (Section 2.6.1). The 1- and 3-mm flux density factors are the factors by which the data must be multiplied in the best-fit solution. These factors account for errors in the gain calibration of the data, which may be as much as 20% (see Section 2.2). $\widehat{\chi^2}$ is the reduced χ^2 of the best-fit model, as defined in Eq. (4). The thermal profile used in each model is specified.

Data	TP profile	CO (ppm)	1-mm flux density factor	3-mm flux density factor	$\widehat{\chi^2}$
1 mm					
	nominal	0.50 ± 0.02	1.050 ± 0.003		15.3
3 mm					
	nominal	0.37 ± 0.05		1.09 ± 0.004	14.6
1 mm + 3 mm					
	nominal	0.49 ± 0.02	1.052 ± 0.003	1.081 ± 0.002	15.3
	Bézard et al. (1999)	0.45 ± 0.01	1.055 ± 0.003	1.083 ± 0.002	15.4
	extreme cool	0.264 ± 0.008	1.061 ± 0.003	1.090 ± 0.002	18.3
	moderate cool	0.37 ± 0.01	1.055 ± 0.003	1.085 ± 0.002	16.2
	moderate warm	0.60 ± 0.02	1.056 ± 0.003	1.079 ± 0.002	16.5
	extreme warm	0.67 ± 0.03	1.069 ± 0.004	1.080 ± 0.003	21.5

mbar) to 0.0 (1 bar). The best-fit solutions as a function of transition pressure are shown in Fig. 2.7 for a selection of thermal profiles. We find that for a given TP profile, the $\widehat{\chi^2}$ value has a global minimum, and all the parameters are smooth functions of the $\log P(\text{bar})$ of the transition pressure. We therefore take the solution with the lowest $\widehat{\chi^2}$ value as our overall best-fit model for each test TP profile; for example, for our nominal profile (no H_2S), the minimum $\widehat{\chi^2}$ reveals a transition pressure of $\log P(\text{bar}) = 0.9$, or 0.13 bar (Fig. 2.7, top panel). This corresponds to a CO abundance of 1.1 ppm at altitudes above 0.13 bar (middle panel) and 0.1 ppm at altitudes below 0.13 bar (lower panel). These best-fit values are reported in Table 2.4. As when modeling a constant CO mole fraction, we repeat the two-level fit for the 1- and 3-mm datasets separately. We also test the effect of H_2S absorption on the best-fit two-level CO profile, by repeating the two-level fits assuming a 10 and 50 times solar abundance of H_2S. These results are reported in Table 2.4 as well.

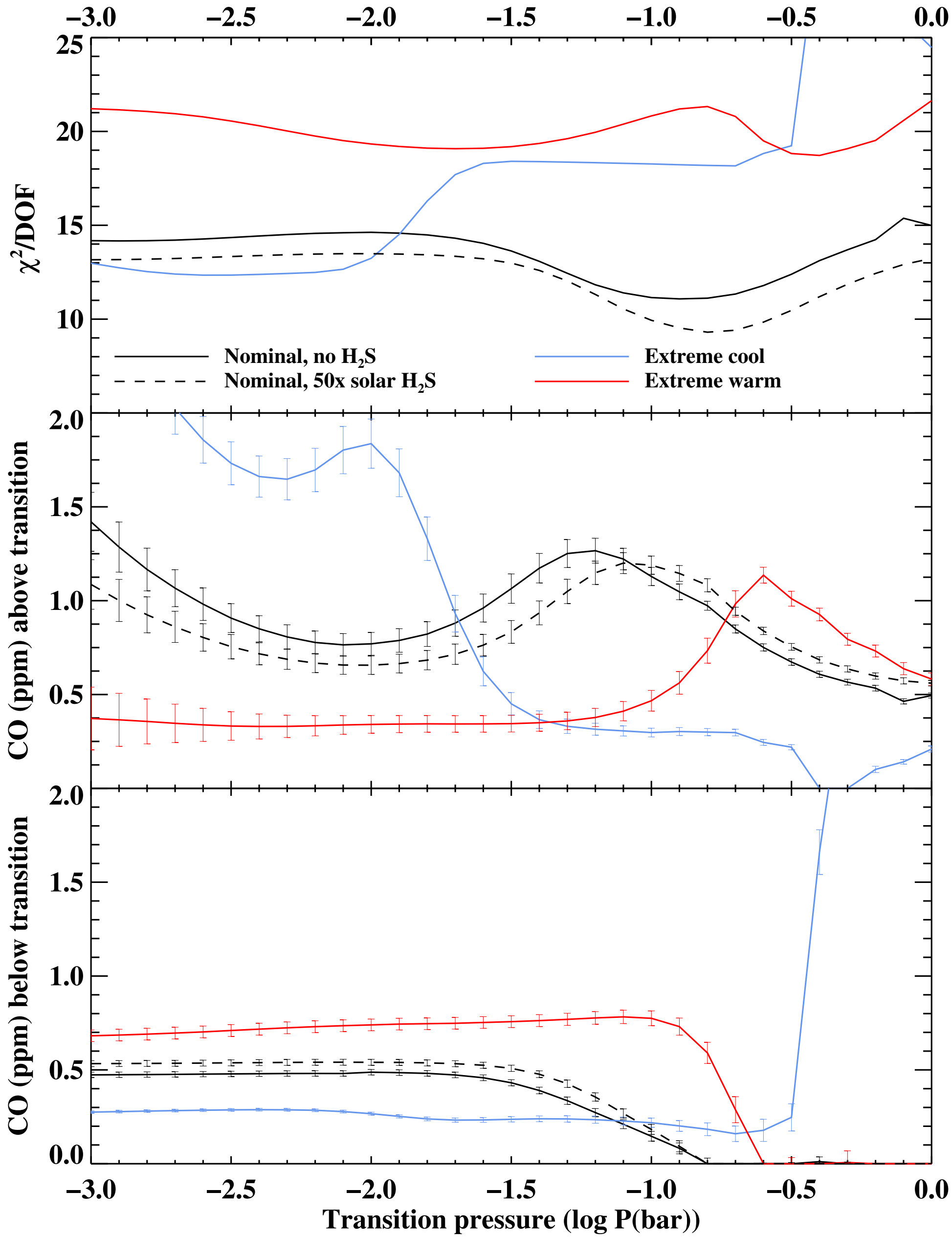

Figure 2.7: Best-fit parameters as a function of transition pressure level for the nominal thermal profile (black), both with (dashed) and without (solid) H_2S opacity; and for the extreme warm (red) and extreme cool (blue) thermal profiles. Pressure is given in units of $\log(P(\mathrm{bar}))$, from $\log(P(\mathrm{bar})) = -3.0$ (1 mbar) to $\log(P(\mathrm{bar})) = 0.0$ (1 bar).

Table 2.4: Best-fit two-level CO profiles. The CO mole fraction transitions between a high altitude value (“CO above") and a deep atmosphere value (“CO below") at the best-fit transition pressure P which is given in units of $\log P$(bar) as well as in bars (Section 2.6.2-2.6.3). As in Table 2.3, the 1- and 3-mm flux density factors are the factors by which the data must be multiplied to match the model in the best-fit solution, and $\widehat{\chi^2}$ is the reduced χ^2 of the best-fit model, as defined in Eq. (4).

Data	TP profile	CO below (ppm)	CO above (ppm)	$\log P$(bar)	P(bar)	1-mm flux density factor	3-mm flux density factor	$\widehat{\chi^2}$
1 mm								
	nominal	0.09 ± 0.03	$1.12 \pm .04$	-0.9	0.13	1.079 ± 0.003		10.7
3 mm								
	nominal	0.00 ± 0.01	$0.89 \pm .08$	-1.0	0.100		$1.100 \pm .0002$	9.3
all								
	nominal	0.08 ± 0.03	1.06 ± 0.04	-0.9	0.13	1.082 ± 0.003	1.088 ± 0.002	11.1
	Bézard et al. (1999)	0.12 ± 0.03	1.05 ± 0.05	-1.0	0.10	1.080 ± 0.003	1.088 ± 0.002	11.4
	extreme cool	0.285 ± 0.007	1.9 ± 0.1	-2.6	0.0025	1.062 ± 0.003	1.089 ± 0.002	12.3
	moderate cool	0.30 ± 0.01	1.37 ± 0.09	-1.6	0.025	1.066 ± 0.003	1.085 ± 0.002	12.7
	moderate warm	0.001 ± 0.03	1.13 ± 0.04	-0.7	0.20	1.094 ± 0.003	1.090 ± 0.002	12.3
	extreme warm	0.00 ± 0	0.93 ± 0.03	-0.4	0.40	1.100 ± 0.003	1.092 ± 0.002	18.7
+10× solar H_2S[a]	nominal	0.00 ± 0	1.08 ± 0.02	-0.8	0.16	1.036 ± 0.002	0.904 ± 0.001	9.3
+50× solar H_2S[b]	nominal	0.00 ± 0	1.08 ± 0.02	-0.8	0.16	1.039 ± 0.002	0.909 ± 0.001	9.3

[a] Opacity due to 10× solar enrichment in H_2S included

[b] Opacity due to 50× solar enrichment in H_2S included

Finally, we use a model to derive several 'physical' CO profiles. To model the vertical diffusion rate, the eddy diffusion coefficient (K) profiles of Moses (1992) and Romani et al. (1993), which were developed to match photochemical models of observed hydrocarbon distributions, are used (Fig. 2.8). Molecular diffusion is included using Marrero & Mason (1972):

$$D_{CO} = \frac{1}{P(atm)} \frac{1.539 \times 10^{-2} T^{1.548}}{\left(\ln\left[T/3.16 \times 10^{7}\right]\right)^{2} e^{-2.8/T} e^{1067/T^{2}}} \quad \mathrm{cm^2\ s^{-1}} \tag{2.5}$$

Using these profiles, we solve the diffusion equation:

$$\phi_{\rm CO} = -K\left(\frac{\partial n_{\rm CO}}{\partial z} + n_{\rm CO}\left[\frac{1}{H} + \frac{1}{T}\frac{\partial T}{\partial z}\right]\right) - D_{\rm CO}\left(\frac{\partial n_{\rm CO}}{\partial z} + n_{\rm CO}\left[\frac{1}{H_{\rm CO}} + \frac{1}{T}\frac{\partial T}{\partial z}\right]\right) \tag{2.6}$$

where $n_{\rm CO}$ is the number density of CO molecules in cm^{-3}, z is the altitude in cm, H is the total atmospheric pressure scale height, and $H_{\rm CO}$ is the scale height of CO. We then

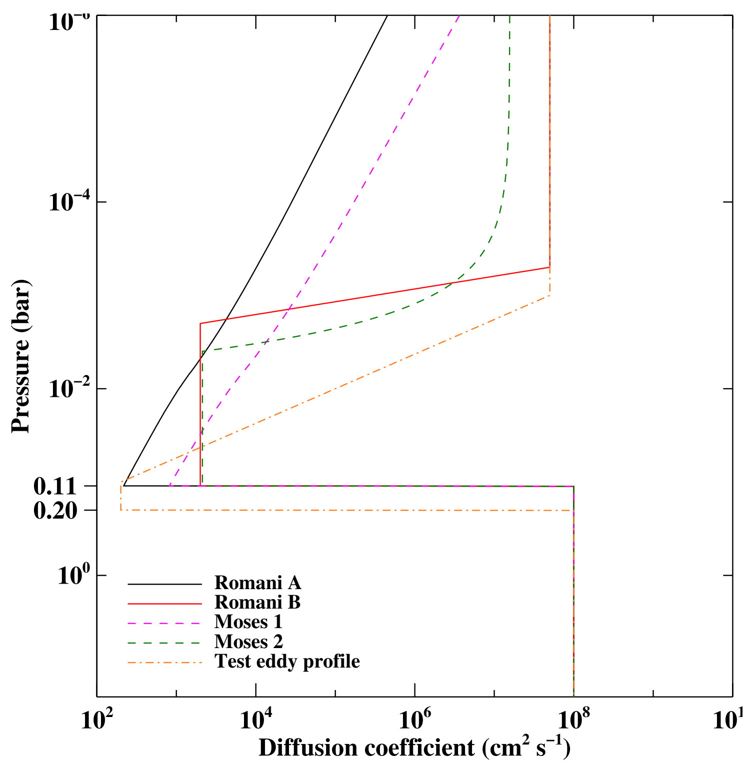

Figure 2.8: Eddy diffusion coefficient profiles from Moses (1992) and Romani et al. (1993). Also included is one of our 'test profiles', designed to produce a CO profile more similar to our best-fit two-level CO profile (see Section 2.6.4 for discussion). The tropopause pressure values of 0.11/0.20 bar are indicated.

find the best-fit value for the external flux $\phi_{\rm CO}$ from the upper atmosphere, allowing for an additional CO contribution from the planet's interior ($n_{\rm CO}/n_{\rm TOT}|_{(z=0)}$). Sample physical CO profiles, assuming an influx rate of $\phi_{\rm CO} = 10^8$ cm^{-2}s^{-1} and no internal contribution of CO, are illustrated in Fig. 2.9. To demonstrate the effect of internal CO on these physical CO profiles, we show the same profiles with 0.2 ppm of internal CO added for two of the eddy profile cases. Best-fit values of $\phi_{\rm CO}$ and $n_{\rm CO}/n_{\rm TOT}|_{(z=0)}$ from our least-squares modeling are summarized in Table 2.5.

Table 2.5: Best-fit physical CO profiles. The external flux $\phi_{\rm CO}$ and the mole fraction of CO brought up from the deep atmosphere ("internal CO") that produce the best match between the spectrum and model are given, for a selection of thermal and eddy diffusion coefficient profiles (see Section 2.6.4). $\widehat{\chi^2}$ is the reduced χ^2 of the best-fit model, as defined in Eq. (4). The flux density scale factors for these fits are not shown.

TP profile	eddy diffusion profile	$\log \phi_{\rm CO} ({\rm cm}^{-2}{\rm s}^{-1})$	internal CO (ppm)	$\widehat{\chi^2}$
nominal	Romani 'A'	7.37 ± 0.07	0.48 ± 0.01	14.2
moderate low	Romani 'A'	7.71 ± 0.05	0.37 ± 0.01	13.2
extreme low	Romani 'A'	8.07 ± 0.04	0.260 ± 0.007	13.0
nominal	Romani 'B'	7.55 ± 0.08	0.48 ± 0.01	14.4
moderate cool	Romani 'B'	7.93 ± 0.04	0.38 ± 0.01	13.0
extreme cool	Romani 'B'	8.33 ± 0.03	0.279 ± 0.007	12.3
nominal	Moses '1'	7.94 ± 0.07	0.48 ± 0.01	14.2
moderate cool	Moses '1'	8.27 ± 0.05	0.37 ± 0.01	13.1
extreme cool	Moses '1'	8.60 ± 0.04	0.254 ± 0.007	12.9
nominal	Moses '2'	7.93 ± 0.08	0.48 ± 0.01	14.5
moderate cool	Moses '2'	8.38 ± 0.04	0.37 ± 0.01	13.0
extreme cool	Moses '2'	8.85 ± 0.03	0.259 ± 0.008	12.2
nominal	test profile[a]; $p_{trop} = 0.11$ bar	9.33 ± 0.04	0.26 ± 0.02	11.8
nominal	test profile[a]; $p_{trop} = 0.2$ bar	9.17 ± 0.03	0.15 ± 0.03	11.2
moderate cool	test profile[a]; $p_{trop} = 0.2$ bar	9.06 ± 0.04	0.12 ± 0.03	13.5
extreme cool	test profile[a]; $p_{trop} = 0.2$ bar	8.4 ± 0.2	0.21 ± 0.03	18.2

[a]see description in Section 2.6.4

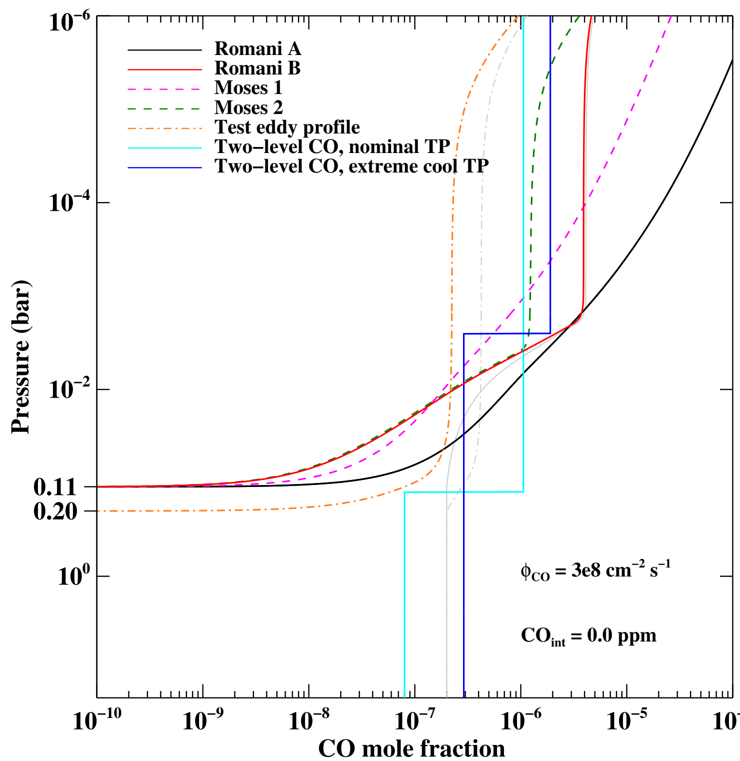

Figure 2.9: Sample CO profiles that result from eddy profiles in Fig. 2.8, assuming $\phi_{\rm CO} = 3 \times 10^8$ cm^{-2}s^{-1} and no internal contribution to the CO. To illustrate the effect of internal CO on the CO profile, we also show the CO profile for the Romani B eddy profile (solid red line) with the addition of 0.2 ppm of internal CO (solid grey line); and the 'test eddy profile' (orange dot-dashed line) with 0.2 ppm of internal CO included (grey dot-dashed line). The best-fit parameters for physical CO profiles depend on the TP profile in addition to the eddy profile; fits are summarized in Table 2.5. For reference, the best-fit two-level profiles from our nominal (no H_2S, cyan line) and extreme cool (blue line) TP profile fits are shown.

2.5 Errors and uncertainty

As described in Section 2.2, the least-squares fitting utilizes the residual map rms scatter to weight the data for calculating $\widehat{\chi^2}$. This weighting scheme compensates for the difference in signal-to-noise between the narrow ($\sim$ 1 MHz) and wide ($\sim$ 33 MHz) frequency channels, which we expect to differ by a factor of $\sim$6. Noisy channels that are not flagged during data reduction are down-weighted. Day-to-day variations due to weather or array performance, and differences in the noise between 1 and 3 mm, are also accounted for. However, we expect that these weights underestimate the total data uncertainties. While the overall calibration offset is a free parameter in the least-squares fits, additional systematic errors in the flux densities, for example due to errors in the bandpass calibration, could affect the relative flux between frequency windows. A visual comparison of individual 1-mm tracks (see Fig. 2.3) shows small day-to-day offsets in the average flux density in a given frequency window, for example at 230 GHz and 235 GHz, that are likely due to this type of systematic error.

Additionally, gain calibration offsets between each of our 1-mm tracks could also cause systematic, frequency-dependent errors in the final spectrum. Since we expect a residual uncertainty of 3% in the relative gain calibration between our 1-mm datasets, we tested the effect of such errors using a Monte Carlo method. We assume 3% random errors in the relative gains between data sets and perform 300 trials of our constant-value $n_{\mathrm{CO}}/n_{\mathrm{TOT}}$ fit. We find that the fit solution is stable to the inclusion of these errors, but the statistical uncertainty of the best-fit CO abundance increases by a factor of 2. While this experiment is too time intensive to repeat for the other model cases, this result suggests that 1) in general we are underestimating the errors in the fits by ignoring the error in the relative gains between 1-mm tracks, and 2) at least in this case, including the errors in the relative gains between 1-mm tracks leads to an increase in the uncertainties, but does not change the best-fit solution.

Because of the systematic errors, we consider our values of $\sigma_{meas,m}$ to be weights rather than true estimates of the uncertainties in our data points. This is reflected in the values of $\widehat{\chi^2}$ for our fits, which we would expect to be 1.0 for a model that fully captures the data *if* the values of $\sigma_{meas,m}$ were reflective of the true data uncertainties. A $\widehat{\chi^2}$ of 11.1 for our best-fit, two-level model implies that if this model were a perfect representation of the data, then the data weights $\sigma_{meas,m}$ underestimate the total data uncertainty by a factor of 3.3. However, the high value of $\widehat{\chi^2}$ is likely due to deficiencies in the model in addition to an underestimate in the data errors. Factors that contribute to this include errors in the continuum opacity: either in the mixing ratios of the continuum species or in the coefficients/line profiles used to derive continuum absorption. Our tests with H_2S, a species which we observe to affect our millimeter spectrum but whose abundance is poorly constrained, provide one example of this. Errors in the shape of the TP profile and CO profile can also contribute, since we only investigate a finite number of TP and CO profile shapes.

In summary, the $\widehat{\chi^2}$ parameter does not reach the theoretical expectation of $\widehat{\chi^2} \approx 1$ for a perfect fit because 1) while the values of $\sigma_{meas,m}$ adopted from the rms scatter in the maps are good estimates of the relative dispersions of the data points, they do *not* characterize the total intrinsic uncertainties; and 2) the models (even our best models) are not perfect. Regardless, $\widehat{\chi^2}$ is a useful measure of the variance of the data point residuals (δy_m^2, see above) for our different fits. We encourage the reader to use both the reported $\widehat{\chi^2}$ values and the plots when evaluating the success of various models in reproducing the data.

2.6 Results

The results of our model fits, which are summarized in Tables 3-6, are illustrated in Figs. 10-21 and discussed below. Plots of the CO spectra show both the unbinned single-channel data with uncertainties $\sigma_{meas,m}$, and the data binned to 3 times the channel width; 1- and 3-mm flux densities are typically scaled by the amplitude correction factors from the nominal TP profile best two-level fit (not including H_2S), before being converted to brightness temperature. For ease of comparison, additional model spectra are also scaled to align with this nominal two-level model.

2.6.1 Constant CO models

Our best-fit model for a constant CO distribution uses the nominal TP profile and a CO mole fraction of 0.5 ppm. The best-fit CO abundance decreases for cooler TP profiles, and increases for warmer TP profiles, within a range of $0.3 - 0.7$ ppm (Table 2.3). Figure 2.10 illustrates that a constant CO profile that has the appropriate line depth is generally too broad in the wings. The emission peak at line center is also a poor match to the data.

2.6.2 Two-level CO models, no H_2S

Model spectra produced with our two-level CO profiles offer an improved fit to the data; this is also illustrated in Figure 2.10. Overall, our nominal TP profile allows the best fit to the data, in a $\widehat{\chi^2}$ sense, with the Bézard et al. (1999) TP profile solution a close second. The best two-level model solution has a $\widehat{\chi^2}$ of 11.1, with 1.1 ppm of CO in the upper atmosphere and 0.1 ppm CO in the lower atmosphere. The transition pressure for this model is located near the tropopause, at $\log P(bar) = -0.9$ ($P = 0.13$ bar). The best-fit parameters for several transition pressures near the $\widehat{\chi^2}$ minimum value of $\log P(bar) = -0.9$ ($P = 0.13$ bar) are presented in Table 2.6; the model CO (2–1) spectrum for three of these solutions is plotted against the scaled 1-mm data in Fig. 2.11. The good match of all of these spectra to the data implies that there is a range of transition pressure levels that produce quality fits to the data. This is also clear from the best-fit $\widehat{\chi^2}$ values; for example, the fit solution at $\log P(bar) = -0.8$ ($P = 0.16$ bar) also has a $\widehat{\chi^2}$ of 11.1, with a slightly lower best-fit CO abundance of 1.0 ppm in the upper atmosphere and 0.0 ppm CO in the lower atmosphere.

Table 2.6: Best-fit two-level CO profiles for a series of transition pressure levels, for models using our nominal thermal profile (Fletcher et al. 2010). The CO mole fraction transitions between a high-altitude mole fraction ("CO above") and a deep-atmosphere mole fraction ("CO below") at a transition pressure P which is given in units of $\log P(\text{bar})$ as well as in bars (Section 2.6.2). Transition pressures in the range of $\log P(\text{bar}) = -3.0$ to 0.0 were tested with the model, and a subset of these tests is shown here. As in Table 2.3, the 1- and 3-mm flux density factors are the factors by which the data must be multiplied to match the model in the best-fit solution, and $\widehat{\chi^2}$ is the reduced χ^2 of the best-fit model, as defined in Eq. (4).

$\log P(\text{bar})$	$P(\text{bar})$	$\widehat{\chi^2}$	CO below (ppm)	CO above (ppm)	1-mm flux density factor	3-mm flux density factor
-1.2	0.063	11.8	0.27 ± 0.02	1.27 ± 0.07	1.074 ± 0.003	1.084 ± 0.002
-1.1	0.079	11.4	0.21 ± 0.02	1.22 ± 0.06	1.077 ± 0.003	1.085 ± 0.002
-1.0	0.10	11.2	0.15 ± 0.03	1.15 ± 0.05	1.079 ± 0.003	1.087 ± 0.002
-0.9	**0.13**	**11.1**	$\mathbf{0.08 \pm 0.03}$	$\mathbf{1.07 \pm 0.04}$	$\mathbf{1.082 \pm 0.003}$	$\mathbf{1.088 \pm 0.002}$
-0.8	0.16	11.1	0.01 ± 0.02	0.98 ± 0.03	1.084 ± 0.003	1.090 ± 0.002
-0.7	0.20	11.3	0.000 ± 0.003	0.86 ± 0.02	1.082 ± 0.002	1.090 ± 0.002
-0.6	0.25	11.8	0.004 ± 0.005	0.75 ± 0.02	1.079 ± 0.002	1.090 ± 0.002

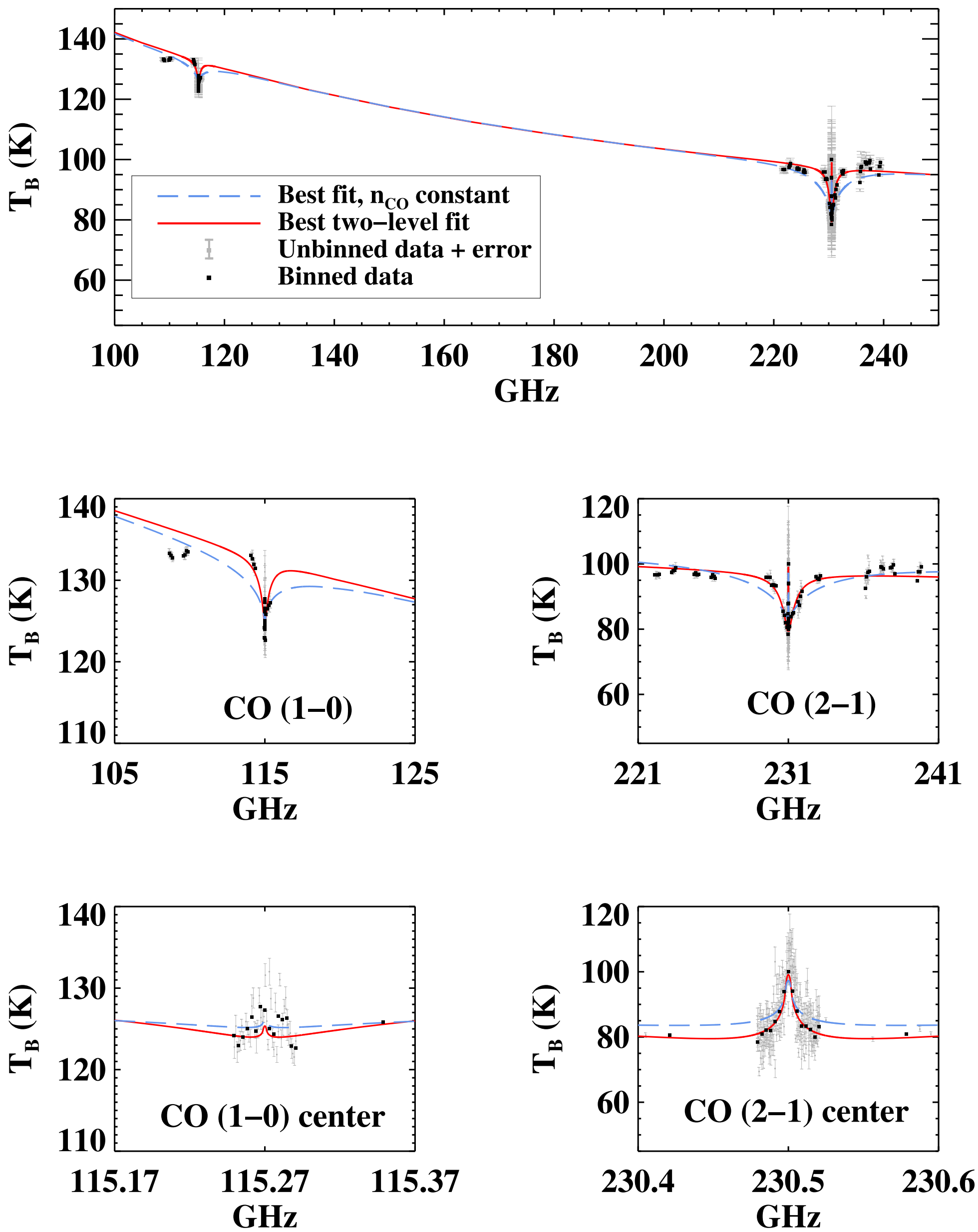

Figure 2.10: Models of the millimeter spectrum corresponding to the best-fit constant (0.5 ppm) CO profile in blue; and two-level (1.1 ppm above the 0.13 bar level, 0.1 ppm deeper than 0.13 bar) CO profile in red. H_2S absorption is omitted here. For plotting purposes, the 1- and 3-mm data were scaled up by 8.2% and 8.8% respectively, to match nominal TP, best-fit two-level model; likewise, subsequent models are all scaled by the relative flux correction factors to permit comparison. This plot shows that a two-level profile fits the data significantly better than a one-level profile.

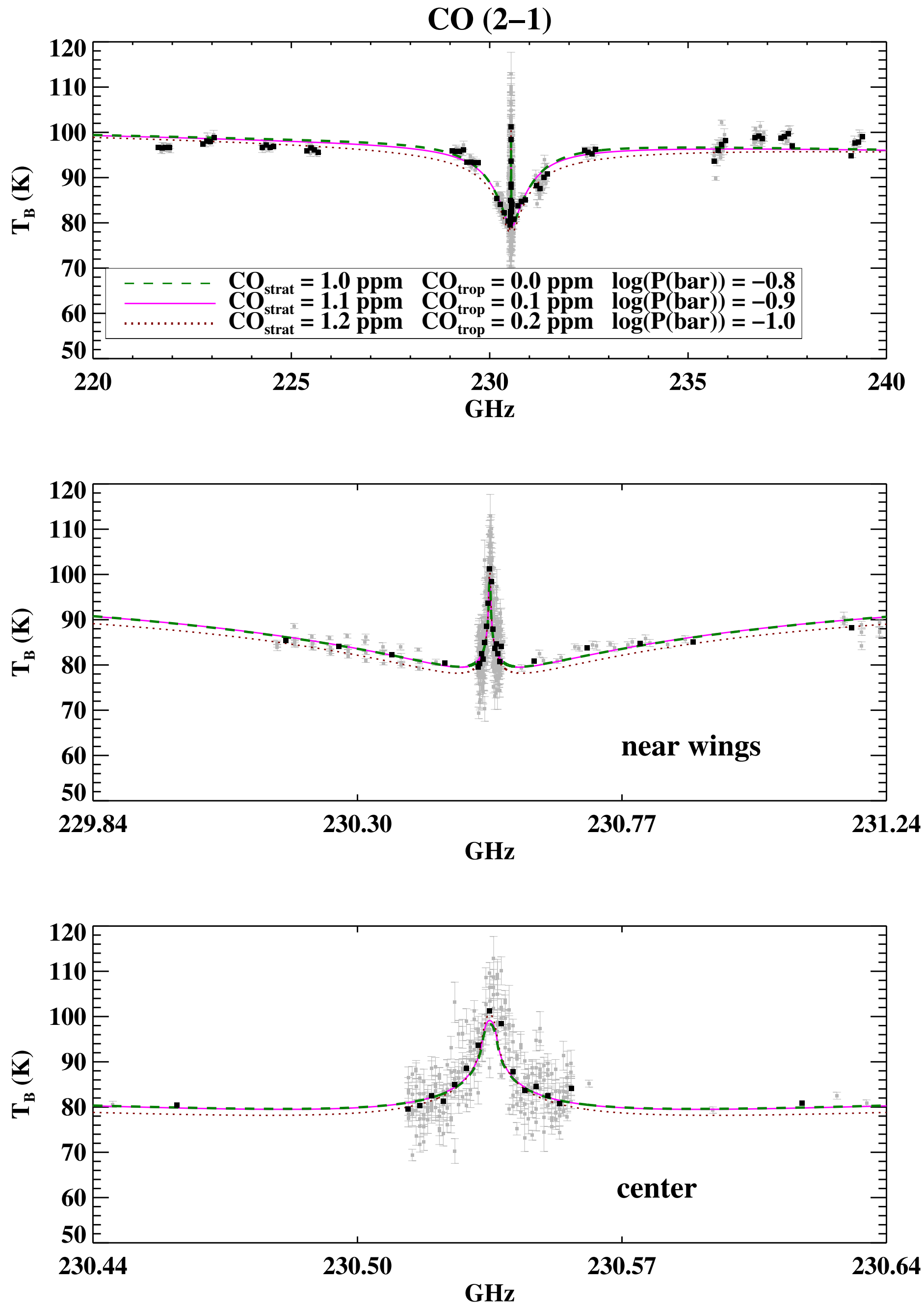

Figure 2.11: Spectral models for transition pressures of $\log(P(\text{bar})) = -0.8, -0.9$ and -1.0 (0.16, 0.13, and 0.10 bar, respectively), and our nominal TP profile, shown for the CO (2–1) line (see Table 2.6). Solutions for $\log P(bar) = -0.8$ (green dashed line) and -0.9 (solid magenta line) are somewhat more favorable in the far wings (2-3 GHz from line center), but all three models match the data quite well.

Therefore, the best-fit answer alone does not fully characterize the range of solutions allowed by our data. We also find that models using our nominal thermal profile produce solutions with lower values of $\widehat{\chi^2}$ than the best solutions from models using other thermal profiles, for a range of transition pressures (see Tables 2.4 and 2.6). These solutions have CO mole fractions of 0.0-0.3 ppm in the troposphere and 0.8-1.3 ppm in the stratosphere, with level transitions between 0.06 and 0.25 bar. This very shallow minimum in $\widehat{\chi^2}$ as a function of transition pressure is likely a result of the thermal profile being nearly isothermal in this region around the tropopause. In addition to the default assumption of a dry adiabat, we also test thermal profiles that used a wet adiabat to extrapolate to high pressures. We find that, in general, using a wet adiabat for the thermal profile does not alter the models significantly, and increases the values of $\widehat{\chi^2}$ slightly.

Of all of our test thermal profiles, models using the extreme warm profile agree least well with the data, in a $\widehat{\chi^2}$ sense. This thermal profile is also the least consistent with the published TP profiles (see Fig. 2.6). The best-fit transition pressure for this thermal profile is at 0.4 bar, which is below the tropopause, and therefore probably unphysical. The best-fit moderate warm CO profile is qualitatively similar to the best model from the nominal TP profile, with 1.1 ppm of CO in the stratosphere and 0.0 ppm CO below the tropopause. Figures 2.12 and 2.13 show that both warm TP profiles produce line profiles that are too high in the near wings of the line ($\leq$ 200 MHz from center), particularly at 1 mm. The extreme warm profile is also too broad in the far wings of the CO line.

Model fits using the cooler TP profiles favor two-level profiles with level transitions occurring well above the tropopause; the transition for the best-fit, moderate cool thermal profile case is at 25 mbar; and at 2.5 mbar for the extreme cool profile. Fits using cooler TP profiles favor higher CO mole fractions in both levels of the atmosphere: the best-fit solutions give 0.3 ppm CO in the lower level of the atmosphere for both thermal profiles, and 1.4 and 1.9 ppm CO in the upper atmosphere for the moderate and extreme TP profiles, respectively. As Figs. 2.12 and 2.13 show, models using the cooler TP profiles have the correct absorption depth and match the emission peak well; but are too broad in the far wings, particularly at 1 mm.

Given these findings, we conclude that the data are best matched by the Fletcher et al. (2010) thermal profile, with $0.1^{+0.2}_{-0.1}$ ppm of CO in the troposphere and $1.1^{+0.2}_{-0.3}$ ppm of CO in the stratosphere, as indicated by the range of values in Table 2.6. Fits to the 1-mm and 3-mm lines separately, which are performed using the nominal TP profile, give consistent best-fit solutions. Visual inspection of all of the models generally indicates better agreement with the data at 1 mm; however since the 3-mm data have lower signal-to-noise, the $\widehat{\chi^2}$ value for the 3-mm data alone is actually lower than for the 1-mm data. Best-fit corrections to the flux density are 6-10% at 1 mm and 9-10% at 3 mm (Table 2.4).

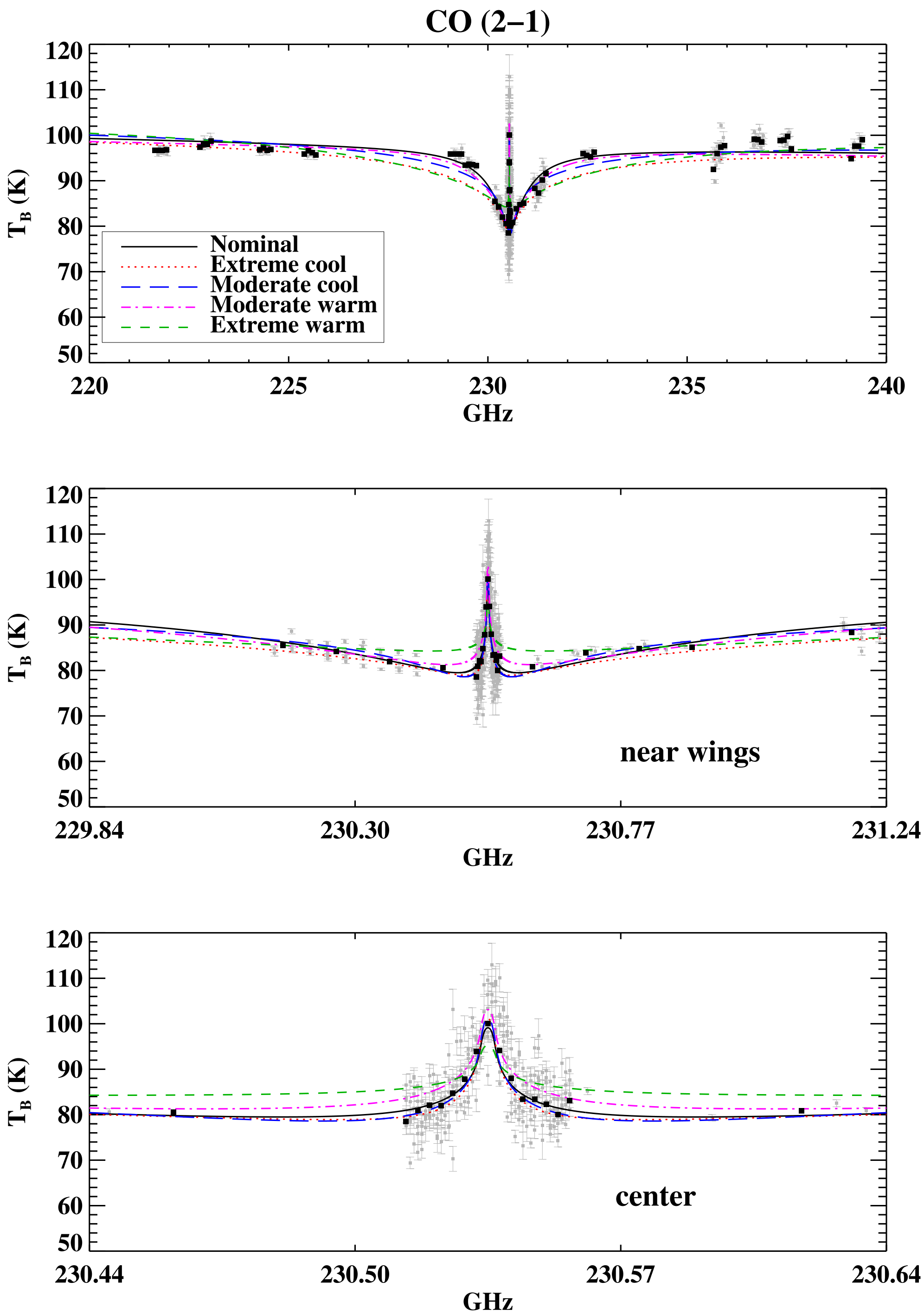

Figure 2.12: Comparison of best-fit two-level models to the CO (2–1) data using different TP profiles.

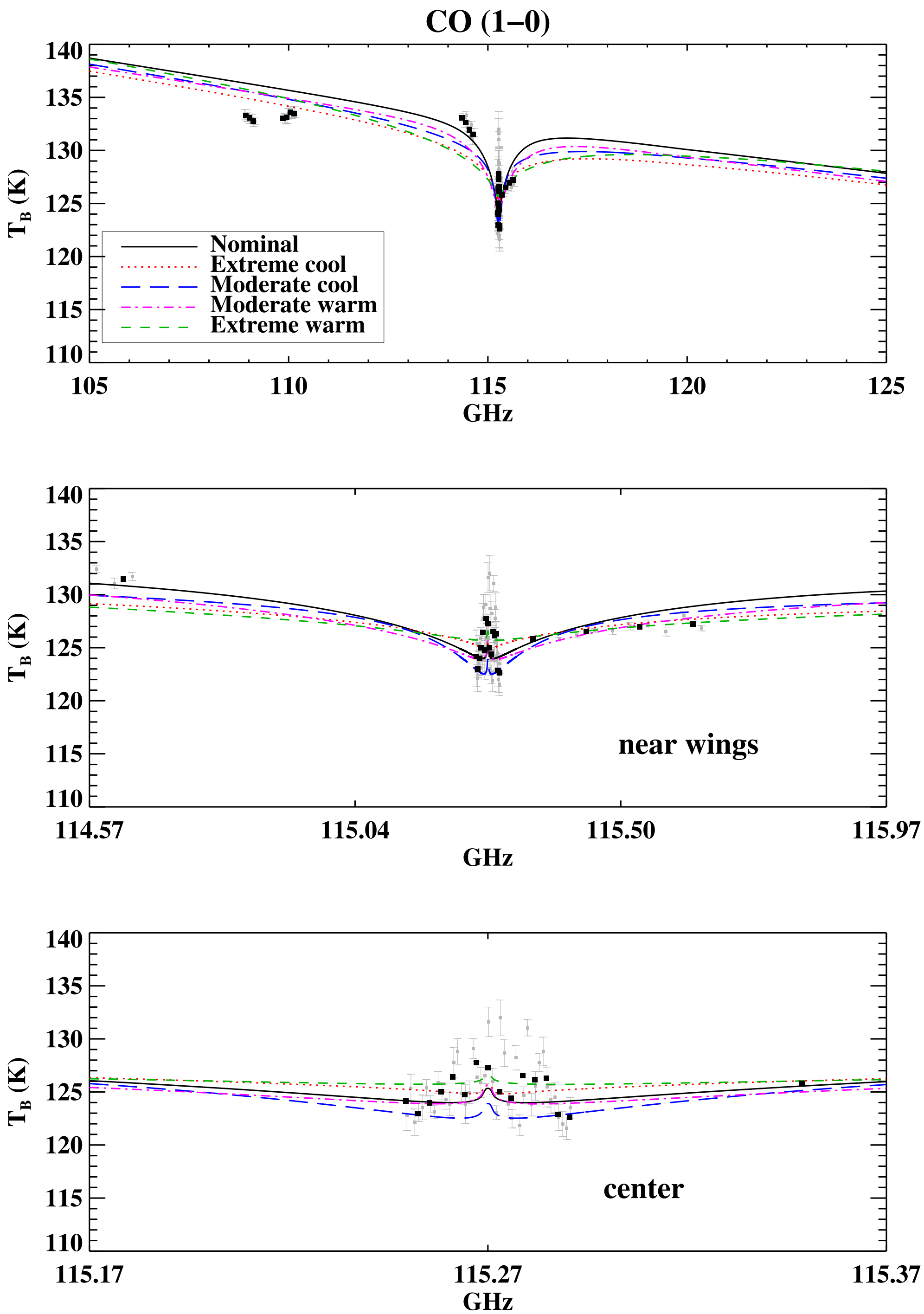

Figure 2.13: Comparison of best-fit two-level models to the CO (1–0) data using different TP profiles.

2.6.3 Two-level models, H_2S included

As discussed in Section 2.3, we test the effect of including opacity due to a 10 and 50 times protosolar enrichment in H_2S. We find that the main effect of adding H_2S on the best-fit model parameters is to change the amplitude scaling factors for the 1- and 3-mm data. Most notably, without H_2S, the 3-mm data are lower than the model by $\sim 9\%$, whereas with $10\times$ protosolar H_2S the data are higher than the model by $\sim 9\%$ (Fig. 2.14). Abundances of H_2S higher than $10\times$ the protosolar value do not further change the millimeter spectrum, due to condensation into the H_2S ice cloud at pressures of a few bars (de Pater et al. 1991a).

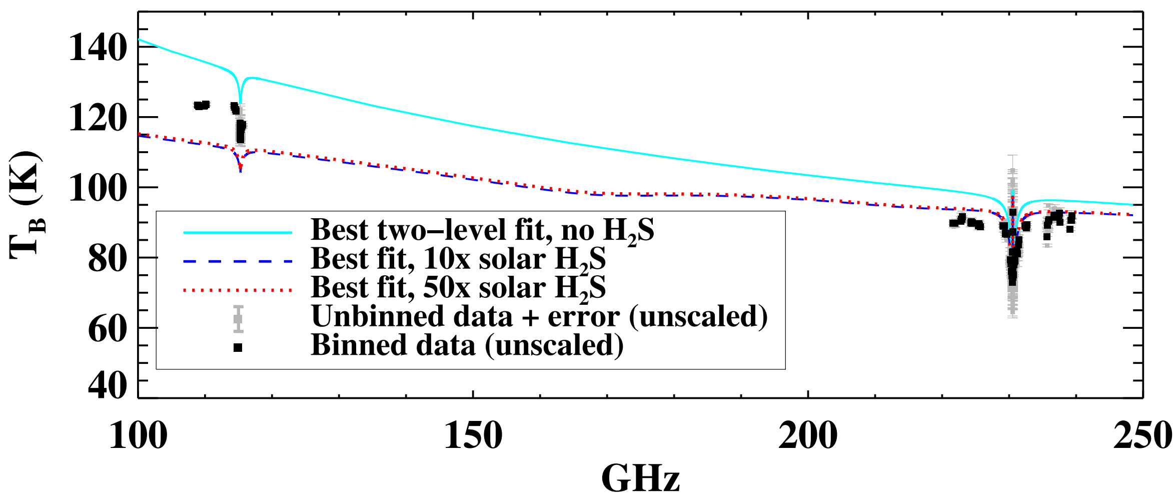

Figure 2.14: Best-fit solutions for models containing no H_2S absorption (solid cyan), 10 times solar H_2S (blue dashed) and 50 times solar H_2S (red dotted). In this Figure, the data and models have *not* been scaled by any flux density correction factor. Generally, all models are higher than our raw data at 1 mm. At 3 mm, the no-H_2S model is higher than the raw data, whereas the H_2S-enriched models are lower. The 10 and 50 times protosolar H_2S models match one another closely.

Despite the significant effect of H_2S absorption on the 3-mm continuum, we find that the best-fit CO solution is not strongly affected by the inclusion of H_2S absorption: the best-fit CO vertical profile has 1.1 ppm CO in the stratosphere and 0.0 ppm of CO in the troposphere (Table 2.4). The best-fit CO model spectra, scaled to match the best two-level fit for the no-H_2S case, are plotted with the (scaled) data in Figs. 2.15 and 2.16. The $\widehat{\chi^2}$ value for the fit improves with the addition of H_2S, which is primarily due to an improved fit to the shape of the far wings of the CO (1–0) line (Fig. 2.16). There is also some improvement to the fit at the center of the CO (1–0) line.

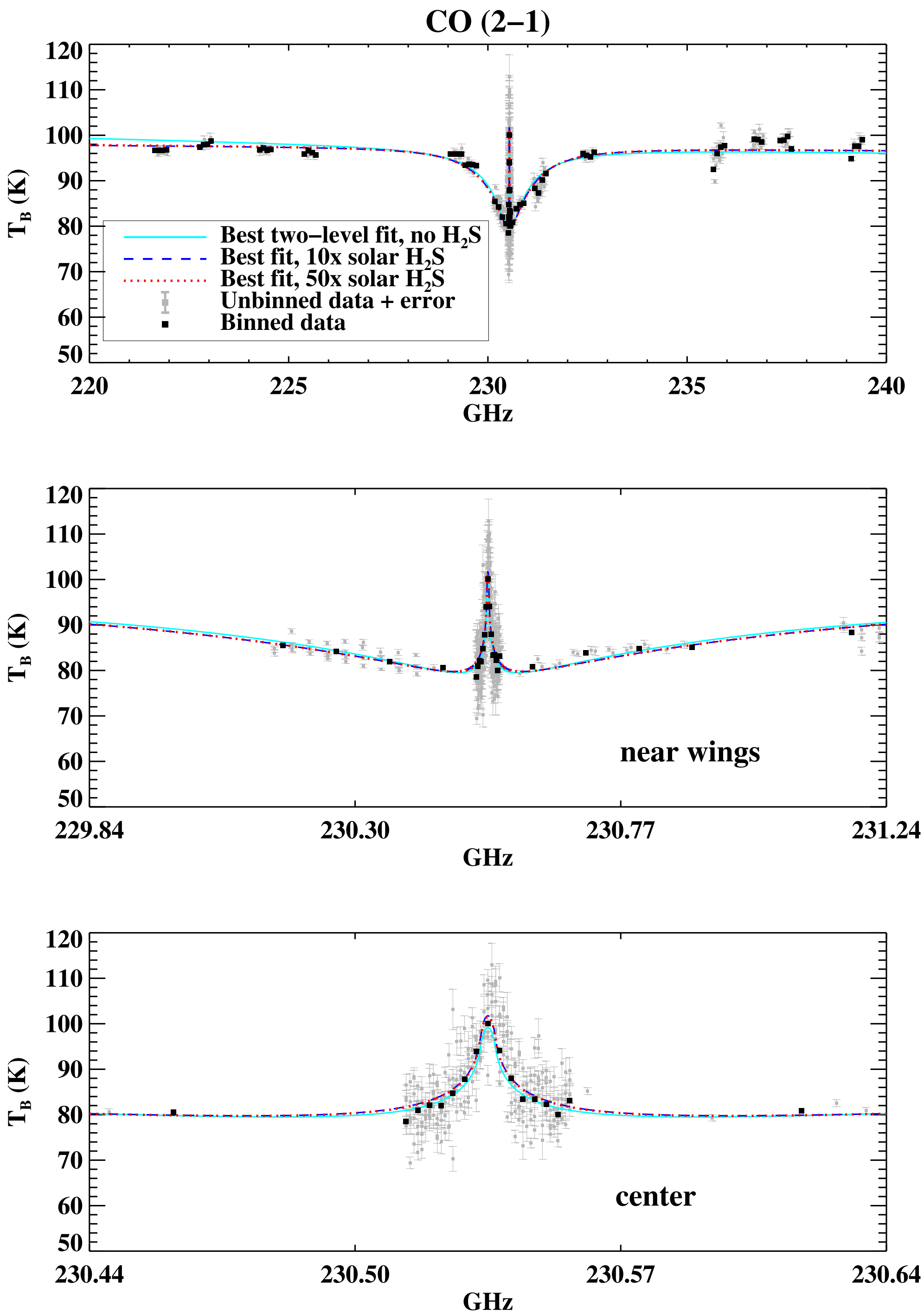

Figure 2.15: Model fits to the CO (2–1) line as in Fig. 2.14, except that the data and H_2S-enriched models are scaled to match the brightness temperature of the best-fit, no-H_2S model.

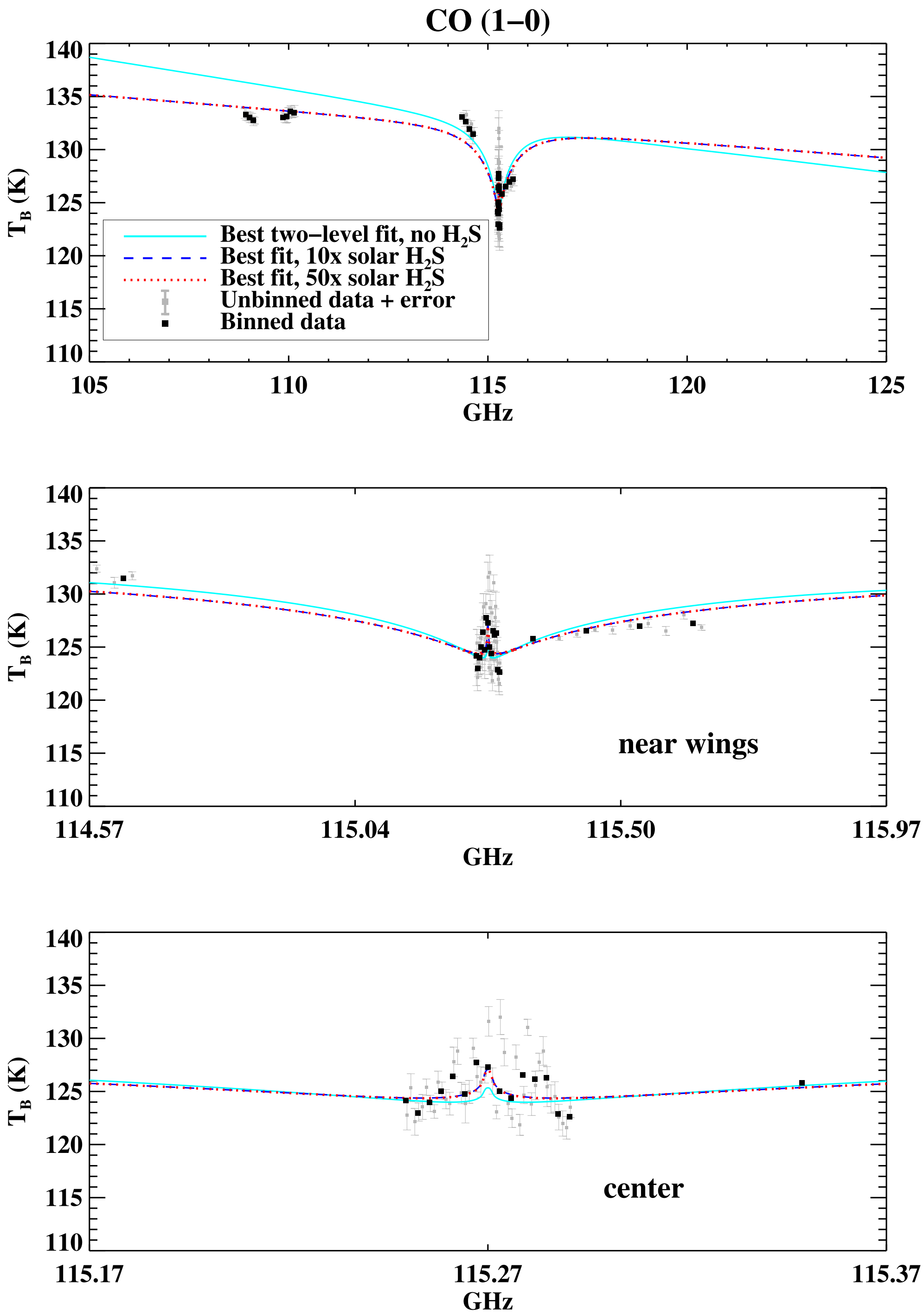

Figure 2.16: Same as Fig. 2.15, except for the CO (1–0) line.

2.6.4 Physical models

Physical CO profiles based on the diffusion models of Moses (1992) and Romani et al. (1993) produce the best model spectra when cool thermal profiles are used. The reason for this can be inferred from Fig. 2.9: for all of these diffusion models, the mole fraction of CO in the atmosphere from an external source falls off at pressures less than ∼10 mbar, which is much higher in altitude than the transition level for the best-fit two-level model using our nominal thermal profile, but is consistent with the transition levels for the best-fit moderate and extreme cool TP profile models. The internal CO contribution for these fits is roughly independent of the eddy diffusion profile, with mole fractions of 0.3 and 0.4 ppm for the extreme and moderate cool thermal profiles, respectively. These values are very similar to the CO abundances found for the two-level fits using the same thermal profiles. The external CO flux is dependent on the choices for the eddy diffusion coefficient and thermal profiles: values range from $\phi_{\rm CO} = 0.5 - 7 \times 10^8$ cm^{-2}s^{-1}.

To produce a physical CO profile that is more like our best-fit two-level CO distribution, we created two 'test' eddy diffusion coefficient profiles (Fig. 2.8). The profiles are designed to have a more rapid increase in the mixing from the diffusion rate minimum just above the tropopause, to allow high concentrations of externally supplied CO to reach deeper levels. No attempt is made to evaluate the physical likelihood of such an eddy profile. The two test profiles are identical except for the location of the tropopause, which is defined by a sharp transition from fast to slow mixing. In addition to using a value for the tropopause of 0.11 bar as in the Moses (1992) and Romani et al. (1993) cases, we also try locating the tropopause level at 0.20 bar. Using these test eddy profiles, we are able to produce physical CO models using the nominal TP profile that are in better agreement with the data. The best-fit parameters for the test profiles are $\phi = 10 - 20 \times 10^8$ cm^{-2}s^{-1} and $\rm CO_{\it int} = 0.2 - 0.3$ ppm. Unsurprisingly, the test eddy profiles, which are designed to be used with the nominal TP profile, do not do as well when used with the cool TP profiles. A selection of the best model spectra based on physical CO distributions is shown in Figs. 2.17 and 2.18.

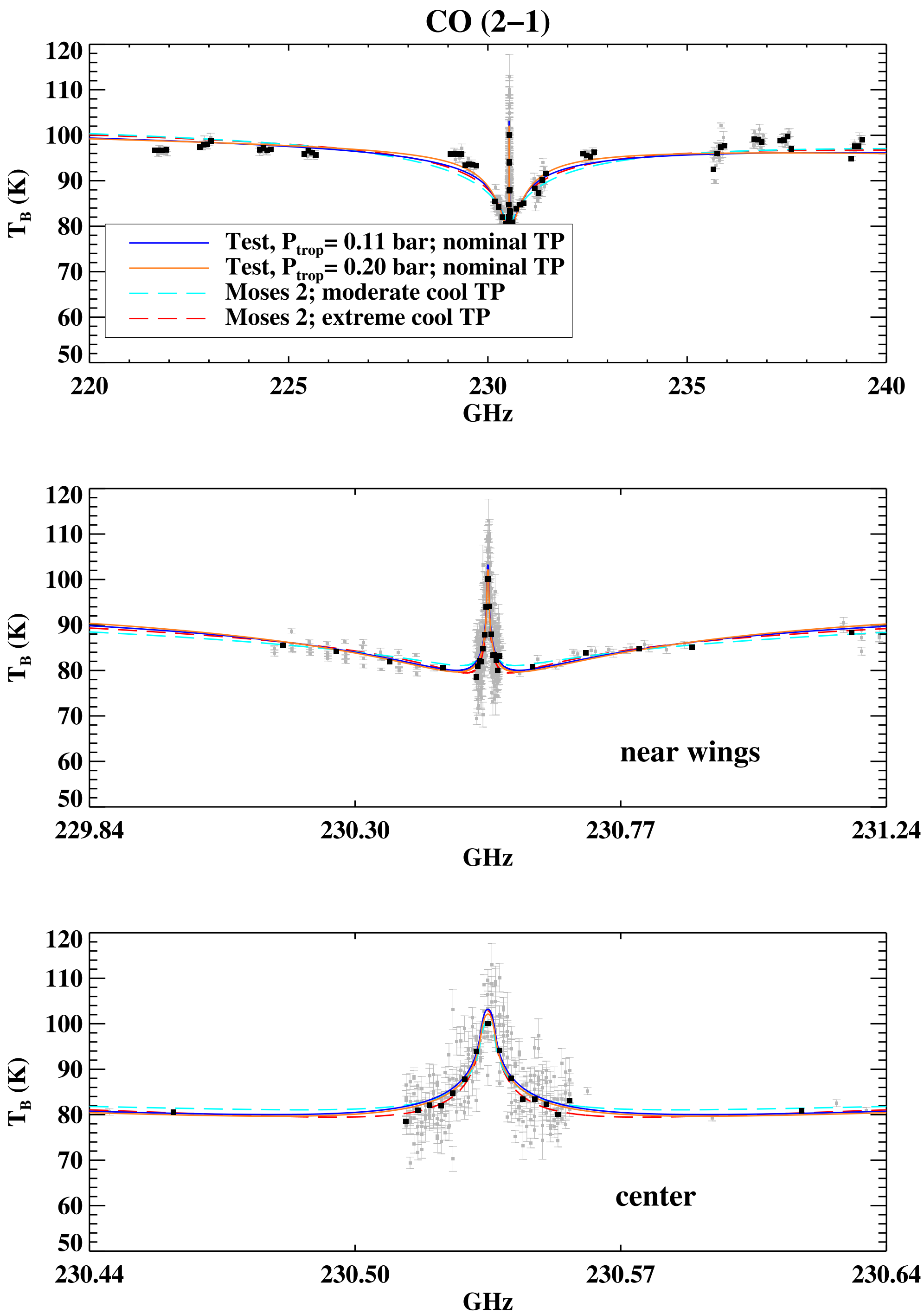

Figure 2.17: Model fits to the CO (2–1) line from a selection of best-fit physical CO profiles (see Table 2.5).

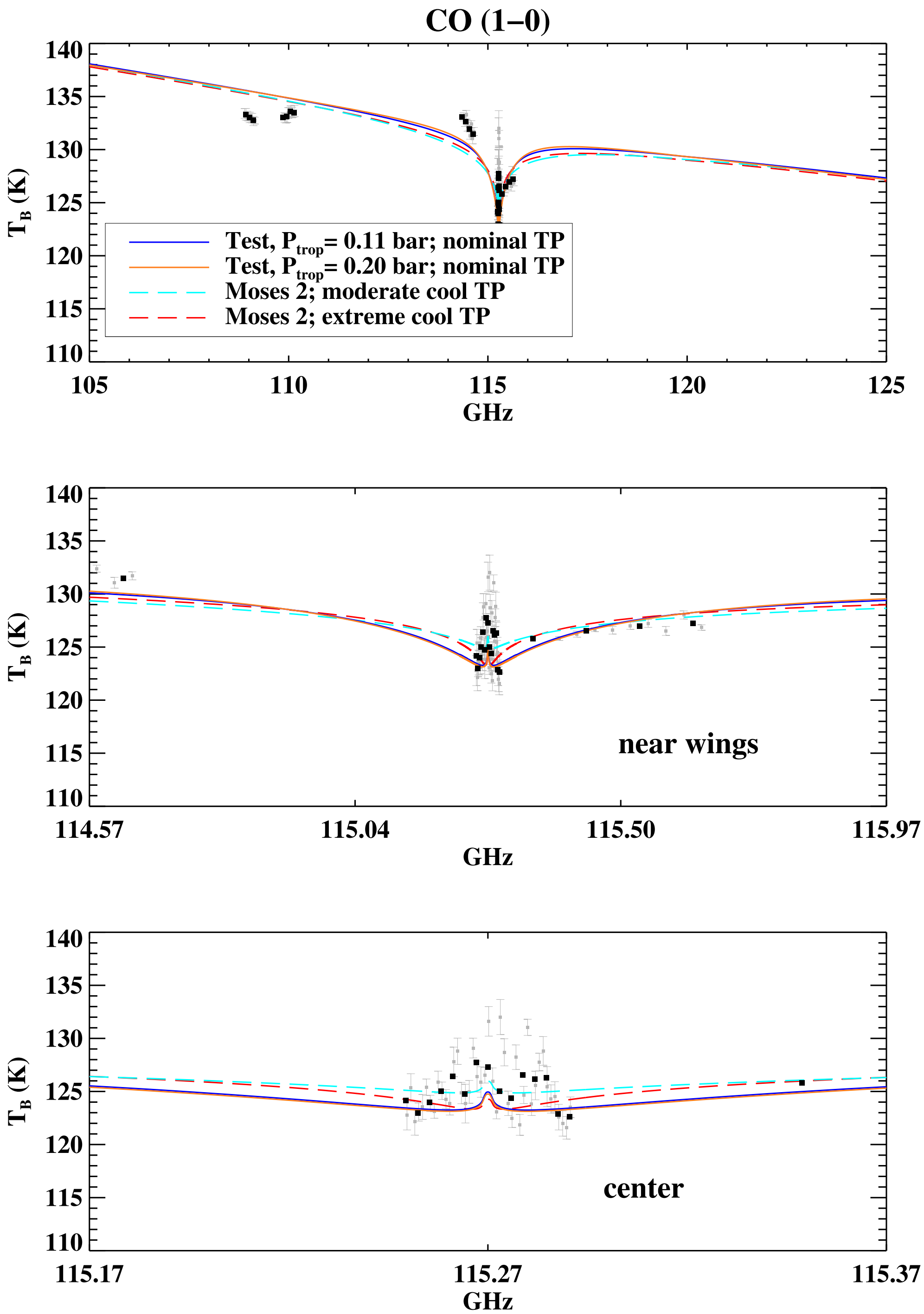

Figure 2.18: Same as Fig. 2.17, except for the CO (1–0) line.

2.7 Discussion

Our analysis of the CARMA CO (2–1) and (1–0) data indicates a preference for the Fletcher et al. (2010) thermal profile in Neptune's upper atmosphere over warmer and cooler profiles. Good fits are characterized by CO mole fractions of 0.0-0.3 ppm below the tropopause and 0.8-1.3 ppm in the stratosphere. This is true for the independent fits of the 1- and 3-mm lines, as well as the combined fit. The Bézard et al. (1999) thermal profile and our moderate warm profile give best-fit CO profiles that are consistent with the nominal thermal profile results. Cooler thermal profiles also produce acceptable fits to the data, but models using the cooler TP profiles are generally too broad in the far wings of the CO lines. The vertical CO profiles derived using our moderate and extreme cool thermal profiles are qualitatively different than the nominal TP profile best-fit solution: we find CO mole fractions of 0.3-0.4 ppm in the troposphere and lower stratosphere, and 1.4-1.8 ppm above 2.5-25 mbar. Using a physical diffusion model, we determine that the stratospheric CO abundances for all thermal profiles correspond to an external CO flux of $\phi_{\mathrm{CO}} = 0.5 - 20 \times 10^8$ cm^{-2}s^{-1}. Internal CO contributions for the physical CO profile solutions are typically 0.2-0.4 ppm.

Plots of the 3-mm spectrum (e.g. Figs. 2.10, 2.13, 2.16, 2.18) show greater deviations between the data and models than we find at 1 mm. We attribute this to the fact that, at 3 mm, we probe deeper levels of the atmosphere (Fig. 2.1), where the atmospheric opacity is not well constrained. However, we are encouraged by the fact that the independent fits to our two CO lines give consistent CO profile solutions. Additionally, we find that the inclusion of 10-50$\times$ solar H_2S opacity improves the $\widehat{\chi^2}$ goodness-of-fit, but does not significantly affect the best-fit CO vertical profile.

2.7.1 Comparison with previous results

In Fig. 2.19 we compare our best-fit two-level CO profiles with previously reported values and profiles. Figures 2.20 and 2.21 use several of these recent results for the CO profile in conjunction with our radiative transfer code to produce model spectra. In each case we fit only the data amplitude scale factors at 1 and 3 mm; the lowest $\widehat{\chi^2}$ for these literature CO profiles and our data are presented in Table 2.7.

Of the three most recent previous measurements of millimeter CO line shapes (Marten et al. 2005; Lellouch et al. 2005; Hesman et al. 2007), only Marten et al. (2005) found a result consistent with a constant CO mole fraction. However, their data only cover wavelengths up to 50 MHz away from the center of the CO (4-3) line. From the CO line contribution functions of the first three rotational transitions (Fig. 2.1), we estimate that their data are only sensitive down to pressures of a few tens of mbar, which implies that they would not detect a tropospheric decrease in the CO abundance. Our best-fit two-level, nominal TP profile model has an abundance of 1.1 ppm in the upper atmosphere, which agrees well with the Marten et al. (2005) value. As Figs. 2.20 and 2.21 and Table 2.7 illustrate, this profile

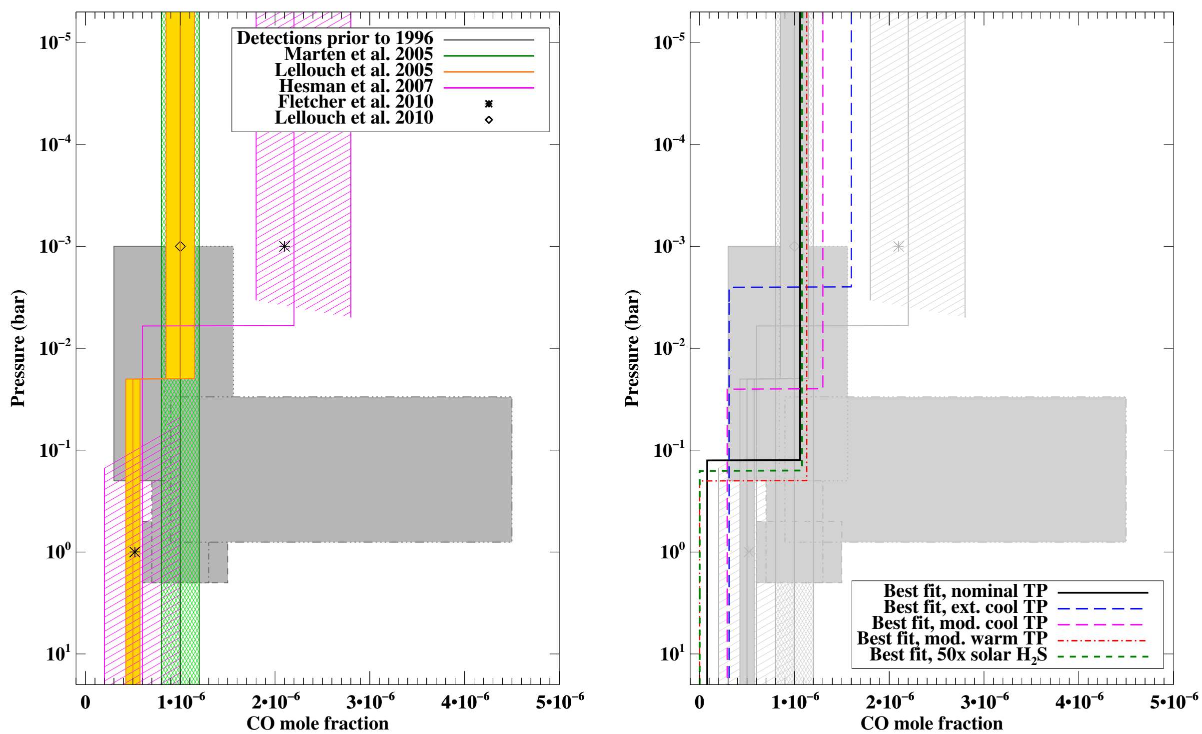

Figure 2.19: Selected published CO profiles with errors (left), compared to our best-fit profiles (right). Grey boxes indicate all the published results from prior to 1996, as described in Courtin et al. (1996). Colored regions indicate the best-fit CO profiles of Marten et al. (2005) (green, cross-hatched), Lellouch et al. (2005) (orange, shaded) and Hesman et al. (2007) (magenta, hatched); along with their uncertainties. The symbols indicate the values reported by Fletcher et al. (2010) (stars) and Lellouch et al. (2010) (diamond) for the stratospheric CO abundance. On the right, our best-fit two-level profiles are shown for several different thermal profiles, as well as for the case where absorption due to 50× solar H_2S is included.

is the least successful of those tested at reproducing our data.

Our two-level solutions, which have a smaller abundance of CO in the lower atmosphere, are qualitatively consistent with the results of the two recent millimeter studies by Lellouch et al. (2005) and Hesman et al. (2007). Quantitatively, there are important differences between these two previous works and with our own result. The Hesman et al. (2007) best-fit solution has a stratospheric CO abundance that is inconsistent with the Lellouch et al. (2005) result, as well as a lower pressure that defines the transition between the upper and lower levels of a two-level model. Our analysis demonstrates that there is a strong relationship between the stratospheric CO mole fraction and the pressure that defines the transition between the upper and lower levels of a two-level model. Furthermore, the

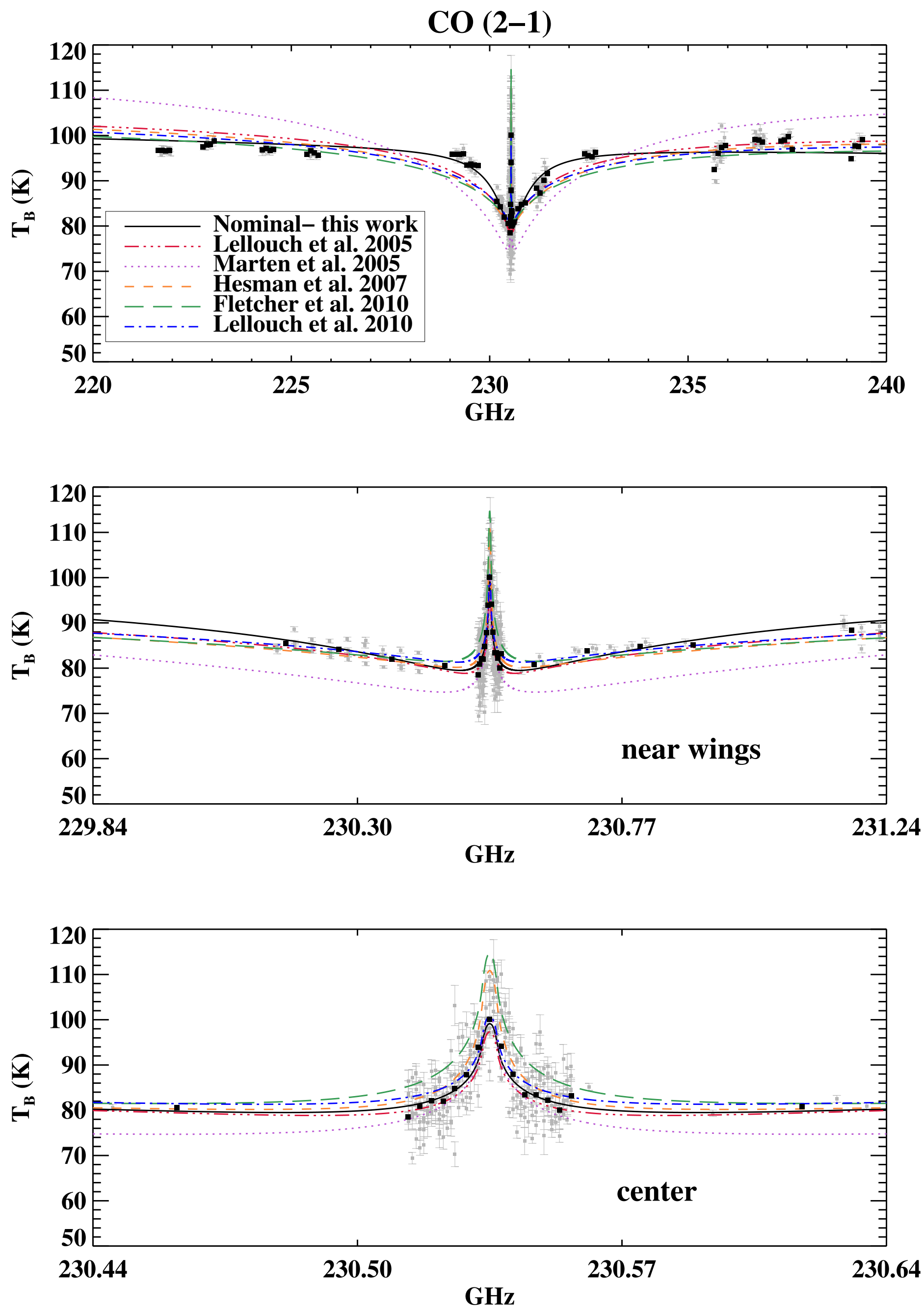

Figure 2.20: Comparison of the CO (2–1) line data (this work) with a selection of best-fit CO profiles from previous authors (see Table 2.7). In each case, we use the reported CO and temperature profiles from the indicated study. Using our model code, we fit the 1- and 3- mm gain uncertainties to minimize $\widehat{\chi^2}$ and plot the scaled model. For reference, the best-fit two-level solution from this work is plotted as well (black).

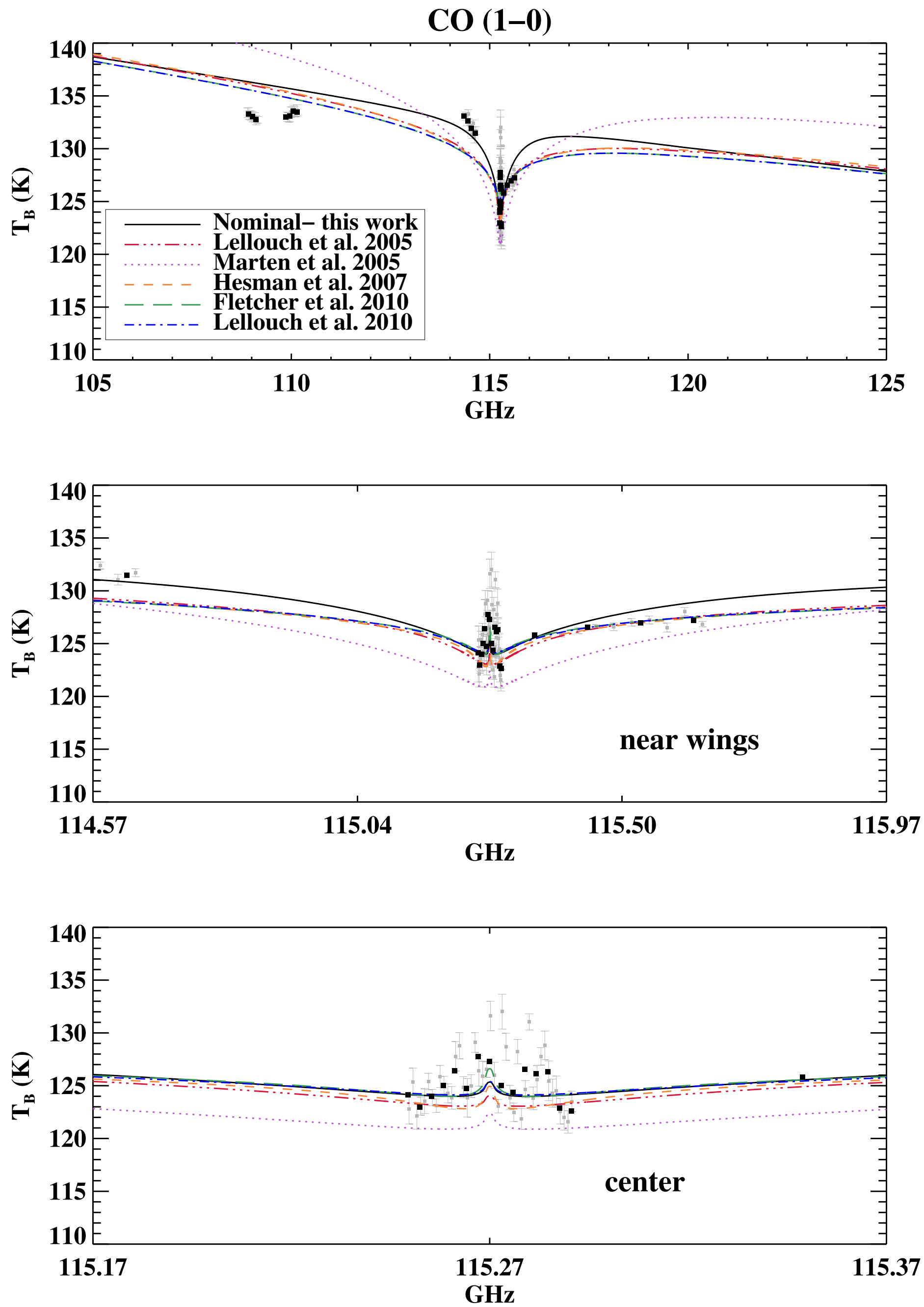

Figure 2.21: Same as Fig. 2.20, except for the CO (1–0) line data.

goodness-of-fit, as measured by $\widehat{\chi^2}$, tends to be relatively constant over a wide range of transition pressures, so that small variations in the data may lead to significant changes in the derived CO abundances. This leads to uncertainties in the CO abundances that are greater than the 20% uncertainties adopted by Lellouch et al. (2005), and may be a dominant source of inconsistency between the solutions of Lellouch et al. (2005) and Hesman et al. (2007). In comparison with our results, Lellouch et al. (2005) and Hesman et al. (2007) have higher tropospheric CO abundances (0.5 ± 0.1 and 0.6 ± 0.4 ppm, respectively) and transition altitudes (20 and 6 mbar, respectively) than our nominal best-fit solution of less than 0.1 ppm in the troposphere, with a transition near the tropopause. Interestingly, our best-fit solution using a moderate cool thermal profile, which is similar to the TP profiles used by Lellouch et al. (2005) and Hesman et al. (2007), produces a two-level CO profile that is roughly similar to the Lellouch et al. (2005) CO vertical profile (see Table 2.4), although still outside of their quoted uncertainties; and a tropospheric CO abundance that is consistent with Hesman et al. (2007). Using a cooler thermal profile also pushes the best-fit transition pressure to lower pressures (Fig. 2.19). As an additional test of the effect of the thermal profile on the CO best-fit solution, we used the plot from Hesman et al. (2007) to approximate the Hesman et al. (2007) data, and modeled the CO (3–2) line in a similar way to our own data. We note that we do not include the small leakage correction (Hesman et al. 2007) when converting from antenna temperature to brightness temperature. We find that our best-fit model to the approximate Hesman et al. (2007) data using our nominal thermal profile has a CO mole fraction of 1.1 ppm in the upper atmosphere; this value increases to 1.7 ppm of CO in the upper atmosphere if we perform the fit using a cooler thermal profile, which is closer to the best-fit value found by Hesman et al. (2007). This behavior is similar to what we see when fitting our own CO (2–1) and (1–0) line data.

While we find better agreement with the CO profiles of Lellouch et al. (2005) and Hesman et al. (2007) when we use a cooler thermal profile, our results do favor the warmer nominal thermal profile. As Figs. 2.20 and 2.21 illustrate, model spectra produced using the Lellouch et al. (2005) and Hesman et al. (2007) CO and thermal profiles, but with our radiative transfer code, are less consistent with our data than our nominal fit; this is particularly true in the line wings, 0.5-2 GHz from line center. The Hesman et al. (2007) solution also appears to be too high in the CO (2–1) emission peak. In addition to their use of a cooler thermal profile, the remaining cause of discrepancy between our result and that of Lellouch et al. (2005) may be the more limited frequency coverage of their dataset: if we consider only our data within the frequency range covered by the Lellouch et al. (2005) dataset, we find a best-fit vertical CO profile with 1.00 ± 0.08 ppm in the stratosphere (above 3 mbar) and 0.62 ± 0.05 ppm in the troposphere. We considered two additional factors that may contribute to the difference between our solution and that found by Hesman et al. (2007): the fact that Hesman et al. (2007) observe a higher frequency line, which probes slightly higher altitudes in the atmosphere (Fig. 2.1); and the uncertainty in the JCMT beam efficiency, which is used to convert the Hesman et al. (2007) data from antenna temperature to brightness temperature. By fitting the approximate Hesman et al. (2007) data, we find that of the two, the uncertainty in the JCMT beam efficiency has a stronger effect on the best-fit CO profile solution. The authors allow for a 5% uncertainty in the beam efficiency. With this constraint, our best fit to their data has a mole fraction of 0.5 ppm in the lower stratosphere and troposphere. If we allow for a beam efficiency uncertainty of ±10%, our best-fit models to the approximate Hesman et al. (2007) data have mole fractions of only 0.0-0.1 ppm of CO in the lower atmosphere. We therefore conclude that an underestimate of the uncertainties in the beam efficiency could potentially account for the remaining difference between our best-fit solution and the best-fit solution of Hesman et al. (2007).

Table 2.7: Goodness-of-fit $\widehat{\chi^2}$ values obtained using the best-fit CO profiles from previous authors with our radiative transfer code and our data. See Section 2.7.

CO profile reference	TP profile	$\widehat{\chi^2}$(1 mm)	$\widehat{\chi^2}$(3 mm)	$\widehat{\chi^2}$all
this work[a]	nominal	15.3	14.6	15.3
Marten et al. (2005)[b]	Marten et al. (2005)	70.2	71.5	70.3
this work[c]	nominal	10.7	9.3	11.1
Lellouch et al. (2005)[d]	Bezard et al. (1991)[e]	15.8	19.9	16.3
Hesman et al. 2007[f]	Hesman et al. (2007)	18.0	21.0	18.4
Fletcher et al. (2010)[g]	nominal [h]	25.3	16.8	24.0
Lellouch et al. (2010)[i]	Lellouch et al. (2010)	14.2	16.6	14.5

[a]best-fit one-level model, from Table 2.3
[b]1.0 ppm CO everywhere
[c]best-fit two-level model, no H_2S, from Table 2.4
[d]1.0 ppm CO at altitudes above 20 mbar; 0.5 ppm CO deeper than 20 mbar
[e]same as used in Lellouch et al. (2005)
[f]2.2 ppm CO at altitudes above 6 mbar; 0.6 ppm deeper than 6 mbar
[g]2.1 ppm CO at altitudes above 10 mbar; 0.5 ppm deeper than 10 mbar
[h]from Fletcher et al. (2010)
[i]we assume the same CO profile as in Lellouch et al. (2005); only the stratospheric CO was constrained from Lellouch et al. (2010)

Two other recent papers look at the CO abundance on Neptune using (far)infrared data. Fletcher et al. (2010) observed fluorescent lines with AKARI, and fit two profiles to the CO (2–1) fluorescent line: in their Profile 1, CO is limited to altitudes above 10 mbar. Profile 2 is similar to the Hesman et al. (2007) best-fit profile: 2.1 ppm of CO is present in the stratosphere, decreasing by a factor of four at altitudes below 10 mbar. They find that they require some CO below 10 mbar (their Profile 2) to reproduce their data. As with the Hesman et al. (2007) result, we find that the Fletcher et al. (2010) CO profile produces models that are a poor fit in the line core and far wings. We note that for a physical CO distribution, the CO abundance will not be constant with altitude, and the derived value for the stratospheric CO abundance will be dependent on the pressure levels one is sensitive to (see Fig. 2.9). Using Herschel measurements of CO lines at 153-187 μm, Lellouch et al. (2010) find a stratospheric CO abundance that is similar to the Lellouch et al. (2005) number; roughly 1 ppm. This value is consistent with our results (though inconsistent with the Fletcher et al. (2010) solution).

2.7.2 Implications: internal CO

The CO abundance that originates from Neptune's deep atmosphere acts as a probe of Neptune's global oxygen abundance: according to the net thermochemical reaction (Eq. 1) the equilibrium CO mole fraction is directly proportional to the equilibrium abundance of H_2O, and under the conditions of Neptune's deep atmosphere, nearly all the gas phase oxygen is contained in water. As first described by Prinn & Barshay (1977), the observed tropospheric CO mole fraction (0.0-0.3 ppm from our analysis) represents the equilibrium abundance at the CO 'quench level', which is defined as the depth at which

$$\tau_{chem} = \tau_{mix} \tag{2.7}$$

where τ_{chem} is the timescale for chemical conversion of CO into CH_4 and τ_{mix} is the atmospheric mixing timescale. Above the quench level, vertical mixing transports CO to higher altitudes before the constituents have a chance to equilibrate ($\tau_{chem} > \tau_{mix}$); and the CO mole fraction remains constant at a level which can be much higher than the equilibrium value. The H_2O mole fraction can then be determined from the CO mole fraction via the equilibrium relation

$$\frac{q\mathrm{CO}\,(q\mathrm{H_2})^3\,(P_\mathrm{T})^2}{q\mathrm{CH_4}\;q\mathrm{H_2O}} = e^{-\frac{\Delta_f G^0(\mathrm{CO})-\Delta_f G^0(\mathrm{CH_4})-\Delta_f G^0(\mathrm{H_2O})}{RT}} \tag{2.8}$$

where R is the gas constant, T is the temperature and P_T is the total pressure in bars at the quench level, qX is the mole fraction of species X, and $\Delta_f G^0(\mathrm{X})$ is the Gibbs free energy of formation of species X at the temperature of the quench level.

Determining the CO quench level requires knowledge of the limiting reaction rate for converting CO to CH_4; this is set by the slowest reaction step in the fastest chemical pathway for CO $\rightarrow$ CH_4 conversion. The original chemical scheme analyzed by Prinn & Barshay (1977) for Jupiter had as the rate-limiting step

$$\mathrm{H_2CO} + \mathrm{H_2} \rightarrow \mathrm{CH_3} + \mathrm{OH} \tag{2.9}$$

This scheme was adopted by Lodders & Fegley (1994) to estimate the O/H ratio implied by the early detections of ∼1 ppm of CO on Neptune (Marten et al. 1991; Rosenqvist et al. 1992; Guilloteau et al. 1993; Naylor et al. 1994). They found that a 440 times solar oxygen abundance is required to produce a 1 ppm CO abundance; this is roughly a factor of 10 higher than the C/H enrichment suggested by CH_4 measurements. Using updated laboratory measurements for the rate coefficients, Griffith & Yelle (1999) showed that the Prinn & Barshay (1977) reaction is actually about 4 orders of magnitude slower that originally calculated, and is therefore too slow to play a role in CO quenching kinetics. Griffith &

Yelle (1999) adopted instead a chemical scheme first advocated by Yung et al. (1988) for their analysis of Gliese 229B, which has as its rate-limiting step

$$\mathrm{H + H_2CO + M \rightarrow CH_3O + M} \tag{2.10}$$

where M represents any third body (atom or molecule). Bézard et al. (2002) also use the Yung et al. (1988) scheme for their analysis of CO chemistry on Jupiter. More recently, Visscher et al. (2010), Moses et al. (2011) and Visscher & Moses (2011) incorporate further updates to reaction rate coefficients, and compare the rates of all relevant reactions to determine the dominant kinetic mechanism for CO $\rightarrow$ CH_4 conversion. Visscher & Moses (2011) find that the dominant pathway for conditions in Jupiter, cool brown dwarfs and hot Jupiters is:

$$\mathrm{H + CO + M \rightarrow HCO + M} \tag{2.11a}$$
$$\mathrm{H_2 + HCO \rightarrow H_2CO + H} \tag{2.11b}$$
$$\mathrm{H + H_2CO + M \rightarrow CH_2OH + M} \tag{2.11c}$$
$$\mathrm{H_2 + CH_2OH \rightarrow CH_3OH + H} \tag{2.11d}$$
$$\mathrm{CH_3OH + M \rightarrow CH_3 + OH + M} \tag{2.11e}$$
$$\mathrm{H_2 + CH_3 \rightarrow CH_4 + H} \tag{2.11f}$$
$$\mathrm{H + OH + M \rightarrow H_2O + M} \tag{2.11g}$$

in which Eq. (2.11e) is the rate-limiting step. (Note: Visscher & Moses (2011) indicate a second reaction scheme which may be important under some conditions. We include this second reaction in our models as well, but find the rate is always more than two orders of magnitude slower than the above scheme. For simplicity, we omit this second reaction pathway here.)

A second source of error in the Lodders & Fegley (1994) determination of Neptune's CO quench level was described by Smith (1998), who showed that the typical estimate of the mixing time

$$\tau_{mix} = L^2/K \tag{2.12}$$

is not correct when the pressure scale height H is used for the characteristic mixing length scale L. According to the calculations of Smith (1998), effective mixing lengths are typically of order $0.1 - -0.2H$ which means that assuming $L = H$ will lead to an overestimate of τ_{mix} by up to two orders of magnitude.

Using the Visscher & Moses (2011) rate-limiting step and the Smith (1998) recipe for estimating the effective mixing length, we evaluate the O/H enrichment implied by our observed deep CO mole fractions.

Pursuant to Eq. 2.8, the equilibrium CO abundance depends on the H_2, CH_4 and H_2O mole fractions, temperature, and pressure. Therefore, in order to determine the CO quench level implied by our data, we extend our model of the thermal profile and

Table 2.8: Mole fractions in the deep atmosphere (below condensation levels) for different O enrichments. The enrichment factor for C is 48× solar, S is 50× solar, N is 1× solar, and the O enrichment varies.

Molecule	mole fraction				
	O/H=50× solar	=100× solar	=400× solar	=600× solar	=700× solar
H_2	0.785	0.744	0.483	0.292	0.191
He	0.141	0.134	0.0869	0.0526	0.0345
CH_4	0.0250	0.0252	0.0266	0.0276	0.0281
NH_3	1.28×10^{-4}	1.29×10^{-4}	1.36×10^{-4}	1.41×10^{-4}	1.44×10^{-4}
H_2O	0.0473	0.0954	0.402	0.626	0.744
H_2S	1.28×10^{-3}	1.29×10^{-3}	1.36×10^{-3}	1.41×10^{-3}	1.44×10^{-3}

composition to the deep atmosphere (P of order 10^5 bar). As described in Section 2.3.1, the atmospheric C, N and S abundances are constrained by previous studies. We assume that in the deep atmosphere the C/H and S/H enrichments are ~50 times the protosolar value, and that the CH_4 and H_2S abundances represent the total elemental abundances of C and S, respectively. For nitrogen, we assume that the NH_3/H ratio is equal to the protosolar N/H value, as constrained by cm wavelength observations, noting that the total atmospheric N/H enrichment can be higher if much of the nitrogen is in N_2. The O/H enrichment is the quantity we wish to determine from these calculations.

For large enrichments of H_2O, the approximation $O_{gas}/H \approx qH_2O/(2 \cdot qH_2)$, where qX is defined as the mole fraction of species X, does not hold, since a significant fraction of the hydrogen is contained in species other than H_2. Therefore to relate the solar oxygen enrichment to the various abundances we approximate

$$O_{gas}/H \approx \frac{qH_2O}{2 \cdot qH_2 + 2 \cdot qH_2O + 3 \cdot qNH_3 + 4 \cdot qCH_4 + 2 \cdot qH_2S} \tag{2.13}$$

Similar equations relate the C/H, S/H and NH_3/H enrichments to the mole fractions of CH_4, H_2S and NH_3. Table 2.8 presents the deep atmospheric mole fractions for relevant species, for several different values of the oxygen enrichment. In relating the global composition of Neptune to protosolar abundances, we have assumed that the atmospheric abundances of C, N, O and S represent Neptune's global C, N, O and S enrichments. In particular, we ignore the removal of oxygen from the atmosphere by the formation of rock: for protosolar composition gas, of order 20% of the oxygen is trapped in rock (Lodders 2004; Visscher & Moses 2011). This means that Eq. 2.13 is an underestimate of Neptune's total global O/H ratio. The protosolar abundances are taken from Asplund et al. (2009). We note that the values for the protosolar abundances have been revised significantly over the past two decades; for example, the protosolar O/H ratio has been adjusted downwards by more than 10% from the Grevesse & Noels (1993) values used by Lodders & Fegley (1994).

The model used for calculating the thermal profile down to high pressures is described in de Pater et al. (1991a) and references within; starting with the deep composition (Table 2.8) at an initial temperature and pressure, the model calculates the temperature at successive steps upwards in altitude by assuming the temperature follows either (1) a dry adiabat (regardless of the relative humidity of the atmospheric constituents); or (2) the appropriate wet adiabat (Fig. 2.22). We expect the wet adiabat case to be more appropriate. Clouds condense when the partial pressure of a given species exceeds its saturation vapor pressure, and the atmospheric composition changes accordingly. No clouds form at temperatures above the critical temperature of water (647 K). To calculate the adiabatic TP profile, we use an ideal gas equation of state and "intermediate" hydrogen, i.e. the specific heat is near that of normal hydrogen, and the *ortho* to *para* ratio is close to the equilibrium value (Wallace 1980). As in Section 2.3.3, we adjust the starting temperature at the deepest layer so that the thermal profile roughly matches the Lindal (1992) value of 71.5 K at 1 bar.

Utilizing the Visscher & Moses (2011) rate-limiting reaction, the chemical lifetime of CO is given by

$$\tau_{chem} = \frac{[\mathrm{CO}]}{d[\mathrm{CO}]/dt} = \frac{[\mathrm{CO}]}{k_{2.11e}[\mathrm{CH_3OH}][\mathrm{M}]} \tag{2.14}$$

where [X] is the number density of species X and $k_{2.11e}$ is the reaction rate of step (2.11e). Given the rate of the reverse reaction $k_{2.11eR}$ we can write τ_{chem} as

$$\tau_{chem} = \frac{[\mathrm{CO}]}{[\mathrm{CH_3}][\mathrm{OH}][\mathrm{M}]k_{2.11eR}} \tag{2.15}$$

$$= \frac{nK_{eq}}{P_{\mathrm{T}}[\mathrm{H_2}]^2[M]k_{2.11eR}} \tag{2.16}$$

$$= \frac{K_{eq}}{n^2 P_{\mathrm{T}} q\mathrm{H}_2^2 k_{2.11eR}} \tag{2.17}$$

where P_{T} is the total pressure in bars, n is the total number density in cm^{-3}, and K_{eq} is the equilibrium constant of $\mathrm{OH} + \mathrm{CH_3} \leftrightarrow \mathrm{CO} + 2\mathrm{H_2}$:

$$K_{eq} = e^{-\frac{\Delta_f G^0(\mathrm{CO}) - \Delta_f G^0(\mathrm{CH_3}) - \Delta_f G^0(\mathrm{OH})}{RT}} \tag{2.18}$$

The Gibbs free energies of formation as a function of temperature are taken from the NIST-JANAF tables (Chase 1998). The reverse reaction rate $k_{2.11eR}$ is calculated as described in Visscher & Moses (2011) using the expression

$$k = \frac{k_0}{1 + (k_0[\mathrm{M}]/k_\infty)} F_c^\beta \tag{2.19}$$

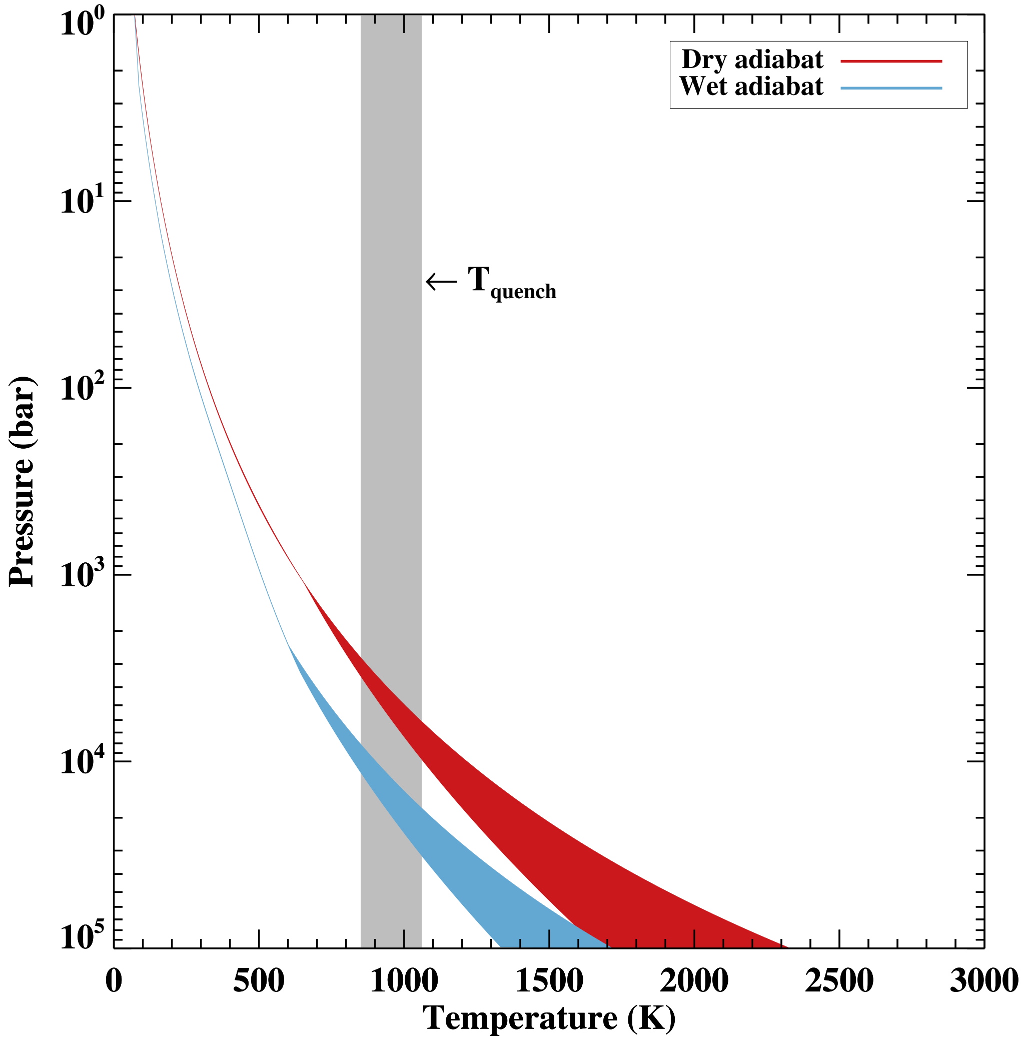

Figure 2.22: Thermal profiles for the deep atmosphere, assuming an adiabatic extrapolation. The value at 1 bar is matched to the Voyager 2 measurement. The red profile assumes a dry adiabatic lapse rate throughout the atmosphere; the blue profile assumes the appropriate wet lapse rate at expected cloud condensation levels. The range in the profiles indicates variation in composition, from 50 to 600 times the solar O/H ratio. The range of CO quench temperatures (T_{quench}) for $K = 10^7 - 10^9$ cm^2 s^{-1} is indicated by the vertical grey bar.

where

$$\beta = \left(1 + \left[\frac{\log_{10}(k_0[\mathrm{M}]/k_\infty)}{0.75 - 1.27\log_{10} F_c}\right]^2\right)^{-1} \tag{2.20}$$

and the parameters for calculating $k_{2.11eR}$ are given by Jasper et al. (2007):

$$k_0 = 1.932 \times 10^3 T^{-9.88} e^{-7544/T} + 5.109 \times 10^{-11} T^{-6.25} e^{-1433/T} \quad \mathrm{cm}^6\ \mathrm{s}^{-1} \tag{2.21}$$

$$k_\infty = 1.031 \times 10^{-10} T^{-0.018} e^{16.74/T} \quad \mathrm{cm}^3\ \mathrm{s}^{-1} \tag{2.22}$$

$$F_c = 0.1855 e^{-T/155.8} + 0.8145 e^{-T/1675} + e^{-4531/T} \tag{2.23}$$

We calculate the atmospheric mixing timescale τ_{mix} according to Eq. (2.12) using the Smith (1998) recipe for determining the effective mixing length L. In general, we find that $L \approx 0.12 - 0.18H$, which is consistent with the Smith (1998) findings. The eddy mixing coefficient in the deep atmosphere is constrained by the observed heat flux $\phi = 433 \pm 46$ erg cm^{-2} s^{-1} (Pearl & Conrath 1991). Using the scaling relationship for free dry convection (Stone 1976)

$$K \sim \left(\frac{\phi R}{C_P \rho}\right)^{1/3} H \tag{2.24}$$

we estimate that K is of order 2×10^8 cm^2 s^{-1}. In Eq. (2.24), ρ is the gas density, R is the gas constant and C_P is the specific heat at constant pressure. Following Lodders & Fegley (1994) we assume a plausible range for K of $10^7 - 10^9$ cm^2 s^{-1}.

Using Eqs. (2.7) and (2.8), we now solve for the CO quench level and the predicted CO mole fraction, as a function of the eddy diffusion coefficient and the assumed value of the O/H ratio. We find that, for $K = 10^7 - 10^9$ cm^2 s^{-1}, Eq. (2.7) becomes true at a temperature $T_{quench} = 850 - 1100$ K; coincidentally this is quite similar to the Lodders & Fegley (1994) value of $T_{quench} = 998$ K. The quench temperature, which is indicated in Fig. 2.22, is insensitive to the thermal profile (dry or wet lapse rate) used. Since the quench level is below the condensation level of the deepest cloud, the abundances of H_2, CH_4, and H_2O are the same for the dry and wet adiabat cases; however the pressure at which the quench temperature is reached changes (Fig. 2.22), which affects the CO mole fraction at the quench level (Eq. 2.8). The quench level (and therefore, the predicted observable) CO mole fractions are plotted in Fig. 2.23 for the dry and wet adiabat cases; for reference, we have indicated CO abundances of 0.03, 0.1 and 0.3 ppm with horizontal lines. We find that, for the dry adiabat case, 0.1 ppm of upwelled CO and $K \leq 10^9$ cm^2 s^{-1} implies a global oxygen enrichment of at least 400 times solar; this is roughly 8 times the C/H enrichment implied by Neptune's observed CH_4 abundance. For a wet adiabat, 0.1 ppm of upwelled CO and $K \leq 10^9$ cm^2 s^{-1} implies a global oxygen enrichment of at least 650 times solar.

We might expect the planets to be uniformly enriched in heavy elements (Owen et al. 1999); if this is so, then for fast mixing (K$\sim 10^9$ cm^2 s^{-1}) we would expect an upwelled CO

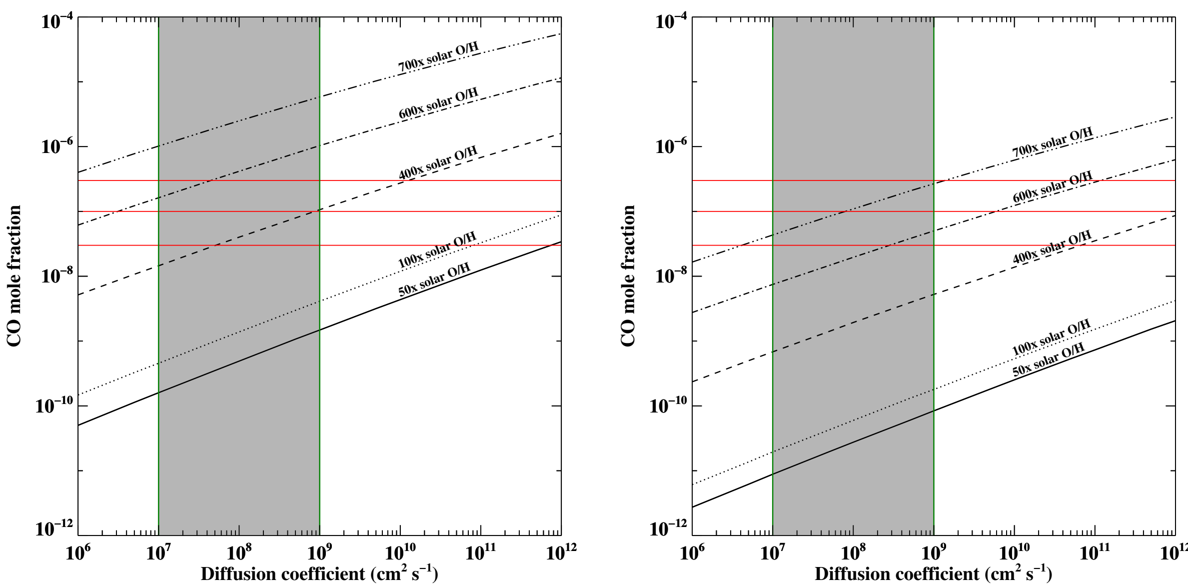

Figure 2.23: Predicted CO mole fraction in the visible atmosphere of Neptune due to upwelling from the deep atmosphere as a function of the eddy mixing coefficient K and the O/H enrichment over solar, using a dry adiabatic extrapolation (left) and a wet adiabatic extrapolation (right) for the thermal profile. Horizontal lines indicating 0.3, 0.1 and 0.03 ppm of CO are shown (red); the shaded region indicates the plausible range of K values. O/H enrichments of 50, 100, 400 and 600 times solar are shown.

abundance of 1.5×10^{-9} or 8.4×10^{-11}, for the dry and wet adiabat cases, respectively. We note that such low internal CO mole fractions are consistent with our data.

2.7.3 Implications: external CO

In addition to the abundance of CO that is vertically transported from Neptune's deep atmosphere, a significant external source ($\phi_{\rm CO} = 0.5 - 20 \times 10^8$ molecules cm^{-2} s^{-1}) is implied by our analysis (see Table 2.5). These inferred CO production rates are in general agreement with the 10^8 molecules cm^{-2} s^{-1} found by Lellouch et al. (2005) and lower than the 10^{10} molecules cm^{-2} s^{-1} estimated by Hesman et al. (2007). The precise value of $\phi_{\rm CO}$ depends strongly on the eddy diffusion and thermal profiles used in the model.

The high rates of $\phi_{\rm CO}$ inferred by the stratospheric CO mole ratio, and the high CO/H_2O ratio on Neptune have led to the suggestion that comet impacts are the primary supply mechanism of CO to Neptune's upper stratosphere (Lellouch et al. 2005; Hesman et al. 2007). We explore effectiveness of producing these abundances of CO through cometary impacts by calculating the approximate CO production from estimates of impact rates, similar to the analysis performed by Bézard et al. (2002) for Jupiter. We use for the impact rates of comets at Jupiter the estimate from Zahnle et al. (2003):

$$\dot{N}_J(D > 1.5 \text{ km}) = 0.005^{+0.006}_{-0.003} \quad \text{yr}^{-1} \tag{2.25}$$

as well as their approximation that the rate for Neptune is roughly

$$\dot{N}_N(D > 1.5 \text{ km}) \approx 0.25\dot{N}_J(D > 1.5 \text{ km}) \tag{2.26}$$

where D is the comet diameter. We test two possible comet size distributions: the first is the Shoemaker and Wolfe (1982) distribution:

$$\dot{N}_N(> D) = \dot{N}_N(D > 1.5 \text{ km}) \left(\frac{D(\text{km})}{1.5}\right)^{-2} \qquad \text{yr}^{-1} \tag{2.27}$$

Secondly, we test the Zahnle et al. (2003) "Case B" impact distribution, which was determined from the size distribution of craters on Triton:

$$\dot{N}_N(> D) = 2.62\ \dot{N}_N(D > 1.5\text{km}) \left(\frac{D(\text{km})}{1.5}\right)^{-1.7} \qquad \text{yr}^{-1} \qquad (D < 1.5 \text{ km}) \tag{2.28a}$$

$$\dot{N}_N(> D) = 0.129\ \dot{N}_N(D > 1.5\text{km}) \left(\frac{D(\text{km})}{5}\right)^{-2.5} \qquad \text{yr}^{-1} \qquad (D > 1.5 \text{ km}) \tag{2.28b}$$

Using these comet distributions, we calculate the mass rate of CO due to comet impacts as

$$\dot{M} = f_{\text{O}} f_{\text{CO}} \int_{R_{min}}^{R_{max}} 4\pi R^2 \rho \dot{N}(> R)\ dR \quad \text{g yr}^{-1} \tag{2.29}$$

where R is the comet radius, f_{O} is the fraction of the comet mass in the form of oxygen and f_{CO} is the fraction of the oxygen that ends up as CO. Following Bézard et al. (2002) we adopt values of $f_{\text{O}} = 0.5$ and $f_{\text{CO}} = 0.9$, and a typical comet nucleus density $\rho = 0.55$ g cm^{-3}.

To calculate the size range of comets to use, we follow Bézard et al. (2002) in choosing a minimum radius of $\text{R}_{min} = 0.15$ km, and calculate the maximum radius R_{max} as the maximum size for a comet for which the impact timescale is equal to the diffusion timescale:

$$\frac{1}{\dot{N}(> D_{max})} \sim \tau_K \tag{2.30}$$

The diffusion timescale can be approximated as

$$\tau_K \approx \frac{2H_0^2}{K_0} \tag{2.31}$$

where H_0 and K_0 are the scale height and diffusion rate at the tropopause, where mixing is slowest. We consider three values of K_0: 200, 800 and 2000 cm^2 s^{-1}. The slowest mixing rate of 200 cm^2 s^{-1} corresponds to the minimum eddy diffusion rate in the Romani 'A' profile and our 'test' eddy profile; the Romani 'B' and Moses '2' profiles have K$_0$ values near 2000 cm^2 s^{-1} , and the Moses '1' profile has an intermediate K$_0$ $\sim$ 800 cm^2 s^{-1}. The CO production rate ϕ_{CO} is determined from the CO mass influx rate $\dot{M}$ for the range of $\dot{N}_N(D > 1.5$ km) and for the two different comet size distributions described above. These calculated CO production rates are shown in Table 2.9.

Using a CO flux to the upper atmosphere of $0.5 - 20 \times 10^8$ cm^{-2} s^{-1}, as inferred by our physical fits, we calculate the diameter D_1 of a single large comet impact required to reproduce the observed CO abundance, given τ_K and for each value of K_0. We also report the timescales for impacts of size D_1 – which can be compared to the timescale estimates reported by Lellouch et al. (2005) and Hesman et al. (2007). We note that, without detailed knowledge of the vertical eddy diffusion profile, the two-level CO profiles reported by Lellouch et al. (2005) and Hesman et al. (2007) do not preclude a constant CO influx by (sub)kilometer-sized comets (rather than the single event discussed by these authors.) Eddy diffusion profiles like the Romani 'B' and Moses '2' profiles will produce CO profiles that, when mimicked by a two-level profile, will have transition pressures in the 10 mbar range (Section 2.6.4). Since very large impacts are rare, a constant infall rate of smaller comets may be a preferable explanation. We find that, of our two comet size distributions, the Zahnle et al. (2003) Case B distribution gives more optimistic predictions for CO production: the rates of CO injection found for the small and intermediate K$_0$ values are $0.44^{+0.90}_{-0.33} \times 10^8$ cm^{-2} s^{-1} and $0.20^{+0.55}_{-0.17} \times 10^8$ cm^{-2} s^{-1} , respectively, suggesting that cometary impacts are in fact a feasible mechanism for supplying the observed abundance of CO to Neptune's upper atmosphere. However, Zahnle et al. (2003) suggest that their impact rate for 1.5 km comets at Neptune is likely an overestimate, meaning the true CO production rate due to comets could be smaller.

Table 2.9: Production rate of CO from comets.

			Shoemaker and Wolfe			Zahnle et al. Case B		
K_0 (cm^2 s^{-1})	τ_K (yr)[a]	D_1 (km) [b]	D_{max} (km)	$\log\phi$[c] (cm^{-2} s^{-1})	τ_{D_1} (yr)[d]	D_{max} (km)	$\log\phi^c$(cm^{-2} s^{-1})	τ_{D_1} (yr)
200	930	$3.4 - 12$	$1.6^{+0.8}_{-0.6}$	$7.1^{+0.5}_{-0.7}$	$1900 - 120000$	$2.3^{+0.9}_{-0.7}$	$7.7^{+0.5}_{-0.6}$	$1100 - 130000$
800	230	$2.2 - 7.4$	$0.8^{+0.4}_{-0.3}$	$6.7^{+0.6}_{-0.8}$	$750 - 49000$	$1.3^{+0.6}_{-0.5}$	$7.3^{+0.6}_{-0.8}$	$350 - 41000$
2000	93	$1.6 - 5.4$	$0.5^{+0.2}_{-0.2}$	$6.3^{+0.7}_{-1.4}$	$410 - 26000$	$0.7^{+0.4}_{-0.3}$	$6.9^{+0.7}_{-1.0}$	$160 - 19000$

[a] diffusion time scale

[b] diameter of single comet impact required to produce $\phi_{CO} = 0.5 - 20 \times 10^8$ cm^{-2} s^{-1}

[c] total CO flux expected based on impact rates

[d] $1/\dot{N}_N(> D_1)$

2.7.4 Summary/conclusions

We have observed Neptune in the CO (2–1) and (1–0) rotational lines with the Combined Array for Research in Millimeter-wave Astronomy. Our radiative transfer analysis indicates a preference for the Fletcher et al. (2010) thermal profile in Neptune's upper atmosphere over warmer and cooler profiles, and we find that the best-fit solution for the CO vertical profile is strongly dependent on the atmospheric TP profile. Adopting the Fletcher et al. (2010) thermal profile, we find that good fits to the data (both to the individual lines and to the combined dataset) are characterized by CO mole fractions of $0.1^{+0.2}_{-0.1}$ parts per million (ppm) in the troposphere, and $1.1^{+0.2}_{-0.3}$ ppm in the stratosphere. Higher CO mole fractions, particularly in the stratosphere, are favored when cooler thermal profiles are used. If the CO mole fraction resulting from vertical mixing is greater than 0.1 ppm, our calculations imply an O/H abundance that is at least 400 times the protosolar value. However, since we do not rule out a 0.0 ppm tropospheric CO mole fraction, we cannot place a lower limit on Neptune's global O/H ratio, and our data do not require that Neptune's oxygen enrichment exceeds its carbon enrichment. We find that the stratospheric deposition rate of CO is $0.5 - 20 \times 10^8$ CO molecules cm^{-2} s^{-1}; such a high abundance could be supplied by impacts from (sub)kilometer-sized comets, as long as the eddy diffusion rate near the tropopause is small.

This work will be followed up with spatially-resolved mapping of Neptune in the CO (2–1) line with CARMA, to look for latitudinal variations in the CO abundance. ALMA will play a key role in the three dimensional mapping of trace species on Neptune, as well as on the other Solar System giant planets. Such studies will provide further insight into the composition, atmospheric circulation, and environments of the giant planets.

Acknowledgements

The data presented in this work were obtained with CARMA. Support for CARMA construction was derived from the states of California, Illinois, and Maryland, the James S. McDonnell Foundation, the Gordon and Betty Moore Foundation, the Kenneth T. and Eileen L. Norris Foundation, the University of Chicago, the Associates of the California Institute of Technology, and the National Science Foundation. Ongoing CARMA development and operations are supported by the National Science Foundation under a cooperative agreement, and by the CARMA partner universities. This work was supported by NASA Headquarters under the NASA Earth and Space Science Fellowship program - Grant NNX10AT17H; and by NSF Grant AST-0908575. The authors would like to thank L. Fletcher for providing his temperature and CH_4 profiles, and G. Orton for providing his H_2 CIA absorption coefficients. The authors would also like to acknowledge R.L. Plambeck, M. Wright and A. Bauermeister for many helpful discussions.

Chapter 3

Spatially-Resolved Millimeter-Wavelength Maps of Neptune

We present maps of Neptune in and near the CO (2–1) line from the Combined Array for Research in Millimeter-wave Astronomy (CARMA). We find latitudinal intensity variations at the 2–3% level in the CO line; these variations are consistent with the variations in zonal-mean temperature near the tropopause found by Conrath et al. (1998) and Orton et al. (2007a). At continuum wavelengths, we observe a gradient in the brightness temperature, increasing by 2–3 K from 40°N to the south pole. This corresponds to an opacity decrease of about 0.3 (30%) near the south pole between 1 and 5 bar. If the opacity change is restricted to pressures greater than 4 bar, a factor of 100 decrease in the opacity is implied.

3.1 Introduction

Composed predominantly of volatiles referred to as 'ices', Uranus and Neptune belong to a fundamentally different class of planets than the gas giants Jupiter and Saturn. Significant questions remain about the interior structure and composition, large-scale circulation and seasonal variability of the ice giants. Trace species such as carbon monoxide (CO) provide important probes of the global composition and atmospheric circulation on these planets.

The rotational lines of CO probe the CO abundance and temperature in the stratosphere and upper troposphere. Disk-integrated vertical CO profiles have been derived for Neptune using observations of the CO (1–0) (Chapter 2), (2–1) (Lellouch et al. 2005; Chapter 2) and (3–2) (Hesman et al. 2007) lines at high spectral resolution (1.25–4 MHz) over a wide (8–20 GHz) frequency range. All of these authors find that the CO abundance increases with altitude, which suggests a substantial external oxygen supply mechanism. Based on the atmospheric CO/H_2O ratio, Lellouch et al. (2005) proposed that a recent large cometary impact could be responsible for Neptune's observed stratospheric CO abundance; however, comets of the necessary size are expected to be exceedingly uncommon. In Chapter 2, we show that a constant influx of (sub)kilometer-sized comets could supply the observed abundance of CO. Lellouch et al. (2005) and Hesman et al. (2007) also find a substantial tropospheric CO abundance of 0.5 ± 0.1 and 0.6 ± 0.4 ppm respectively. Our analysis, described in Chapter 2, which favors a warmer thermal profile than Lellouch et al. (2005) and Hesman et al. (2007), produces a lower best-fit tropospheric CO abundance of $0.1^{+0.2}_{-0.1}$ ppm. Since CO is not thermochemically stable in the upper troposphere, it must be upwelled from warmer, deeper levels of the atmosphere (Prinn & Barshay 1977; Fegley & Prinn 1986), and the abundance of CO observed is directly tied to the internal H_2O abundance of the planet. We find that a tropospheric CO mole fraction of 0.1 ppm implies a global oxygen enrichment of at least 400, and likely more than 650 times the protosolar O/H value.

Information on the spatial distribution of CO could provide evidence of localized infall/production, as was observed after the impact of comet Shoemaker-Levy 9 (SL9) with Jupiter. Moreno et al. (2003) estimated that for SL9, latitudinal variations in the CO abundance would persist for roughly a decade. Furthermore, Neptune's CO abundance could act as a tracer of the large-scale circulation. Maps in the CO line are also affected by temperature variations near the tropopause.

Continuum emission from millimeter wavelengths is sensitive to absorption by other trace species, particularly H_2S, PH_3 and NH_3. Currently, the abundances of these species in Neptune's atmosphere have yet to be uniquely determined, though good fits to centimeter-wavelength disk-integrated spectra, which probe depths of several bars down to 10's of bars, are obtained using an H_2S abundance 30-50 times the solar S/H value (de Pater et al. 1991a; Deboer & Steffes 1996) and a solar abundance or less of NH_3 (Romani et al. 1989; de Pater et al. 1991a). Spatially-resolved maps of the emission at centimeter wavelengths have been obtained by several authors (de Pater et al. 1991a; Martin et al. 2006, 2008; Hofstadter et al. 2008). Martin et al. (2006), Martin et al. (2008) and Hofstadter et al. (2008) find a substantial (tens of K) increase in the 1.3–2 cm brightness temperature near the south pole. This observation is consistent with a global circulation pattern in which air rises at mid- southern and northern latitudes and subsides near the equator and south pole. Recently, Butler et al. (2012) presented maps at 1 cm obtained with the upgraded VLA, with a resolution of better than 0.1": they observe that Neptune's bright polar cap extends from the pole to 70°S. They also see evidence for equatorial brightening, which would be consistent with the circulation pattern outlined above.

We present the first spatially-resolved measurements of Neptune at 1.3 mm, originally reported by Luszcz-Cook et al. (2010b). We compare these maps to a uniform composition, uniform temperature model based on our nominal solution for the disk-integrated CO vertical profile from Chapter 2, for a 50 times solar abundance of H_2S. Our maps range from the center of the CO (2–1) line at 230.538 GHz, to an offset of 6 GHz from line center, where the continuum is probed. We look at latitudinal variations in our maps as a measure of potential spatial variations in the composition and temperature in the troposphere and stratosphere.

3.2 Observations and data reduction

We observed Neptune with the 6- and 10-meter antennas of the Combined Array for Research in Millimeter-wave Astronomy (CARMA). The 15-element array has 105 baselines and 2900 m^2 of total collecting area, and can be configured in 5 patterns. In order to spatially resolve Neptune's < 2.5" disk, we observed in the B configuration with baselines of 82-946 meters and a synthesized beam of approximately 0.35" at 230 GHz. A total of 14 tracks were taken in this configuration: one test track in December 2008, 9 tracks in the winter of 2009-2010, and four tracks in January 2011. Of these, two of the 2011 tracks were of poor quality and were not included in the analysis. The mean length of each remaining track was 4.3 hours, consisting of a 15-minute observation of the passband calibrator, followed by a series of observing cycles of 8 minutes on source and 2 minutes (prior to 2011) or 3 minutes (in 2011) on the phase calibrator. Optical pointing was performed every hour (every 1/2 hour in 2011); radio pointing was performed every 4 hours during the night and every 2 hours during the day. The weather conditions during the observations were generally fair, with root mean square (rms) path errors ranging from 100 to 325 μm on a 100-m baseline, and an average zenith optical depth of 0.18. The total time on source in

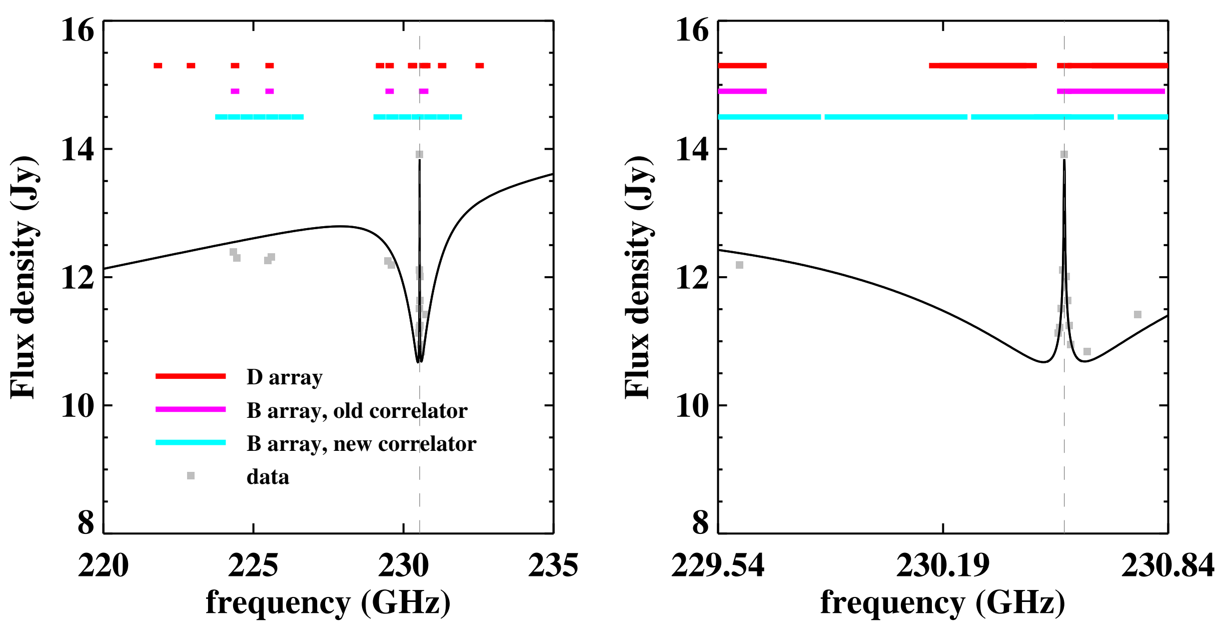

Figure 3.1: Spectral coverage of our observations. The short-baseline D-array data windows are shown in red. The long-baseline B-array data are shown in pink (prior to 2011) and cyan (2011). The model disk-integrated spectrum is shown in black and the integrated flux density from each of the CLEAN maps is shown as a grey square. The plot on the right is zoomed in on line center.

the B-array configuration was 28.2 hours.

For the majority of our observations, the CARMA correlator offered three dual bands with configurable bandwidth of either 500, 62, 31, 8 or 2 MHz. Each band could be placed independently anywhere within the 4-GHz IF bandwidth, and appears symmetrically in the upper and lower sidebands of the first local oscillator. We configured one of the bands to 62-MHz bandwidth at the center of the CO (2–1) line; the remaining two bands were configured to maximum bandwidth and placed at an offset from line center. Due to upgrades to the correlator in 2010, five additional dual bands were available during the two 2011 tracks. These additional bands were all configured to maximum bandwidth mode, allowing for more continuous coverage of the wide CO line. To provide information at shorter baselines, we combined our B-array data with 14.9 hours on source in the more compact D-array configuration from spring 2009; these data are described in Chapter 2. Figure 3.1 illustrates the location of the correlator bands prior to and after the correlator upgrade, as well as the frequency coverage of the D-array data.

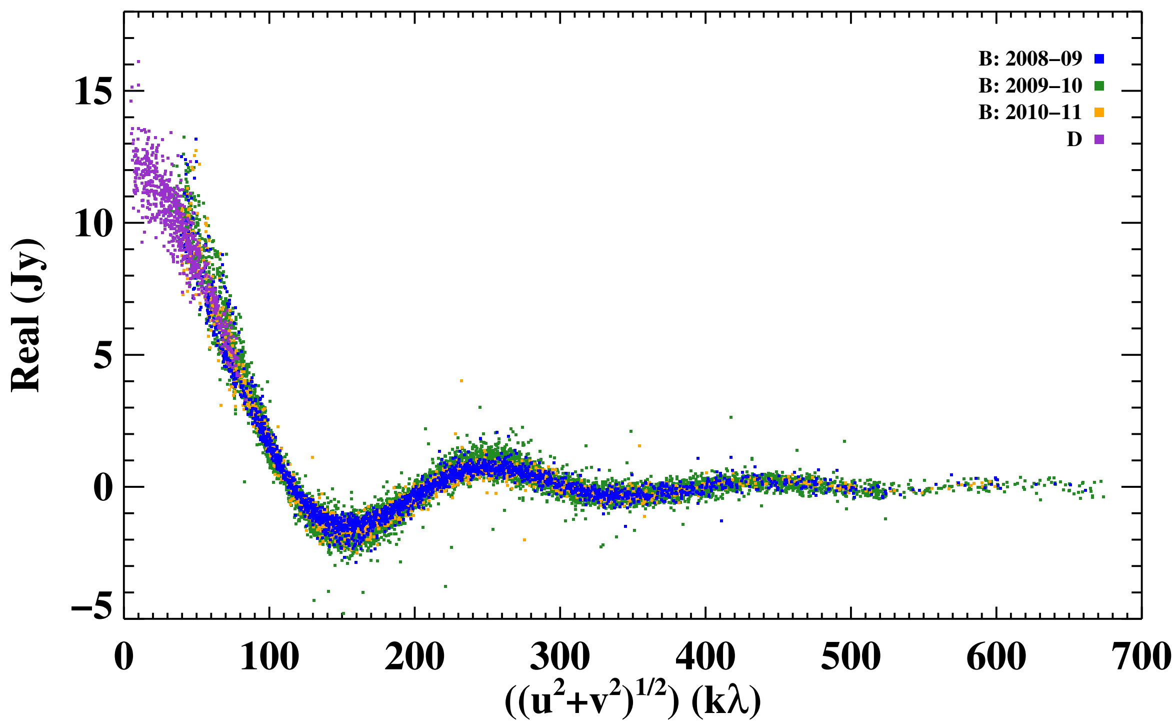

Figure 3.2: The real part of the visibilities, shown as a function of (u,v) distance, illustrating the (u,v) coverage of each of our data sets. Each data point is the average over a 15 minute integration. The purple points are the short baseline, D-array data. B-array data from each year of observations are shown in a different color.

The visibility data were calibrated using the MIRIAD software package (Sault et al. 2011). We flag 10 edge channels in the narrow band centered on the CO line and 3 edge channels in the wide bands; the narrow window in the opposite sideband from the CO line is flagged entirely. Poor quality data are also flagged. After performing passband calibration using our bright quasar observations, time-dependent gain solutions are derived using the wide-band data, and then applied to the full data set. We do an initial self calibration using the phase calibrator. This first calibration is performed in two steps: a record-by-record phase solution is found for the phase calibrator to remove short-term variations. Then, a phase and amplitude self calibration is performed using an interval corresponding to one observing cycle, and applied to the Neptune data. Finally, a record-by-record phase-only self calibration is performed on Neptune itself to remove short-term phase variations in the Neptune data. Absolute flux calibration is performed by scaling the visibilities to match the amplitudes of the D-array data at overlapping (u,v) distances, where the D-array data were flux calibrated to match the best-fit model found in Chapter 2. The real part of the amplitudes of the visibility data are plotted as a function of (u,v) distance in Fig. 3.2, where each point is the average over one observing cycle.

3.3 Model

A series of model image cubes were created using the line-by-line radiative transfer code described in Chapter 2, and using the atmospheric properties described therein. We adopt the thermal profile of Fletcher et al. (2010) in the upper atmosphere, and a 50 times solar H_2S abundance. We first model the CO (2–1) absorption assuming that the CO abundance is vertically distributed according to our best-fit solution for an atmosphere containing H_2S: 1.1 ppm of CO above 0.158 bar and 0.0 ppm of CO deeper than this level. At each of 155,575 locations on the disk (0.005" pixels), we integrate the equation of radiative transfer for the appropriate viewing angle μ (the cosine of the emission angle), accounting for the Doppler shift due to the planet's rotation (Moreno et al. 2001). These high-resolution models can be converted from brightness temperature units into Jy/pixel, to be used as starting models for the deconvolution process (Section 3.4). They can also be rebinned to the coarser map resolution and convolved with the `CLEAN` beam, and directly compared with the data (Section 3.5). For the latter purpose, alternative models are also produced by assuming the same vertical CO structure (the same transition pressure, and no tropospheric CO), but varying the stratospheric CO abundance, or alternatively by maintaining the nominal CO structure and abundance but varying the temperature and composition (other than CO) in the upper atmosphere. For simplicity, temperature variations were modeled by adding or subtracting a constant offset at all altitudes above 1 bar.

3.4 Imaging and deconvolution

Data imaging and deconvolution are performed using the CLEAN routine in the CASA software package. The resolution of the maps is selected to be lower than the original channel widths of the data (which increased with the upgrades to the correlator) in order to improve the signal-to-noise in the images: we produce 9 'narrow band' maps of width 4.6 MHz, centered at 230.538 GHz. Away from line center, we map in frequency intervals of 125 MHz. We choose to map only frequencies where both B- and D-array data are available, for a total of eight wideband maps spanning the frequencies covered by both the old and new correlator setups. The frequency coverage of these maps is indicated in Fig. 3.1.

We apply intermediate weighting with a Briggs visibility weighting robustness parameter (Briggs 1995) of 0.0. The beam is 0.33-0.37" x 0.38-0.39" and the pixel size used in the maps is 0.09". Deconvolution is performed using the Clark CLEAN method with a gain factor of 0.05. A starting CLEAN model is provided based on the radiative transfer solution for the nominal CO profile described in Chapter 2. A maximum of 100,000 iterations are permitted, unless a CLEAN threshold equal to the theoretical root-mean-square (rms) noise of the map (0.9 mJy in the wideband maps, 4 mJy for the narrowband maps) is reached. In general, we find that the algorithm reaches 100,000 iterations before achieving the CLEAN threshold. We note that the resulting maps do not appear to be affected by the details of the starting CLEAN model. For a more complete comparison of the imaging and deconvolution strategies tried, see the Appendix to this Chapter.

After the initial mapping procedure, we average maps where possible: the contribution function (Fig. 3.3) shows that at an offset of 5 GHz from line center, the maps are almost entirely due to continuum emission from pressures of 1-5 bar. We therefore average the four wideband maps at offsets of 5-6 GHz from line center to produce a single continuum image (Fig. 3.4). We also combine the wideband maps at 229.48 and 229.60 GHz (1.04 and 0.96 GHz from line center, respectively), leaving us with three wideband images at offsets of 66 MHz, 213 MHz and 1.0 GHz from line center (Fig. 3.5).

For the narrowband maps, we elect to average pairs of maps with the same absolute frequency offset from line center. Prior to averaging, we compare each pair of maps to look at latitudinal and longitudinal variations. We used the ephemeris data from JPL Horizons[1] to get the value of the latitude and longitude at each pixel location in the image if it were not convolved with the synthesized beam. To determine the variation of the intensity in the maps, which are convolved with the beam, with physical location on the planet, we select 7 non-overlapping latitude bins. For each latitude bin, we make a model mask: a pixel in the mask is set to 1 if the latitude at that pixel location is within the latitude bin range; otherwise it is set to 0. We convolve the mask with the synthesized beam, and multiply this mask by the data. The total of this masked image divided by the number of pixels in the mask gives a weighted average of the data over the desired latitude range. We repeat this process for bins of longitude. For direct comparison with the models, we

[1] http://ssd.jpl.nasa.gov/?horizons

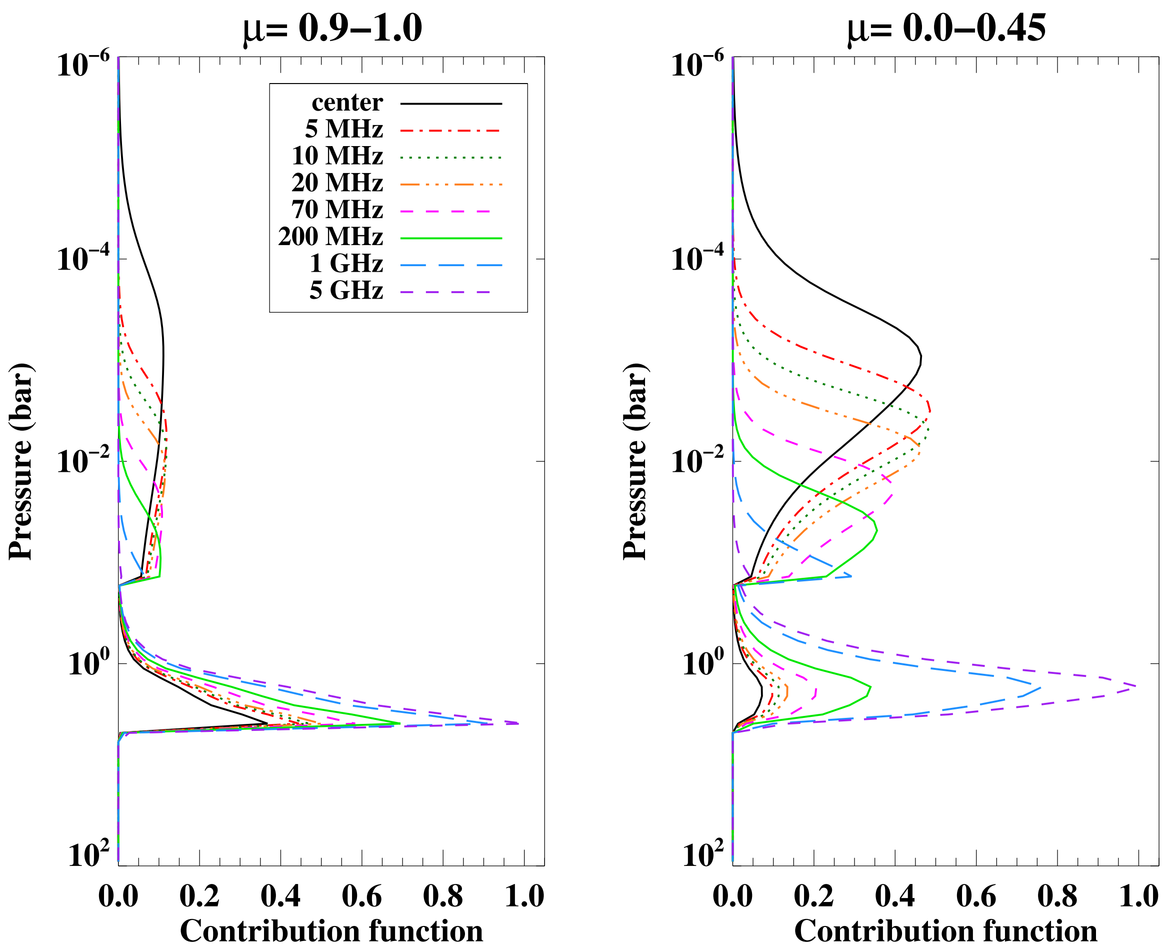

Figure 3.3: Contribution functions, shown for disk center (left) and near the limb (right), for a selection of offsets from line center. In each case the mode was produced assuming a CO profile with 1.1 ppm CO in the stratosphere and no CO in the troposphere. The cutoff of the CO is responsible for the sharp decrease in the contribution functions near 0.1 bar.

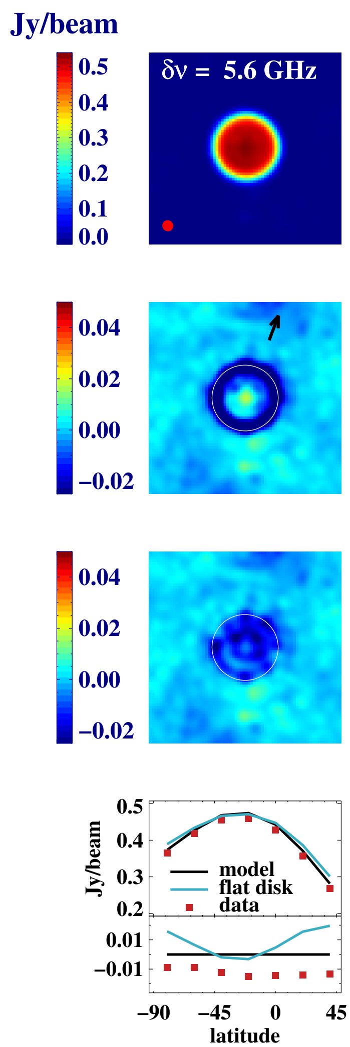

Figure 3.4: Average of the four maps with a frequency offset from line center of 5-6 GHz. Top image is the `CLEAN` map. The average beam is indicated by the filled red circle in the bottom left corner of the image. Second image from the top is the `CLEAN` map with a (beam-convolved) uniform-brightness disk subtracted. The white circle indicates the location of the planet's limb, and the black arrow indicates the direction of the rotation axis. The third image from the top has the beam-convolved uniform composition, uniform temperature model subtracted. In the plot (bottom) we zonally average the image (red points) and nominal model (black) as described in Section 3.3. For reference, we also show the average of the beam-convolved uniform brightness disk as a function of latitude. The differences between the data and the nominal model are shown in the bottom part of the plot.

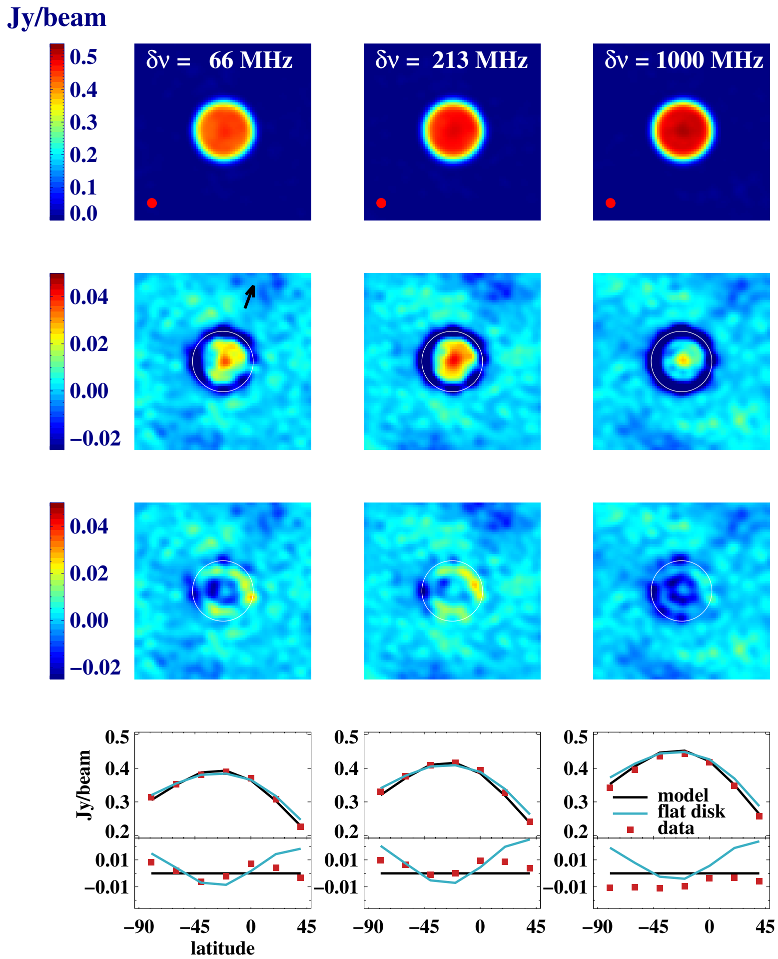

Figure 3.5: Same as Fig. 3.4, except for the wideband images within the CO absorption.

convolve the models with the `CLEAN` beam and multiply by the same masks. The differences between our nominal model and the data are shown for two pairs of narrowband images in Fig. 3.6. We find variations of order 2% in the narrowband maps as a function of both latitude and longitude. However, variations in latitude show systematic agreement between the two images in each positive and negative frequency offset pair, which is not seen in the longitudinal variations. We expect longitudinal brightness variations to be averaged out in the long data integrations, so the consistency of the deviations in latitude but not longitude gives us confidence that these are real variations. The significance of these fluctuations is discussed in Section 3.5.

We use this same approach to look at latitude variations in our averaged maps as well; these are shown in the bottom panels of Figs. 3.4, 3.5, and 3.7 .

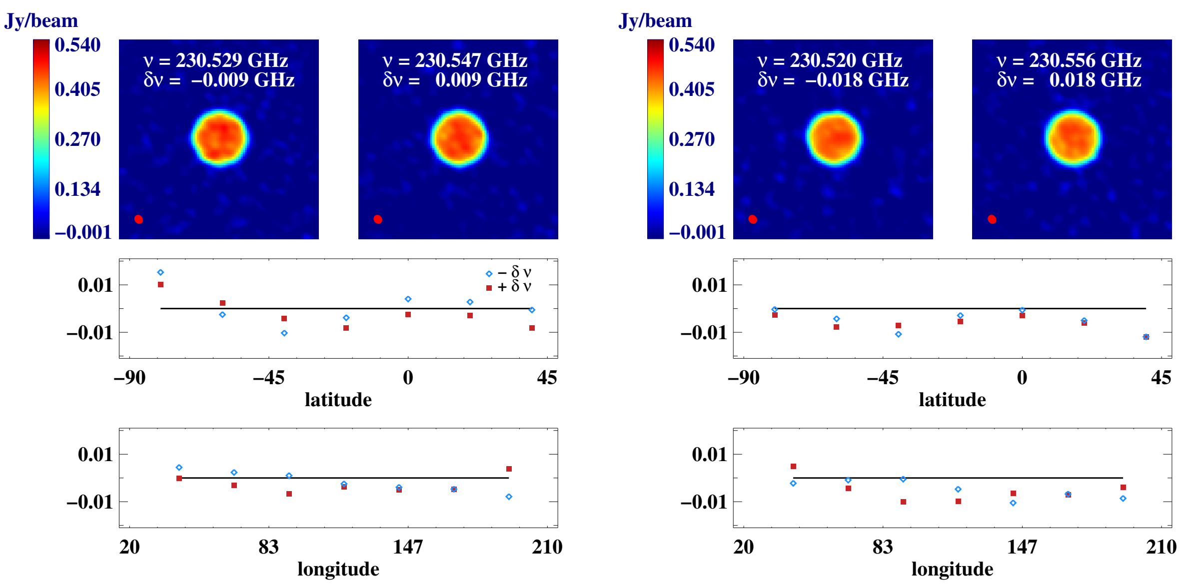

Figure 3.6: Two of our four pairs of narrowband images near the CO emission peak. Each pair of images has the same absolute frequency offset from line center. The latitude- and longitude-binned data are presented in the plots below, shown as offsets from the constant composition, constant temperature model (black line). The data from each pair of images show similar latitudinal behavior.

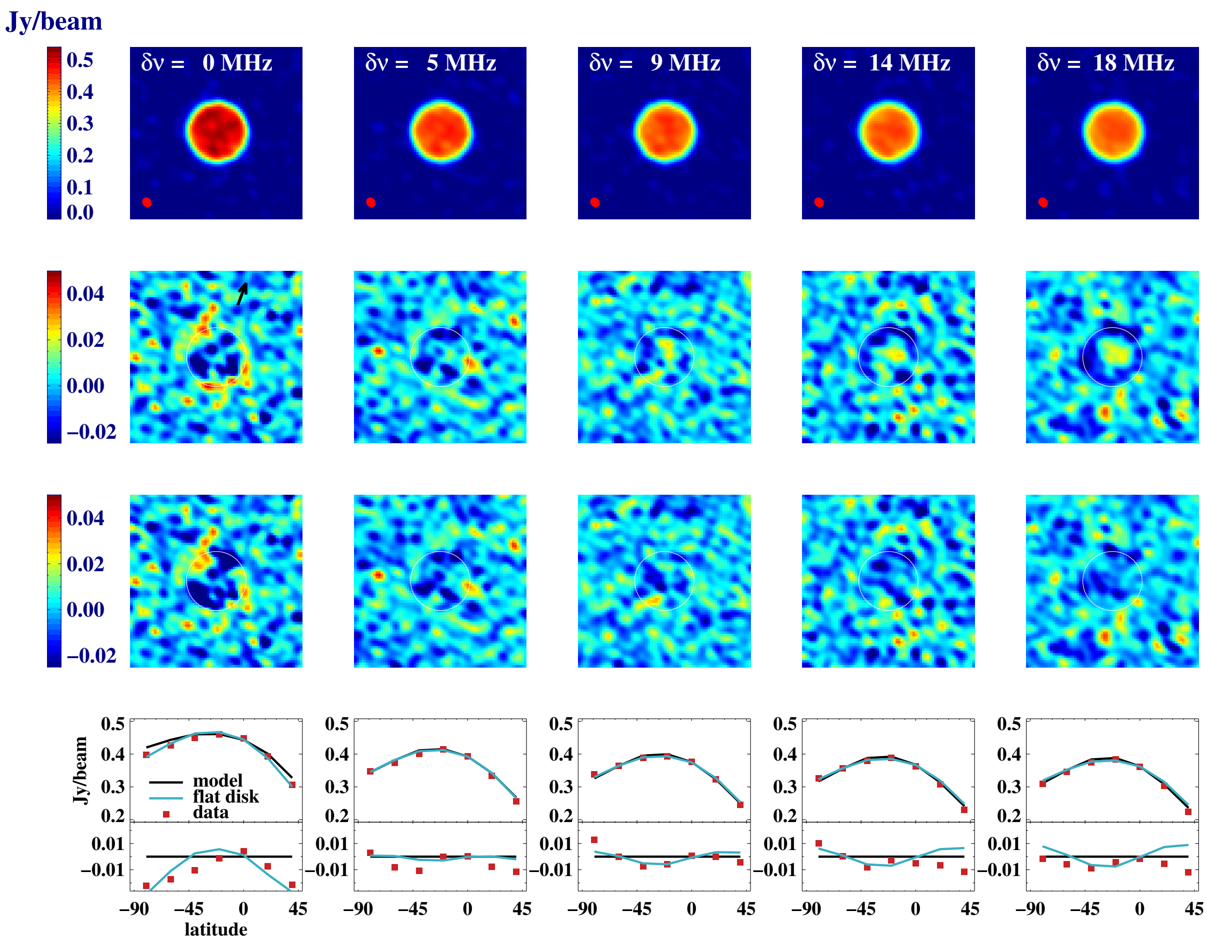

Figure 3.7: Same as Fig. 3.4, except for the narrow images within the CO absorption and emission.

3.5 Results

3.5.1 Continuum variations

Figure 3.4 shows that, in addition to an overall offset of about 3% between the data and the nominal (constant composition and constant temperature) model, there appears to be latitudinal variation in the intensity at the level of roughly 3%. This corresponds to an increase in brightness temperature of 2–3 K at high southern latitudes over the brightness temperature at 40°N. The 3% continuum offset could be due to issues in calibration as well as real deficiencies in our model of the continuum – this is discussed more thoroughly in Chapter 2. Here we concentrate on the observed gradient in the continuum brightness.

The contribution function at 5 GHz from the CO line center peaks at a depth of 4 bar, with most of the emission originating from depths of 1.1–4.7 bar. We expect that variations at these frequencies are likely due to opacity variations, rather than temperature variations, as the temperature profile is likely adiabatic. A decrease in opacity near the south pole would mean that warmer, deeper layers are probed. To estimate the change in optical depth that could produce the observed variations, we scale the total optical depth at the relevant pressures. We find that we require an opacity decrease of about 0.3 (30%) in the south at pressures greater than 1 bar to match the observed latitudinal gradient. If we vary the opacity only at pressures greater than 2 bar, we require the opacity to be lower by a factor of 2 in the south (e.g. from the nominal opacity at 40°N to 0.5 times nominal near the south pole). If we restrict the opacity variations to pressures greater than 3 bar, we require a factor of 7 change and if variations are only at pressures greater than 4 bar, the opacity must be more than 100 times lower in the south than at 40°N. Therefore, the total abundance change across the disk implied by our data depends on where the opacity changes, which is determined by which opacity source is responsible for these variations.

The dominant opacity sources in our model at these pressures are H_2S opacity and H_2 collision-induced absorption (CIA). For an H_2S abundance of 50 times solar, H_2S opacity begins to dominate at pressures greater than 3.3 bar. We find that if the H_2S opacity changes by a factor of $\sim$30 from the south pole to 40°N, we can reproduce the observed latitudinal behavior. Figure 3.8 shows the data residuals from a uniform model (scaled to match the brightness at 40°N), and the expected residuals for a case where the H_2S opacity has the nominal value from 10°N to 40°N, 0.3 times the nominal value from 40°S to 10°N, and 0.03 times the nominal value between 90°S and 40°S.

A decrease or increase in CH_4 can affect the brightness temperature, even though methane on its own does not contribute directly to the opacity (de Pater & Mitchell 1993). CH_4 condensation can change the adiabatic profile; however, we adopt a dry adiabat in the upper atmosphere (Chapter 2), so CH_4 does not affect our models in this way. Although the CH_4 mole fraction in the troposphere is only 2.2% (Baines et al. 1995), the absorption coefficient for H_2-CH_4 pairs is roughly 20 times higher than for H_2-H_2 pairs under the relevant conditions. As a result, H_2-CH_4 CIA accounts for as much as 35% of the total optical depth in the 1–4 bar region. As for H_2S, we determine the magnitude of CH_4

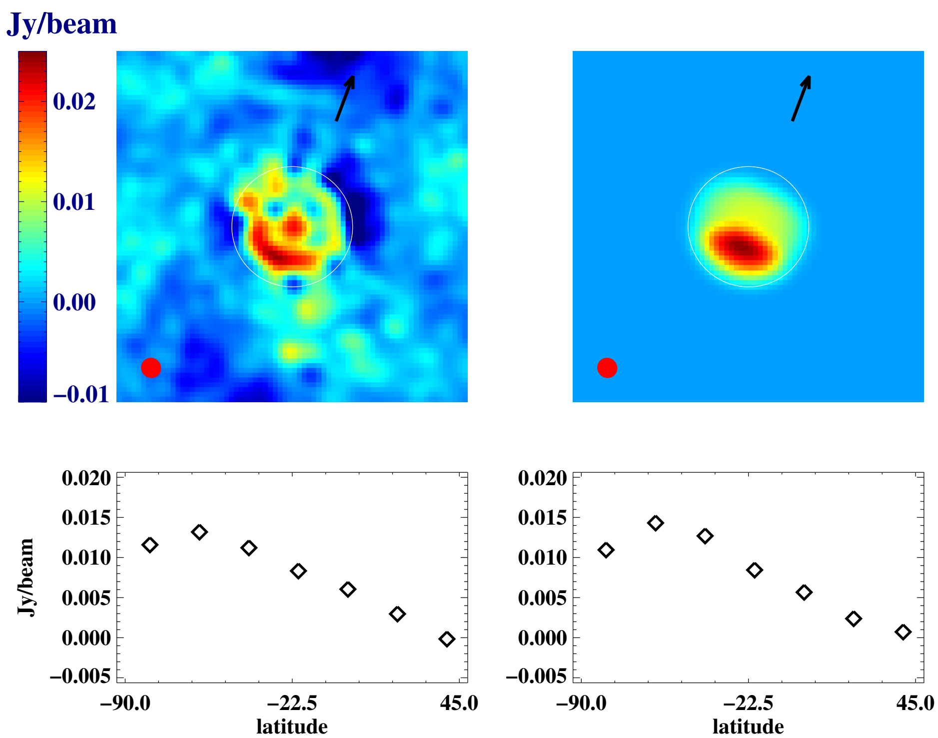

Figure 3.8: Left: continuum map (5.6 GHz offset from CO line), with a uniform composition, uniform TP model subtracted. Data have been scaled up so that offsets are positive. Right: model where the H_2S opacity has the nominal value from 10°N to 40°N, 0.3 times the nominal value from 40°S to 10°N, and 0.03 times the nominal value between 90°S and 40°S. Again, the uniform composition, uniform TP model has been subtracted. Below each image is a plot of the zonally-averaged residuals.

abundance variations that are required to reproduce the observed intensity gradient: we find that the south polar region must be depleted in tropospheric CH_4 by a factor of order 10 relative to 40°N. Figure 3.9 shows the expected residuals for a case where the tropospheric CH_4 mole fraction is 0.044 (twice the nominal value of 0.022) from 10°N to 40°N, 0.022 from 40°S to 10°N, and 0.0055 (25% of nominal) between 90°S and 40°S. The disk-averaged CH_4 mole fraction for this example is 0.021, which is close to the expected nominal value. As in Fig. 3.8, a scale factor has been applied to the model in Fig. 3.9 so that the data residuals match the deviations between the nominal model and the variable CH_4 model.

Finally, we consider variations in the H_2 *ortho*/*para* ratio as a source of continuum intensity variations. As in Chapter 2 we assume 'intermediate' hydrogen as the nominal case. That is, the *ortho* and *para* states of hydrogen are in equilibrium at the local temperature,

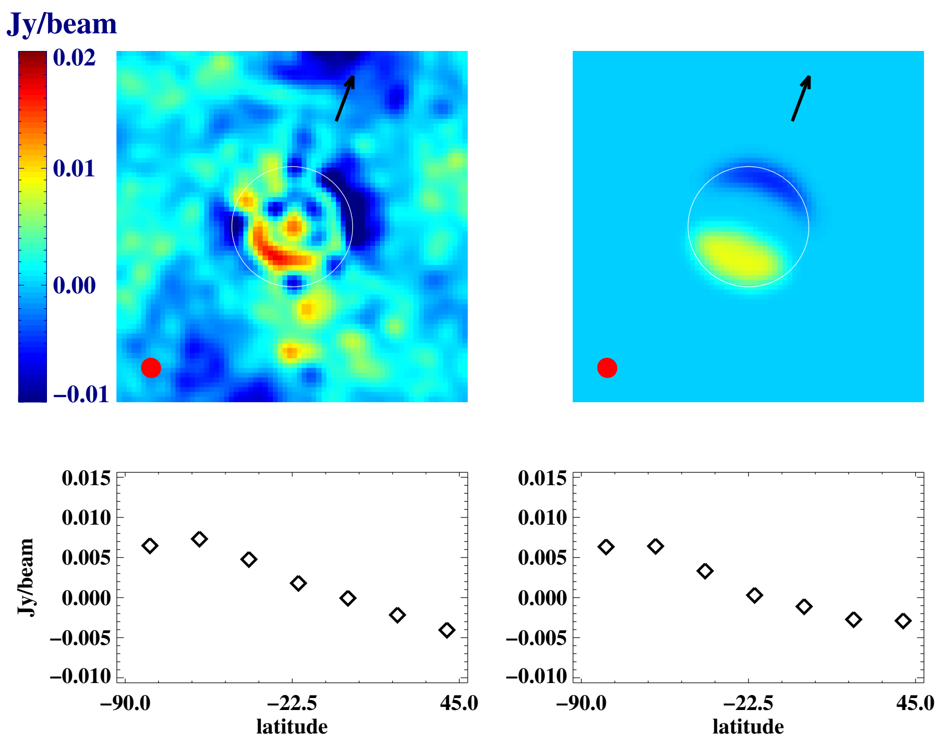

Figure 3.9: Left: continuum map (5.6 GHz offset from CO line), with a uniform composition, uniform TP model subtracted. Data have been scaled up as described in the text . Right: model where the tropospheric CH_4 mole fraction is 0.044 (twice the nominal value of 0.022) from 10°N to 40°N, .022 from 40°S to 10°N, and 0.0055 (25% of nominal) between 90°S and 40°S. The uniform composition, uniform TP model has been subtracted from both maps. Below each image is a plot of the zonally-averaged residuals.

but the specific heat is near that of 'normal' hydrogen. This situation is described in Massie & Hunten (1982). Fast vertical mixing from the deep interior, however, could bring the *ortho*/*para* ratio closer to the 3:1 ratio expected for normal hydrogen. We investigate the effect of variations in the fraction of *para*-H_2 on the opacity, while assuming the adiabatic profile for normal hydrogen everywhere. We find that normal hydrogen has a higher opacity than 'equilibrium' hydrogen. The average intensity is 5—-6 K lower when we assume normal hydrogen rather than equilibrium hydrogen. This implies that variations in the *ortho*/*para* ratio are more than capable of causing intensity variations of the magnitude observed in our data. We can match the observed latitudinal variations by decreasing the fraction of hydrogen in the equilibrium state from 1.0 at the south pole to 0.6 at 40°N (Fig. 3.10).

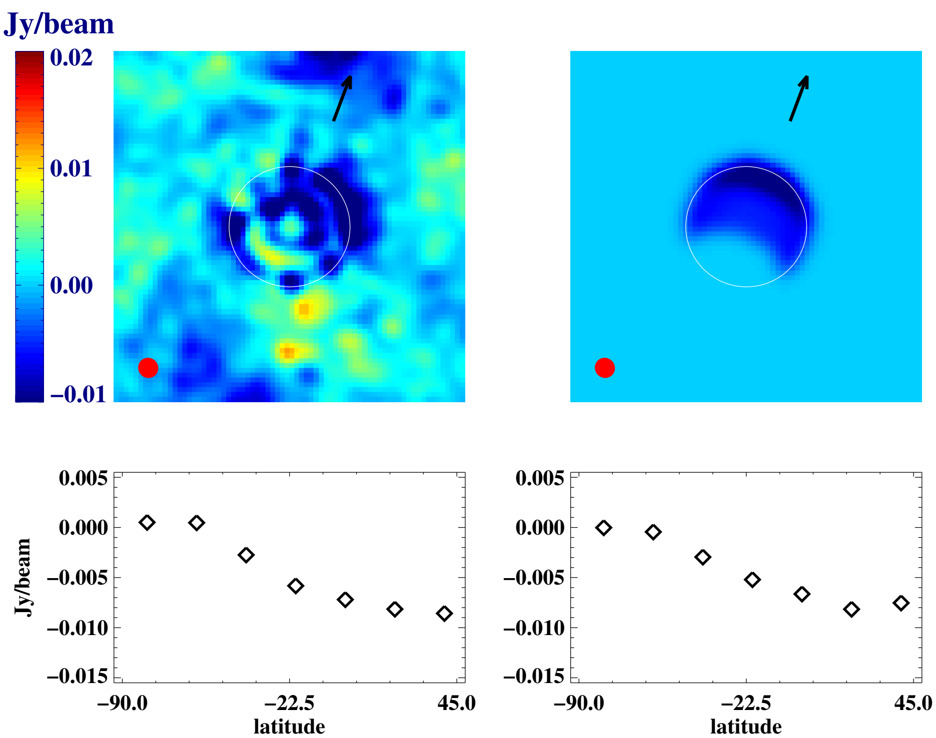

Figure 3.10: Left: continuum map (5.6 GHz offset from CO line), with a uniform composition, uniform TP model subtracted. Data have been scaled so that the intensity at the south pole matches the equilibrium hydrogen model. Right: model where the equilibrium hydrogen fraction is 0.6 from 10°N to 40°N, 0.8 from 40°S to 10°N, and 1.0 between 90°S and 40°S. The uniform composition, uniform TP model has been subtracted. Below each image is a plot of the zonally-averaged residuals.

3.5.2 Variations near the tropopause

For frequency offsets of 5–200 MHz (shown in Figs. 3.5 and 3.7), the maps show consistent latitudinal behavior: the south pole appears bright relative to our nominal model, southern mid latitudes are relatively dark, and additional brightening occurs near the equator before the intensity falls off again at northern mid latitudes. These variations are only about 2–3% of the average disk intensity, and are therefore best observed in the residual maps and residual plots (nominal model subtracted). Variations at these frequencies could potentially be due to variations in the CO abundance, variations in the temperature, or a combination of the two. We compare these data to three sets of models with the following properties: uniform CO, uniform temperature; varying CO, uniform temperature; and uniform CO, varying temperature.

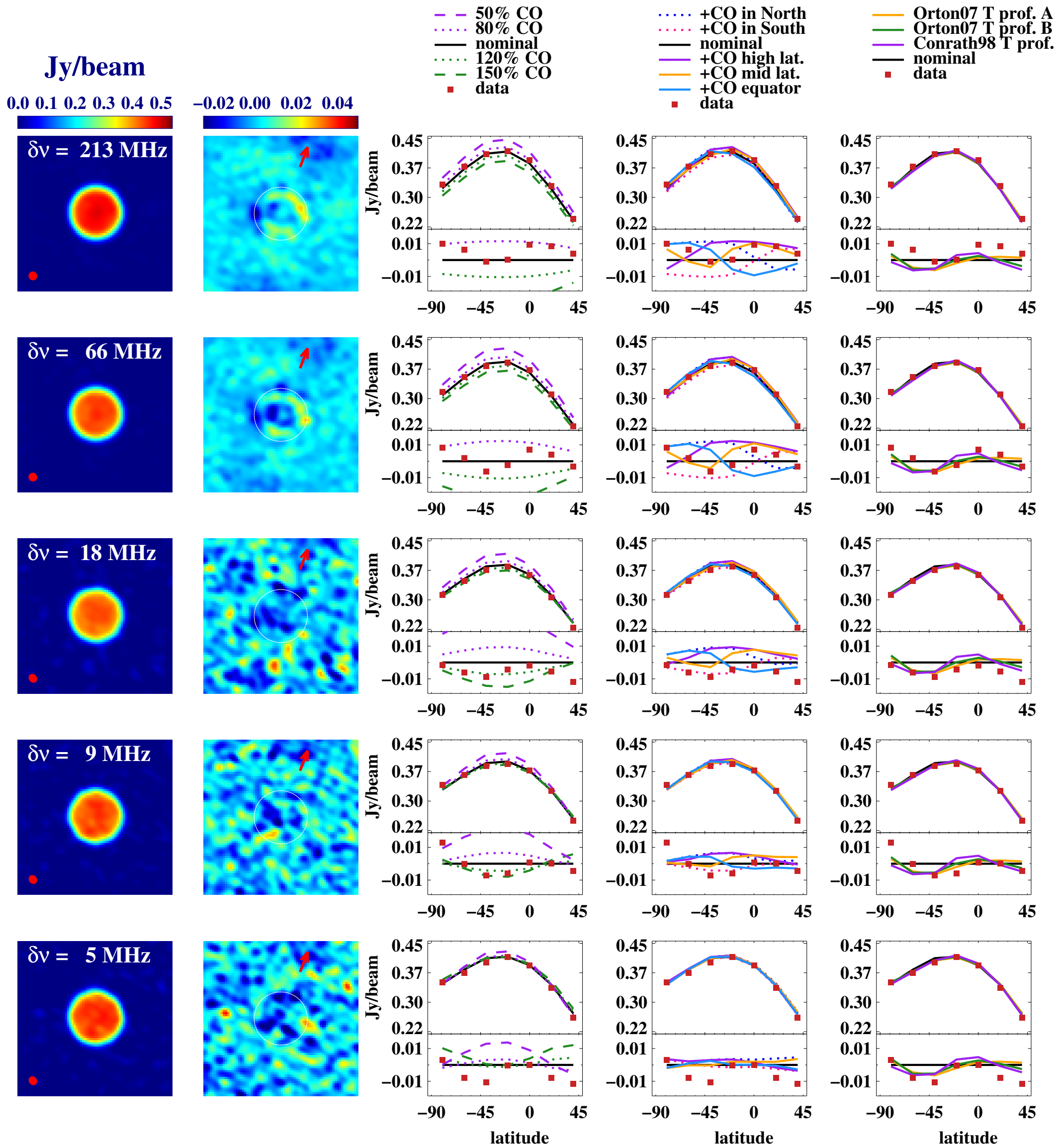

Figure 3.11: Comparison of the zonally-averaged data and models, for frequency offsets of 5–213 MHz. First two columns are the CLEAN maps and nominal-model subtracted maps. In the difference maps, the limb is indicated by a white circle and the direction of the rotation axis is shown by a red arrow. For each set of data-model comparisons, the top portion of each plot shows the binned data (red squares) and several models. Below each plot is a difference plot, showing the same data and models with the nominal model subtracted. The first column of plots shows a selection of uniform CO, uniform temperature models; the second column of plots presents several uniform temperature, varying CO models; and the final column presents three uniform CO, varying temperature models (Section 3.5.2).

Uniform CO, uniform temperature

In addition to our nominal model, which maintains a uniform abundance of 1.1 ppm of stratospheric CO, we produce models with 0.5, 0.8, 1.2 and 1.5 times this nominal CO abundance, with no latitudinal variation. At large offsets from line center (66 and 213 MHz) we observe that deviations in the CO abundance of more than 20% would be systematically too high/low to match the data at any latitude, for the given spatial resolution. At smaller offsets, the effect of changing the CO abundance becomes more complex. At an offset of 5 MHz, for example, an increase or decrease in the CO abundance will lead to an overall brighter model: increasing the CO abundance would increase the limb brightening, while decreasing the CO abundance would increase the intensity at disk center. We find that models of this form (with no latitudinal variations in the CO abundance or temperature) are not capable of reproducing the observed trend in the CO abundance with latitude.

Varying CO, uniform temperature

An interesting possibility would be if the observed variations were due to latitudinal variations in the CO abundance, related to localized infall or circulation effects. We compare the data to several simple models. First, we increase the CO abundance by 20% over the nominal value in the northern hemisphere and decrease it by 20% in the south, and vice versa. A southern hemisphere increase in the CO abundance is perhaps the better match of the two, but does not reproduce the brightening we observe near the south pole. We then try three slightly more complex models. In the first case, we increase the CO abundance by 20% at high latitudes (above 60°), and decrease it by 20% elsewhere. We repeat this for an increase at mid latitudes (between 30 and 60°N and S) and near the equator (30°S to 30°N). We find that an increase in the CO at mid latitudes provides a qualitatively good match to the data at 66 and 213 MHz. However, the agreement begins to fail closer to line center.

To quantify this, we calculate the weighted sum of the squares of the deviations of the latitude-binned data from the model:

$$s^2 = \frac{1}{M}\Sigma_{m=0}^{M-1}\delta y_m^2 w_m$$

where δy_m is the difference between the average intensity (in Jy/beam) and the model for latitude bin m. The quantity w_m is the weighting factor of a given measurement:

$$w_m = \frac{1/\sigma_m^2}{\frac{1}{M}\Sigma 1/\sigma_m^2}$$

We estimate the measurement error σ_m^2 as the root mean square (rms) of the pixel values in the original residual maps, divided by the square root of the number of images that were averaged together to produce the final map. We also divide by the square root of the number of beams contributing to the average intensity in bin m – this number varies from just over one at the pole and at 40°N, to a maximum of nearly six at 20°S. Calculations of

s^2 between the data and a selection of models are shown in Table 3.1. We see that only at a large offset from line center (213 MHz) does the model with increased CO at mid latitudes perform better than the nominal uniform CO, uniform temperature model.

Furthermore, from the constant CO models discussed in the previous section, we conclude that CO variations of this magnitude are generally not capable of producing the variations we observe at 5 MHz. It is possible that CO variations occur only at the depths probed by the 66- and 213-MHz maps, and that another mechanism caused variations at the higher altitudes probed nearer to line center. However, the similarities in the latitudinal behavior in all of these maps suggests that a common mechanism may be responsible.

Table 3.1: Measure of fit variances for the nominal model, the three varying temperature models and the best varying CO model.

offset from line ctr	$s^2 \times 10^5$				
	nominal model	Orton 2007 'A'	Orton 2007 'B'	Conrath 1998	+CO at mid-latitudes
213 MHz	3.84	4.50	4.76	5.91	2.07
66 MHz	2.63	1.58	1.68	2.84	3.04
18 MHz	3.70	2.12	2.10	2.84	8.07
9 MHz	2.86	1.45	1.87	3.94	4.53
5 MHz	4.82	2.65	2.16	2.27	5.74

Uniform CO, varying temperature

Variations in the zonal mean temperature have been observed near Neptune's tropopause in infrared images from the *Voyager 2* spacecraft (Conrath et al. 1998) and the Very Large Telescope (VLT) (Orton et al. 2007a). The latitude coverage of the *Voyager* IRIS data extends from 80°S to 30°N: Conrath et al. (1998) find a temperature minimum (4–5 K cooler than the equator) near 45°S, as well as a decrease in temperature at the northernmost extent of their data. The measurements of Orton et al. (2007a) extend all the way to the south pole. These authors find similar latitudinal behavior of the temperature from their 17.6 (Orton model 'A') and 18.7 μm VLT (Orton model 'B') images. Near the south pole, they observe temperatures that are 7–10 K higher than elsewhere on the planet.

To test the impact of these temperature variations on our models, we adjust the Fletcher et al. (2010) temperature profile with latitude to match the temperature variations reported by Conrath et al. (1998) and Orton et al. (2007a) at 100 mbar. For simplicity, the temperature profile is modified by the same temperature offset at all altitudes above 1 bar; however the 2D temperature cross sections of Conrath et al. (1998) show that these variations appear to be primarily near the tropopause, decreasing to nearly uniform within a few scale heights.

We find that these varying temperature models provide a good match to the data (Fig. 3.11 and Table 3.1). The Orton models of the zonal mean temperature profile are in general a better match to the data than the Conrath et al. (1998) solution; this is partially because the Conrath et al. (1998) data do not extend to the south pole. At 213 MHz, we find that these varying temperature models do not reduce s^2. Figure 3.11 shows that these models do qualitatively reproduce the latitudinal behavior seen at 213 MHz; however, there is an overall offset between the data and models at this frequency.

3.5.3 Line center

At line center, we are most sensitive to mbar levels in the atmosphere. Unlike in our other maps, at line center the south pole appears to be darker than the equator by 20 mJy/beam, which is roughly 5 times the rms error in the map. However, we find that there are artifacts in our images that are much greater than the theoretical rms errors. Since we only have a single map at line center, and we only have coverage of about one beam of latitudes below 70°S, we do not trust this result.

3.6 Summary and conclusions

We observe small, 2–3% latitudinal variations in our zonally-averaged maps both in and near the CO (2–1) line at 230.538 GHz. At frequency offsets from 5–200 MHz from line center, where we are sensitive to the CO abundance and temperature in the lower stratosphere, we find that the south pole and equator are relatively bright compared to the regions near 45°S and 40°N. Introducing the temperature variations derived by Orton et al. (2007a) into our models successfully reproduces the observed latitudinal variations. As discussed by Conrath et al. (1998) and Martin et al. (2008), the low temperatures at mid latitudes are consistent with upward motion and adiabatic cooling. The increase in temperature near the south pole is likely due to increased solar insolence in this region (Hammel et al. 2007; Orton et al. 2007a) and/or subsidence and adiabatic heating (Martin et al. 2008).

Further evidence for a global circulation pattern in which air rises at mid- southern and northern latitudes and subsides near the equator and south pole comes from centimeter wavelengths, which indicate that the south pole (Martin et al. 2006, 2008; Hofstadter et al. 2008) and equator (Butler et al. 2012) are bright compared to the rest of the planet. Subsidence of dry air at these latitudes would decrease the atmospheric opacity and cause this brightening. Our millimeter continuum observations also indicate that the south pole is brighter than the north by 2–3%. We can reproduce our observations if the H_2S opacity has the nominal value from 10°N to 40°N, 0.3 times the nominal value from 40°S to 10°N, and 0.03 times the nominal value between 90°S and 40°S. Such a decrease in the H_2S opacity near the south pole could also cause an increase in the brightness temperature in this location at longer wavelengths.

For opacity sources that dominate at higher altitudes in the atmosphere, such as H_2 CIA, a smaller change in the opacity is enough to produce the latitudinal trend in brightness observed in our data. We can alternatively model the observed latitudinal variations by decreasing the CH_4 mole fraction from 0.044 at 10°N–40°N to 0.022 at 40°S–10°N and 0.0055 between 90°S and 40°S. While most previous studies (e.g. Roe et al. 2001; Gibbard et al. 2002; Irwin et al. 2011) assume that Neptune's methane mole fraction is constant in the troposphere with latitude, Karkoschka & Tomasko (2011) find that CH_4 is depressed between 1.2 and 3.3 bar at high southern latitudes, compared to its abundance at low latitudes. While we estimate somewhat larger variations in the CH_4 mole fraction (a total change of a factor of 8 rather than a factor of ∼3 found by Karkoschka & Tomasko (2011)), the similarities between our estimated latitudinal CH_4 profile and that derived by Karkoschka & Tomasko (2011) are conspicuous.

Variations in the *ortho/para* ratio of hydrogen can also cause variations in the continuum intensity. We find that a decrease from an equilibrium hydrogen fraction of 1.0 at the south pole to 0.6 at 40°N produces the observed latitudinal trend. Baines et al. (1995) determined that the hydrogen in Neptune's upper troposphere is near equilibrium; however, Conrath et al. (1998) measured a decrease in the *para* hydrogen fraction from equilibrium at latitudes of 0°–60°S, and an increase in the *para* fraction over the equilibrium value near the south pole and in the northern hemisphere. This result qualitatively agrees with the pattern we observe near the south pole and equator, although we do not see a rise in the intensity in the northern hemisphere, which we would expect from an increase in the *para* ratio at these latitudes. We note that we do not investigate the effects of changing the adiabatic profile. This has been studied previously: de Pater & Mitchell (1993) show the effect of equilibrium, normal and intermediate hydrogen on Neptune's microwave spectrum between 0.1 and 10 mm by changing both the adiabatic profile and the CIA opacity. They show that the brightness temperature is highest for intermediate H_2 and lowest for equilibrium H_2.

With these data alone we cannot distinguish between these three potential mechanisms for varying Neptune's millimeter opacity; the true cause of the latitudinal variations we observe may well be a combination of these effects.

Finally, we do not see strong evidence for latitudinal variations in the CO abundance at the sensitivity of our data. We expect that any variations in the CO abundance must be less than 20%. Several things would improve our ability to look for CO variations: first of all, a better characterization of Neptune's continuum opacity would allow better modeling within the CO line. Our analysis from Chapter 2 indicates that H_2S opacity has a small but non-negligible affect on the retrieved vertical CO profile. Additionally, in order to disentangle the effect of temperature and CO variations, spatial maps of several CO transitions are required. These improvements will be possible with ALMA; in particular we expect ALMA will provide better millimeter continuum measurements and higher sensitivity CO maps for several CO rotational transitions.

Acknowledgements

The data presented in this work were obtained with CARMA. Support for CARMA construction was derived from the states of California, Illinois, and Maryland, the James S. McDonnell Foundation, the Gordon and Betty Moore Foundation, the Kenneth T. and Eileen L. Norris Foundation, the University of Chicago, the Associates of the California Institute of Technology, and the National Science Foundation. Ongoing CARMA development and operations are supported by the National Science Foundation under a cooperative agreement, and by the CARMA partner universities. This work was supported by NASA Headquarters under the NASA Earth and Space Science Fellowship program – Grant NNX10AT17H; and by NSF Grant AST-0908575. The authors would like to thank L. Fletcher for providing his temperature and CH_4 profiles, and G. Orton for providing his H_2 CIA absorption coefficients. The authors would also like to acknowledge R.L. Plambeck, M. Wright and A. Bauermeister for many helpful discussions.

3.7 Appendix: Comparison of deconvolution techniques

Neptune, with its smooth, bright disk and sharply defined edges, presents a challenge for imaging and deconvolution. In order to evaluate the effect and significance of our weighting function and deconvolution technique, we perform a series of comparisons using a subset of our data that spans 437.5 MHz in frequency, centered at 225.74 GHz (nearly 5 GHz from the center of the CO (2–1) line). These data represent an instance where there is overlap between the D-array data and all epochs of B-array data. To determine the importance of the short-spacing (D-array) data in the final maps, we imaged the B-array data separately, in addition to imaging the full combined data set. The dirty maps from both data subsets are shown in Figs. 3.12 and 3.13, with three different weighting functions (natural, uniform and intermediate) applied. Natural weighting (top), which weights each visibility by the inverse of its noise variance, gives the best sensitivity, at the expense of the shape of the synthesized beam and sidelobe levels. Uniform weighting (middle) adjusts the weight of each visibility so that the density of visibilities is uniform across the (u,v) plane. This minimizes sidelobe levels, but increases the noise level in the map. Robust weighting with a Briggs visibility weighting robustness parameter (Briggs 1995) of 0.0 (bottom) is a good compromise between the two; maintaining a well-behaved beam shape with less increase to the noise level.

We experimented with several deconvolution techniques; six of them are presented here. The results are summarized in Table 3.2 and shown in Figs. 3.14 – 3.17.

Table 3.2: Comparison of deconvolution strategies.

					B-array data only			Full dataset		
	Algorithm	region	input model	threshold (mJy/beam)	Flux [a] (Jy)	rms [b] (mJy/beam)	niter[c]	Flux[a] (Jy)	rms (mJy/beam)	niter[c]
(a)	CLEAN	-	-	6	9.18	1.8	9972	12.25	1.8	4154
(b)	CLEAN	1.5” circle	-	0.6	12.12	1.9	17942	12.24	2.0	7809
(c)	CLEAN	square[d]	nominal	0.6	12.63	0.64	64492	12.26	0.54	100000
(d)	CLEAN	square[d]	flat	0.6	10.90	0.47	100000	12.25	0.52	100000
(e)	MSCLEAN	2.5” circle	-	1.2	13.11	1.8	1393	12.23	2.0	1217
(f)	Max. entropy	4” square	-	1.2	12.02	3.2	5000	11.96	3.5	5000

[a] Total flux recovered; nominal clean model gives a total flux of 12.740 Jy
[b] standard deviation of the full residual map
[c] number of `CLEAN` or maximum entropy iterations performed
[d] square extends just beyond the Neptune model disk – approximately 2.3” on a side

(a) Classical `CLEAN` no clean region: We used the CASA implementation of the Clark `CLEAN` routine with a gain factor of 0.05. A maximum of 100,000 iterations were permitted, unless a clean threshold of 6 mJy was reached. This threshold was selected to be about 10 times the theoretical rms of the map. We find that even with such a high threshold, a significant amount of noise is cleaned. This is particularly true for the B-array data subset, for which a strong negative “clean bowl” is present due to

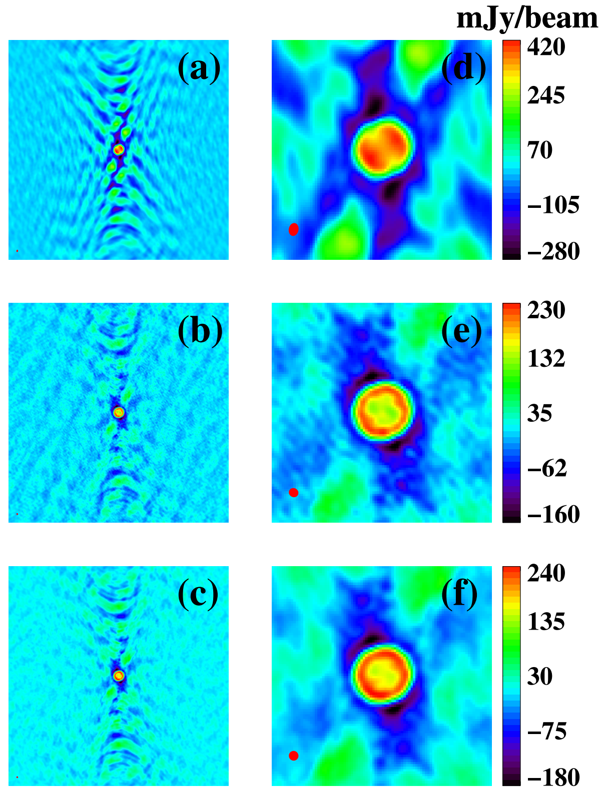

Figure 3.12: Dirty maps, B-array (long-baseline) data only. Made using natural weighting (top), uniform weighting (middle) and robust weighting with a Briggs visibility weighting robustness parameter (Briggs 1995) of 0.0 (bottom).

the missing short spacing information. As a result, the residual map is artificially low, and only 3/4 of the total flux from the planet is recovered when only B-array data are included.

(b) Classical `CLEAN`, inside a circle of radius 1.5”: We restrict `CLEAN` to a circular region of radius 1.5”, just outside of the planet. Since most of the flux within this region is source (not noise), we use a lower clean threshold of 0.6 mJy, equal to the theoretical rms of the map. This technique recovers more than 95% of the expected (model) flux from Neptune, even when the D-array data are not included. However, the noise outside of the `CLEAN` region is higher than for any other technique tried, and the disk appears very ‘lumpy’ in the final `CLEAN` map, presumably because the flux is being reproduced by a set of point sources, which is unrealistic in the case of Neptune.

(c) Classical `CLEAN`, starting with best-guess `CLEAN` model: `CLEAN` is given a starting model, which is taken from our radiative transfer model described in Section 3.3. The

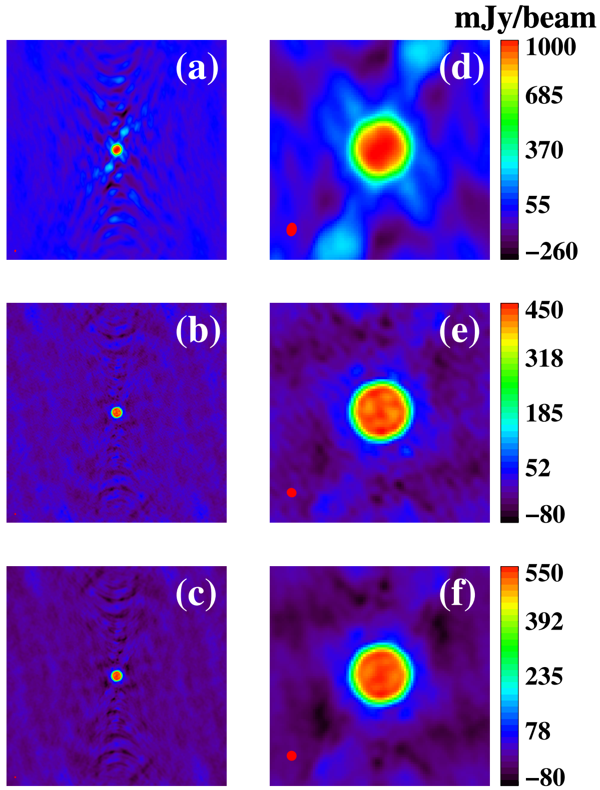

Figure 3.13: Dirty maps, using all data (B and D arrays). Made using natural weighting (top), uniform weighting (middle) and robust weighting with a Briggs visibility weighting robustness parameter (Briggs 1995) of 0.0 (bottom). On the left we show the full maps; on the right we zoom in on the planet. The beam is indicated by the red oval in the bottom left corner of each image.

input model uses 0.005" pixels that cover a square region that extends just beyond Neptune's limb. CLEAN then proceeds in the same way as before, adding additional point source components (both positive and negative) within the spatial range of the starting model until the maximum number of iterations or CLEAN threshold is reached. In general, we find this approach gives the best result when the D-array data are omitted. The noise is low across the map (even beyond the CLEAN region), and the disk appears far smoother than for the previous two techniques.

(d) Classical CLEAN, starting with a flat clean model: To address the possibility that our choice of input model has an unexpected effect on the output map (perhaps forcing the data to match our nominal model), we repeat case (c) using a flat input model, which is a disk of constant intensity, equal to the lowest intensity value of the best guess model in (c). We find that without D-array data, some of the negative bowl from the missing short-spacing data remains. However, when the D-array data are included, a flat input starting model produces a very similar map to the more detailed model in (c). The noise properties of the map are similar for the two starting model cases.

(e) Multiscale `CLEAN`: As an alternative to classical `CLEAN` we try the CASA implementation of multi-scale `CLEAN`. Rather than modeling the sky brightness with a set of point-sources, multi-scale `CLEAN` models the sky with components of several different size scales. For a detailed comparison of Multi-scale clean, see Rich et al. (2008). We use a `CLEAN` gain of 0.3 and a `CLEAN` region of radius 3"; the threshold is set to 1.2 mJy, or twice the theoretical rms. Five scales are specified, ranging from a point source up to the diameter of Neptune. We find that multi-scale clean is able to recover Neptune's flux even when the short spacing data were omitted. Multi-scale clean also requires significantly fewer iterations to converge, and agrees well with (c) without depending at all on an input `CLEAN` model. However, the noise level outside of the `CLEAN` region is much higher than in (c) and (d).

(f) Maximum Entropy: We use the `mosmem` routine in MIRIAD, which is an implementation of the Maximum Entropy Method (MEM). This algorithm, which is an alternative to `CLEAN` produces a smooth positive image. We restrict the deconvolution to a square 4" on a side, and specify the total flux based on the expected value from the model. We allow for as many as 5000 iterations to reduce the image residuals to 1.2 mJy/beam, which is twice the theoretical rms. We found that `mosmem` failed to converge after 5000 iterations, and the rms did not appear to improve much with additional iterations. This approach had the highest residual level of any method.

From this comparison, we conclude that when we include the D-array (short baseline) data, there is no significant difference in the maps from the different deconvolution methods. In particular, while a starting input `CLEAN` model appears to improve the appearance of the final maps, it does not artificially force the resulting maps to agree with the starting model, as long as the short baseline data are included. Table 3.2 lists the total flux densities in the maps. The maps produced using the full dataset produce a final flux density that is consistently lower than the model predicts. This result is consistent with our disk-integrated spectrum, which indicates that at 225 GHz our models over-predict Neptune's total flux. When we include only the B-array data in the imaging process, the use of a starting model is more influential, reducing the `CLEAN` bowl seen in case (a), and increasing the the total flux in case (c) to better agree with the model.

The ringing in the final maps is not an artifact of deconvolution, but is a result of amplitude and phase errors in the data. This is supported by the fact that the rippling is observed in both `CLEAN` and Maximum Entropy deconvolution methods. These ripples have an amplitude as high as 1 mJy/pixel, and the average deviation between map (c) and a smooth model (scaled to the data amplitude) is 0.3 mJy/pixel or 5.7 mJy/beam.

Since the maps are not overly influenced by the inclusion of an input model, the appearance of map (c) is best, and the residuals in case (c) are the lowest, we select method (c) for our image deconvolution.

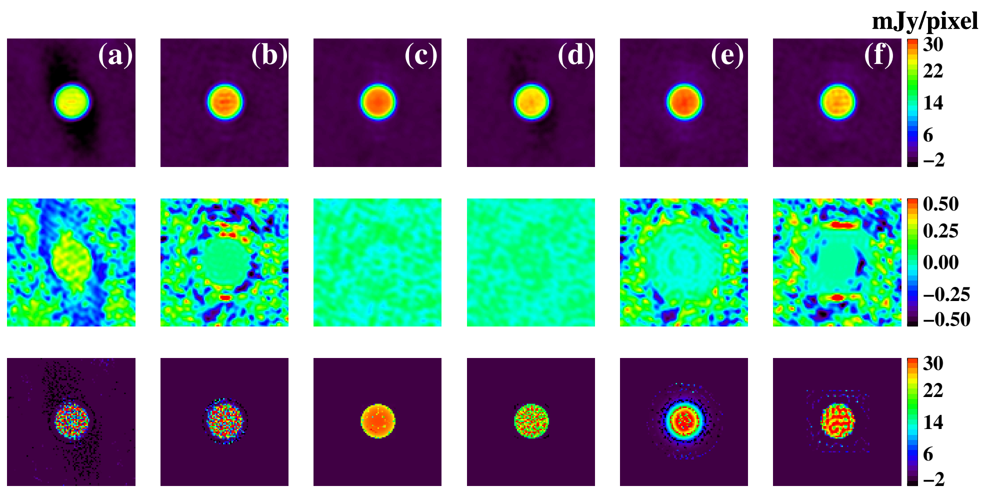

Figure 3.14: Comparison of deconvolution techniques, for the B-array data only. Discussion of techniques (a)-(f) is given in the Appendix. For each technique, the deconvolved map (top), residual map (middle) and model (bottom) are shown.

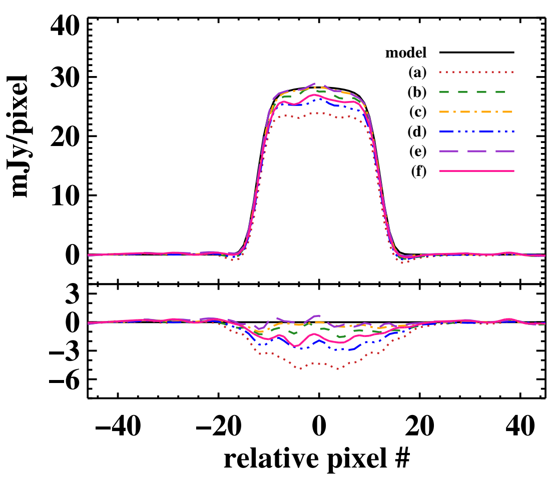

Figure 3.15: Comparison of maps from deconvolution techniques (a)-(f), for the B-array data only. Plots are made by slicing horizontally through the center of the maps. Also shown is our nominal model (black) for the data. In the bottom plot, we subtract the nominal model from each of the map slices.

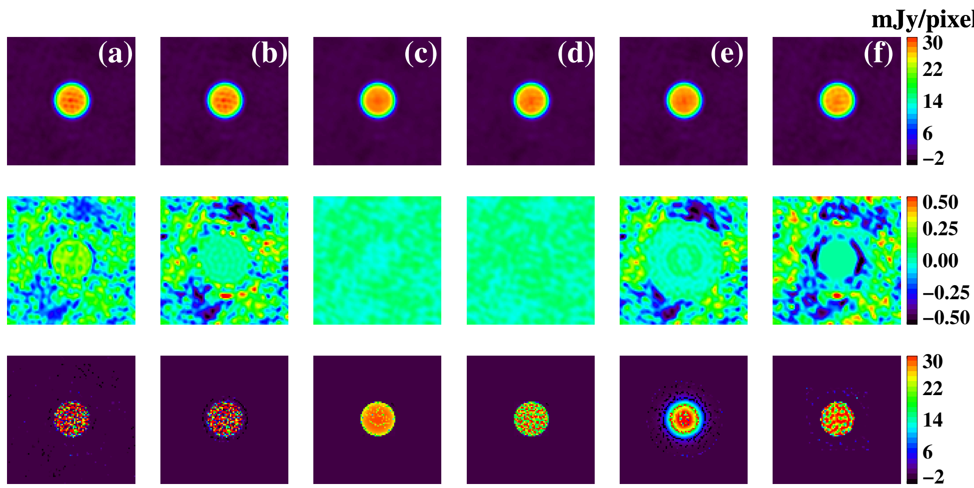

Figure 3.16: Same as Fig. 3.14, except for all data (B and D arrays).

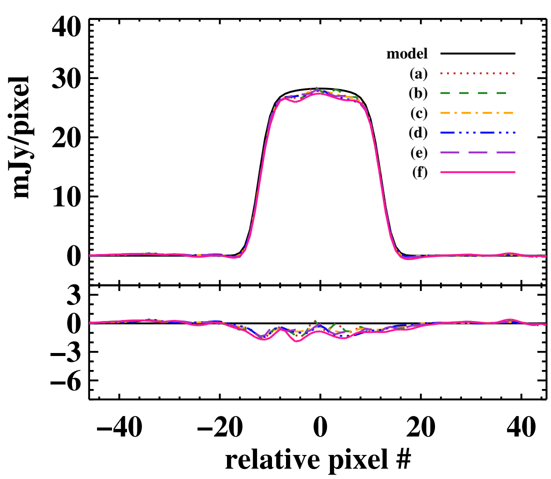

Figure 3.17: Same as Fig. 3.15, except for all data (B and D arrays).

Chapter 4

Seeing Double at Neptune's South Pole

Keck near-infrared images of Neptune from UT 26 July 2007 show that the cloud feature typically observed within a few degrees of Neptune's south pole had split into a pair of bright spots. A careful determination of disk center places the cloud centers at $-89.07 \pm 0.06°$ and $-87.84 \pm 0.06°$ planetocentric latitude. If modeled as optically thick, perfectly reflecting layers, we find the pair of features to be constrained to the troposphere, at pressures greater than 0.4 bar. By UT 28 July 2007, images with comparable resolution reveal only a single feature near the south pole. The changing morphology of these circumpolar clouds suggests they may form in a region of strong convection surrounding a Neptunian south polar vortex.[1]

4.1 Introduction

The atmosphere of Neptune is active. In addition to global changes on decadal scales (Lockwood & Jerzykiewicz 2006; Hammel & Lockwood 2007b), individual clouds evolve on time scales as short as hours (e.g. Limaye & Sromovsky 1991; Sromovsky et al. 1995, 2001b). Near-infrared (NIR) images, which probe Neptune's lower stratosphere and upper troposphere in reflected sunlight, reveal bright bands and cloud features against a dark disk. The pattern of zonal circulation, which is most pronounced at mid latitudes, continues to high southern latitudes, where a bright, unresolved cloud feature is present within a few degrees of the pole. This feature has been seen since the Voyager 2 era (Smith et al. 1989).

Interest in Neptune's global dynamics has been reignited by mid-IR observations of enhanced emission over the south pole relative to the rest of the planet (Hammel et al. 2007; Orton et al. 2007a). This enhancement suggests a temperature increase of 4-5 K in the south polar region, and has led these authors to draw parallels with Saturn, where the summer pole is similarly warm in the stratosphere and troposphere (Orton & Yanamandra-Fisher 2005). Recently it has been observed that both of Saturn's poles exhibit a localized hot spot surrounded by cooler zones, forming circulation cells that make up part of a planet-wide

[1]This chapter has been previously published in Icarus (Luszcz-Cook et al. 2012) and has been reproduced with permission from all coauthors.

circulation (Fletcher et al. 2008; Dyudina et al. 2008). A global dynamical pattern has also been inferred for Neptune's atmosphere (Martin et al. 2008); it remains to be seen if this pattern includes a polar circulation cell like those on Saturn.

Table 4.1: Observations

Date	Time (UTC)	Filter	Central λ (μm)^a	Bandpass (μm)^a	Airmass	T_{exp} (sec)	N_{exp}
26 July 2007							
Neptune	11:37	J	1.25	0.163	1.21"	60	3
Neptune	11:43	Kp	2.12	0.351	1.21"	60	3
Neptune	11:49	H	1.63	0.296	1.21"	60	5
Neptune	11:58	H	1.63	0.296	1.22"	60	5
Neptune	12:07	H	1.63	0.296	1.22"	60	5
HD 22686	15:10	J	1.25	0.163	1.33"	6	3
HD 22686	15:13	H	1.63	0.296	1.32"	6	3
HD22686	15:15	Kp	2.12	0.351	1.31"	10	3
SAO 146732	15:21	Kp	2.12	0.351	1.22"	5	3
SAO 146732	15:23	Kp	2.12	0.351	1.22"	5	3
SAO 146732	15:24	H	1.63	0.296	1.23"	5	3
SAO 146732	15:27	J	1.25	0.163	1.23"	5	3
28 July 2007							
Neptune	11:28	H	1.63	0.296	1.21"	60	5
Neptune	11:37	H	1.63	0.296	1.21"	60	5
Neptune	11:45	H	1.63	0.296	1.22"	60	5
SAO 146732	15:20	H	1.63	0.296	1.24"	5	3

We obtained high spatial resolution NIR images of Neptune's south pole in July 2007, revealing temporal evolution of discrete circumpolar clouds. Here we describe these features, model their properties, and discuss the implications for the dynamics of the Neptunian south polar region.

4.2 Observations and data processing

We observed Neptune from the 10-meter W.M. Keck II telescope on Mauna Kea, Hawaii, on 26-28 July (UT) 2007, as part of a long-term program studying the planet's atmosphere in the NIR. J-, H-, and Kp-band images were taken using the narrow camera of the NIRC2 instrument, coupled to the adaptive optics (AO) system (Table 1). The 1024x1024 array has a pixel size of 9.963 ± 0.011 mas/pixel in this mode (Pravdo et al. 2006), which at the time of observations corresponded to a physical size of ∼210 km at disk center.

The data were flat fielded and sky-subtracted, and bad pixels were replaced with the median of the 8 surrounding pixels. All images were corrected for the geometric distortion of the array using the 'dewarp' routines provided by P. Brian Cameron[2], who estimates

[2] http://www2.keck.hawaii.edu/inst/nirc2/post_observing/dewarp/nirc2dewarp.pro

residual errors at $\lesssim$ 0.1 pixels. We measured a full width at half maximum (FWHM) of $0.039 \pm 0.005''$ for a stellar point source (SAO 146732) on the days of observation, which is consistent with the diffraction limit of the telescope at 2 μm, and corresponds to an effective resolution of ~800 km at the center of the disk.

The images were photometrically calibrated using the star HD 22686, then converted from units of observed flux density to units of I/F, which is defined as (Hammel et al. 1989):

$$\frac{I}{F} = \frac{r^2}{\Omega}\frac{F_N}{F_\odot}$$

where r is Neptune's heliocentric distance, $\pi F_\odot$ is the sun's flux density at Earth's orbit (Colina et al. 1996), F_N is Neptune's observed flux density, and Ω is the solid angle subtended by a pixel on the detector. By this definition, $I/F = 1$ for uniformly diffuse scattering from a Lambert surface when viewed at normal incidence.

The 26 July data (Fig. 4.1) show two distinct features near Neptune's south pole. Other unresolved sources, such as moons and other clouds, do not appear double, so it seems unlikely this is an artifact. The 28 July data (Fig. 4.2), at comparable resolution, show only a single unresolved polar cloud feature. To determine the total I/F of the unresolved features above the background, we model them as one (for the single cloud on 28 July) or two (for the pair of clouds on 26 July) 2D Gaussians. We use the best-fit parameters from the least-squares fitting routine MPFIT[3] to find the I/F of each cloud feature (Table 2). From experience we estimate the error in the photometry to conservatively be 20%; the errors in the cloud fits are between 4% and 12%. In Kp band, we do not see the polar cloud features above the noise (Fig. 4.1). To set an upper limit for the I/F of the clouds in Kp band, we assume the clouds will be detectible when the mean value of the signal plus noise is equal to one standard deviation above the noise mean. We confirmed this upper limit by convolving the maximum Kp I/F with a Gaussian having the FWHM of the point spread function (PSF) and adding the observed level of noise.

4.3 Navigation and cloud locations

Neptune's bright and dynamic activity limits the accuracy of image centering when using the planet's limb as a reference, since the PSFs of bright features near the limb often extend off the edge of the disk. To perform the centering more precisely, we found the positions of three of Neptune's moons in each H-band image, and shifted the images in x and y so that the positions of the moons were best fit to lie on their orbits, as derived from the Planetary Rings Node ephemeris data[4] (Fig. 4.3). While other methods of aligning images do not necessarily give you the location of disk center, this technique allows us to improve both the relative alignment of the images as well as the determination of disk center coordinates.

[3]Markwardt, C.B. 2008 in proc. Astronomical Data analysis Software and Systems XVIII

[4]http://pds-rings.seti.org/tools/ephem2_nep.html

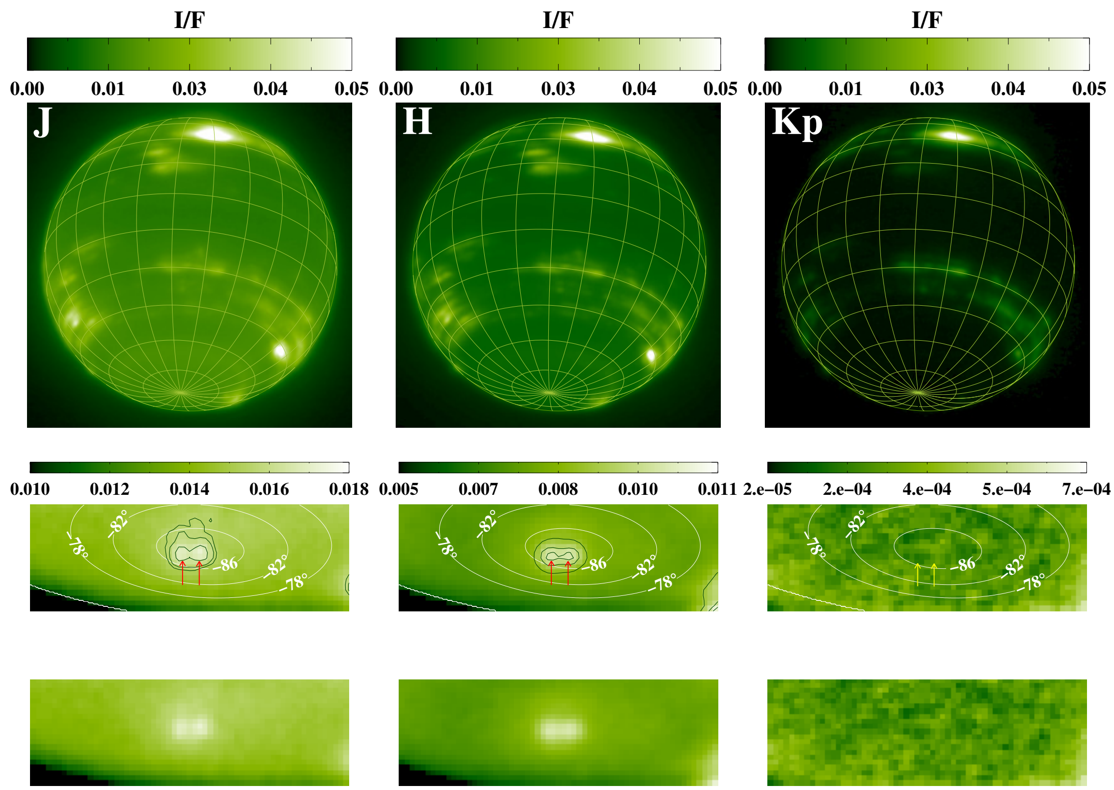

Figure 4.1: J-, H- and Kp-band images from 26 July 2007 in units of I/F. The first three images in each filter were averaged together to produce the figure. The top panels all have same color bar. In the top images, the pole is bright due to the convergence of longitude lines; therefore we zoom in on the pole in the bottom panels. The top row highlights the features by superposing contours at 10% 20% and 26% above the H-band background; and 3%, 5% and 10% above the J-band background level. Latitude circles at 4° spacings are also shown. The arrows indicate the positions of the two cloud features; in Kp band the clouds are not above the noise; therefore no intensity contours are plotted.

The centering error in our least-squares fit is on average 0.4 pixels per image, which agrees well with the image-to-image scatter of the positions of individual cloud features. This is an improvement over our centering by limb detection, which we estimate to result in 1–2 pixel errors in the determination of disk center. In J- and K- band we do not have a sufficient number of images to implement our moon centering technique; therefore these images are aligned to the H-band images by eye, to sub-pixel accuracy. To find the positions of the clouds near the pole, we use the moon-centered H-band images and the solutions from the 2D Gaussian fits (Section 2). We determine the weighted mean location of each cloud in image coordinates, which we then transform into planetocentric latitude and longitude, using the JPL Horizons ephemeris information[5] for sub-observer latitude and longitude at

[5]http://ssd.jpl.nasa.gov/?horizons

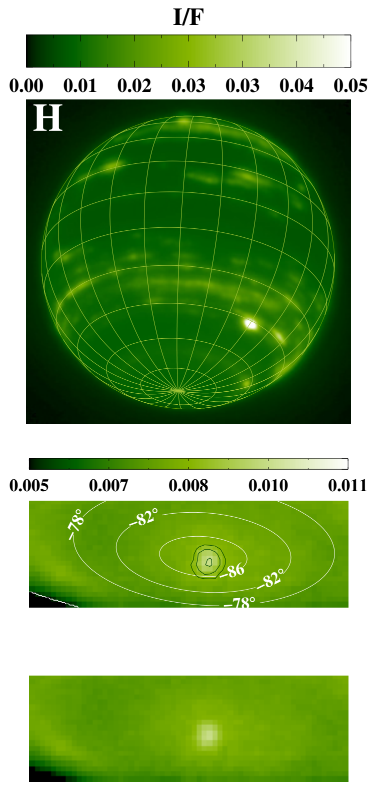

Figure 4.2: Average of first three H-band images from 28 July 2007, in units of I/F, with latitude and longitude lines plotted. The middle image highlights the single cloud feature with contours of 5% 10% and 20% above the background level.

the time of the observations. The errors in the latitude and longitude of the clouds are estimated using a Monte Carlo method, whereby for each parameter involved in calculating the latitude and longitude, a random distribution of values consistent with its probability distribution is generated. These parameters include the array rotation angle (Pravdo et al. 2006), image center coordinates, and cloud center coordinates. For each set of generated parameter values, the latitude and longitude are then calculated; errors are determined as the standard deviations of these simulated data sets.

We find that on 26 July the two cloud features are near, but not directly at the pole as determined by moon orbits: the spot nearest the pole is located at $-89.07 \pm 0.06°$ latitude and $293 \pm 3°$ longitude. The second cloud resides approximately 500 km further from the pole, at $-87.84 \pm 0.06°$ latitude, $238 \pm 2°$ longitude. The single spot on 28 July is likewise near, but not at, the south pole, at $-88.47 \pm 0.03°$ latitude, $86 \pm 2°$ longitude (Table 2).

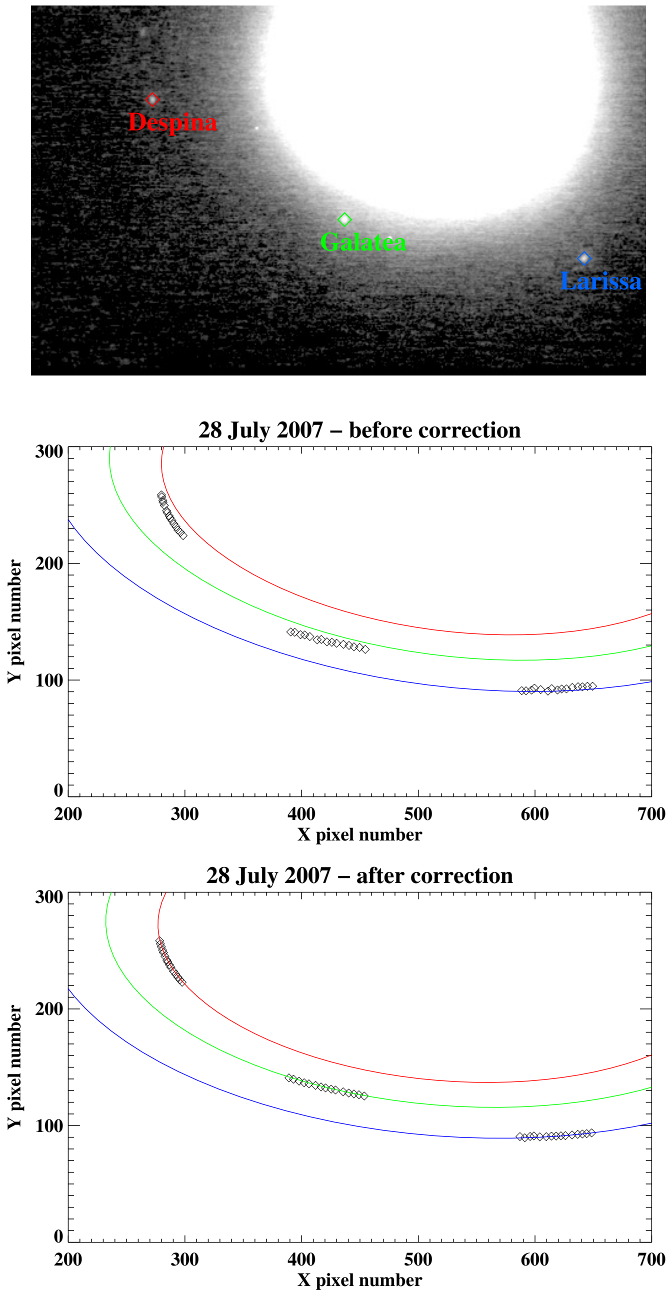

Figure 4.3: Fitting disk center using Neptune's moons. The positions of Galatea (green), Larissa (blue) and Despina (red) were found in each image and aligned with the moon orbits to establish the planetary coordinates. The top panel shows the moons in the first H-band image on 28 July. The middle plot shows the orbits relative to the positions of the moons in the images when centered using the planet's limb. The bottom plot shows the moon positions after fitting them to their orbits.

Table 4.2: Spot locations and flux densities in units of I/F, as well as the I/F of the region surrounding the clouds. For the clouds, the maximum Kp/J and Kp/H ratios allowed by the data are also given.

		I/F				
latitude	longitude	J	H	Kp	max(Kp/J)	max(Kp/H)
26 July 2007						
$-89.08 \pm 0.06°$	$293 \pm 3°$	0.039 ± 0.009	0.036 ± 0.008	< 0.004	0.11 ± 0.02	0.12 ± 0.02
$-87.84 \pm 0.06°$	$238 \pm 2°$	0.038 ± 0.008	0.033 ± 0.007	< 0.004	0.12 ± 0.02	0.13 ± 0.03
background		0.015 ± 0.003	0.008 ± 0.002	0.00023 ± 0.00006		
28 July 2007						
$-88.47 \pm 0.03°$	$86 \pm 2°$	0.017 ± 0.009	0.042 ± 0.009	< 0.005	0.3 ± 0.1	0.12 ± 0.01
background		0.014 ± 0.003	0.008 ± 0.002	0.00026 ± 0.00009		

4.4 Radiative transfer modeling of features

The J, H, and Kp filters probe various depths through the stratosphere and upper troposphere (Fig. 4.4); therefore we can use the data to set limits on the heights of the south polar cloud features. To do this, we adapted the radiative transfer (RT) code for Titan from Ádámkovics et al. (2007) for Neptune. We adopt the Neptune temperature profile derived by Lindal (1992) from occultation measurements, and incorporate the major opacity sources that dominate Neptune's 1- 5 μm spectrum: we use the H_2 collision-induced absorption coefficients for hydrogen and helium (Borysow et al. 1985, 1988; Borysow 1991, 1992, 1993), assuming an equilibrium ortho/para ratio for H_2; and the k-distribution coefficients for H_2-broadened methane (Irwin et al. 2006). Following Gibbard et al. (2002), our lower boundary is an optically thick cloud at 3.8 bar, presumably the H_2S cloudtop (de Pater et al. 1991a), with a Henyey-Greenstein asymmetry parameter of -0.1. Aerosols are treated as Mie scatterers with real indices of refraction of 1.43 and imaginary indices of refraction $n_i = 0$. Within a given haze layer, aerosols are characterized by a single particle radius; this radius, along with the altitude range and number density of aerosol particles, are free parameters, chosen to fit the data. The RT equations are then solved using a two-stream approximation (Toon et al. 1989).

To model the south polar cloud features, we first developed two cloud-free 'background atmosphere' models. For the first model, we choose the simplest haze distribution consistent with the J-, H-, and K-band I/F values in the region surrounding the polar clouds (Table 3). For comparison, we also find a best model fit to a medium-resolution spectrum from the IRTF Spectral Library (Fig. 4.5), taken with the SpeX instrument on the NASA Infrared Telescope Facility (IRTF) on Mauna Kea (Rayner et al. 2009). These data are averaged over a significant fraction of Neptune's disk. Although this disk-integrated model has little contribution from the south pole, this second model, which has very different haze properties from the first (Table 3), provides a qualitative test of the sensitivity of our cloud modeling

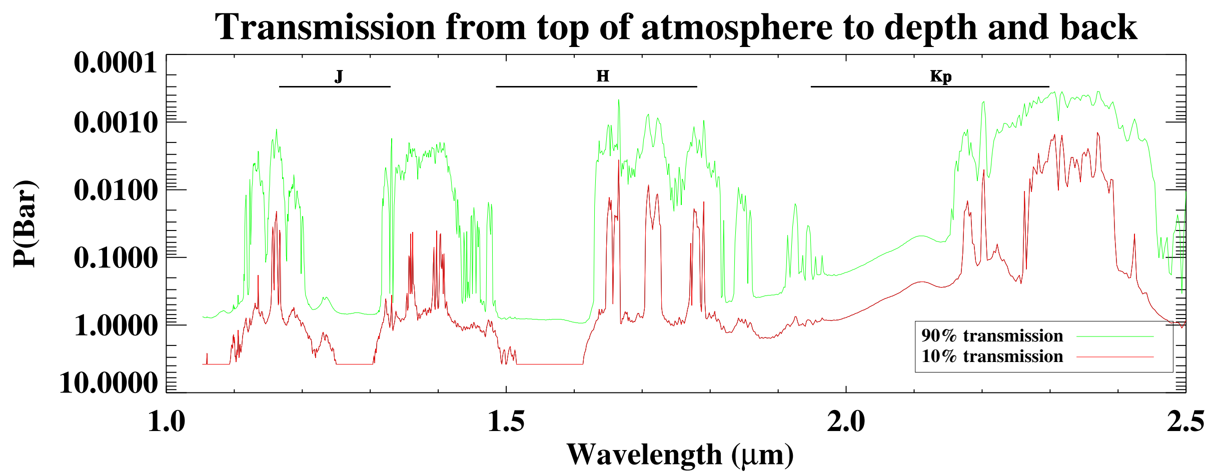

Figure 4.4: Two-way transmission in Neptune's atmosphere as predicted by our RT model. The curves show the pressure levels at which 10% and 90% of the light is transmitted to the top of the atmosphere and back.

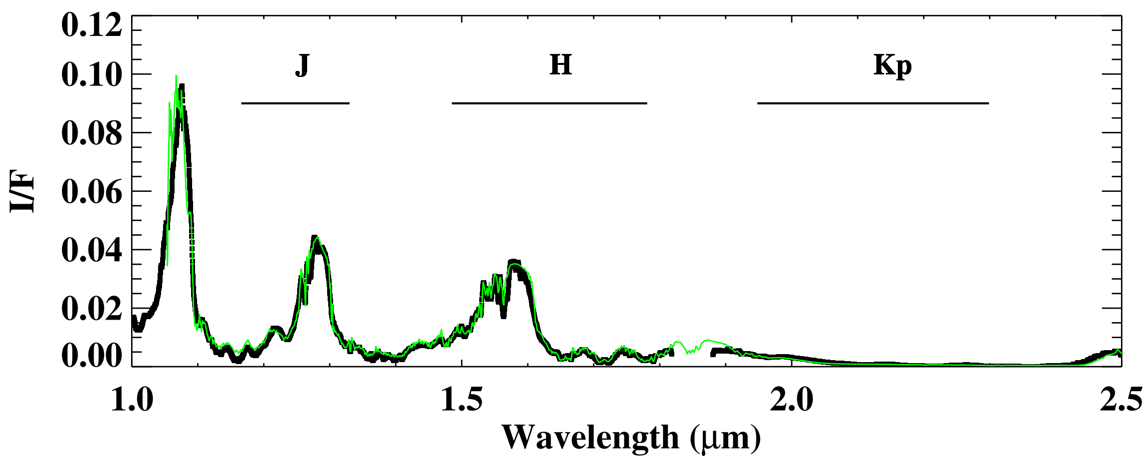

Figure 4.5: Comparison of radiative transfer model (green) and long-slit IRTF SpeX spectrum (black).

to the choice of model hazes. In addition, fitting to the SpeX data allows us to model the albedo of the deep 'surface' cloud: we find that given our choices of bottom cloud depth and scattering properties, the single-scattering albedo (ω) of the cloud must decrease from 0.55 at 1.1 μm to 0.20 at 1.27 μm and 0.13 at 1.56 μm. These values are reasonably consistent with Roe et al. (2001).

We then model each of the south polar clouds as a perfectly reflecting ($\omega = 1$), optically

Table 4.3: Haze layers, chosen to fit the I/F in the three spectral windows in the the region around the polar clouds (top); and the IRTF SpeX data (bottom).

P_{min} (mbar)	P_{max}(mbar)	rad(μm)	n(cm^{-3})
south polar region fit			
5	10	0.8	0.002
45	50	0.2	100
540	1540	0.5	3
SpeX fit			
1.4	20	0.2	12.5
340	1540	2.5	0.07

thick cloud layer with a Mie asymmetry parameter of 0.5. We consider clouds at each of 100 altitudes between 0.4 mbar and 3.8 bar. For each case, we average the resulting 'cloudy' model over H, J, and Kp bands for comparison with our image data, and subtract the I/F of the 'cloud-free' model to get the I/F contribution from the cloud.

For the 26 July data, we find the ratio of the intensities of the two clouds, which is affected by spot fitting errors but not calibration errors, to be 1.1 ± 0.1 in H band and 1.0 ± 0.1 in J band. Therefore, our results are consistent with the clouds being of the same size and at the same altitude. However, since the clouds are unresolved, we do not know the pixel filling fraction for each of the clouds. We can set an upper limit on the clouds' altitudes by comparing the maximum model-derived Kp-to-H and Kp-to-J I/F ratios to the observed values: the higher a cloud is in the atmosphere, the greater the expected Kp-band intensity. The upper limit Kp-to-H and Kp-to-J intensity ratios for each of the clouds, given the uncertainties in H and J, are presented in Table 2. Figure 4.6 shows the results of the modeled Kp/H and Kp/J intensities, compared to the maximum of these ratios from the 26 July data.

We find that the upper limit to the altitude of both clouds on 26 July is 0.4 bar. This also provides an estimate on the minimum size of the clouds: if either of the clouds is at 0.4 bar, it must fill at least 10% of a NIRC2 narrow camera pixel to be consistent with the observed H and J-band intensities. A deeper cloud would necessarily be larger to produce the same values of I/F. For the single cloud on 28 July, we find that its altitude also has an upper limit of 0.4 bar.

The models used in Fig. 4.6 use the haze distribution that best matches the I/F of the background atmosphere near the cloud features. However, we expect our choice of haze parameters to have little effect on our results. This is because we are interested primarily in the I/F increase due to adding a cloud into the background 'cloud-free' atmosphere. When we ran our second set of models using the simpler haze distribution used to fit the IRTF SpeX data (Table 2), we found that changing the haze parameters affected the 'cloud-free' and 'cloudy' spectra in a similar way, so that to within 3%, the calculated change in I/F from a given cloud was independent of the haze parameters.

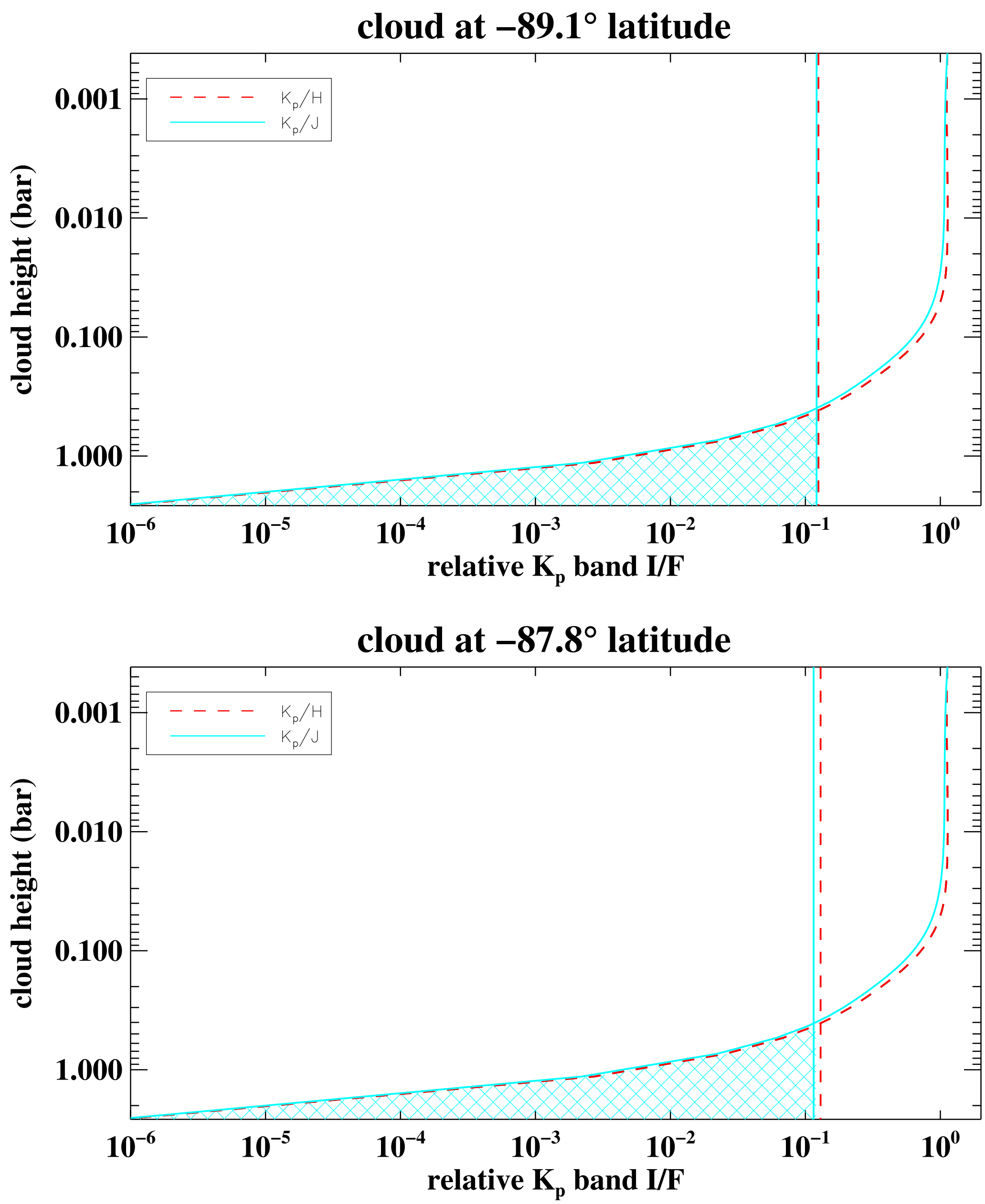

Figure 4.6: These plots show the model results for Kp/H intensity ratio (solid red) and Kp/J ratio (solid cyan) as a function of cloud altitude for each of the two cloud features from 26 July 2007. Dotted lines are at the maximum ratios allowed by the data, showing that the Kp/H ratio sets a stronger limit on the maximum cloud height than the Kp/J ratio. The allowed parameter space is cross-hatched.

4.5 Discussion

A small bright feature at Neptune's south pole has been consistently observed since the Voyager era, implying a stability that contrasts the short (∼hours) lifetime of most small cloud features at lower latitudes (Limaye & Sromovsky 1991). Our derived upper limit of the altitude of the circumpolar features observed here is consistent with clouds formed by the upwelling and condensation of methane gas, suggesting this may be a region of continuous cloud formation by convection.

The persistence of south polar cloud activity suggests that there is an organized circulation pattern at Neptune's south pole. Such a pattern has been inferred before: Hammel et al. (2007) show that there is a mid-IR temperature enhancement at Neptune's south pole, and Martin et al. (2008) find that the pole is warmer than its surroundings at microwave wavelengths as well. The latter authors suggest that a global dynamical pattern, in which air near the south pole is subsiding in both the stratosphere and troposphere, can explain the observed high temperatures at both the mid-IR and radio wavelengths. Subsiding motions will adiabatically heat the atmosphere, visible as elevated temperatures in the mid-IR. The subsiding air is likely 'dry', as condensable gases will condense out during the ascending branch of the dynamical pattern. Such dry conditions enables one to probe much deeper warmer levels at radio wavelengths, leading to temperature enhancement in microwave observations.

On Saturn, a south polar circulation cell has been observed, in the form of subsidence in a polar vortex surrounded by a region of upwelling (Fletcher et al. 2008). The structure of Saturn's south polar vortex (SPV) (Dyudina et al. 2009) possesses similarities with terrestrial hurricanes, such as a well-formed central eye, concentric eyewalls, and a surrounding ring of strong convection (Fig. 4.7). The region corresponding to the eye of the SPV is a hot, nearly circular region within a diameter of 4200 km around the south pole. The eye is mostly clear of clouds above ∼1 bar (Dyudina et al. 2008), and depleted in phosphine gas (Fletcher et al. 2008), suggesting that this is a region of subsiding air. Surrounding the eye is a ring of discrete, bright clouds in the lower troposphere, which may be analogous to the heavily precipitating clouds encircling the eye of terrestrial hurricanes (Dyudina et al. 2009). The similarity between the temperature enhancement at Neptune's south pole to the enhancement at Saturn's south pole (Hammel et al. 2007, and references therein) first led to the suggestion that Neptune, like Saturn, harbors a long-lived hot south polar vortex (Orton et al. 2007a). Our finding that Neptune's south polar cloud feature(s) may be indicative of rigorous convection near, but not at, the pole, supports the analogy between Neptune and Saturn's south polar environments.

The unexpected discovery of a vortex at Saturn's north (winter) pole (Fletcher et al. 2008) implies that polar vortices can exist despite considerable variations in seasonal insolation, and may be general features of giant planet atmospheres. However, possible analogues to Saturn's vortices have yet to be directly observed, as they await the measurement of polar wind speeds by high-inclination space missions. Further details about the morphology of

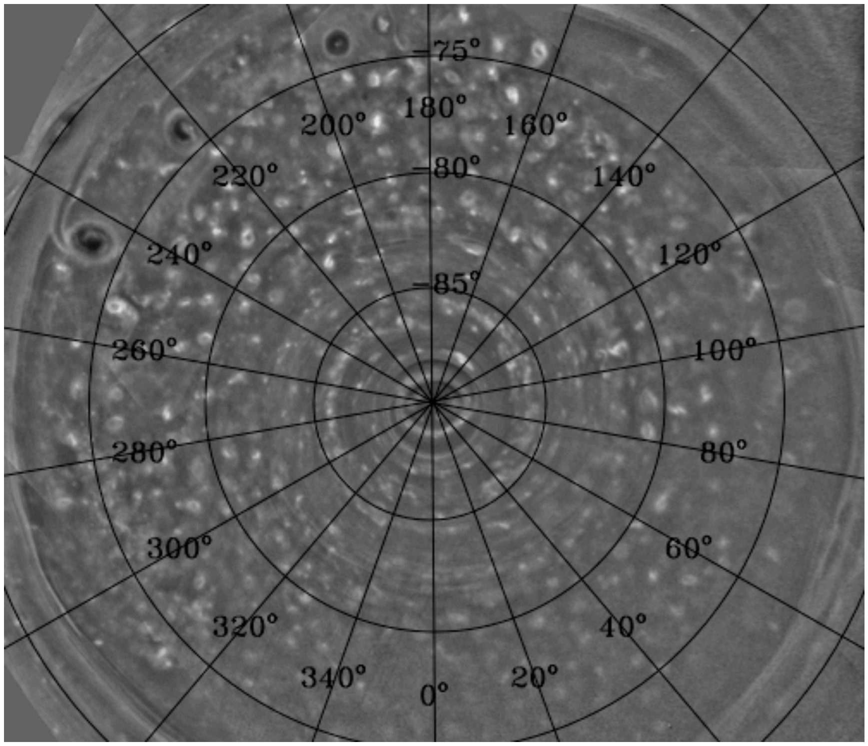

Figure 4.7: Map of Saturn's SPV [adapted from Dyudina et al. (2009)] illustrating the small, bright clouds encircling the storm's 'eye', many of which have the same general appearance between 2004 and 2006 observations. Dyudina et al. (2008) conclude these clouds are located in Saturn's lower troposphere.

clouds near Saturn's north pole may help us understand the types of cloud morphologies we might expect around polar vortices, and provide insight into how to interpret the behavior of Neptune's polar cloud features in the context of a possible vortex.

4.6 Summary

We have observed a transient double cloud feature near Neptune's south pole on 26 July 2007. The locations of the two features, as determined by the orbits of three of Neptune's moons, suggest they are both circumpolar clouds separated in latitude by $\sim 1.2°$. The single circumpolar feature seen on 28 July 2007 is at an intermediate latitude. Radiative transfer modeling indicates that the features on both days are at depths of greater than 0.4 bar, which is consistent with the formation of methane condensation clouds. The morphological change we observe on 26 July, combined with the location of the single cloud on 28 July, may indicate that the bright south polar spot seen since Voyager is not a single stable feature, but rather the signature of persistent cloud activity related to strong convection, perhaps in the region surrounding a polar vortex. Continued high-resolution observations of Neptune's south pole will provide more insight into the dynamics of this region. Such observations should be performed over several hours to capture the evolution of the features. We also await more high-inclination observations of planetary atmospheres to provide further context for understanding giant planet polar environments.

Acknowledgements

The data presented in this work were obtained with the W.M. Keck Observatory, which is operated by the California Institute of Technology, the University of California, and the National Aeronautics and Space Administration. The Observatory was made possible by the generous financial support of the W.M. Keck Foundation. This work was supported by the National Science Foundation Science and Technology Center for Adaptive Optics, managed by the University of California at Santa Cruz under cooperative agreement AST 98-76783. Further support was provided by NSF grant AST-0908575. HBH acknowledges support for this work from NASA grants NNX06AD12G and NNA07CN65A. The authors extend special thanks to those of Hawaiian ancestry on whose sacred mountain we are privileged to be guests. Without their generous hospitality, none of the observations presented would have been possible.

Chapter 5

Near-Infrared Observations of Neptune's Clouds with the OSIRIS Integral-Field Spectrograph

We observed Neptune in the near-infrared with the OSIRIS integral-field spectrograph on the 10-meter W.M. Keck II telescope. We present three-dimensional data cubes with a spatial resolution of 0.035"/pixel and spectral resolution of R$\sim$3800 in the H (1.47–1.80 μm) and K (1.97–2.38 μm) broad bands. On 26 July 2009 our observations covered more than 90% of the visible hemisphere in these filters. On 22 August 2010, a series of images were taken of the bright band of clouds at 30–45°S. Radiative transfer models were compared to the July 2009 data cubes in order to determine altitudes for ten bright features and three dark regions. We find that the observed spectra are generally well fit by models with three cloud layers: a stratospheric haze layer, a tropospheric haze layer and a low albedo, 2-bar optically thick bottom cloud. Our derived cloud altitudes are consistent with the north-south hemispheric asymmetry noted by previous authors (e.g. Gibbard et al. 2003). The highest altitude cloud appears to be at 40°N; the fit for this region places the stratospheric haze at 0.015 bar. At the other extreme, a bright feature at 60°S is well matched by a bright haze near the 2.0 bar depth of the bottom cloud. This is nearly 5 scale heights deeper than the northern stratospheric haze. Latitudinal variations are observed in the dark regions as well: dark areas near the equator and in the north are well fit with a 200 mbar haze whereas dark regions in the south are consistent with haze near the depth of the bottom cloud. The highest concentration of features can be found in a bright band extending from 30–45°S. We find that these features can all be fit by hazes at the same altitude, by varying only the haze particle densities. In contrast, we find that the two features near 60°S appear to be at very different altitudes.

5.1 Introduction

In the near-infrared (NIR), where we probe Neptune's stratosphere and upper troposphere, Neptune's active nature is perhaps most evident. Several distinct bright bands and cloud features stand out against a dark disk, particularly near 30–45°S (Figs. 5.1 and 5.2). These features act as both tracers and indicators of atmospheric chemistry and dynamics. Observations of individual clouds indicate that small-scale structures can change shape or dissipate on timescales as short as hours or even minutes (Limaye & Sromovsky 1991; Martin et al. 2012), while the planet as a whole exhibits decadal-scale trends that are not easily explained by seasonal models (Hammel & Lockwood 2007a).

The circulation on Neptune, as on all of the giant planets in our Solar System, is dominated by zonal jets. Efforts have been undertaken to track Neptune's zonal wind pattern by following the rotation of clouds (Limaye & Sromovsky 1991; Martin et al. 2012). These studies have found that, unlike for the other giant planets, where clouds at a given latitude appear to all move at the same speed, on Neptune cloud features at the same latitude appear to possess a wide range of velocities. One hypothesis is that the cloud features being measured are actually at different altitudes, where wind velocities differ. This would present a unique probe of Neptune's vertical velocity profile, a property that is difficult to measure on any giant planet (Tavenner et al. 2004; Pérez-Hoyos & Sánchez-Lavega 2006). However, the observed velocity dispersion is so great ($\sim$ 500 m s^{-1}) that vertical wind shear is unlikely to be sufficiently large. Knowledge of the variability of cloud altitudes for many features all at the same latitude could provide insight into the circulation patterns underlying the observed velocity variations.

Thermochemical equilibrium models indicate that Neptune's condensible gases should form a series of thick global cloud layers in the troposphere (de Pater et al. 1991a). Baines & Smith (1990) found that an optically thick cloud at 3.2–3.8 bar is required to match their full-disk molecular line observations. The composition of this cloud is presumed to be H_2S based on its altitude, though this has not been determined via direct observations. The existence of this thick cloud has been assumed as a starting point for several other analyses of Neptune's upper troposphere and stratosphere (e.g. Sromovsky et al. 2001b; Gibbard et al. 2003, Chapter 4). However, several observations have called into question the existence of a 3–4 bar optically thick cloud in the atmospheres of both Uranus and Neptune: Sromovsky et al. (2001a) state that if this cloud is really present and opaque on Neptune, it must have a very low single scattering albedo (less than 0.2 at 1.6 microns), and suggest that their data do not seem vary compatible with such a cloud. Karkoschka & Tomasko (2009, 2011) found that models of distinct cloud layers did not match their STIS Hubble data for Uranus and Neptune as well as models with extended cloud layers, with a total optical depth on Neptune of < 2 down to the 12-bar level.

Though the composition of Neptune's discrete bright cloud features is also difficult to measure directly, they are likely composed of methane ice, which in equilibrium condenses at a temperature of $\sim$ 80K, or roughly the 1-bar level. Vigorous convection could bring these clouds to higher altitudes. Methane has been observed to have an average stratospheric abundance that is well above the saturation value at the tropopause (Orton et al. 1992; Baines et al. 1995). This suggests that methane somehow leaks through the 'cold trap' of the tropopause to reach the stratosphere, perhaps at the south pole where the tropopause temperature appears to be warmer (Orton et al. 2007a). In the upper stratosphere, methane is photodissociated by solar ultraviolet photons, which results in the production of a variety of hydrocarbons. These hydrocarbons then sink and can condense into stratospheric hazes. Radiative transfer models can be compared to NIR spectra to derive properties of observed clouds (e.g. Gibbard et al. 2003; Max et al. 2003), in particular their altitudes and scattering properties. In 2002, Gibbard et al. (2003) measured K-band spectra for several features at various latitudes across the disk. They determined that the northern features were at altitudes of 0.023-0.064, as compared to 0.10–0.14 bar for features in the 30–60°S band. Sromovsky et al. (2001b) found the altitudes of three cloud features: one in the north at 60 ± 20 mbar, one at 45°S at 230 ± 40 mbar and one at 30°S at 190 ± 40 mbar. Similar observations by Roe et al. (2001) and Max et al. (2003) derived consistent patterns of altitudes for a few features. All of these observations exhibit a trend of features in the northern hemisphere at higher altitudes than those in the south. Gibbard et al. (2003) suggest this might imply a different origin for the different features – perhaps southern mid-latitude features are methane haze circulated from below, while northern bright features are due to the subsidence of stratospheric haze material. Alternatively, this pattern could suggest seasonally driven differences in the temperature of the atmosphere, as is seen on Saturn.

Traditional slit spectroscopy does not facilitate the clean separation of individual features from the quiescent background. The resulting confusion translates into an uncertainty in cloud altitudes and other properties. Integral-field spectrographs, which are capable of producing three-dimensional data cubes (x, y, and wavelength), offer a strong advantage for studying the properties of individual clouds. OSIRIS, the near-IR AO-assisted integral field spectrograph on the 10-m Keck telescope, is capable of obtaining spatially-resolved spectral information over a significant fraction of Neptune at once, allowing us to address this major obstacle. On 26 July 2009 we imaged over 90% of Neptune's disk with OSIRIS. These observations were followed up in 22 August 2010 by a set of observations of Neptune's southern bright band.

In September 2009, Irwin et al. (2011) performed a similar set of observations in H band only with the Near-Infrared Integral Field Spectrometer (NIFS) instrument on the 8.1-m Gemini-North Telescope. They do not use an optically thick 3.8 bar cloud in their models. Instead, they find a thin, variable-opacity ($\tau = 0.1 - 0.6$) 2-bar bottom cloud and a variable-altitude upper cloud match their data well at all locations. Their upper cloud is determined to be at an altitude of 0.02–0.08 bar in the southern bright band, and as deep as 0.2 bar near the equator. They do not report a general trend of higher clouds in the north; in fact, the altitude variations in their retrieved latitudinal cloud profiles appear roughly symmetrical relative to the equator (though with higher cloud densities in the south). However, their data do not extend to the longer wavelengths of K band (2–2.4 μm), where high-altitude features are distinguishable (Chapter 4).

In this chapter, we present our three-dimensional OSIRIS data. One primary advantage of our data over the Irwin et al. (2011) study is that we have both H-band and K-band data cubes, which improves our ability to determine cloud altitudes and increases our sensitivity to high-altitude features. Using our radiative transfer code, described in Appendix B, we fit spectra to determine altitudes for several bright and dark regions. We evaluate whether clouds in the north are consistently higher in altitude than those into the south, and relate our findings to the global circulation. We also compare the altitudes of features at the same latitude in order to determine if these clouds show altitude variability that could be tied to the observed dispersion in Neptune's cloud velocities.

5.2 Observations and data reduction

We present H- and K- broadband spectral data cubes of Neptune, taken on 26 July 2009 and 22 August 2010 with the near-infrared imaging spectrometer OSIRIS on the 10-meter W.M. Keck II telescope. We selected an instrumental plate scale of 0.035"; at this resolution a 0.56"×2.24" patch of the sky is sampled with each exposure. The light passing through each individual lenslet is diffracted, producing a moderate resolution (R∼3800) spectrum at each of 1019 locations.

Table 5.1: Observations

Date	Start Time (UTC)	Filter	Airmass	T_{exp} (sec)	# frames
26 July 2009					
Neptune	12:02	K	1.19	300	8[a]
SAO164840	12:53	K	1.21	45	2
SAO164840	12:56	H	1.22	45	2
Neptune	13:10	H	1.26	300	8[a]
22 August 2010					
Neptune	12:14	H	1.38	300	2[b]
Neptune	12:27	K	1.42	300	2[b]
Neptune	12:39	H	1.48	300	1
Neptune	12:44	K	1.51	300	1
Neptune	12:51	H	1.55	300	1
Neptune	12:57	H	1.59	300	1
HD220825	13:14	H	1.13	2	2
HD220825	13:14	K	1.14	2	2

[a]first and last frames are sky frames
[b]second frame is sky frame

On 26 July 2009, Neptune had an angular diameter of 2.34" and was 29.09 AU from Earth. At this distance, each 0.035" pixel corresponds to 740 km at disk center. We oriented the exposures so that the long direction of each frame pointed east-west (parallel to the equator) along the planet. Because Neptune's diameter is slightly larger than the length of each frame, we elected to not observe the western limb of the planet. A set of eight 300-second exposures were taken in each of H and K broad bands. Features rotated 800 km during a single exposure, which is 1.1 pixels at disk center. The first and last of each set were 'sky' frames, to be subtracted from the data frames during processing. The remaining frames were positioned on Neptune in a series of horizontal slices starting at the south pole and stepping across the disk until the northern limb was reached. In several cases the instrument did not dither as requested; when this occurred the data were re-observed immediately following the end of the original set of exposures.

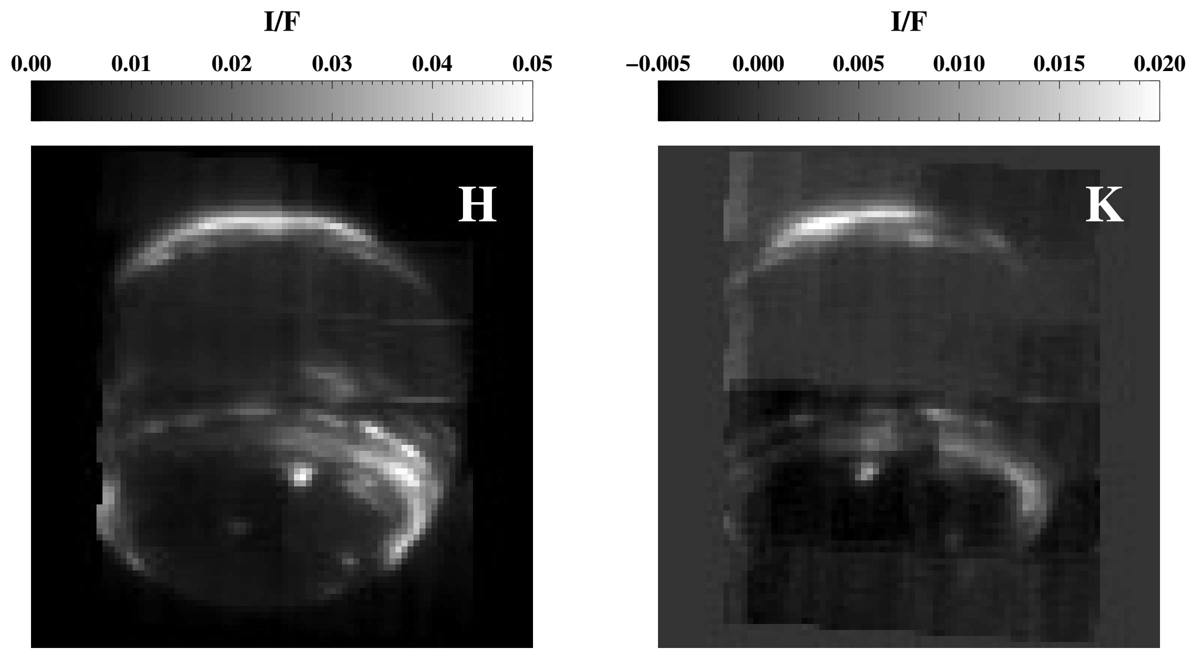

Figure 5.1: Mosaicked and calibrated 26 July 2009 data cubes, averaged over wavelength. Color bars indicate average reflectance, in units of I/F.

On 22 August 2010, we focused our observations on a strip of Neptune's southern hemisphere (centered at roughly 35°S). We took four 300-second exposures in H band and two in K band, spanning a total time of about 45 minutes ($\sim 15°$ rotation). A sky frame was taken after the first science exposure in each band.

Initial data reduction proceeded using version 2.3 of the OSIRIS data reduction pipeline[1],

[1]http://irlab.astro.ucla.edu/osiris/pipeline.html

which performs sky subtraction, cleans the data of cosmic rays and common instrumental issues, extracts spectra from the raw frames and assembles output data cubes. The pipeline also mosaics multiple exposures into a single cube when desired.

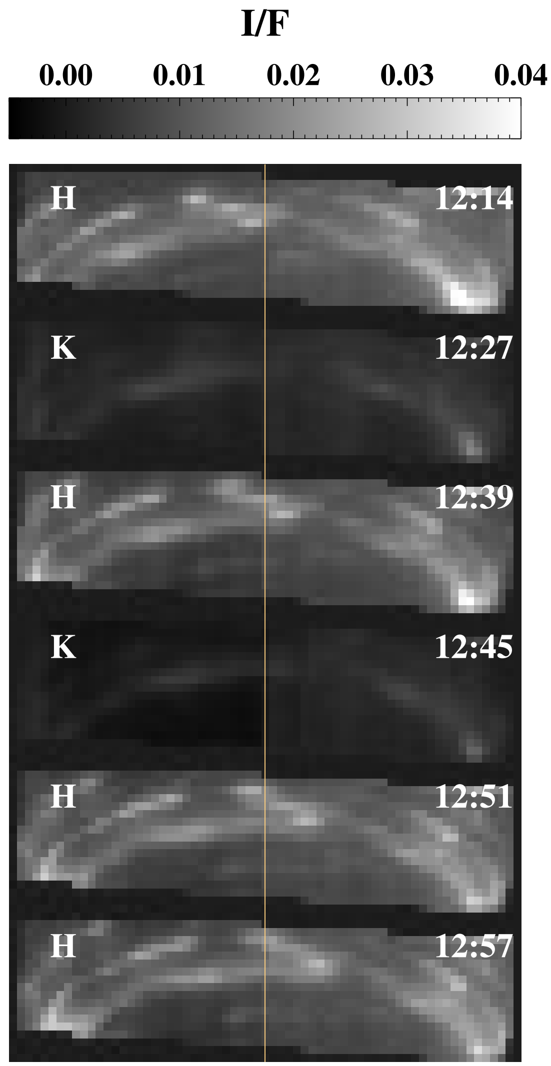

Figure 5.2: Series of data cubes, observed at the same location on Neptune's disk in H and K bands. Time (UT) of each individual strip is indicated; a thin vertical line has been added to aid the eye in observing the motions of features over time.

During both nights, one or more A0-type stars with known J, H, and K magnitudes were observed, to serve as telluric and photometric standards (Table 5.1). We use for calibration the star observed under the most similar atmospheric conditions (in time and airmass) to our science target. Two exposures were taken of each star, dithering between the two halves of the array so that the two exposures could serve as sky frames for one another. After processing the data with the OSIRIS pipeline, we calibrate our Neptune data cubes using the calibrator star spectra. Each stellar spectrum is extracted using aperture photometry, then divided by a model of an A0 spectrum that is calibrated to the 2MASS J, H and K magnitudes (Castelli & Kurucz 2004) and adjusted for reddening (Fitzpatrick & Massa 1999). Each pixel in the science data cubes is then divided by this stellar spectrum to correct for telluric lines and convert from units of counts into units of flux density. Finally, we convert the data from units of observed flux density to units of I/F, which is defined as (Hammel et al. 1989):

$$\frac{I}{F} = \frac{r^2}{\Omega}\frac{F_N}{F_\odot}$$

where r is Neptune's heliocentric distance, $\pi F_\odot$ is the sun's flux density at Earth's orbit (Colina et al. 1996), F_N is Neptune's observed flux density, and Ω is the solid angle subtended by a pixel on the detector. By this definition, $I/F = 1$ for uniformly diffuse scattering from a Lambert surface when viewed at normal incidence. These reduced and calibrated data are shown in Figs. 5.1 and 5.2, averaged over wavelength.

We determine planetocentric latitude, longitude and μ for each pixel in our data by fitting the limb of the planet by eye as best as possible, where $\mu = \cos\theta$ with θ defined as the angle between the line of sight and local vertical. This approach is probably accurate at the 1–2 pixel level for our full-disk data, but inaccurate for the 2010 strips. We use the JPL Horizons ephemeris information[2] for sub-observer latitude and longitude at the time of the observations.

5.3 Modeling

We produce model spectra using a 300-layer two-stream radiative transfer code, which is described in detail in Appendix B. We adopt the temperature profile derived by Fletcher et al. (2010) throughout the atmosphere. Temperature variations, such as those discussed in Chapter 3 could certainly affect the spectrum, but are neglected here. We assume a mixing ratio of 0.15 for He and 0.003 for N_2. The CH_4 abundance follows Fletcher et al. (2010) and remains at a mole fraction of 0.022 in the troposphere below the condensation level. The gas opacity at these wavelengths is dominated by H_2 collision-induced absorption (CIA) and CH_4 opacity. For CIA, we use the coefficients for hydrogen, helium and methane from Borysow et al. (1985, 1988); Borysow (1991, 1992, 1993), assuming an equilibrium ortho/para ratio for H_2. For methane, we use the correlated-k method. In choosing which of the published CH_4 coefficients to adopt, we follow the recommendations by Sromovsky et al. (2012) for outer planet NIR spectra.

[2] http://ssd.jpl.nasa.gov/?horizons

We assume in the nominal case that the bottom cloud is optically thick and set the depth of the cloud to 2 bar (see Section 5.4). We set the Henyey-Greenstein asymmetry parameter of the bottom cloud to -0.1 (preferentially backscattering) and adjust the single scattering albedo to match the data as in Chapter 4. Aerosols (both hazes and clouds, which are handled identically) are treated as Mie scatterers: we assume that ensembles of particles are distributed according to

$$n(r) \propto r^6 \exp\left(-6 \cdot r/r_{\max}\right)$$

where $n(r)$ is the number density of particles of radius r and $r_{\max}$ is the maximum in the particle distribution (Hansen & Pollack 1970). Characteristic sizes of $r_{\max}= 0.1$ to 2.0 μm are tested, and for each size, the extinction cross section and Henyey-Greenstein asymmetry parameter of the scattering (Figs. 5.3 and 5.4) are calculated using Mie theory. The number density of cloud particles at the bottom (maximum) pressure of each haze/cloud is a free parameter; we assume that the particles have a scale height that is 0.5 times the gas scale height.

For this preliminary analysis, we modeled only the 26 July 2009 data cubes. We adjusted

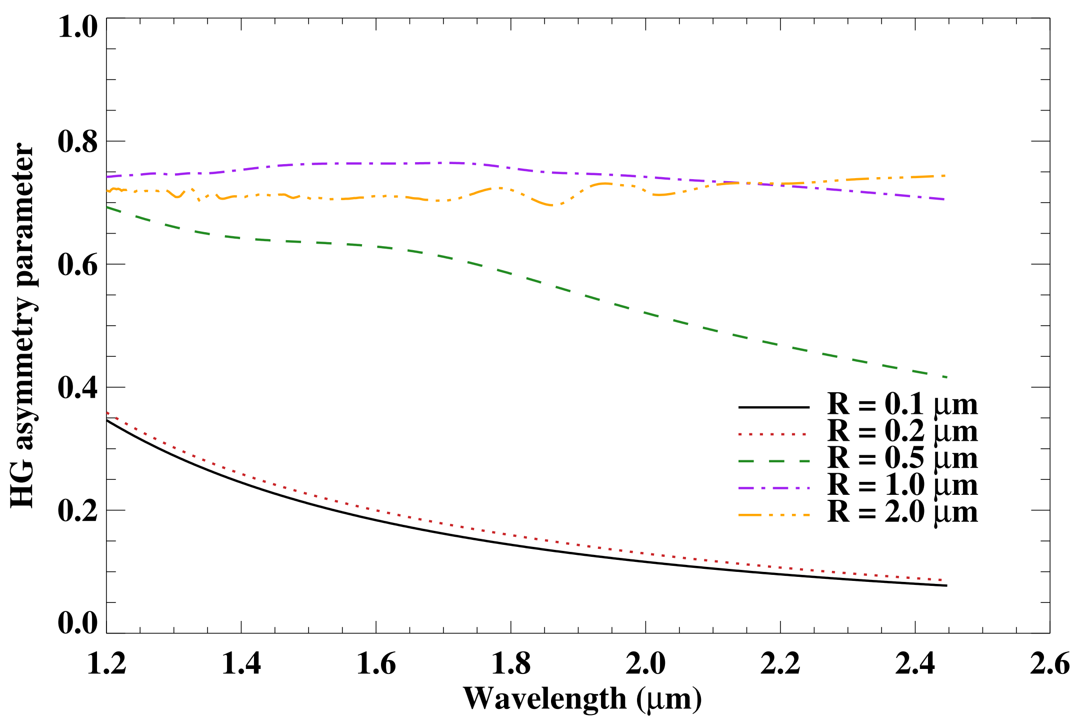

Figure 5.3: Asymmetry parameter as a function of wavelength, for several different particle sizes. R is the particle size of the peak in the distribution, in microns.

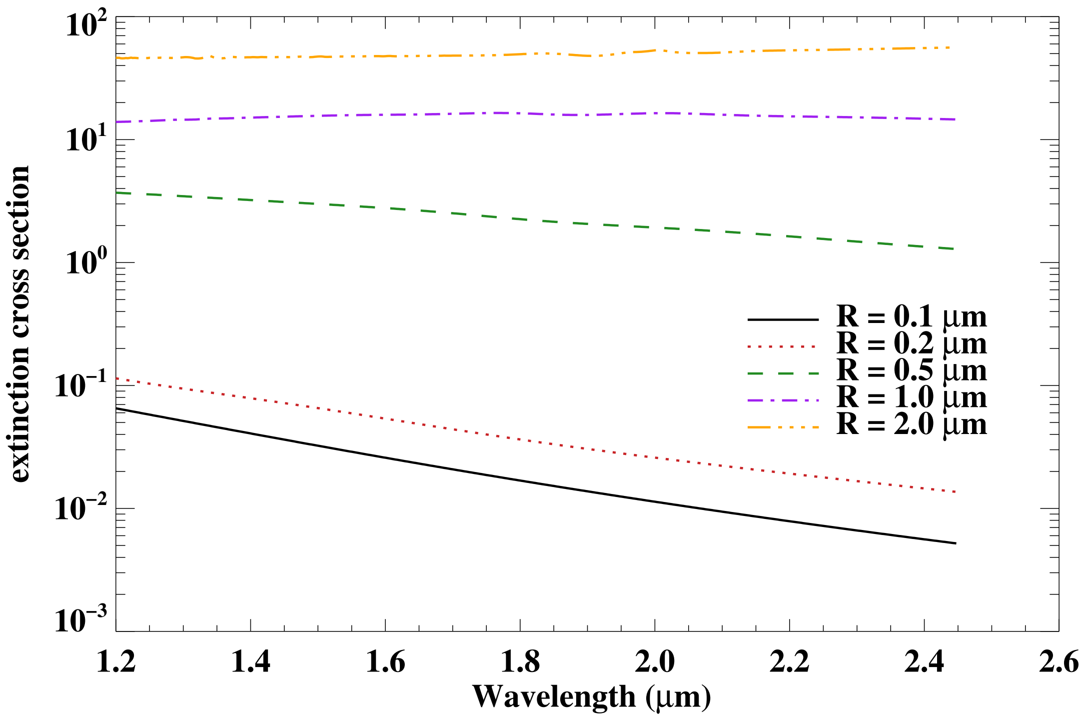

Figure 5.4: Average extinction cross section as a function of wavelength, as calculated from Mie theory for the particle sizes specified in Fig 5.3. Extinction cross section is the geometric cross section multiplied by the extinction efficiency.

the parameters of models by hand; our goal was to observe trends in the cloud/haze altitudes, rather than precisely model their absolute properties. The main free parameters of our fits are the particle size, bottom pressure and density of each haze. In each case, we initially attempt to fit features with a single haze positioned above the bottom cloud. When the fit is poor, we add a second haze layer. In the following sections, we present the disk-averaged spectrum, followed by spectra for three dark regions and ten bright regions in our full-disk cubes from 26 July 2009.

5.4 Disk-averaged spectrum

We average our 26 July 2009 data cubes over the full disk, which we compare to the medium-resolution spectrum from the IRTF Spectral Library taken with the SpeX instrument on the NASA Infrared Telescope Facility (IRTF) on Mauna Kea (Rayner et al. 2009) (Fig. 5.5). We find that the two spectra show remarkable agreement. In Chapter 4 we present a simple model that matches the SpeX data set fairly well. Here, we investigate

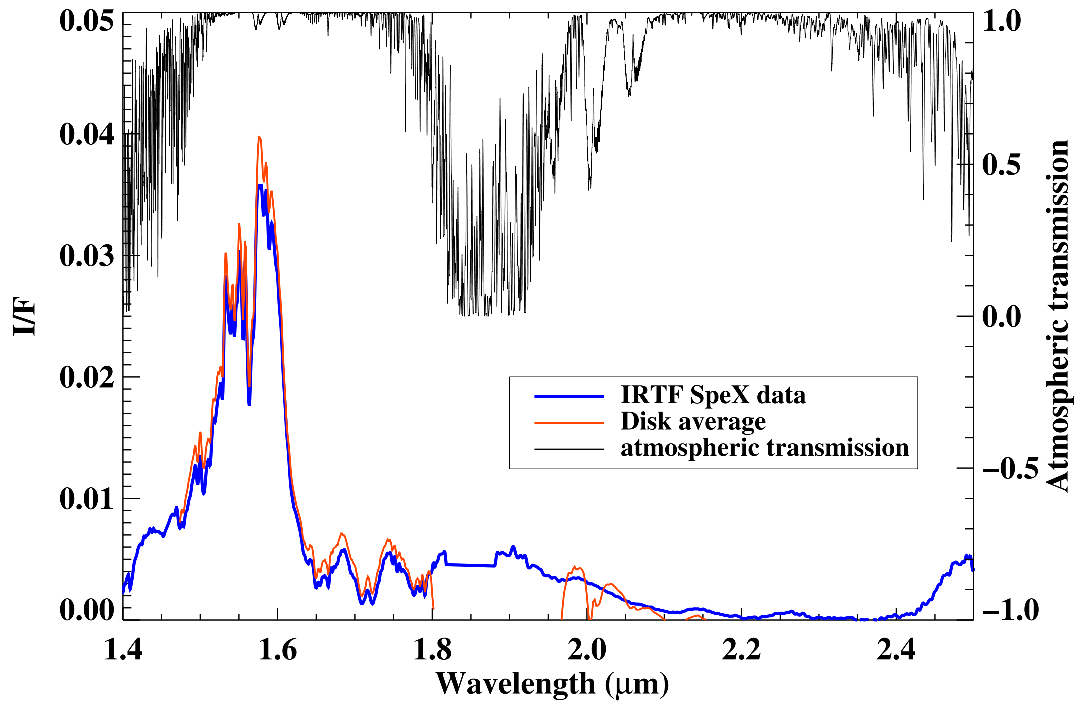

Figure 5.5: Spatial average of our 26 July 2009 data cubes (red), compared with the IRTF SpeX spectrum (blue). A transmission spectrum of Earth's atmosphere is shown at the top (Lord 1992)

whether a 2 bar or 4 bar bottom cloud gives a better fit. We find that the data agree better with a 2 bar bottom cloud. This is consistent with the result of Irwin et al. (2011), but not with the earlier Baines & Smith (1990) result.

To match their H-band data, Irwin et al. (2011) model each bright feature with a single layer of aerosols between 0.02 and 0.08 bar, above their 2-bar bottom cloud. We compare models with a single haze in this region to models with two hazes. We find that a second haze layer dramatically improves the fit to the SpeX data at longer wavelengths. In general, we find that two hazes are required to match our data at most locations, when the K-band data are considered (Fig. 5.6).

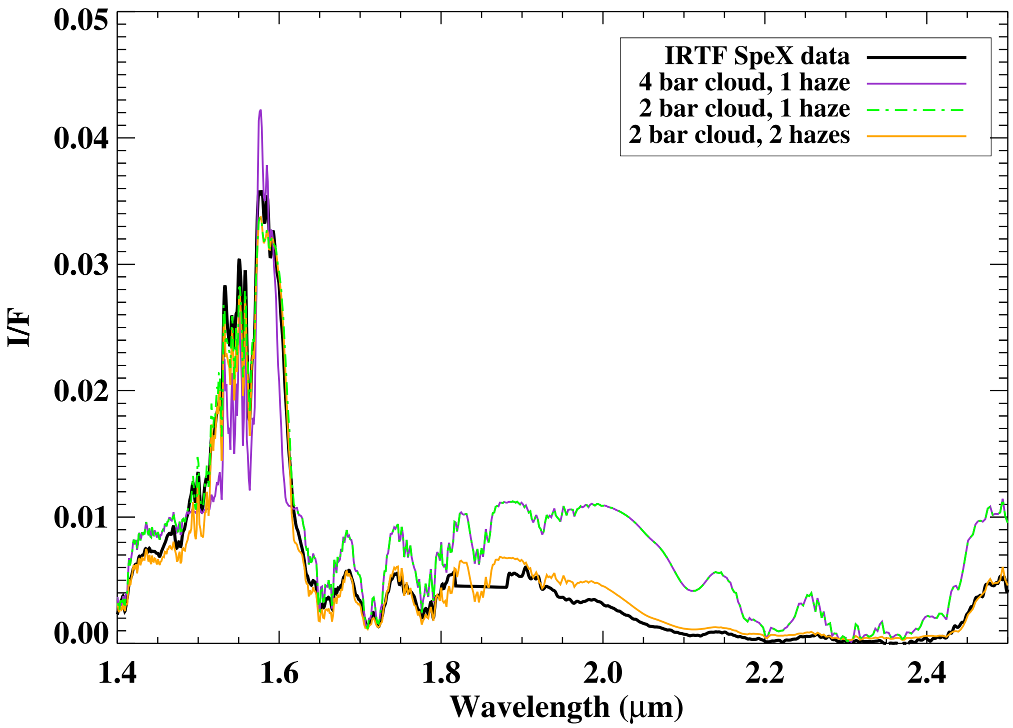

Figure 5.6: Models with a 4 bar (purple) and 2 bar (green dashed) bottom cloud; a 2 bar cloud fits the data better near 1.5 microns. We also show a two-haze model (orange), illustrating the improvement in the fit with the addition of a second haze to the model, particularly at longer wavelengths.

5.5 Discrete features – 26 July 2009

Figure 5.7 shows the wavelength-averaged July 2009 H and K band data with latitude and longitude lines indicated. We also identify several regions of interest that are studied in more detail. Each location was first selected from the H band image and then where possible, identified in the K band image. The locations (latitude, longitude, μ) of these features are listed in Table 5.2.

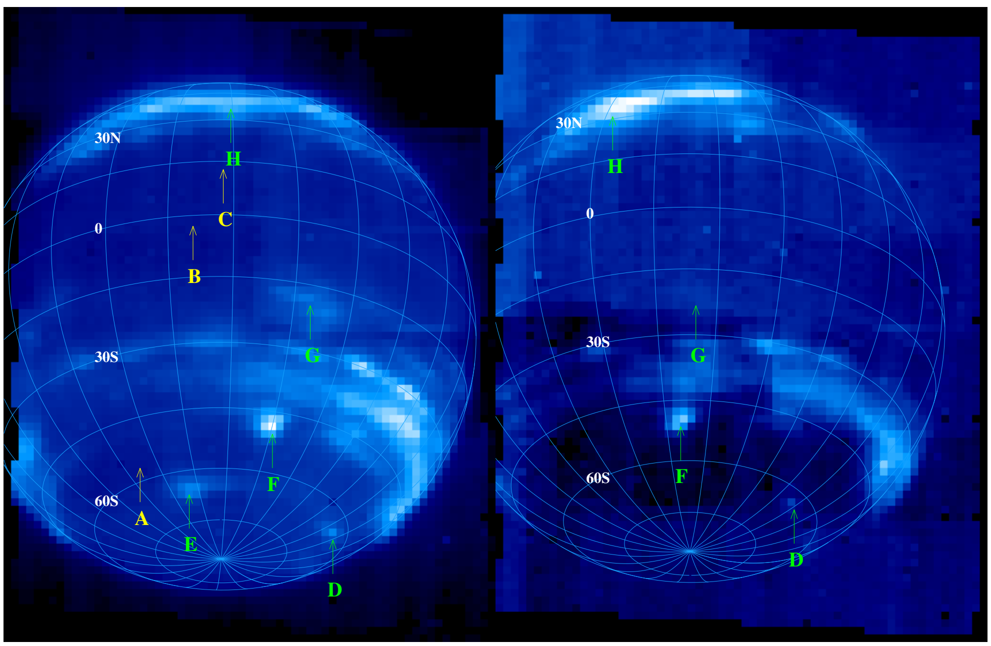

Figure 5.7: Wavelength-averaged 26 July 2009 data cubes. Latitude and longitude lines have been added for reference; the locations of several modeled regions are indicated. Regions A–C are dark areas; Regions D–H are bright features.

Table 5.2: Locations of modeled regions. Locations were determined by eye in the H- and K-band data cubes, which are separated in time by about one hour.

Feature	H band location			K band location		
	latitude	longitude	μ	latitude	longitude	μ
A	−56	189	0.78	−60	155	0.80
B	−1	160	0.88	−3	129	0.91
C	+15	153	0.73	+13	122	0.76
D	−65	63	0.43	−65	61	0.58
E	−66	173	0.77			
F	−50	136	0.90	−51	131	0.92
G	−19	132	0.94	−22	126	1.00
H	+40	151	0.38	+36	150	0.38
a	−31	193	0.81			
b	−31	158	0.99	−32	155	0.90
c	−39	134	0.95	−42	131	0.97
d	−31	114	0.83	−32	108	0.96
e	−39	95	0.67	−40	96	0.88

5.5.1 Dark regions

As is typical for Neptune, we find that cloud activity is focused in particular latitude bands, while other latitude regions appear free of discrete and/or bright features. We identify three feature-free regions to study: these are labeled A–C in Fig. 5.7. The spectra for these locations are shown in Fig. 5.8, relative to the disk-averaged spectrum. Since these regions are so dark, the signal in K band was consistent with noise and not included here. It is immediately noticeable that the spectrum in Region A, which is located at 55–60°S, has a different morphology than Regions B (equator) and C (15°N). We find that Region A can only be modeled with a very deep (1–2 bar) haze, with no other cloud or haze opacity above it. The model fit is shown in Fig. 5.9, along with a plot of the model haze optical depth as a function of pressure. Regions B and C can both be modeled with a thinner haze at higher altitude (200 mbar – Fig. 5.10).

Since the region between −10° and +20° appears featureless in both H- and K-band wavelength-averaged images, we look at the behavior of the data in this latitude region and the model for Regions B and C as a function of emission angle. In particular, we are interested in whether the limb brightening of the data favors an optically thick or optically thin bottom cloud. As mentioned in Section 5.1, several recent papers favor models with an optically thin cloud, in contrast with the results of Baines & Smith (1990). Figure 5.11 illustrates our model from Fig. 5.10, which assumes an optically thick bottom cloud, at several different emission angles. We also show a similar fit to Regions B and C that was made using an optically thin bottom cloud. In the bottom panel, we show the data from −10° to +20° binned in intervals of μ; each bin has a width of 0.1 and the bin centers are at intervals of 0.2 in μ. For reference, features B and C are both near $\mu = 0.9$, where the

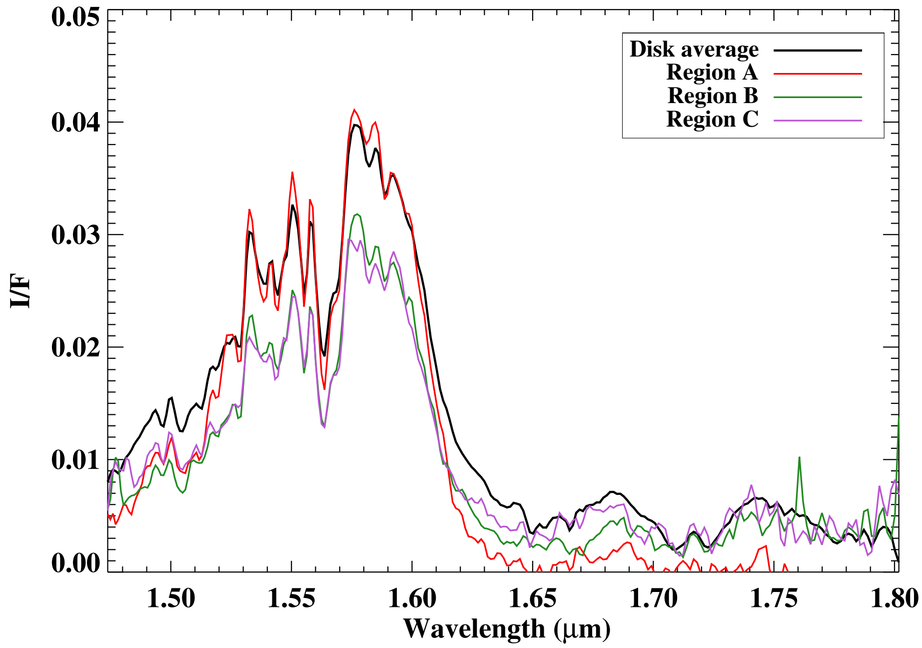

Figure 5.8: Comparison of spectra for Region A in the south (red) to Regions B (equator – green) and C (northern hemisphere – purple) in H band only (the K band data in these regions were consistent with noise). The disk-averaged spectrum is also shown.

data and both models appear to agree, except at 2.0 μm where the I/F of the averaged data is much lower than we would expect for either of the test models. Towards the limb, the data and models appear to diverge. We plot the reflectance of the data and models as a function of μ at three different wavelengths (indicated in Fig. 5.11): we observe that both the optically thin and optically thick bottom cloud models appear to limb-brighten, whereas the data appear to limb-darken at these latitudes (Fig. 5.12). Further exploration of the model parameters is required to better constrain the spectrum at these latitudes; we expect that this work will also improve models of bright features.

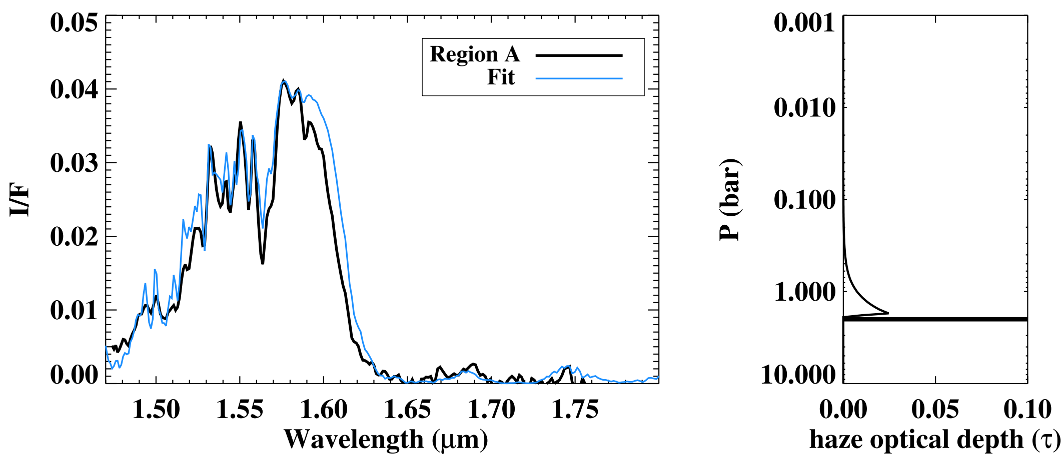

Figure 5.9: Spectrum for Region A (black) and a model fit. Model haze optical depth as a function of altitude is shown to the right. The thick black line indicates the location of the optically thick bottom cloud, used in all models.

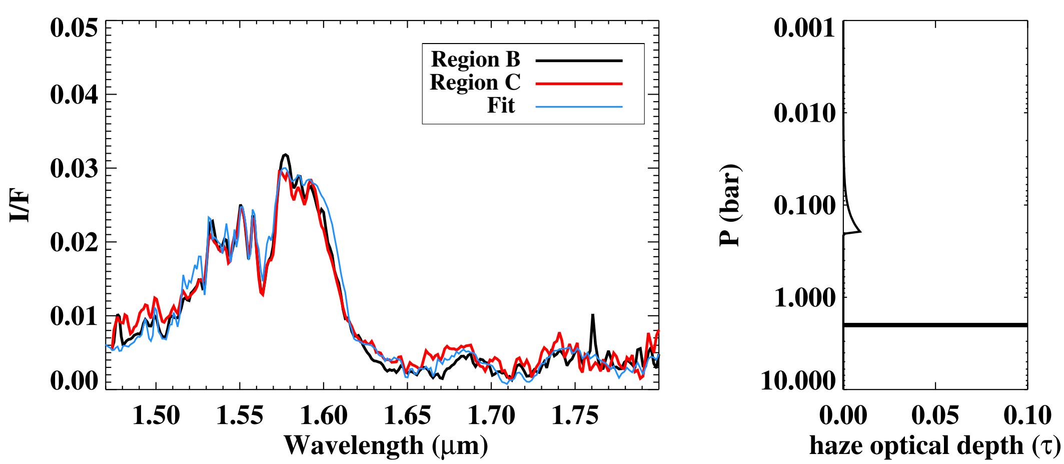

Figure 5.10: Spectra for Regions B (black) and C (red), and a model to fit both (blue). Model haze optical depth as a function of altitude is shown to the right.

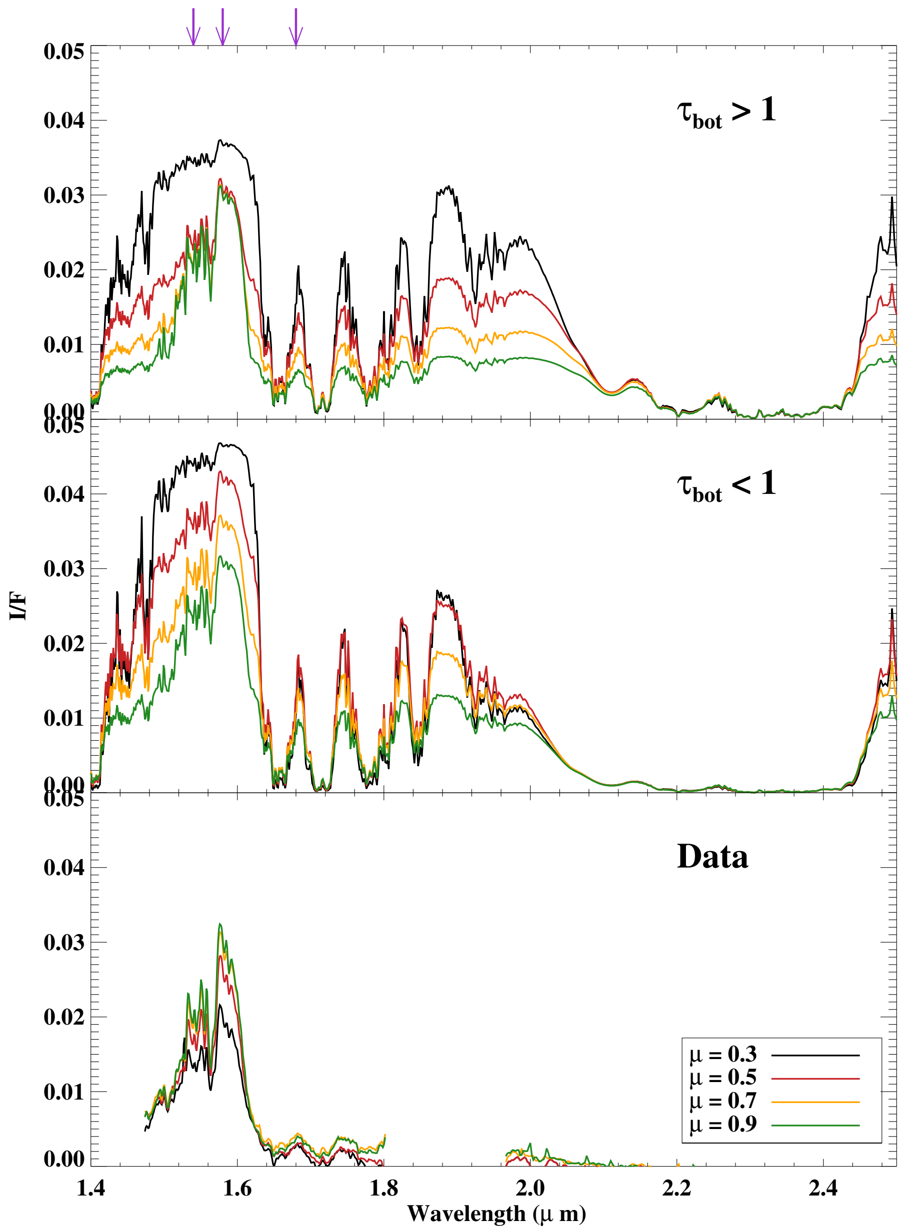

Figure 5.11: Behavior of model in Fig. 5.10 with changing μ (top). In the middle panel, the Region B/C spectra are fit using a model with an optically thin bottom cloud. In the lower panel, the data between 10°S and 20°N have been averaged in several μ bins. Center-to-limb profiles for the wavelengths indicated by arrows at the top of the plot are shown in Fig. 5.12.

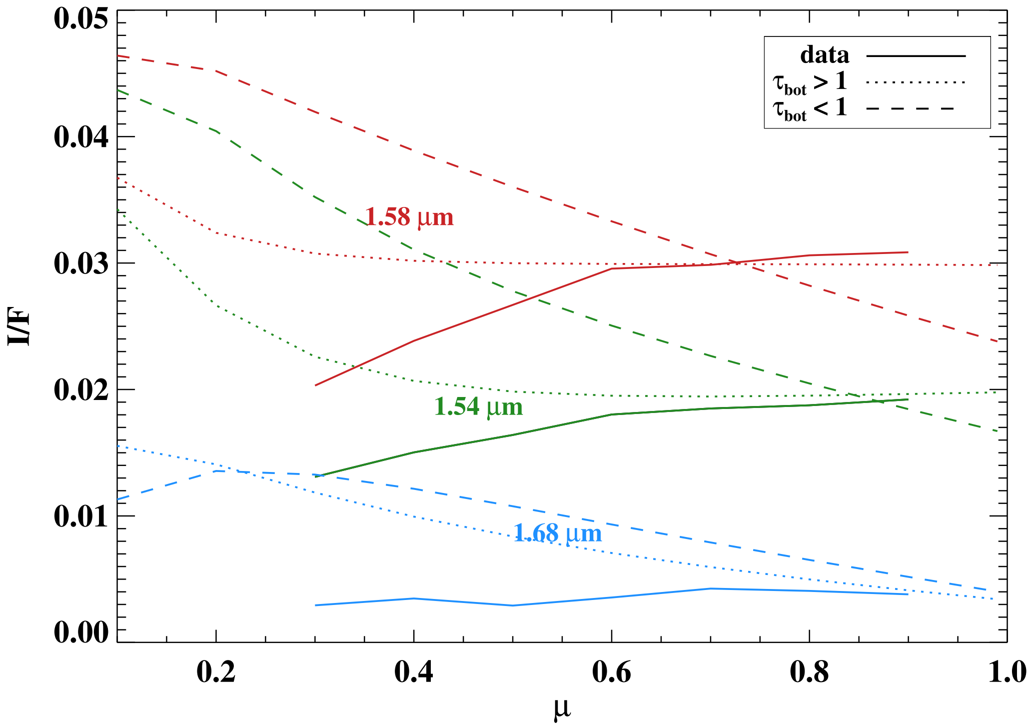

Figure 5.12: Reflectance as a function of μ at the wavelengths indicated in Fig. 5.11. These plots show that the data appear to darken towards the limb ($\mu = 0$), whereas the two models appear to limb-brighten.

5.5.2 Discrete features

We identify 10 additional regions in the H-band cube to model, corresponding to discrete bright features, Labeled as D–H in Fig. 5.7 and a–e in Fig. 5.13. In all but two cases, we were able to identify these same features in the K-band dataset and produce a combined spectrum.

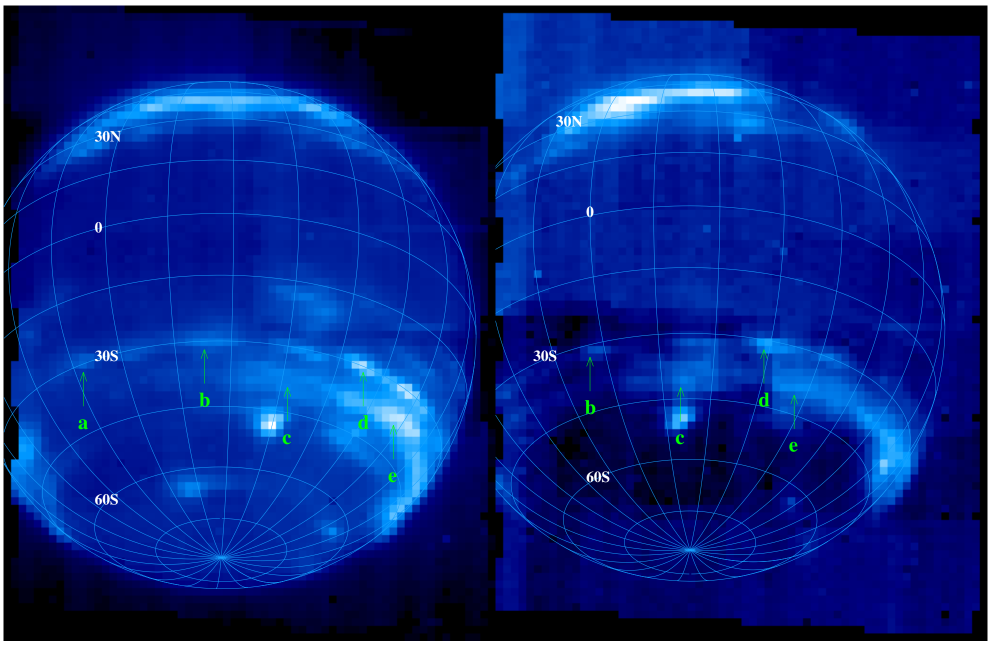

Figure 5.13: Same as Fig. 5.7, identifying five features within the southern bright band that are modeled.

Features D and E are both at a latitude of 65°S, and appear very similar in the wavelength-averaged cube. However, we observe that their spectra are quite different (Fig. 5.14). Region E is brighter at 1.6 μm, but its reflectance falls off dramatically at longer wavelengths. In contrast, Region D remains bright enough to be identified in the K band cube. The Region E spectrum is reminiscent of that of dark Region A, and is best fit with an optically thick bright haze just above the bottom cloud at 2 bar. Region D, in contrast, is fit with a combination of an optically thin ($\tau \sim 0.2$) deep (1.3 bar) bright haze and a very thin ($\tau \sim .03$) 0.05-bar haze. We note that we were not able to match the K-band data in Region D at all with this model. Irwin et al. (2011) also found what they referred to as 'localized bright spots' near 60°S in their data.

Regions F and G straddle the bright band of clouds at 30–45°S. Feature F has the highest peak H-band reflectance of any location in our July 2009 dataset. We model it as a tropospheric $\tau \sim 0.7$ haze at 0.5 bar and a second $\tau \sim 0.2$ haze at 0.02 bar (Fig. 5.15). For Region G, we find that using the same $\tau \sim 0.7$ haze at 0.5 bar but a deeper (0.08 bar),

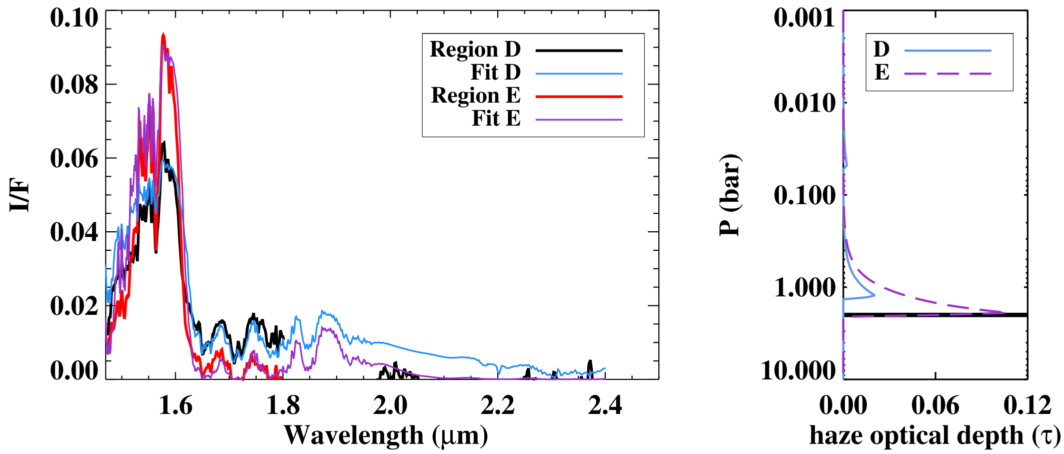

Figure 5.14: Spectra for Regions D (black) and E (red), both near 65°S. Models (blue and purple, respectively) are shown as well; Model haze optical depth as a function of altitude is shown to the right.

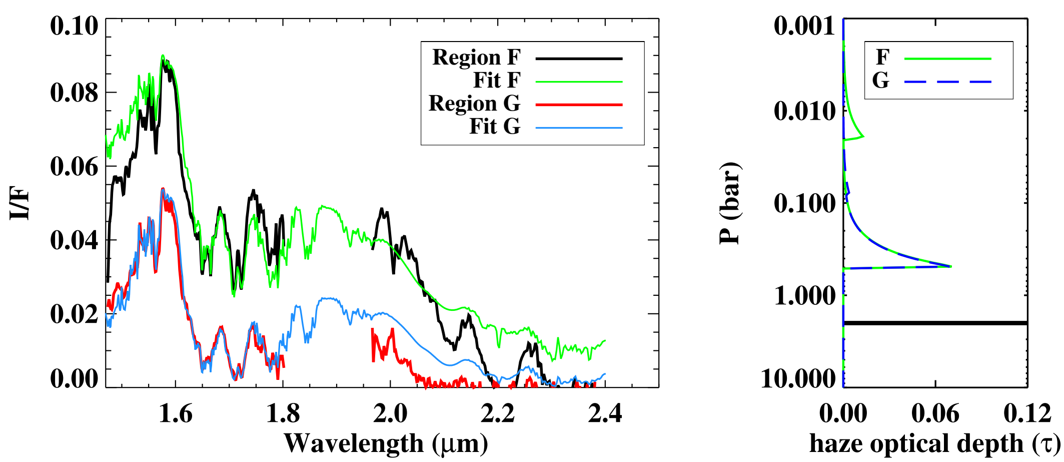

Figure 5.15: Spectra and models for regions F and G, which straddle the southern bright band. Model haze optical depths as a function of altitude are shown to the right.

thinner ($\tau = .04$) upper haze gives a reasonable match to the data in H band. We note that these fits are not as successful at matching the K band data.

Within the southern bright band, which is itself comprised of several zonal bands of clouds, we identify five additional features for study (Fig. 5.13): features a, b, and d are part of a narrow band at 30°S; features c and e are at 40°S. Figure 5.16 illustrates that the spectra for all five of these features have a very similar morphology to one another and to the spectrum for Region G. Under the hypothesis that a 0.5-bar haze extends across the entire southern bright band, we attempt to model all five of these features with a Region G-like haze structure. We find this approach very successful, and find 80 mbar haze opacities of $\tau \sim 0.01$–0.1 and 0.5 bar haze opacities of $\tau \sim 0.3$–0.7.

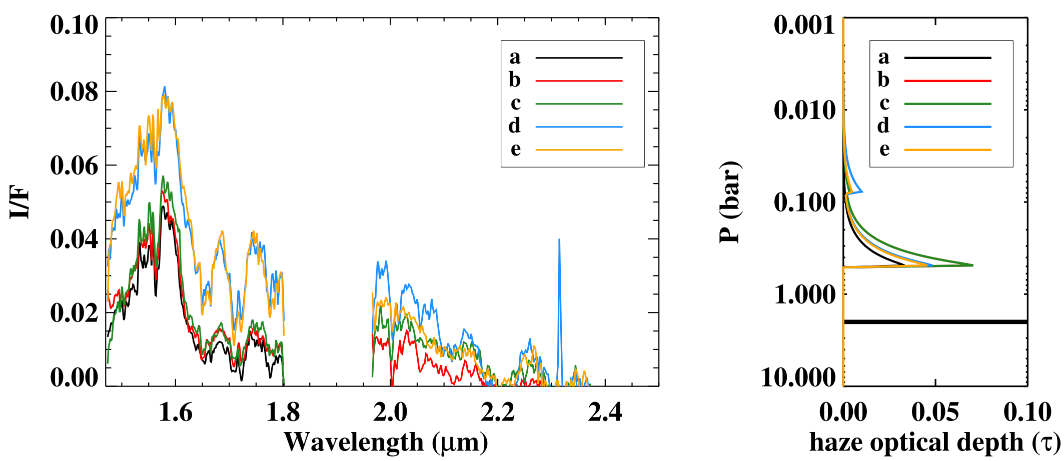

Figure 5.16: Spectra for five features in the southern bright band. For simplicity, model fits are not shown, but solutions for the model haze optical depths are shown to the right. The altitudes of both hazes are held constant between features, though the haze density varies.

Perhaps the most unique of our spectra is that for Region H, the K-band bright feature near 40°N. We model this feature as a second haze above a 0.2 bar haze like that found in the fit for dark Regions B and C. Our best fit has this second haze at 0.015 bar, the highest of any of our fits. However, this fit differs significantly from the data at several wavelengths.

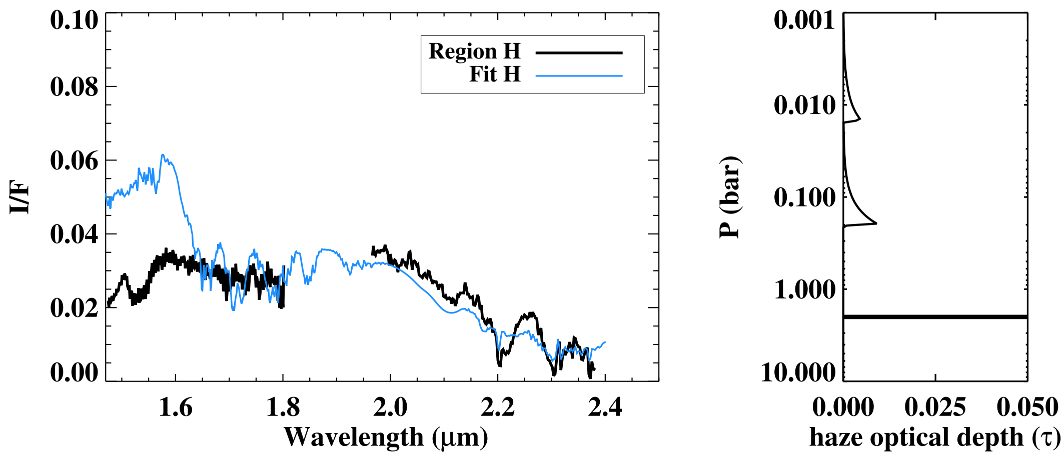

Figure 5.17: Spectrum and model for Region H, the northernmost cloud feature and brightest feature in K band.

5.6 Summary and conclusions

We have observed Neptune in the H- and K- NIR bands with the OSIRIS integral field spectrograph, yielding moderate resolution spectra at every location across more than 90% of Neptune's visible hemisphere. We find that the cloud/haze structure must be more complex than the two-layer models of previous studies (e.g. Irwin et al. 2011), if we are to match the H- and K- band data simultaneously. We note that Gibbard et al. (2002) also favored a three-layer (two hazes plus a bottom cloud) model over a simpler two-layer model for their narrowband imaging data; Karkoschka & Tomasko (2011) suggested a haze structure of even greater complexity, with four distinct haze altitude regions in the troposphere and discrete clouds near the tropopause. For our models, we adopt a three-layer structure consisting of an optically thick bottom cloud and two additional scattering layers. We find that the bottom cloud layer, which has often been assumed to be located at 3.8 bar, fits our data better at 2.0 bar. This is similar in altitude to the bottom cloud layer determined by Irwin et al. (2011).

The details of Neptune's cloud structure above this bottom cloud appear to vary with position, even between regions that appear dark in the wavelength-averaged H- and K-band images. We find that dark regions near the equator and in the northern hemisphere (Regions B and C) may be fit by an optically thin haze at 200 mbar, whereas the dark region in the southern hemisphere (Region A) appears to be mostly clear of hazes above the 2.0 bar level.

With one exception (Region E), we find that our model fit solutions for bright regions possess a tropospheric haze and a thinner stratospheric haze component. We wished to determine if features in the same latitude band appear to have the same altitude. We find that all of the features in the southern bright band between 30 and 45°S can be fit using nearly the same haze model, by varying only the number density of the haze particles in each of the two haze layers. In contrast, the two features at 60°S appear to have very different properties. Region E is best fit by an optically thick, bright cloud down at the 2 bar level, whereas region D appears to have at least some haze in the stratosphere.

The general finding that aerosols in the north tend to be higher than those in the south appears to be upheld in our data. The brightest feature in our K-band data is at 40°N, which is the northernmost extent of our data. The spectrum at this location (Region H) is strikingly different than anywhere else on the disk, and our fit is consistent with a very high haze at 15 mbar. Our deepest feature (E) is the southernmost distinct feature in our data. Furthermore, as previously mentioned. the dark regions in the north appear to have a higher altitude haze than we observe in the southern dark region. However, the aerosol structure appears to be more complex than a simple trend of high-altitude features in the north and deep clouds in the south. In addition to the variations between features at 60°S mentioned above, we find that Region F, which is located at 50°S, appears to have a stratospheric component at 0.02 bar, as compared to the 0.08 bar altitude of the other features in the nearby southern bright band.

Several authors (Conrath et al. (1998); Orton et al. (2007a); Martin et al. (2008) and Chapter 4) have advocated a circulation pattern in which warm, moist air is circulated upwards at mid-latitudes and subsides at the poles. The plethora of bright clouds just above the tropopause at southern mid-latitudes may be consistent with the upwelling of CH_4 due to such a circulation. However, the appearance of northern mid latitudes is very different, and we derive a much higher altitude for the bright region. Gibbard et al. (2003) suggest that northern bright features are subsidence of stratospheric haze material rather than upwelling of methane gas. For features near 60–70°S, Gibbard et al. (2003) propose they are isolated areas of upwelling in a general area of subsidence. This is similar to our conclusions regarding the south polar features described in Chapter 4. However, this explanation doesn't explain the differences observed between the two features in this latitude range.

We caution that the cloud/haze altitudes derived in this investigation are provisional. Improved constraints on the cloud structure can be obtained from a more systematic approach to feature fitting and exploration of the full parameter space, which will be performed in the future. Our plots of Neptune's center-to-limb reflectance illustrate that the current radiative transfer models do not match all of the properties in our data. We anticipate that a detailed analysis of the time series of images from 22 August 2010 will help to remove degeneracies in the cloud structure and help us to reconcile the models with the center-to-limb behavior of the data. Additionally, we have not yet addressed the potential effect of several atmospheric properties on our derived cloud altitudes. The same properties that could be responsible for latitudinal variations in our millimeter data (Chapter 3), including variations in temperature, the hydrogen *ortho/para* ratio and the CH_4 abundance are likely to play an important role here.

Acknowledgements

The data presented in this work were obtained with the W.M. Keck Observatory, which is operated by the California Institute of Technology, the University of California, and the National Aeronautics and Space Administration. The Observatory was made possible by the generous financial support of the W.M. Keck Foundation. H.B. Hammel, I. de Pater and K. de Kleer were instrumental in gathering these data; K. de Kleer and M. Ádámkovics aided in the development of the radiative transfer code. The author extends special thanks to those of Hawaiian ancestry on whose sacred mountain we are privileged to be guests. Without their generous hospitality, none of the observations presented would have been possible.

Chapter 6

Conclusions and Future Directions

Composed predominantly of volatiles referred to as 'ices', Uranus and Neptune are a fundamentally different class of planet than the gas giants Jupiter and Saturn. These ice giants are poorly understood: significant questions remain about their interior structure and composition, large-scale circulation, and seasonal variability. Recent years have brought the first direct measurements of extrasolar planet atmospheres, and while these observations have thus far focused on the hot, close-in planets known as hot Jupiters, many exoplanets are intrinsically different than hot Jupiters: they contain more rock and ice, and have cooler temperatures (Fortney et al. 2008). As we begin to investigate the atmospheres of these Neptune analogs with models, a coherent picture of ice giant atmospheric dynamics is more crucial than ever. I have observed Neptune at millimeter and near-infrared wavelengths to improve our understanding of the circulation and chemistry of ice giant planet atmospheres. To analyze these data, I have developed radiative transfer codes that model the atmospheric spectra of the giant planets as a function of the temperature and composition throughout the atmosphere.

6.1 Millimeter observations of disequilibrium species

Carbon monoxide (CO) is one of several trace species that in equilibrium should be confined to the warm interiors of the giant planets (Lodders & Fegley 1994). Its presence in the upper atmosphere, therefore, indicates disequilibrium processes at work: either rapid transport from deeper levels where the molecules are thermodynamically stable, or production high in the atmosphere as a result of infall of material from the planet's environment. Thus, the CO distribution has far-reaching implications: besides revealing atmospheric dynamics, it provides insight into the environment in the outer Solar System. Using the Combined Array for Research in Millimeter-Wave Astronomy (CARMA), I have observed Neptune's millimeter spectrum, and retrieved the vertical profile of CO from the shape of its rotational lines (Chapter 2). I determined that the data are well matched by a CO mole fraction of $1.1^{+0.2}_{-0.3}$ parts per million (ppm) in the stratosphere and $0.1^{+0.2}_{-0.1}$ ppm in the troposphere. The increased abundance in the stratosphere implies that there is a flux of 0.5–20 $\times$ 10^8 CO molecules cm^{-2} s^{-1} to the upper atmosphere – either from deposition and production by cometary impacts, or produced from a large influx of water from meteorites, moons or ring particles. The stratospheric CO/H_2O ratio supports a comet impact origin (Lellouch et al. 2002; Bézard et al. 2002; Lellouch et al. 2005), and I showed that if the diffusion rate near the tropopause is small (200 cm^2 s^{-1}) and the impact rate follows the estimates of Zahnle et al. (2003), then impacts from (sub)kilometer-sized comets could produce Neptune's observed CO flux.

The quantity of CO mixed upwards from the deep atmosphere is directly tied to Solar System formation, models of which predict compositional ratios for the giant planets. I revisited the calculation of Neptune's internal CO contribution using revised calculations for the CO $\rightarrow$ CH_4 conversion timescale in the deep atmosphere (Visscher & Moses 2011). I found that a tropospheric CO mole fraction of 0.1 ppm can be supplied by rapid vertical mixing if the global oxygen abundance is at least 400, and likely more than 650 times the protosolar value. This value of the O/H enrichment, which implies that Neptune's interior is dominated by H_2O, is much higher than the 30 times protosolar C/H enrichment observed for Neptune, and is not consistent with a formation scenario in which the heavy elements were present in solar proportions in the icy planetesimals that formed the giant planets (Owen et al. 1999). However, a tropospheric CO mole fraction of 0.0 ppm is consistent with my results within the uncertainties, in which case no over-enrichment of oxygen is required in Neptune's interior.

To further investigate the infall and circulation patterns of Neptune's CO, I have spatially resolved Neptune in the CO line for the first time (Chapter 3). I measured latitudinal intensity variations at the 2-3% level in the CO line. The intensity pattern is more consistent with temperature variations than with variations in the CO abundance, and I found that the latitudinal temperature structure observed by Orton et al. (2007a) near the tropopause provides a good match to our observations. At continuum wavelengths, I observed a gradient in the brightness temperature, increasing by 2-3 K from 40°N to the south pole. This corresponds to an opacity decrease of about 0.3 (30%) near the south pole at altitudes below 1 bar, or alternatively a factor of 100 decrease in the opacity at pressures greater than 4 bar. These findings can be interpreted in the context of a large-scale meridional circulation pattern on Neptune, in addition to the zonal flow that dominates giant planet circulation. Multi-wavelength observations (Hammel et al. 2007; Orton et al. 2007a; Martin et al. 2008) indicate that Neptune's south pole is warmer than its surroundings at mid-infrared and centimeter wavelengths as well. Such a temperature enhancement can be explained by a global dynamical pattern in which dry air near the south pole is subsiding and adiabatically heating the atmosphere. In comparison with Saturn, this circulation may include a south polar circulation cell, centered on a stable polar vortex (Hammel et al. 2007; Orton et al. 2007a; Chapter 4). An important step towards understanding the nature of this atmospheric circulation in detail will be a combined analysis of data from several wavelengths.

The radiative transfer code that I have developed for this work can be readily applied to the study of other giant planet atmospheres and molecules. With the construction of the Atacama Large Millimeter/Submillimeter Array (ALMA), such work is particularly timely. Measurements of the CO profile on Uranus would help to characterize impact rates throughout the outer Solar System; however Uranus's CO abundance is too low to be detected with current millimeter instruments. ALMA will achieve about 100 times greater sensitivity than current instruments during mid-construction Cycle 1 observing next year. When ALMA reaches full capabilities in 2013, it will be possible to map Uranus's CO distribution across the planet in order to learn more about the mechanisms responsible for enriching Uranus in CO.

In addition to CO, ALMA will be able to map the giant planets in several other trace species with unprecedented spatial and spectral resolution, including HCN, H_2S and PH_3. These species constrain different aspects of the bulk internal composition, which in turn reveal the conditions under which the planets formed. Like for CO, thermochemical modeling suggests that HCN from the interiors of the giant planets must condense out before it reaches observable levels in the atmosphere; however, HCN has been detected on Neptune (Marten et al. 1993). Two possible sources have been proposed: HCN could be produced from atomic nitrogen (N) in the upper atmosphere as a result of infall, perhaps from Neptune's moon Triton. Alternately, the atomic N required to produce HCN may originate when molecular nitrogen (N_2) from the interior is dissociated in the upper atmosphere (Marten et al. 1993). Spatially resolved HCN data for Neptune would help to determine the origin of HCN. ALMA can also be used to constrain the HCN abundance on Uranus, where it has yet to be detected: ALMA will achieve a detection limit an order of magnitude better than the current upper limit from previous millimeter studies. These investigations into HCN production on both planets will allow constraints to be placed on the nitrogen abundance in ice giant interiors.

6.2 Near-infrared spectroscopy

For the giant planets in our Solar System, near-infrared (NIR) wavelengths sense sunlight reflected from clouds and hazes in the upper atmosphere. These clouds act as both tracers and indicators of the underlying circulation. When combined with information from longer wavelengths, NIR spectroscopy and modeling allow us to develop a more complete three-dimensional picture of the atmospheric dynamics and chemistry. For younger planets outside our Solar System, the NIR corresponds to a part of the spectrum where the contrast between the star and planet is favorable for detection (Macintosh et al. 2008). NIR spectroscopy will allow us to determine the composition of these extrasolar planets, and enable us to see what our Solar System may have been like at earlier times.

One example of how the properties of clouds can tell us about the global circulation is the feature at Neptune's south pole (Chapter 4): Keck near-infrared images of Neptune from UT 26 July 2007 show that the cloud feature typically observed within a few degrees of Neptune's south pole had split into a pair of bright spots. A careful determination of disk center places the cloud centers at $-89.07 \pm 0.06°$ and $-87.84 \pm 0.06°$ planetocentric latitude. If modeled as optically thick, perfectly reflecting layers, I found the pair of features to be constrained to the troposphere, at pressures greater than 0.4 bar. By UT 28 July 2007, images with comparable resolution reveal only a single feature near the south pole. The changing morphology of these circumpolar clouds suggests they may form in a region of strong convection surrounding a Neptunian south polar vortex. The unexpected discovery of a vortex at Saturn's north (winter) pole (Fletcher et al. 2008) implies that polar vortices can exist despite considerable variations in seasonal insolation, and may be general features of giant planet atmospheres. However, possible analogues to Saturn's vortices have yet to be directly observed, as they await the measurement of polar wind speeds by space missions. Further details about the morphology of clouds near Saturn's north pole may help us understand the types of cloud morphologies we might expect around polar vortices, and provide insight into how to interpret the behavior of Neptune's polar cloud features in the context of a possible vortex.

Near-infrared spectroscopy provides detailed constraints on the properties of Neptune's clouds and hazes. Whereas traditional slit spectroscopy does not facilitate the clean separation of individual features from the quiescent background, the NIR AO-assisted integral field spectrometer OSIRIS on the 10-m Keck telescope is capable of obtaining spatially-resolved spectral information over its entire field of view. Using OSIRIS, I collected near-infrared spectra for clouds and hazes on Neptune (Chapter 5). These three-dimensional data cubes were then analyzed with my NIR radiative transfer code (Luszcz-Cook et al. 2010a; de Pater et al. 2010b,a; Appendix B) to derive latitudinal and vertical variations in cloud properties such as height, composition and optical depth. I found that both bright and dark regions in the southern hemisphere are associated with greater depths than those in the north. This result is generally consistent with previous studies (Gibbard et al. 2002; Max et al. 2003), and may suggest that clouds form differently in the two hemispheres. I also saw significant variability in cloud altitudes within the southern hemisphere. The highest concentration of features was found in a bright band extending from 30 – 45°S. I found that these features could all be fit by hazes at the same altitude, by varying only the haze particle densities. In contrast, I determined that the two features near 60°S appeared to be at very different altitudes. Further work is required to interpret this pattern of cloud activity in terms of the underlying atmospheric circulation and chemistry.

Another aspect of Neptune's circulation that is not well understood is the cause of temporal variability: individual clouds evolve on incredibly short (minutes to hours) timescales, while the planet as a whole exhibits decadal-scale variations. For Uranus, this long-term variability can be interpreted as seasonal; however, for Neptune, global atmospheric variations are not well understood (Hammel & Lockwood 2007b). Neptune has been observed regularly in the near-infrared over the last decade; radiative transfer analysis of these data to look for changes in cloud properties and regions of cloud activity over time will help to identify the role of sunlight in powering weather and seasonal variability on ice giant planets.

NIR integral field spectroscopy can also be used to study the atmospheres of extrasolar planets, enabling us to explore the connection between our own Solar System giants and the planets around other stars. While spectroscopic measurements of exoplanet atmospheres have thus far generally been limited to hot Jupiters (Knutson et al. 2011), recent surveys such as Kepler have revealed that cooler planets located further from their parent stars are far more common (Cumming et al. 2008; Seager & Deming 2010). In the upcoming year, the Gemini Planet Imager (GPI) will achieve first light. GPI will perform spectroscopy on young planets in the range corresponding to the giant planets region in our Solar System (Macintosh et al. 2008). Comparisons between these young extrasolar ice giants and the Solar System giants will allow us to unravel some of the mysteries in the formation and evolution of planetary systems.

Appendix A

Monitoring of Secondary Calibrator Fluxes at CARMA

A record of historical secondary calibrator fluxes (more correctly, flux densities) is maintained at CARMA through two types of monitoring: through dedicated flux calibration (fluxcal) tracks and by extracting calibrator fluxes from science tracks. In this chapter, fluxcal on science tracks is described, emphasizing the changes implemented in flux monitoring using science tracks in May 2012. (A description of dedicated fluxcal tracks may be found in CARMA Memo #59, Bauermeister et al. 2012.) We briefly review the causes of variation in the measurements of secondary calibrator fluxes: both the intrinsic variability in the flux of calibration sources (the motivation for flux monitoring) as well as system-induced variations. We also present an overview of how the historical fluxes may be accessed by a CARMA user and how this record of fluxes should be used in the calibration of a science dataset.[1]

A.1 Introduction

A.1.1 Overview

Proper calibration of a dataset involves setting the flux scale using observations of a calibrator with a known flux. Typically, CARMA observations use three calibrators: a primary calibrator (i.e., a planet), a bright bandpass calibrator and a less bright, but close-to-the-source, gain or phase calibrator to monitor the antenna gains over the course of the track. With perfect data, one can determine the flux of the bandpass and phase calibrators using the primary calibrator observation (using a program like **`bootflux`**). However, data are not always perfect and it is therefore always advised to check the derived calibrator fluxes against historical values. If the primary calibrator observation is of poor quality or even missing, it may be necessary to use a calibrator flux taken from historical values.

[1]This chapter is part of CARMA Memorandum Series #59, Bauermeister, Cook, Hull, Kwon & Plagge, and is reproduced with the permission of all coauthors.

There is an ongoing effort at CARMA to monitor the fluxes of secondary calibrators over time in order to maintain this historical record of fluxes. This record is used for the calibration of datasets as described above as well as in planning observations, allowing CARMA users to make informed decisions on which calibrators to observe. Calibrator fluxes are tracked in the three bands available (1-cm, 3-mm and 1-mm) through two separate avenues: dedicated observations (see CARMA Memo #59, Bauermeister et al. 2012) and extraction of fluxes from science tracks (Fluxcal on Science Tracks, Section A.3). In both cases, the fluxes of the secondary calibrators are calibrated using a primary calibrator: typically Mars, Neptune, or Uranus. It is important to note that the planet models used are only known to $\sim 20\%$ and therefore the fluxes we derive are similarly uncertain at this level. Prior to May 2012, secondary calibrator fluxes from science tracks were assigned an error of 15% to reflect this model uncertainty. From May 2012 forward however, fluxes from science tracks are reported with measured uncertainties when possible (see Section A.3.2, step 11), which reflect the data quality but do not account for planet model uncertainties. The planet models and associated errors are discussed in detail in a separate memo on primary calibrators, Kwon et al., in preparation.

In this chapter, we clarify how the fluxes of these secondary calibrators are calculated from science tracks and describe various issues regarding flux variability that may be relevant to a user of CARMA data. A brief description of how one might use the flux monitoring data is given below.

A.1.2 How to make use of flux monitoring data

All the secondary calibrator fluxes extracted from both the dedicated fluxcal tracks and science tracks are stored in the MIRIAD catalog file `FluxSource.cat`. This can be found in each installation of MIRIAD, but will only be as up-to-date as the MIRIAD install. The current version of FluxSource.cat for CARMA can be found on this internal site:
`http://cedarflat.mmarray.org/information/carmaFluxSource.cat`
The user may read the calibrator fluxes directly from the catalog file or use one of following interactive tools:

- the new website interface written by Ted Yu:
  `http://carma.astro.umd.edu/cgi-bin/calfind.cgi`
- the MIRIAD program **calflux**. Running `cvs update` in $MIRCAT will update to the latest version of the flux catalog.
- `xplore`, the CARMA calibrator locator tool by Ted Yu, which can be found at this url:
  `http://cedarflat.mmarray.org/observing/tools/xplore.html`
  Use File→Update to get the latest version of the flux catalog.

If you have a dataset with observations of a primary flux calibrator, a standard strategy for flux calibration is to first flag and bandpass calibrate the data as you would normally then perform a phase-only **selfcal**. Running **bootflux** on the phase-only **selfcal**'d file will automatically calculate the true flux of the secondary calibrator over the course of the track (an averaging interval of 5 to 10 minutes is appropriate) using the planet brightness temperature written in the MIRIAD dataset by the CARMA system. If desired, the brightness temperature may be specified in the **bootflux** call by `primary=PlanetName,Tb`. It is wise at this point to compare the fluxes you derive to the historical fluxes recorded in `FluxSource.cat`, being sure to compare values taken at a similar date and frequency. Fluxes derived from science tracks from May 2012 onward also report the spectral index of the calibrator when it can be derived (see Section A.3.2). This can be used to extrapolate a flux to a different frequency in the band if desired, but should be used with caution. It is up to the discretion of the user to determine if the derived flux is appropriate or if some average from historical data should be used.

When using **bootflux**, it is important to keep the following points in mind. First, calibrator polarization, elevation-dependent gains and other issues can cause variation in the fluxes over the course of the track. See §A.2 for details. Second, the planet brightness temperature in the MIRIAD dataset is the planet model brightness temperature evaluated at the frequency of the LO. Therefore, if you are determining the flux in a window many GHz away from the LO, you may want to use a brightness temperature appropriate for the window via the `primary=PlanetName,Tb` keyword of **bootflux**.

The flux scale in your data can be set during the amplitude and phase gain calibration using the phase calibrator. For this discussion, we use an amplitude and phase **selfcal** for this step. If `options=apriori` is specified, the **selfcal** program will automatically read the `FluxSource.cat` file in your MIRIAD repository and select a flux appropriate for the date and frequency of your observation. This functionality should be used with caution: while some interpolation in time is performed, the frequency is mostly disregarded (the program only notes which of the three bands (1-cm, 3-mm, 1-mm) the data is relevant for). Alternatively, the user can force a certain flux value in one of two ways: use the flux keyword of **selfcal** (this only works if `options=apriori` is NOT specified) or make a copy of `FluxSource.cat` in the working directory which contains the desired flux. The **selfcal** program will default to reading the local copy. A different flux catalog file can also be pointed to with the $MIRFLUXTAB variable.

Summary:

- Flag and bandpass calibrate (ie. **mfcal**) normally
- Phase-only **selfcal** with a short interval on the gain, passband and flux calibrators. Use `options=apriori` to treat the planet appropriately (as a disk).
- Run **bootflux**: ie. for the flux of 2232+117 from Uranus in the first wideband window
  `bootflux vis=A1.phsc.uv select=source(2232+117,URANUS),-auto taver=10 line=chan,1,1,39,39 primary=URANUS`

- Compare the flux calculated by **bootflux** to historical fluxes from `FluxSource.cat` and decide on an appropriate flux for your calibrator. If desired, write the selected flux for your frequency and date into a local copy of `FluxSource.cat`.

- Perform an amplitude **selfcal**, setting the desired flux either in a local copy of `FluxSource.cat` or with the flux keyword of **selfcal** (and without `options=apriori`).

A full example script for the flux calibration of a typical dataset is provided in Appendix A of CARMA Memo #59.

A.2 Observed flux variation: intrinsic and system-induced

A.2.1 Intrinsic variability

Monitoring the fluxes of secondary calibrators is important as these objects are in no way steady. For an extreme example of intrinsic variation, see Figure A.1, which shows the flux of 3C454.3 in each CARMA band as a function of time for the past four years (fluxes taken from `FluxSource.cat`).

A.2.2 Polarized calibrators: 3-mm perceived variability

The 3-mm feeds at CARMA are linearly polarized. The state of the system in 2011/2012 is such that the 'evector' MIRIAD variable is defined at 90° so that the polarization of the data appears to be YY. Note that currently (Feb 2012), the data are incorrectly labeled as LL. For stokes I intensity I, linear polarization fraction p_{qu}, and polarization angle PA, the observed YY intensity as a function of parallactic angle χ is described by

$$YY = I\{1 - p_{qu}\cos[2(PA - \chi)]\}$$

This means that the 3-mm flux of a polarized calibrator will appear to vary over the course of a track if the parallactic angle coverage is significant. This is illustrated in Figure A.2, which shows the flux versus parallactic angle of 0854+201 at 98 GHz from two datasets in November 2011.

A.2.3 Elevation dependence

We have noticed in the past that some datasets show evidence for an elevation dependence in the derived flux, presumably arising from elevation-dependent gains. We merely note this here but do not investigate this effect.

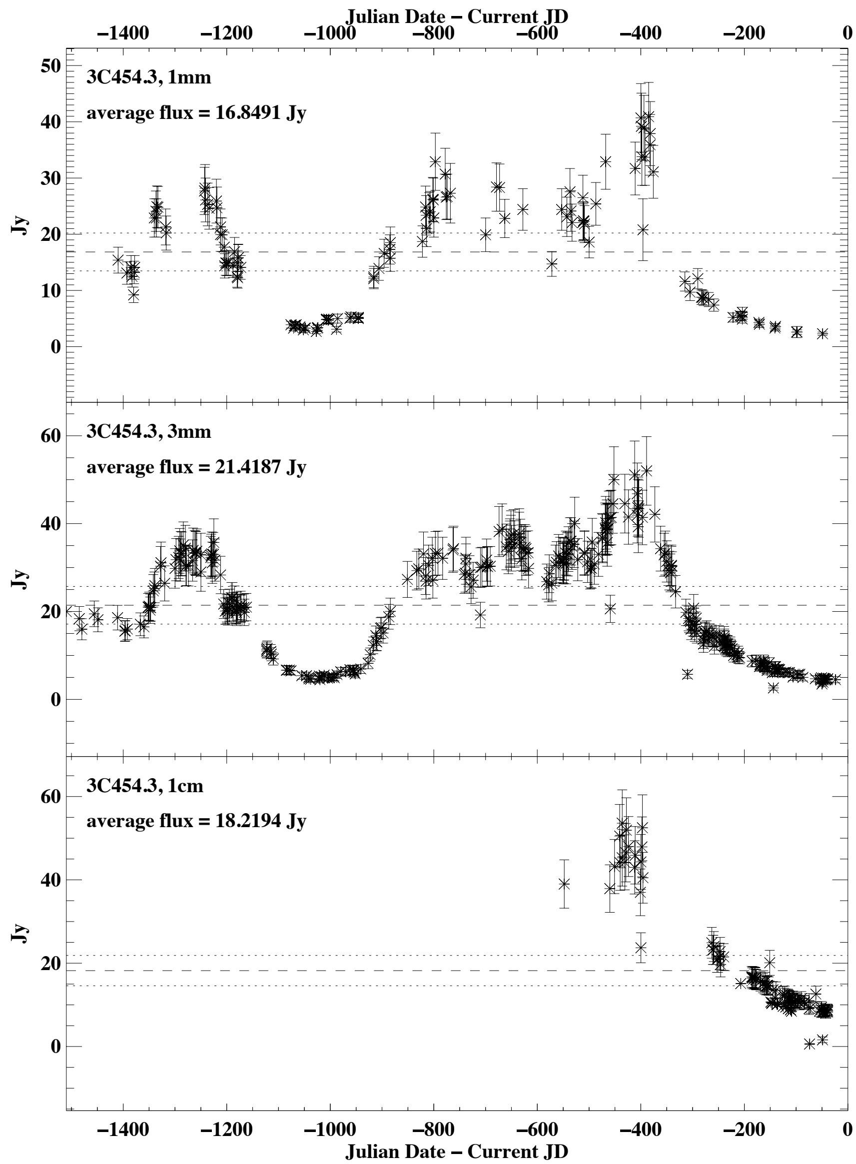

Figure A.1: Historical fluxes of the standard calibrator 3C454.3 (taken from `FluxSource.cat`) in each of the three CARMA bands. Time is plotted as 'Julian Date - Current JD' where the 'Current JD' is February 8, 2012. The dashed line indicates the average flux, with dotted lines showing plus and minus 20%.

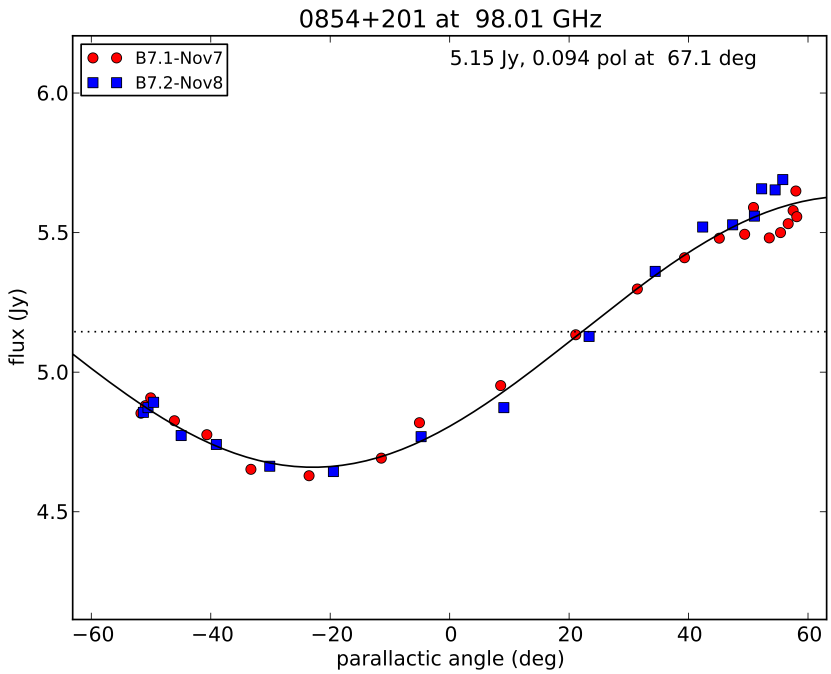

Figure A.2: Flux of 0854+201 versus parallactic angle at 98 GHz on November 7-8 2011 from datasets c0834.7D_98B7.1 and c0834.7D_98B7.2.

A.3 Fluxcal on science tracks

Prior to May 2012, the fluxes of secondary calibrators were extracted from science tracks with the interactive Python script `GetNewCalFlux.py`, written by Scott Schnee. Berkeley CARMA postdoc Frank Bigiel ran fluxcal on science tracks prior to February 2011, and Berkeley graduate students Amber Bauermeister, Statia Cook, Chat Hull and Katey Alatalo ran fluxcal on science tracks using this script until May 2012. This old script, `GetNewCalFlux.py`, was time-intensive to run and out-of-date, so the Berkeley graduate student team has developed a new fluxcal on science tracks reduction script, based on John Carpenter's flux extraction script, `fluxes.py`. The new script, `fluxcalOnScience.py`, has been running since May 2012, monitored by Amber Bauermeister. This task will be transferred to Manuel Fernández-López in the summer of 2012. The scripts and documentation for both the old and new fluxcal on science task can be found on the high site machines in ∼`obs/fluxcalOnScience/`.

We describe the new system for fluxcal on science tracks in detail in Section A.3.2. We also give a brief description of the old script in Section A.3.1 to inform the interpretation of secondary calibrator fluxes prior to May 2012.

calibrator name	3-mm flux (Jy)	calibrator name	3-mm flux (Jy)
0136+478	2.35	1911-201	2.00
0238+166	1.93	1924-292	10.18
0359+509	7.28	2148+069	2.99
0423-013	5.22	2229-085	2.72
0457-234	-	2232+117	2.67
0522-364	-	3C84	10.71
0530+135	2.26	3C111	3.12
0730-116	3.99	3C120	1.82
0854+201	4.60	3C273	14.34
0927+390	4.83	3C279	14.90
1058+015	3.81	3C345	4.43
1337-129	3.66	3C446	4.21
1517-243	1.81	3C454.3	22.18
1658+076	1.43	BLLAC	4.34
1733-130	3.93	MWC349	1.23
1751+096	4.51		

Table A.1: Secondary calibrators monitored by fluxcal on science tracks prior to May 2012, with average 3-mm fluxes from `FluxSource.cat` (from March 2007 to February 2012). No historical fluxes were found for 0457-234 or 0522-364.

A.3.1 Flux monitoring prior to May 2012 (manual)

The extraction of fluxes from science tracks prior to May 2012 was done using `GetNewCalFlux.py`. With this script, the secondary calibrators given in Table A.1 were monitored (this list is hard-coded into the script). Only science datasets which had one of these secondary calibrators as well as an acceptable primary calibrator (Mars, Uranus or Neptune) were processed.

The `GetNewCalFlux.py` script by Scott Schnee performs a simple calibration of each dataset, extracting the flux of the secondary calibrator in the first wide-band window in the dataset using **`bootflux`**, which uses the planet brightness temperature written in the dataset by the CARMA control system. The script displays plots of amplitude versus time and phase versus time on the calibrator, and amplitude versus uv distance on the planet so that the user can determine if any antennas or baselines are bad. The user must then flag bad data by hand and re-run the script. The error in the flux is set to either 15% of the flux value or the rms variation in the flux over the course of the track. The larger value is used, which is almost always 15% of the flux value.

Fluxes were extracted in this way for all data files on the high site which began with ‘cx’, ‘c0’ or ‘c1’ (science tracks) and which had acceptable primary and secondary calibrators (see above). We also made a cut based on the length of the track (typically must be longer than 1 to 2 hours) and the weather grade (B and above typically accepted). This flux monitoring

was kept up on a weekly basis: every Friday, one of the members of the fluxcal on science tracks team ran this analysis on the datasets from the past week on the high site computers. A rotation was kept so that each of the four team members did this task approximately monthly. More information on the week-to-week upkeep of fluxcal on science tracks can be found on the team's wiki site here:
http://badgrads.berkeley.edu/doku.php?id=carma_fluxcal

A.3.2 Flux monitoring after May 2012 (automated)

The automatic extraction of fluxes from science tracks is done on the archive computers at Illinois as tracks are copied to the archive. The script that handles the automated reduction is `fluxcalOnScience.py`, which is adapted from John Carpenter's automatic flux extraction script, `fluxes.py`. The reduction method in `fluxcalOnScience.py` is mostly the same as the original script, with added functionality for amplitude flagging, spectral index fitting and logging. In the following sections we describe the method in which fluxes are extracted by this script and then give an overview of how the script is used.

Method

The main steps of the reduction (with intermediate data files indicated in bold) are as follows

1. **Initial evaluation:** Determine the sources observed, the track length and weather grade. The weather grade is calculated from the average rmspath and tau230 values using the method in the quality script. Tracks must meet the following criteria in order to move forward:
   - Track is a science track: filename starts with 'cx', 'c0' or 'c1'.
   - Track must have a weather grade of B- or better.
   - Track must be at least 1 hour long.
   - Track must contain an acceptable primary calibrator: Mars, Uranus or Neptune.
2. **Remove bad windows** for sci2 and CARMA23 observations, writing **vis_sci2.mir**:
   - Sci2, 1-cm: remove USB, windows 17-32
   - Sci2, 3-mm: remove LSB, windows 1-16
   - CARMA23 (3-mm): remove LSB, windows 1-8

   Note that as of this writing (May 2012), band 16 of the wide-band correlator is bad. Therefore, we remove windows 16 and 32 from sci2 tracks as well.

3. **Extract wide-band windows:** Read the correlator configuration and extract only the wide-band windows to **wb.mir**. At this point, we also extract only the LL polarization.

4. **Basic flagging:**

   - Flag shadowed antennas using **`csflag`**
   - Flag data at elevations above 85 degrees.
   - Flag 3 edge channels on each side of each window (controlled by EDGECHAN_FLAG)

5. **Flag spuriously large amplitudes:** This is done on each calibrator individually, with planets evaluated differently from other calibrators.

   - **Planets:** Use **`uvmodel`** with `options=divide` to divide the uv data by the planet model, writing **wb_planet.mir**. An average amplitude is calculated for each baseline using **`uvaver`** with `interval=10000`. The result is written to **wb_planet_avg.mir**. Note that the averaging method used for non-planet calibrators cannot be used here since **`smauvplt`** does not average planet data. The data divided by the model should have amplitude of 1 in the case of perfect data, so we consider any average data points outside (0.5,2.0) bad. Note that we only evaluate points within the first null since division by the model at the nulls results in large values which are not necessarily bad.
   - **All other calibrators:** The planet data are first removed from the dataset, writing **wb_noplanet.mir**, so that averaging can be done with **`smauvplt`**. The average amplitude of each baseline is extracted using **`smauvplt`**, `average=10000` and `options=scalar`. The minimum acceptable amplitude is set to 0.5 times the median of the average amplitudes (this is controlled by allowAmpFac_min). The maximum acceptable amplitude is set to the minimum of 1.5 times the median (controlled by allowAmpFac_max) and the absolute cut value. Historically (as recorded in `FluxSource.cat`) a flux over 55 Jy has not been observed. Therefore, we set the absolute cut value to 100 Jy for sources 3C273, 3C279, 3C454.3, 3C84 (historically the brightest) and 50 Jy otherwise. This absolute cut is in place in order to catch cases of extremely bad data which would drive the median amplitude so high that the bad data would not be caught by this method.

   Based on the criteria described above, in each window, each baseline in each calibrator observation (time slice) is evaluated as good or bad. The script then searches for trends in the bad points:

   - if > 25% of time slices are bad for a given baseline, the baseline is flagged
   - if > 25% of baselines in a time slice are bad, the time slice is flagged

- if $>25\%$ of baselines with a particular antenna are bad in a particular time slice, flag the antenna in that time slice
- if an antenna is bad in $>25\%$ of time slices, flag the antenna for all times

The parameter trendFraction controls the fraction (25%) of present data points above which a badness trend is established. For each window, if at least one time slice remains not flagged, with at least 50% of antennas not flagged, the window is considered good. Each calibrator is flagged for spurious amplitudes separately, but if a window is found to be bad for any calibrator, it is flagged for the entire dataset.

6. **Passband calibration:** An initial passband and phase-only gain calibration is performed using **`mfcal`** in order to calculate the signal to noise on each calibrator. The (non-planet) calibrator with the highest signal to noise is then used to calibrate the passband with **`mfcal`** using an interval of 0.5 minutes (controlled by parameter INTERVAL_PB). Antennas with average gain amplitudes within ±30% of the median gain amplitude are considered 'good'. If there are at least three 'good' antennas and the reference antenna is one of them, the passband calibration is considered successful. If successful, **pb.mir** is written, removing the 'bad' antennas. If not successful, see step 10.

7. **Phase-only self-calibrate** the planet and each calibrator separately using **`selfcal`** with an interval of 0.5 minutes (controlled by parameter INTERVAL_FLUXCAL), writing **primary.mir** and **source.mir** respectively.

8. **Derive the flux** of each calibrator in each window using **`bootflux`**. The planet brightness temperature is set for each window separately, using the following planet models:

   - Uranus: (134.7 K)$(\nu/100\ GHz)^{-0.337}$ (CARMA control system power law)
   - Neptune: (129.8 K)$(\nu/100\ GHz)^{-0.350}$ (CARMA control system power law)
   - Mars: For 3-mm and 1-mm data, the seasonal variation model returned by the MIRIAD program **`marstb`** is used (this model does not currently include diurnal variations). When running on the high site, the seasonal and diurnal variation model returned by `szaCalcMars` is used for the 1-cm data. When running at Illinois, the 1-cm flux is extrapolated using a straight line calculated from **`marstb`** values at 43 and 50 GHz, which fairly closely matches the `szaCalcMars` values.

9. **Fit the spectral index:** If there are enough wide-band windows, calculate the spectral index, α ($flux \propto \nu^{\alpha}$). If there are 2 wide-band windows, calculate α directly. If there are more than 2 wide-band windows, perform a least-squares fit on the fluxes in each window (using errors reported by **`bootflux`**). The fit gives the spectral index (and error) and the flux at the central frequency (and error). As an example, the

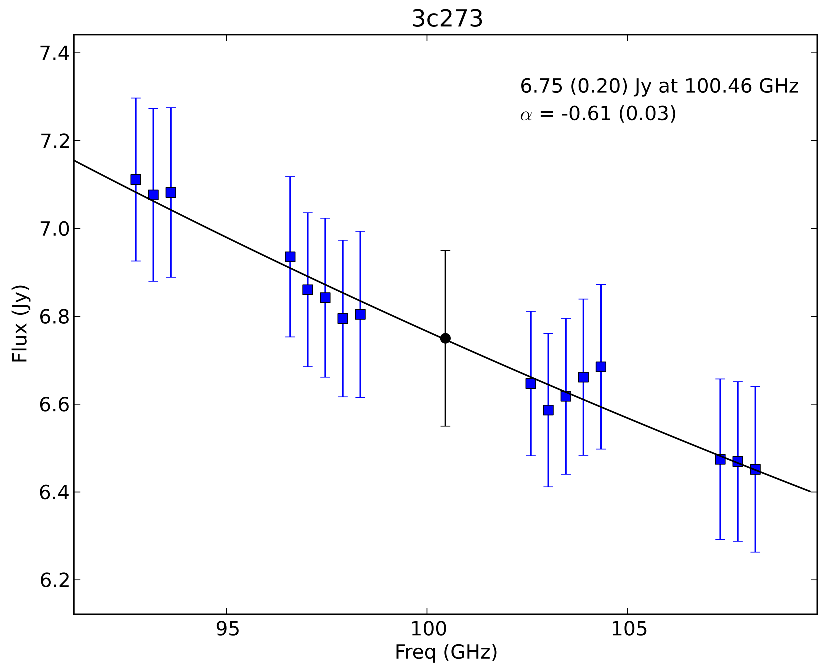

Figure A.3: Flux versus frequency for calibrator 3C273 in the dataset `c0834.5D_97B5.2.miriad`, from the `fluxcalOnScience.py` script. The blue points show the flux (with error bars showing the rms time variation) in each window. The black line shows the fit, with the derived flux (and error) at the central frequency indicated by the black point and error bar. The flux, flux error, spectral index (α) and spectral index error from the fit are listed in the top right corner of the plot.

resulting fit for calibrator 3C273 in dataset `c0834.5D_97B5.2.miriad` is shown in Figure A.3.

10. **Success?** If at least one calibrator flux was derived successfully, the script is finished. If not, the script will loop through steps 6 through 9 again using a different reference antenna. The antennas are ordered by median distance to other antennas, and used as the reference antenna starting with the smallest median distance. This is done in order to minimize atmospheric decoherence, which will have a larger effect on longer baselines.

11. **Report:** Table A.2 describes how the flux error, spectral index and the spectral index error are reported. In reporting the error in the flux, we find that the variation in the measured flux with time due to the weather and system is orders of magnitude larger than the error reported by **`bootflux`** based on the phase scatter of the data. Therefore, we only report an error when the calibrator is observed multiple times over

N_t	N_{wb}	flux	σ_{flux}	α	σ_α
1	1	**bootflux** value	-999.99	-	-
1	2	average value	-999.99	slope	-999.9
1	> 2	fit value	-999.99	fit value	fit error
> 1	1	median **bootflux** value	rms time variation	-	-
> 1	2	average value	rms time variation	slope	-999.99
> 1	> 2	fit value	time rms + fit error	fit value	fit error

Table A.2: Summary of what is reported (flux, flux error (σ_{flux}), spectral index (α), spectral index error (σ_α)) based on the number of wide-band windows (N_{wb}) and the number of times a calibrator is observed in a track (N_t). No spectral index is reported when only one wide-band window is present (indicated by -). When we are unable to accurately estimate the error in the flux or spectral index, the padding value of -999.99 is reported. For calibrators with > 1 time slice and > 2 wide-band windows, the flux error reported is the rms time variation and the fit error added in quadrature.

notScience	track does not start with 'c0', 'c1' or 'c2'
Len/Grade	track is shorter than 1 hour or has a weather grade worse than B-
NoPrimCal	track does not contain a primary calibrator (Mars, Uranus or Neptune)
noConfig	track does not contain a correlator configuration (**uvindex** output)
noWBwin	track does not contain any wide-band windows
allAmpFlag	all of the data were flagged in the amplitude flagging step
configProb0/1/2	more than one correlator configuration in the original file / after wide-band window extraction / after calibrator extraction
passband	unable to successfully passband calibrate with any reference antenna ('refant')
noGoodFluxes	unable to extract good fluxes with **bootflux**
planetRes	**bootflux** crashed with a fatal error, likely because the planet is resolved
bootfluxVar	the **bootflux** values varied by more than 25% for that calibrator (in this case, this error will be logged for each offending calibrator, with the number of offending observations in parenthesis next to the calibrator name)

Table A.3: Failure modes for automated fluxcal on science tracks script, `fluxcalOnScience.py`. If any of these are encountered (except bootfluxVar), fluxes are not derived for the calibrators in the dataset.

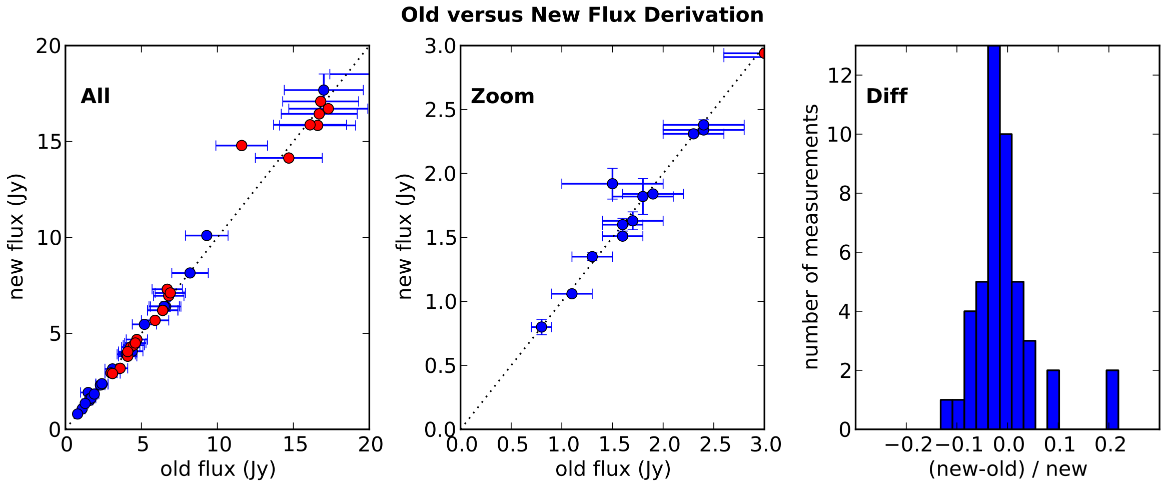

Figure A.4: Comparison of the fluxes derived by the old and new scripts. In the left and middle panels, the old flux is plotted against the new flux, with one-to-one correspondence indicated by the black dotted line. Errors are plotted in both dimensions when available. The old script flux errors are set to 15% for all calibrators. Points for which an error is not reported by the new script (see Table A.2) are plotted in red. The middle panel is the same as the left panel, showing only fluxes less than 3.0 Jy. The right panel shows a histogram of the fractional difference ((new-old)/new) in the derived flux, demonstrating that the old and new scripts almost always agree within 10%.

the course of the track. In this case, we calculate the standard deviation of the flux measurements in each window, and use the largest of these standard deviations as the error in the flux at the central frequency. When a fit is performed, we add the reported fit error in quadrature with the time variation error, but note that the effect of this is negligible since the fit error is always very small due to the nature of the fitting.

Logging and failure modes

The script outputs the derived fluxes (to be entered into `FluxSource_newadd.cat`) to the file `fluxcal.cat`. For each dataset, basic information and the nature of the rejection of the dataset (failure mode) is output to the file `fluxcal.log` so that those managing fluxcal on science tracks can monitor how well the script is extracting fluxes and be alerted to data issues. The possible failure modes are described in Table A.3.

Verification

Before transitioning to the new, automated script, the Berkeley team made several comparisons between the fluxes derived with the new script and the old script. We have done a final comparison of one week's worth of datasets, with fluxes derived using the old and new scripts. The result is shown in Figure A.4. Most of the fluxes agree within 10%. It is worth noting that two of these outliers come from one dataset, which we carefully reduced by hand to find that the new script was finding the correct flux.

Management

The task of managing fluxcal on science tracks now consists of looking over the derived fluxes and associated logfile once a week to check that things are running smoothly and investigate any strange behavior that arises. Before final deployment, the vetted flux data in `fluxcal.cat` must be copied and added to the temporary holding catalog `FluxSource_newadd.cat` in MIRIAD CVS. The nightly script **`calbuild`** by Ted Yu merges `FluxSource_newadd.cat` into `FluxSource.cat`, the master flux table.

A.4 Summary

The fluxes of secondary calibrators are monitored in two ways at CARMA: through dedicated fluxcal tracks and by extracting calibrator fluxes from science tracks. In this memo we have described how each of these is carried out, emphasizing the changes recently implemented in flux monitoring using science tracks. We also describe how these fluxes may be used by a CARMA user and how the historical flux data can be accessed. We discuss both the intrinsic variability of calibration sources (the motivation for flux monitoring) as well as system-induced variations.

Appendix B

Near-Infrared Radiative Transfer Model

Our primary strategy for analyzing near-infrared (NIR) spectra is to compare them with models produced by this radiative transfer code. An earlier version of our radiative transfer code was described in Chapter 4. Here we present a more complete description of the upgraded program, its inputs and its use. This Appendix is intended to be a useful guide for someone intending to utilize the model, or to better understand the steps taken to produce model spectra in Chapter 5. Additional functionality continues to be added as the code is generalized for other applications.

The radiative transfer code is written in IDL. The overall structure of the code is outlined in Fig. B.1. Free parameters, which describe the planet, composition, temperature structure, gas opacity, and scattering properties are input as a structure (IN) that is passed to the SPECTRUM procedure, which runs each stage of the pipeline in turn. Input parameters are either strings, integers or double-precision values ('double'). The code is designed to work for any giant planet atmosphere, with the limitation that gas opacities that are not already included must be written into the TAU_GAS procedure. Additional (extra) keywords are permitted in the input structure, and when deemed useful the code accepts the name of an input IDL procedure, rather than the name of a file, which can be called to describe certain properties of the atmosphere. The following sections describe the individual modules of the code, starting with the main routine, SPECTRUM.

B.1 SPECTRUM

SPECTRUM is the main body of the radiative transfer code. It calculates the NIR spectrum of a giant planet atmosphere, given the input structure (IN). SPECTRUM calls the subroutines ATMOSPHERE, TAU_GAS, and TAU_HAZE in turn. It then adds the haze and gas opacities together to get the total optical depth (TAU). The single scattering albedo of each layer (W) is assigned to be the haze single scattering albedo, multiplied by the ratio of the haze optical depth to the total optical depth in that layer; the Henyey-Greenstein asymmetry parameter (ASYM) is given by the haze asymmetry parameter. The

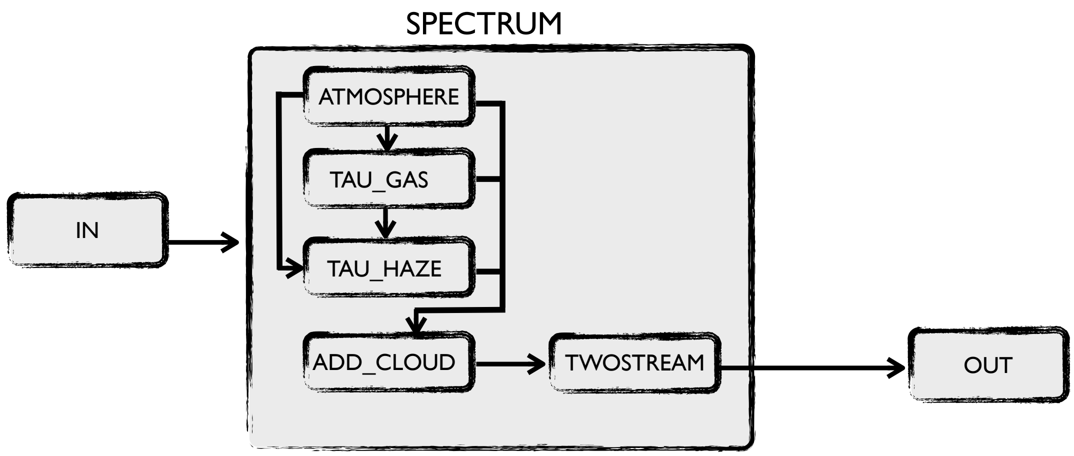

Figure B.1: Structure of the radiative transfer code: the input structure is fed to SPECTRUM, which calls the ATMOSPHERE, TAU_GAS, TAU_HAZE and ADD_CLOUD modules. The optical depth, Henyey-Greenstein asymmetry parameter, single-scattering albedo and μ arrays are fed to the TWOSTREAM code, which produces the output spectrum.

variables TAU, W and ASYM are then modified by ADD_CLOUD. Then, SPECTRUM defines a 'surface spectrum' (RSURF), which is the Lambert reflectivity of a surface below (deeper than) the integration layers, as required by TWOSTREAM (if the model is set up appropriately, so that the optical depth is greater than 1 at every wavelength, the value of this surface spectrum should not matter. In SPECTRUM, RSURF is set to 1 at every wavelength). Finally, SPECTRUM passes TAU, W, and ASYM to TWOSTREAM, which calculates the intensity at every wavenumber and g-ordinate; and sums over g-ordinate to determine the near-infrared intensity, in units of I/F.

Input

SPECTRUM requires the input structure IN, which is used indirectly by the subroutines (described in the following Sections).

Output

The output of SPECTRUM is a structure with two keywords:

- LAMBDA: Array of length [NWN] – wavelength in microns. NWN is defined by TAU_GAS (see Section B.3).
- IFSPEC: Array of length [NWN] – Reflectance in units of I/F, as described in Section 5.3.

Optionally, SPECTRUM will output the ATM, TAUG, and HAZE structures as well; these are the output structures of ATMOSPHERE, TAU_GAS, and TAU_HAZE and are described in the following Sections.

B.2 ATMOSPHERE

The first procedure, entitled ATMOSPHERE, sets up the basic structure of a model atmosphere. ATMOSPHERE reads in or calculates a temperature profile at the specified levels, distributed logarithmically. It uses the specified composition (or procedure) to determine the mole fraction of each species at each level in the model atmosphere. Related quantities (DENSITY, COL, MU) are calculated and returned.

Input

ATMOSPHERE requires the input structure IN to contain at least the following tags, describing the temperature, pressure and composition of the atmospheric layers:

- H0: Double value – km-amagat/bar; converts pressure difference across a layer into an equivalent atmospheric column in km-amagat. The number of amagats of a gas is the ratio of the actual number of particles N at a given temperature and pressure to Loschmidt's number N_0:
$$N_0 \equiv \frac{P_0}{kT_0}$$
where P_0 and T_0 are standard pressure and temperature, respectively.

- NLEV: Integer value – Number of levels to have, equally spaced in log(pressure). Levels define the upper and lower bounds of layers; atmospheric properties are specified at the center of each layer.

- PMIN: Double value – Minimum pressure (bar).

- PMAX: Double value – Maximum pressure (bar).

- TP: String – A single string ending in .dat or .pro. If TP ends in .dat, it should specify the name of a two-column text file giving the input thermal profile, to be interpolated to the pressure levels of the model. The first column is pressure in bar, the second column is temperature in K, and one line at top is assumed to be a header and skipped. If TP ends in .pro, then it should give the name of a procedure for calculating thermal profile. Calling sequence for this procedure (PROC_TP) must be:

  PROC_TP, T, P, IN

where T and P are the output temperatures and pressures, which will then be used to interpolate the temperature at the model pressures. Any additional inputs to the function may be added as tags to the IN structure.

- COMPOS: A structure describing the composition of the atmosphere. Has the following tags of length NSPEC≡ the number of species in the atmosphere.
  - NAME: String array of length NSPEC – Name of each species. This is used for identifying species when calculating gas opacities.
  - DOM: Boolean (1 or 0) array of length NSPEC – a value of 1 means the species should be used as the reference for mixing ratios (the dominant and inert component of the atmosphere). One and only one species should be selected for this; if no species are selected, all compositions must be input as mole fractions.
  - AMU: Integer array of length NSPEC – Molecular weight.
  - MIX: Boolean array of length NSPEC – 1 means that the input is mixing ratio (N/N_{DOM}), 0 means input is mole fraction (N/N_{TOT}), where N is the number density of particles.
  - VAL: Double array of length NSPEC – Set to 0 if there is none of a species in the atmosphere (but you want to leave it in your structure), or to a mixing ratio or mole fractiog-ordinaten value if this value is constant throughout the atmosphere. For example, setting MIX[i] = 1 and VAL[i] = 0.15 maintains a mixing ratio of 0.15 at all levels for species i, as might be appropriate for helium in Neptune's atmosphere. For more complicated vertical profiles, FN should be used, and VAL should be set to 0.
  - FN: String array of length NSPEC – If VAL is to be used or if species has zero abundance, set FN[i] to ‘’; otherwise, FN can be set to the name of a .dat or .pro file (PROC_MIX), following same rules as for TP (above). For a .dat file, the first column should be pressure and the second column should be mixing ratio/mole fraction, with one header line. For a .pro file, the calling sequence must be:

    PROC_MIX, TEMP, PRESSM, i, IN, out

    where i is the index of the species in COMPOS, IN is the entire input structure, and out is the mixing ratio of mole fraction as a function of PRESSM, where PRESSM is an array of pressures at the middle of each layer, calculated by ATMOSPHERE. TEMP is the temperature of each model layer, also calculated by ATMOSPHERE. Additional required inputs should be set as tags to IN.

Output

The output of this procedure is a structure called ATM, which contains the following tags describing the atmosphere:

- NLAY: Double value – Number of atmospheric layers; one less than the number of levels (IN.NLEV). 'Levels' define the upper and lower boundary of 'layers'.
- TEMP: Double array of length NLAY – Temperature at the middle of each layer (K).
- PRESSM: Double array of length NLAY – Pressure at the middle of each layer (bar).
- PRESSB: Double array of length NLAY – Pressure at the bottom of each layer (bar).
- PRESST: Double array of length NLAY – Pressure at the top of each layer (bar).
- COMPOS: A structure describing the composition of the atmosphere at each layer. COMPOS has two tags:
  - NAME: String array of length NSPEC – Name of each species (string), taken directly from IN.
  - MOLF: Double array with dimensions [NSPEC, NLAY] – Mole fraction.
- DENSITY: Double array of length NLAY – Number of amagats of a gas in each layer. Defined as N_{TOT}/N_0
- COL: Double array of length NLAY – Atmospheric column in km-amagat.
- MU: Double array of length NLAY – Average molecular weight, in atomic mass units (amu).

B.3 TAU_GAS

TAU_GAS calculates the total optical depth due to gas opacity (i.e., CH_4 opacity, H_2 pressure-broadened collision-induced absorption, ammonia absorption (currently disabled), and Rayleigh scattering) using the outputs of ATMOSPHERE and several input files that are specified in the IN structure.

Absorption coefficients

CH_4 absorption features dominate the NIR spectra of the giant planets. We use the correlated-k approximation to calculate our spectra; k-distribution lookup tables have been constructed for CH_4 from band models and line data under the conditions relevant to giant planet atmospheres (Irwin et al. 2006; Karkoschka & Tomasko 2010; Sromovsky et al. 2012). Most recently, Sromovsky et al. (2012) considered new line data as well as previously published models and made recommendations for the outer giant planets in several NIR wavelength ranges.

To allow the user to easily choose an input set of k-coefficients (or a combination of sets), we have produced several standardized parameter files based on the following published datasets, which are described in Sromovsky et al. (2012) and references within:

- IRH: Irwin Hydrogen Broadened (2008).
- IRS: Irwin Self-Broadened (2008).
- KAR: Karkoschka (2010).
- SRH: Sromovsky H-wing (2012).
- SRSF: Sromovsky SF-wing (2012).
- SRN: Sromovsky with 50 cm^{-1} far wing cut-off (2012).

These data have been standardized to the same grid of temperatures, pressures, g-ordinates and weights. A subroutine called MAKEPARFILE will use one or more of these standard-format parameter files to produce a standard-format FITS file with 5 extensions, containing the parameters required by the RT code:

- k-coefficients: Four dimensional array with coefficients for each wavenumber, temperature, pressure and g-ordinate value.
- extension #1: wavenumbers.
- extension #2: temperatures.
- extension #3: pressures.
- extension #4: g-ordinates.
- extension #5: weights.

The user specifies the desired wavelength, temperature and pressure ranges required for the parameter file, as well as arrays indicating which coefficients to use in which wavelength ranges. For example, the following example would produce the k-coefficient file recommended by Sromovsky et al. (2012):

```
MAKEPARFILE, ['kar','srsf','kar','srh','srn'],$
        [[1.05, 1.2628], [1.2628, 1.8018], [1.8018, 2.0833], [2.0833, 3.3333], [3.3333, 5.4054]], $
        outfile='srom_recom.fits'
```

The other main absorption is collision-induced opacity (CIA) for H_2-H_2, H_2-He and H_2-CH_4 pairs. Values have been tabulated in units of [cm^{-1} amagat^{-2}] by Borysow et al. (1985, 1988) and Borysow (1991, 1992, 1993). Corrections have been published by Orton et al. (2007a). We produce tables in a standard format: the first column specifies temperature and the first row specifies wavenumber. The remaining values in the table are the absorption coefficients in units of cm^{-1} amagat^{-2} for each temperature and wavenumber.

The procedure

TAU_GAS first interpolates the k-coefficients at the appropriate temperature/pressure for each level and for each wavenumber and g-ordinate in the original CH_4 k-coefficient file. Currently, the wavelength resolution, which is limited by the k-coefficients, is actually defined by the k-coefficient file. If there is no CH_4 in the atmosphere, or no file is provided for CH_4 interpolation, the code will exit with an error. In the future we will generalize the code to work with other k distributions, or atmospheres that do not require the correlated-k method (e.g., an atmosphere with CIA only).

The optical depth τ due to CH_4 in layer i is calculated from the interpolated k-coefficients ($kCH4$) at each wavenumber and g-ordinate as

$$\tau[*, i, *] = kCH4[*, i, *] \cdot \text{ATM.COL}[i] \cdot qCH4$$

where $qCH4$ is given by ATM.COMPOS.MOLF at the index where ATM.COMPOS.NAME is equal to 'CH4'.

The code then checks if the 'H2' mixing ratio is set, in which case TAU_GAS proceeds with H_2 CIA. The tables are first interpolated to the appropriate conditions (temperature and wavenumber, in this case). Then the optical depth for each layer (at all g-ordinates) due to H_2 H_2 CIA is added to the total optical depth:

$$\tau[*, i, *] += kH2H2[*, i, *] \cdot 10^5 \cdot [qH2]^2 \cdot \text{ATM.COL}[i] \cdot \text{ATM.DENSITY}[i]$$

where $kH2H2 \cdot 10^5$ is the interpolated opacity in units of km^{-1} amagat^{-2}, to agree with the units of ATM.COL, and $qH2$ is given by ATM.COMPOS.MOLF at the index where ATM.COMPOS.NAME is equal to 'H2'. Similar calculations are done for H_2-He and H_2-CH_4 pairs.

In addition to calculating τ at each wavenumber, layer and g-ordinate, TAU_GAS also produces IDL save files, saving the interpolated data table for each set of coefficients. This allows the user to run the model with different conditions but the same atmospheric structure (thermal profile, layer pressures) and wavelength array. On future runs the code can be run with FNAME.SAV rather than FNAME.FITS, which speeds up runtime.

Previous iterations of the code have included NH_3 absorption (for use on Jupiter). We have yet to enable this in the new code.

Finally, for each species i in the model, the Rayleigh scattering coefficient is calculated following Hansen & Travis (1974):

$$\frac{P_0}{g * N_0 \mu_a m_p} \frac{8\pi^3 q_i}{3} \frac{(n^2-1)^2}{\lambda^4 N_0} \frac{6+3\cdot\delta}{6-7\cdot\delta}$$

where P_0 is standard pressure = 1.013 bar, N_0 is Loschmidt's number, $g \equiv$ IN.GG is the acceleration due to gravity, $\mu_a \equiv$ ATM.AMU is the mean molecular weight, m_p is the mass of a proton, q_i is the mole fraction of species i, n is the refractive index of i and $\delta \equiv$

IN.COMPOS.DEL is the depolarization factor, which is zero for isotropic scattering and 0.02 for H_2 gas. The index of refraction n is parameterized as

$$n - 1 = A(1 + B/\lambda^2)$$

where λ is in microns. Parameters $A \equiv$ IN.COMPOS.A and $B \equiv$ IN.COMPOS.B are defined in the input structure IN, and are tabulated for several gases in Allen (1963). Opacity due to Rayleigh scattering is then added to the total optical depth.

Input

For TAU_GAS, IN must contain the following tags:

- H0: Double value – km-am/bar.
- GG: Double value – gravitational acceleration in g cm^{-2}.
- COMPOS: Structure describing the composition of the atmosphere. Has the following tags of length NSPEC=# of species, in addition to those already used by ATMOSPHERE:
  - A, B: Double arrays of length NSPEC – Parameters of the refractive index, used for Rayleigh scattering.
  - DEL: Double array of length NSPEC – Depolarization factor, used for Rayleigh scattering.
  - AMU: Double array of length NSPEC – Molecular weight of each species (also used by ATMOSPHERE).
  - NAME: String array of length NSPEC – Name of each species.

  IN should also contain the following tags, if gas absorption is desired:

- kCH4: String – The name of a standard format FITS file OR a .sav file containing methane k-coefficients.
- kH2H2: String – Standard format FITS file containing k-coefficients for a grid of wavenumbers and temperatures OR a .sav file containing the $kH2H2$ table to use (from a previous interpolation).
- kH2He: String – Standard format FITS file containing k-coefficients for a grid of wavenumbers and temperatures OR a .sav file containing the $kH2He$ table to use (from a previous interpolation).
- kH2CH4: String – Standard format FITS file containing k-coefficients for a grid of wavenumbers and temperatures OR a .sav file containing the $kH2CH4$ table to use (from a previous interpolation).

In addition, TAU_GAS reads the following from the ATM structure produced by ATMOSPHERE: NLAY, TEMP, PRESSM, COMPOS, DENSITY, COL.

Output

The output structure TAUG contains the following tags, describing the gas opacity:

- TAU: Double array of size [NWN, NLAY, NG] – The total gas opacity from H_2-H_2, H_2-He, and H_2-CH_4 CIA; CH_4 absorption; and Rayleigh scattering at each wavelength, layer, and g-ordinate.
- WN: Double array of size NWN – Wavenumbers in cm^{-1} set from k-coefficient spectral scale.
- NWN: Integer – Number of elements in the WN array.
- DGORD: Double array of length NG – g-ordinate weights.
- NG: Integer – Number of g-ordinates.

B.4 TAU_HAZE

TAU_HAZE calculates the optical depth and scattering properties of hazes [or clouds] in each model layer. For each haze, TAU_HAZE compares the minimum and maximum pressures of the haze (IN.HAZE.PMIN and IN.HAZE.PMAX) to the top and bottom pressures of each model layer, to determine if part or all of the integration layer contains that haze. Using the center of the layer (or, if a layer is only partially filled with haze, the center of the haze-filled fraction of the layer), TAU_HAZE calculates the pressure scale height of each layer H and physical thickness of each layer z in cm, assuming hydrostatic equilibrium. Then, the haze density at the bottom of the haze (IN.HAZE.PMAX) is assigned a value of IN.HAZE.DEN. The haze density at the top of that layer is calculated by multiplying the gas scale height H by the scale factor IN.HAZE.HFRAC; this value becomes the density for the bottom of the following layer. If $N_B[i]$ is the density at the bottom of haze [i] then the haze density at the top of that layer $N_T[i]$ is given by

$$N_T[i] = N_B[i] \cdot \exp\left(-\frac{z[i]}{H[i] \cdot \text{IN.HAZE.HFRAC}}\right)$$

and the final density of these haze particles in layer i is the straight average of the top and bottom densities. Once the number density of particles is calculated for each integration layer, the optical depth, single-scattering albedo and Henyey Greenstein asymmetry parameters are set for each wavelength and atmospheric layer. If multiple hazes are present in a given layer, then the weighted average of their properties is taken. The haze optical depth τ_h is calculated as

$$\tau_h = (N_T + N_B)/2 \cdot z \cdot \text{IN.HAZE.SIGMA}$$

The extinction cross section IN.HAZE.SIGMA and asymmetry parameter IN.HAZE.HG, which may be wavelength-dependent, are calculated outside of the main radiative transfer code. These properties are generally calculated assuming Mie scattering, either for a single characteristic particle size or for an ensemble of particles having some distribution. The distribution of particles used in this study is specified in Section 5.3. For the modeling discussed in this chapter, we calculate IN.HAZE.SIGMA as weighted averages of ensembles of particles:

$$\text{IN.HAZE.SIGMA} \equiv \sigma_{av} = \Sigma_i w_i \cdot \pi r_i^2 qext_i$$

where w_i is the weighting factor for particles in bin i (the percentage of particles that are in size bin i); r_i is the radius of particles in bin i, and $qext_i$ is the extinction efficiency for particles of size r_i, calculated from Mie scattering. We note that calculating the opacity using an average cross section is the same as adding up the optical depth contributions of particles in each size bin i:

$$\begin{aligned}
\tau_h &= \Sigma_i N_i \pi r_i^2 qext_i z \\
&= \Sigma_i (w_i N) \pi r_i^2 qext_i z \\
&= \Sigma_i N (w_i \pi r_i^2 qext_i) z \\
&= N z \Sigma_i w_i \pi r_i^2 qext_i \\
&= N z \sigma_{av}
\end{aligned}$$

Input

For TAU_HAZE, IN is required to have the following tags:

- GG: Double, value – gravitational acceleration in g cm^{-2}.
- HAZE: A structure describing the properties of each haze. Any number of haze layers can be specified. HAZE has the following tags of length NHAZE $\equiv$ the number of hazes:
  - PMAX: Double array of length NHAZE – Pressure of the bottom of each haze layer (bar).
  - PMIN: Double array of length NHAZE – Top pressure at which to 'cut off' the haze (bar). This can be set to a very low number if one doesn't wish to cut off the haze.

- DEN: Double array of length NHAZE – Number density of haze at HAZE.PMAX in cm^{-3}.
- HFRAC: Double array of length NHAZE – Fractional scale height of the haze (compared to the gas). HFRAC=1 means haze particles fall off with the gas scale height; HFRAC≤0.1 means a 'flat' cloud.
- LAMBDA: Double array – Wavelengths (μm) at which scattering properties are input. LAMBDA can be different than the wavelengths of the final data; for example, it can be sampled more sparsely. If scattering properties are constant with wavelength, this tag is ignored. If not, SIGMA and HG will be interpolated from HAZE.LAMBDA to the data wavelengths. The length of HAZE.LAMBDA is referred to as NL.
- SIGMA: Double array of dimensions [NL,NHAZE] or [NHAZE] – Extinction cross section in cm^2.
- HG: Double array of dimensions [NL,NHAZE] or [NHAZE] – Henyey Greenstein asymmetry parameter.
- SSA: Double array of dimensions [NHAZE] – Single scattering albedo. If this number is not between 0 and 0.999 then HAZE.SSA is set to 0.999 (perfectly reflecting) and a warning message is printed.

TAU_HAZE also reads the following from the ATMOSPHERE module: NLAY, TEMP, PRESSM; and the following from TAU_GAS: WN, NWN.

Output

The output structure HAZE contains the following tags, describing the scattering and absorption due to clouds:

- TAU: Double array of size [NWN, NLAY] – Optical depth due to hazes at each wavelength and atmospheric layer.
- SSA: Double array of size [NWN, NLAY] – Single scattering albedo at each wavelength and atmospheric layer.
- ASYM: Double array of size [NWN, NLAY] – Asymmetry parameter at each wavelength and atmospheric layer.

B.5 ADD_CLOUD

ADD_CLOUD is a second routine for specifying scattering, and is included for convenience. In this routine, the asymmetry parameter and optical depth for an atmospheric layer are specified directly. The single scattering albedo may be specified by a function or data file. ADD_CLOUD directly modifies the optical depth, single-scattering albedo and Henyey-Greenstein asymmetry parameter of the model layer closest in pressure to the pressure given for the cloud(s) in the input structure.

Input

The following inputs are calculated in SPECTRUM for use in ADD_CLOUD: TAU, W, and ASYM (the asymmetry parameter at each wavenumber, wavelength and g-ordinate)

- LAMBDA: Double array of length NWN – wavelengths (microns) of spectrum.
- TAU: Double array of size [NWN,NLAY,NG] – Total optical depth as a function of wavelength, layer and g-ordinate due to gas and hazes.
- W: Double array of size [NWN,NLAY,NG] – single scattering albedo as a function of wavelength, layer and g-ordinate due to hazes.
- ASYM: Double array of size [NWN,NLAY,NG] – Henyey-Greenstein asymmetry parameter as a function of wavelength, layer and g-ordinate due to hazes.

  For this routine IN must contain at least the tag CLOUD : A structure describing the properties of each cloud. CLOUD has the following tags of length NCLOUD ≡ # of clouds:

  - P: Double array of length NCLOUD – Pressure of each cloud layer (bar). Cloud properties will be written into nearest corresponding integration layer.
  - TAU: Double array of length NCLOUD – Optical depth of the cloud. Currently only one number per cloud (wavelength independent).
  - ASYM: Double array of length NCLOUD – Asymmetry parameter (HG) of cloud.
  - SSA: Double array of length NCLOUD – Single scattering albedo of cloud. One number per cloud; for more complicated albedos, use SSA_FILE.
  - SSA_FILE: String array of length NCLOUD – If set, will overwrite CLOUD.SSA. Can be a procedure (SSA_PROC) of the form:

    SSA_PROC, LAMBDA, i, IN, out

    or a .DAT file that contains a column of wavelengths (microns) and of SSA values, with one header row to be skipped.

  ADD_CLOUD also reads the following from the ATMOSPHERE module: PRESSM, TEMP.

Output

ADD_CLOUD directly modifies TAU, W, and ASYM at the pressure best matching that of IN.CLOUD.P; there are no additional outputs.

B.6 TWOSTREAM

TWOSTREAM is a monochromatic plane parallel code that solves the radiative transfer equation using the two-stream approximation. This code is called by SPECTRUM in a loop over wavelength and g-ordinate; the output at each wavelength is then multiplied by the g-ordinate weighting, summed over g-ordinate, and multiplied by π to convert into units of I/F.

Input

The following inputs are calculated in SPECTRUM (and, in some cases, modified by ADD_CLOUD):

- TAU: Double array of size [NWN,NLAY,NG] – Optical depth.
- W: Double array of size [NWN,NLAY,NG] – Single scattering albedo.
- ASYM: Double array ofsize [NWN,NLAY,NG] – Henyey-Greenstein symmetry parameter.
- RSURF: Double array of length NWN – Lambert reflectivity of the bottom surface. If the model extends to appropriately deep pressures, the optical depth should be greater than 1 above this surface, and the value of RSURF should not matter. RSURF is set to 1 by SPECTRUM.

In addition the input structure IN must contain the following tag:

- MU Double value – Number between 0.00 and 0.99999 (code breaks if MU is exactly 1.0), specifying the cosine of the local solar zenith angle.

Output

The output of TWOSTREAM is F_OUT, which is the flux relative to the incident solar flux at a given wavelength and g-ordinate. This output is used by SPECTRUM to produce the final output spectrum in units of I/F.

Bibliography

Ádámkovics, M., Wong, M. H., Laver, C., & de Pater, I. 2007, Science, 318, 962
Allen, C. W. 1963, Astrophysical quantities
Asplund, M., Grevesse, N., Sauval, A. J., & Scott, P. 2009, ARA&A, 47, 481
Baines, K. H., Mickelson, M. E., Larson, L. E., & Ferguson, D. W. 1995, Icarus, 114, 328
Baines, K. H., & Smith, H. W. 1990, Icarus, 85, 65
Bauermeister, A., Cook, S., Hull, C., Kwon, W., & Plagge, T. 2012, CARMA Memorandum Series, #59
Beer, R. 1975, ApJ, 200, L167
Bézard, B., Lellouch, E., Strobel, D., Maillard, J.-P., & Drossart, P. 2002, Icarus, 159, 95
Bezard, B., Romani, P. N., Conrath, B. J., & Maguire, W. C. 1991, J. Geophys. Res., 96, 18961
Bézard, B., Romani, P. N., Feuchtgruber, H., & Encrenaz, T. 1999, ApJ, 515, 868
Borysow, A. 1991, Icarus, 92, 273
—. 1992, Icarus, 96, 169
—. 1993, Icarus, 106, 614
Borysow, J., Frommhold, L., & Birnbaum, G. 1988, ApJ, 326, 509
Borysow, J., Trafton, L., Frommhold, L., & Birnbaum, G. 1985, ApJ, 296, 644
Briggs, D. S. 1995, in Bulletin of the American Astronomical Society, Vol. 27, American Astronomical Society Meeting Abstracts, 112.02
Burgdorf, M., Orton, G. S., Davis, G. R., et al. 2003, Icarus, 164, 244
Butler, B. J., Hofstadter, M., Gurwell, M., Orton, G., & Norwood, J. 2012, in AAS/Division for Planetary Sciences Meeting Abstracts, Vol. 44, AAS/Division for Planetary Sciences Meeting Abstracts, 504.06
Castelli, F., & Kurucz, R. L. 2004, ArXiv Astrophysics e-prints, arXiv:astro-ph/0405087
Cavalié, T., Billebaud, F., Dobrijevic, M., et al. 2009, Icarus, 203, 531
Chase, M. 1998, Journal of Physical and Chemical Reference Data, Monograph No. 9, 1
Colina, L., Bohlin, R. C., & Castelli, F. 1996, AJ, 112, 307
Conrath, B. J., Gautier, D., Lindal, G. F., Samuelson, R. E., & Shaffer, W. A. 1991, J. Geophys. Res., 96, 18907
Conrath, B. J., Gautier, D., Owen, T. C., & Samuelson, R. E. 1993, Icarus, 101, 168
Conrath, B. J., Gierasch, P. J., & Ustinov, E. A. 1998, Icarus, 135, 501
Courtin, R., Gautier, D., & Strobel, D. 1996, Icarus, 123, 37

Cumming, A., Butler, R. P., Marcy, G. W., et al. 2008, PASP, 120, 531
de Graauw, T., Feuchtgruber, H., Bezard, B., et al. 1997, A&A, 321, L13
de Pater, I., Deboer, D., Marley, M., Freedman, R., & Young, R. 2005, Icarus, 173, 425
de Pater, I., & Mitchell, D. L. 1993, J. Geophys. Res., 98, 5471
de Pater, I., Romani, P. N., & Atreya, S. K. 1991a, Icarus, 91, 220
de Pater, I., Schloerb, F. P., & Rudolph, A. 1991b, Icarus, 90, 282
de Pater, I., Wong, M. H., Marcus, P., et al. 2010a, Icarus, 210, 742
de Pater, I., Fletcher, L. N., Pérez-Hoyos, S., et al. 2010b, Icarus, 210, 722
Deboer, D. R., & Steffes, P. G. 1994, Icarus, 109, 352
—. 1996, Icarus, 123, 324
Dyudina, U. A., Ingersoll, A. P., Ewald, S. P., et al. 2008, Science, 319, 1801
—. 2009, Icarus, 202, 240
Encrenaz, T., Drossart, P., Feuchtgruber, H., et al. 1999, Planet. Space Sci., 47, 1225
Encrenaz, T., Lellouch, E., Drossart, P., et al. 2004, A&A, 413, L5
Encrenaz, T., Serabyn, E., & Weisstein, E. W. 1996, Icarus, 124, 616
Fegley, Jr., B., Gautier, D., Owen, T., & Prinn, R. G. 1991, Spectroscopy and chemistry of the atmosphere of Uranus, ed. J. T. Bergstralh, E. D. Miner, & M. S. Matthews (University of Arizona Press; 1st Edition), 147
Fegley, Jr., B., & Lodders, K. 1994, Icarus, 110, 117
Fegley, Jr., B., & Prinn, R. G. 1986, ApJ, 307, 852
Feuchtgruber, H., Lellouch, E., de Graauw, T., et al. 1997, Nature, 389, 159
Fitzpatrick, E. L., & Massa, D. 1999, ApJ, 525, 1011
Fletcher, L. N., Drossart, P., Burgdorf, M., Orton, G. S., & Encrenaz, T. 2010, A&A, 514, A17
Fletcher, L. N., Irwin, P. G. J., Orton, G. S., et al. 2008, Science, 319, 79
Fortney, J., Marley, M., & Saumon, D. 2008, in Spitzer Proposal ID #50107, 50107
Gibbard, S. G., de Pater, I., Roe, H. G., et al. 2003, Icarus, 166, 359
Gibbard, S. G., Roe, H., de Pater, I., et al. 2002, Icarus, 156, 1
Grevesse, N., & Noels, A. 1993, in Origin and Evolution of the Elements, ed. N. Prantzos, E. Vangioni-Flam, & M. Casse, 15
Griffith, C. A., & Yelle, R. V. 1999, ApJ, 519, L85
Guilloteau, S., Dutrey, A., Marten, A., & Gautier, D. 1993, A&A, 279, 661
Hammel, H. B., Baines, K. H., & Bergstralh, J. T. 1989, Icarus, 80, 416
Hammel, H. B., & Lockwood, G. W. 2007a, Icarus, 186, 291
—. 2007b, Icarus, 186, 291
Hammel, H. B., Sitko, M. L., Lynch, D. K., et al. 2007, AJ, 134, 637
Hansen, J. E., & Pollack, J. B. 1970, Journal of Atmospheric Sciences, 27, 265
Hansen, J. E., & Travis, L. D. 1974, Space Sci. Rev., 16, 527
Hesman, B. E., Davis, G. R., Matthews, H. E., & Orton, G. S. 2007, Icarus, 186, 342
Hoffman, J. P., Steffes, P. G., & Deboer, D. R. 2001, Icarus, 152, 172
Hofstadter, M. D., Butler, B. J., Gurwell, M. A., Hesman, B. E., & Devaraj, K. 2008, in

Bulletin of the American Astronomical Society, Vol. 40, AAS/Division for Planetary Sciences Meeting Abstracts #40, 488

Irwin, P. G. J., Sromovsky, L. A., Strong, E. K., et al. 2006, Icarus, 181, 309

Irwin, P. G. J., Teanby, N. A., Davis, G. R., et al. 2011, Icarus, 216, 141

Jasper, A. W., Klippenstein, S. J., Harding, L. B., & Ruscic, B. 2007, The Journal of Physical Chemistry A, 111, 3932, pMID: 17388366

Karkoschka, E., & Tomasko, M. 2009, Icarus, 202, 287

Karkoschka, E., & Tomasko, M. G. 2010, Icarus, 205, 674

—. 2011, Icarus, 211, 780

Knutson, H. A., Madhusudhan, N., Cowan, N. B., et al. 2011, ApJ, 735, 27

Lellouch, E., Feuchtgruber, H., de Graauw, T., et al. 1997, in Bulletin of the American Astronomical Society, Vol. 29, AAS/Division for Planetary Sciences Meeting Abstracts #29, 992

Lellouch, E., Moreno, R., & Paubert, G. 2005, A&A, 430, L37

Lellouch, E., Paubert, G., Moreno, R., et al. 1995, Nature, 373, 592

Lellouch, E., Bézard, B., Moses, J. I., et al. 2002, Icarus, 159, 112

Lellouch, E., Hartogh, P., Feuchtgruber, H., et al. 2010, A&A, 518, L152

Limaye, S. S., & Sromovsky, L. A. 1991, J. Geophys. Res., 96, 18941

Lindal, G. F. 1992, AJ, 103, 967

Line, M. R., Orton, G. S., Fletcher, L. N., et al. 2008, in Bulletin of the American Astronomical Society, Vol. 40, AAS/Division for Planetary Sciences Meeting Abstracts #40, 473

Lockwood, G. W., & Jerzykiewicz, M. 2006, Icarus, 180, 442

Lodders, K. 2004, ApJ, 611, 587

Lodders, K., & Fegley, B. 2002, Icarus, 155, 393

Lodders, K., & Fegley, Jr., B. 1994, Icarus, 112, 368

Lord, S. D. 1992, A new software tool for computing Earth's atmospheric transmission of near- and far-infrared radiation, Tech. rep.

Luszcz-Cook, S. H., de Pater, I., Ádámkovics, M., & Hammel, H. B. 2010a, Icarus, 208, 938

Luszcz-Cook, S. H., de Pater, I., & Plambeck, R. L. 2010b, in AAS/Division for Planetary Sciences Meeting Abstracts, Vol. 42, AAS/Division for Planetary Sciences Meeting Abstracts #42, 11.33

Macintosh, B. A., Graham, J. R., Palmer, D. W., et al. 2008, in Society of Photo-Optical Instrumentation Engineers (SPIE) Conference Series, Vol. 7015, Society of Photo-Optical Instrumentation Engineers (SPIE) Conference Series

Markwardt, C. B. 2009, in Astronomical Society of the Pacific Conference Series, Vol. 411, Astronomical Data Analysis Software and Systems XVIII, ed. D. A. Bohlender, D. Durand, & P. Dowler, 251

Marrero, T. R., & Mason, E. A. 1972, Journal of Physical and Chemical Reference Data, 1, 3

Marten, A., Gautier, D., Owen, T., et al. 1991, in Bulletin of the American Astronomical

Society, Vol. 23, Bulletin of the American Astronomical Society, 1164
Marten, A., Gautier, D., Owen, T., et al. 1993, ApJ, 406, 285
Marten, A., Matthews, H. E., Owen, T., et al. 2005, A&A, 429, 1097
Martin, S., de Pater, I., & Kloosterman, J. andHammel, H. B. 2008, in EPSC Abstracts, EPSC2008
Martin, S., de Pater, I., Kloosterman, J., Gibbard, S., & Hammel, H. B. 2006, in Bulletin of the American Astronomical Society, Vol. 38, AAS/Division for Planetary Sciences Meeting Abstracts #38, 502
Martin, S. C., de Pater, I., & Marcus, P. 2012, Ap&SS, 337, 65
Massie, S. T., & Hunten, D. M. 1982, Icarus, 49, 213
Max, C. E., Macintosh, B. A., Gibbard, S. G., et al. 2003, AJ, 125, 364
Mengel, M., Flatin, D. C., & De Lucia, F. C. 2000, Journal of Chemical Physics, 112, 4069
Moreno, R., Marten, A., Biraud, Y., et al. 2001, Planet. Space Sci., 49, 473
Moreno, R., Marten, A., & Lellouch, E. 2009, in AAS/Division for Planetary Sciences Meeting Abstracts, Vol. 41, AAS/Division for Planetary Sciences Meeting Abstracts 41, 28.02
Moreno, R., Marten, A., Matthews, H. E., & Biraud, Y. 2003, Planet. Space Sci., 51, 591
Moses, J. I. 1992, Icarus, 99, 368
Moses, J. I., Fouchet, T., Bézard, B., et al. 2005, Journal of Geophysical Research (Planets), 110, 8001
Moses, J. I., Lellouch, E., Bézard, B., et al. 2000, Icarus, 145, 166
Moses, J. I., Visscher, C., Fortney, J. J., et al. 2011, ApJ, 737, 15
Naylor, D. A., Davis, G. R., Griffin, M. J., et al. 1994, A&A, 291, L51
Newcomb, S. 1866, Smithsonian Contributions to Knowledge, 6, 1
Noll, K. S., Knacke, R. F., Geballe, T. R., & Tokunaga, A. T. 1986, ApJ, 309, L91
Orton, G. S., Aitken, D. K., Smith, C., et al. 1987, Icarus, 70, 1
Orton, G. S., Baines, K. H., Caldwell, J., et al. 1990, Icarus, 85, 257
Orton, G. S., Encrenaz, T., Leyrat, C., Puetter, R., & Friedson, A. J. 2007a, A&A, 473, L5
Orton, G. S., Gustafsson, M., Burgdorf, M., & Meadows, V. 2007b, Icarus, 189, 544
Orton, G. S., Lacy, J. H., Achtermann, J. M., Parmar, P., & Blass, W. E. 1992, Icarus, 100, 541
Orton, G. S., & Yanamandra-Fisher, P. A. 2005, Science, 307, 696
Owen, T., Mahaffy, P., Niemann, H. B., et al. 1999, Nature, 402, 269
Pearl, J. C., & Conrath, B. J. 1991, J. Geophys. Res., 96, 18921
Pérez-Hoyos, S., & Sánchez-Lavega, A. 2006, Icarus, 180, 161
Pickett, H. M., Poynter, R. L., Cohen, E. A., et al. 1998, J. Quant. Spec. Radiat. Transf., 60, 883
Pravdo, S. H., Shaklan, S. B., Wiktorowicz, S. J., et al. 2006, ApJ, 649, 389
Prinn, R. G., & Barshay, S. S. 1977, Science, 198, 1031
Rayner, J. T., Cushing, M. C., & Vacca, W. D. 2009, ArXiv e-prints, arXiv:0909.0818
Rich, J. W., de Blok, W. J. G., Cornwell, T. J., et al. 2008, AJ, 136, 2897

Roe, H. G., Gavel, D., Max, C., et al. 2001, AJ, 122, 1636
Romani, P. N., Bishop, J., Bezard, B., & Atreya, S. 1993, Icarus, 106, 442
Romani, P. N., de Pater, I., & Atreya, S. K. 1989, Geophys. Res. Lett., 16, 933
Rosenqvist, J., Lellouch, E., Romani, P. N., Paubert, G., & Encrenaz, T. 1992, ApJ, 392, L99
Rothman, L. S., Gordon, I. E., Barbe, A., et al. 2009, J. Quant. Spec. Radiat. Transf., 110, 533
Sault, R. J., Teuben, P. J., & Wright, M. C. H. 2011, in Astrophysics Source Code Library, record ascl:1106.007, 6007
Seager, S., & Deming, D. 2010, ARA&A, 48, 631
Smith, B. A., Soderblom, L. A., Banfield, D., et al. 1989, Science, 246, 1422
Smith, M. D. 1998, Icarus, 132, 176
Sromovsky, L. A., Fry, P. M., Baines, K. H., & Dowling, T. E. 2001a, Icarus, 149, 435
Sromovsky, L. A., Fry, P. M., Boudon, V., Campargue, A., & Nikitin, A. 2012, Icarus, 218, 1
Sromovsky, L. A., Fry, P. M., Dowling, T. E., Baines, K. H., & Limaye, S. S. 2001b, Icarus, 150, 244
Sromovsky, L. A., Limaye, S. S., & Fry, P. M. 1995, Icarus, 118, 25
Stone, P. H. 1976, in Jupiter, 586
Tavenner, T., Chanover, N., Murphy, J., Norwood, J., & Roberts, L. C. 2004, in Bulletin of the American Astronomical Society, Vol. 36, AAS/Division for Planetary Sciences Meeting Abstracts #36, 1105
Toon, O. B., McKay, C. P., Ackerman, T. P., & Santhanam, K. 1989, J. Geophys. Res., 94, 16287
Visscher, C., & Moses, J. I. 2011, ApJ, 738, 72
Visscher, C., Moses, J. I., & Saslow, S. A. 2010, Icarus, 209, 602
Wallace, L. 1980, Icarus, 43, 231
Wizinowich, P., Acton, D. S., Shelton, C., et al. 2000, PASP, 112, 315
Yelle, R. V., Herbert, F., Sandel, B. R., Vervack, Jr., R. J., & Wentzel, T. M. 1993, Icarus, 104, 38
Yung, Y. L., Drew, W. A., Pinto, J. P., & Friedl, R. R. 1988, Icarus, 73, 516
Zahnle, K., Schenk, P., Levison, H., & Dones, L. 2003, Icarus, 163, 263